

Establishment of dynamic culture  
conditions for the fabrication of advanced  
*in vitro* tissue models.

Inaugural-Dissertation  
to obtain the academic degree  
Doctor rerum naturalium (Dr. rer. nat.)

submitted to  
the Department of Biology, Chemistry, Pharmacy  
of Freie Universität Berlin

by  
Marcus Lindner

Berlin, 2022



The research presented in this work was carried out from July 2017 to May 2022 under the supervision of Prof. Dr. Marie Weinhart at the Institute of Chemistry and Biochemistry of Freie Universität Berlin.

1<sup>st</sup> reviewer: Prof. Dr. Marie Weinhart  
Freie Universität Berlin

2<sup>nd</sup> reviewer: Prof. Dr. Rainer Haag  
Freie Universität Berlin

Date of Defense: 8<sup>th</sup> July 2022



## Statutory Declaration

I, Marcus Lindner, hereby declare that I have written the submitted thesis entitled “Establishment of dynamic culture conditions for the production of advanced *in vitro* tissue models” independently and that I have not used any sources or aids other than those indicated.

Berlin, 31<sup>st</sup> May 2022

---

Marcus Lindner



# Acknowledgements

First of all I want to thank Prof. Dr. Marie Weinhart, who made it possible to realize my doctoral thesis at Freie Universität and provided me with excellent scientific support during the time. Furthermore, I would like to thank Prof. Dr. Rainer Haag as co-reviewer of this thesis. I would like to thank all current and former members of the Weinhart group, both in Berlin and Hannover. Anna Laporte and Laura Elomaa: I would not have made it through the last weeks without you. A special thanks also goes to Anke Hoppensack, who guided me particularly in the early stages, but also beyond, and to Johanna Scholz, who keeps our bio lab running. I thank Katharina Achazi and Stefanie Wedepohl from Haag Group for scientific and non-scientific conversations. As part of the supervision of veterinary and biology students, I would like to thank Carlo Fasting, as well as Michael Tully, Christin Treiber and Ernesto Osario for chaotic, challenging but also fun hours. In addition, I would like to appreciate the members of the FU workshop for doing a great job. For the financial support, I would like to thank the Helmholtz Graduate School for Macromolecular Bioscience.

To my friends and family, my parents and my sister: It is difficult to put into words what you have contributed. I could never have done this work without your constant support and hope to be able to give something back someday. I am not able to express my gratitude for everything and what you mean to me, but you, Jany, deserve the last line in this chapter.



**Für meine Familie.**



# Contents

<b>List of Abbreviations</b>	<b>1</b>
<b>1 Introduction</b>	<b>3</b>
1.1 General aspects of <i>in vitro</i> models . . . . .	3
1.1.1 Cells . . . . .	4
1.1.2 2D <i>in vitro</i> models . . . . .	5
1.2 Refinement of <i>in vitro</i> models by increasing structural and compositional complexity . . . . .	5
1.2.1 Intercellular crosstalk . . . . .	5
1.2.2 Cell-matrix interactions . . . . .	7
1.2.3 Hydrogels to proceed from 2D to 3D . . . . .	9
1.2.4 Scaffolds to generate <i>in vivo</i> inspired 3D structures . . . . .	10
1.2.5 Thermoresponsive polymers for cell culture . . . . .	13
1.3 The transition from static to dynamic cell culture . . . . .	17
1.3.1 General aspects of stress and strain . . . . .	17
1.3.2 Stress and strain <i>in vivo</i> . . . . .	17
1.3.3 Cellular mechanosensing of stress and strain . . . . .	18
1.3.4 Implementation of dynamic culture conditions into <i>in vitro</i> models . . . . .	18
1.4 Where fluid flow meets cells . . . . .	21
1.4.1 Mucus . . . . .	22
1.4.2 Glycocalyx . . . . .	23
<b>2 Objectives</b>	<b>25</b>
<b>3 Publications</b>	<b>29</b>
3.1 Step-by-step development of a toolbox for dynamic cell culture . . . . .	30
3.2 Physiological shear stress enhances differentiation, mucus-formation and structural 3D organization of intestinal epithelial cells <i>in vitro</i> . . . . .	58
3.3 Flow-induced glycocalyx formation and cell alignment of HUVECs compared to iPSC-derived ECs for tissue engineering applications . . . . .	91
3.4 <i>In vitro</i> vascularization of hydrogel-based tissue constructs via a combined approach of cell sheet engineering and dynamic perfusion cell culture . . . . .	137
<b>4 Summary and Conclusion</b>	<b>161</b>

Short summary / Kurzzusammenfassung	165
References	169
List of Publications and Conference Contributions	181

# List of Abbreviations

<b>2D</b>	2-dimensional
<b>3D</b>	3-dimensional
<b>CFD</b>	computational fluid dynamics
<b>CNC</b>	computer numerical control
<b>dECM</b>	decellularized extracellular matrix
<b>DLP</b>	digital light processing
<b>ECM</b>	extracellular matrix
<b>EGE</b>	ethyl glycidyl ether
<b>FA</b>	focal adhesion
<b>FFS</b>	fluid flow-derived shear stress
<b>GAG</b>	glycosaminoglycans
<b>GI</b>	gastrointestinal
<b>GME</b>	glycidyl methyl ether
<b>HA</b>	hyaluronic acid, hyaluronan
<b>HDF</b>	human dermal fibroblast
<b>HS</b>	heparan sulfate
<b>hTERT</b>	human telomerase reverse transcriptase
<b>HUVEC</b>	human umbilical vein endothelial cell
<b>iPSC</b>	induced pluripotent stem cell
<b>MSC</b>	mesenchymal stem cell
<b>PA</b>	polyamide
<b>PC</b>	polycarbonate
<b>PCL</b>	polycaprolactone

<b>PDMS</b>	. . . . .	polydimethylsiloxane
<b>PEG</b>	. . . . .	poly(ethylene glycol)
<b>PGE</b>	. . . . .	poly(glycidyl ether)
<b>PLLA</b>	. . . . .	poly( <i>L</i> -lactic acid)
<b>PNIPAM</b>	. . . . .	poly( <i>N</i> -isopropylacrylamide)
<b>RGD</b>	. . . . .	tripeptide arginin (R), glycin (G), aspartate (D)
<b>SDS</b>	. . . . .	sodium-dodecyl-sulfate
<b>SLA</b>	. . . . .	stereolithography
<b>SMC</b>	. . . . .	smooth muscle cell
<b>TCP</b>	. . . . .	cloud point temperature
<b>TEER</b>	. . . . .	transepithelial electrical resistance
<b>WSS</b>	. . . . .	wall shear stress

# 1

## Introduction

### Contents

---

<b>1.1</b>	<b>General aspects of <i>in vitro</i> models</b>	<b>3</b>
1.1.1	Cells	4
1.1.2	2D <i>in vitro</i> models	5
<b>1.2</b>	<b>Refinement of <i>in vitro</i> models by increasing structural and compositional complexity</b>	<b>5</b>
1.2.1	Intercellular crosstalk	5
1.2.2	Cell-matrix interactions	7
1.2.3	Hydrogels to proceed from 2D to 3D	9
1.2.4	Scaffolds to generate <i>in vivo</i> inspired 3D structures	10
1.2.5	Thermoresponsive polymers for cell culture	13
<b>1.3</b>	<b>The transition from static to dynamic cell culture</b>	<b>17</b>
1.3.1	General aspects of stress and strain	17
1.3.2	Stress and strain <i>in vivo</i>	17
1.3.3	Cellular mechanosensing of stress and strain	18
1.3.4	Implementation of dynamic culture conditions into <i>in vitro</i> models	18
<b>1.4</b>	<b>Where fluid flow meets cells</b>	<b>21</b>
1.4.1	Mucus	22
1.4.2	Glycocalyx	23

---

### 1.1 General aspects of *in vitro* models

*In vitro* models are an integral part to study human development and investigate emergence of diseases.<sup>1,2</sup> Furthermore they play a central role in the process of drug development and are used to evaluate safety and efficacy of drug candidates.<sup>3,4</sup> To enhance the reliability of preclinical studies and overcome predictive and ethical issues concerning animal models, highly functional *in vitro* models are needed.<sup>5</sup>

### 1.1.1 Cells

Cells are the most important element for the construction of reliable *in vitro* models. An American biologist and anatomist and a pioneer in experimental embryology, Ross Granville Harrison was the first to report on the culture of animal cells outside the living organism by culturing embryonic neurons from frogs.<sup>6</sup> Since then, culture of innumerable mammalian and non-mammalian cells has been established, which can be distinguished between mortal and immortal depending on their origin and lifetime.<sup>7</sup>

Tumor-derived cell lines have the capacity for almost unlimited growth and are easy to culture.<sup>7</sup> Due to their origin, they are a valuable tool for cancer models<sup>8</sup> and despite alterations in their metabolism and functionality, also for other *in vitro* models.<sup>9</sup> To overcome the limited *in vivo*-like functionality of tumor-derived cell lines, adult somatic cells can be immortalized by delaying or abolishing cellular senescence.<sup>10</sup> This can be achieved by *e.g.*, transfecting the cells to enable expression of human telomerase reverse transcriptase (hTERT). The hTERT-immortalized cells have shown extended lifespan with only few karyotypic changes compared to native cells,<sup>11</sup> even though several studies have reported on their impaired cellular functionality.<sup>12–14</sup>

Primary cells are isolated from embryonic or adult tissues and exhibit higher cellular functionality than immortalized cells.<sup>15</sup> Nevertheless, their use is limited by the availability of (healthy) donor material and primary culture usually requires complex and costly supplementation.<sup>16</sup>

As an alternative to primary cells, induced pluripotent stem cells (iPSCs) were first reported by Takahashi and Yamanaka in 2006.<sup>17</sup> To generate iPSCs, adult cells from varying sources,<sup>18</sup> including hair (keratinocytes), urine (heterogeneous cell population), umbilical cord or peripheral blood are dedifferentiated by the aid of transcription factors (Oct3/4, Sox2, Klf4 and c-Myc).<sup>17</sup> They can then be again differentiated into various cell types other or identical to the progenitor cell type. The minimally-invasive harvest and quasi unlimited availability of the progenitor cells makes iPSCs a promising cell model system,<sup>19,20</sup> although their

culture is more complex compared to cancerous cells, their lifespan is limited and sufficient differentiation is needed.<sup>21</sup>

### 1.1.2 2D *in vitro* models

In general, simple 2-dimensional (2D) *in vitro* models are based on the monoculture of cells on 2D-culture substrates (Figure 1.1). These are for example commonly used for the assessment of compound toxicity or permeability in high throughput screenings.<sup>22</sup>

Immortalized human colorectal adenocarcinoma cells (Caco-2) have been the most extensively used model in the field of drug transport, bioavailability, as well as adsorption and absorption,<sup>23</sup> whereas studies on hepatotoxicity are usually conducted with primary human hepatocytes and immortalized HepaRG™ cells.<sup>24</sup> Nevertheless, it is well known that data obtained from 2D *in vitro* models comprising only a single cell type are difficult to interpret and transfer in context of *in vivo* applications.<sup>25</sup> Thus, in the last decades great efforts have been made to circumvent these limitations by development of reliable *in vitro* models with increased physiological relevance.<sup>3</sup>

## 1.2 Refinement of *in vitro* models by increasing structural and compositional complexity

Reliable *in vitro* models require functional cells that can maintain their *in vivo* behavior or mimic it as close as possible. To achieve this, recreating the cellular micro- and macroenvironment is of utmost importance.<sup>26,27</sup> This includes the implementation of biochemical factors by enabling cellular crosstalk<sup>28</sup> as well moving from flat 2D surfaces to 3D architectures.<sup>29</sup> Additionally, the cell culture conditions implementing physical cues or even the combination of the aforementioned factors can remarkably refine the *in vitro* models.<sup>30</sup>

### 1.2.1 Intercellular crosstalk

#### 1.2.1.1 Principle

Cellular communication can involve direct or indirect pathways including biomechanical and biochemical signaling.<sup>31</sup> Biomechanical intercellular signaling occurs,

once cells come into direct contact with each other. Under *in vitro* conditions, many cells show contact inhibition by *e.g.*, a reduction of proliferation when reaching confluency.<sup>32</sup> This also plays a fundamental role in the *in vivo* organization and maintenance of tissues.<sup>33</sup> The functionality of endothelial and epithelial tissue barriers usually depends on the formation of firm cellular junctions,<sup>34</sup> where intercellular contact is initiated via adherens junctions composed of cadherins and catenins and results in the formation of tight junctions involving occludins and claudins.<sup>35</sup> These resulting cellular junctions control the paracellular transport of the tissue barrier and can add intercellular biomechanical triggers to cells comparable to cell-substrate interactions, which downstream results in *e.g.*, reorganization and polarization of cells, a process called mechanotransduction.<sup>36</sup> Furthermore, a direct exchange of small molecules, such as ions or metabolites,<sup>37</sup> is facilitated by the formation of intercellular channels by connexin family proteins, called gap junctions.<sup>38</sup>

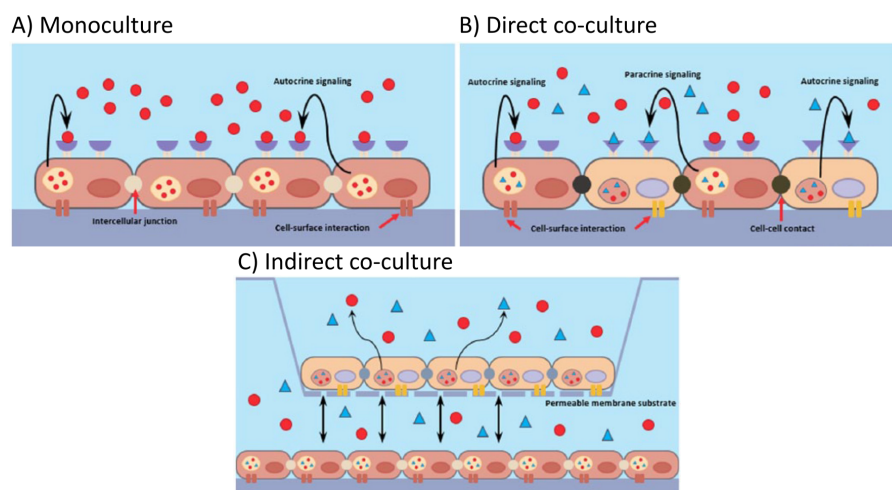


**Figure 1.1:** (a) Monoculture of a single cell type, (b) direct co-culture and (c) indirect co-culture with separated cells. Reprinted under a Creative Common Licence (CC BY-NC 4.0) from reference.<sup>39</sup>

Unlike the direct cell contact, indirect intercellular communication is accomplished via the secretion of bioactive signaling molecules that can be recognized via receptor-ligand-interaction and are translated into biochemical signals (au-

tocrine/paracrine signaling, Figure 1.1). Both the direct and indirect crosstalk play an essential role in cellular functionality and tissue homeostasis.<sup>40</sup>

### 1.2.1.2 Integration into *in vitro* models

The direct or indirect co-culture of different cell types integrates cellular crosstalk into *in vitro* models, thereby increasing their functionality and accordingly refining and enhancing obtained data in comparison to conventional monoculture.<sup>41</sup> This was demonstrated by Beduneau *et al.*, who established a direct co-culture of Caco-2 and HT29-MTX cells on membranes, thereby reflecting the two main cell types of the intestinal epithelium. The co-culture was closer mimicking the *in vivo* intestinal barrier function compared to individual monocultures, as proven by transepithelial electrical resistance measurements (TEER).<sup>42</sup> As a further example, Edling *et al.* established an *in vitro* model by the indirect co-culture of a monocytic cell line (THP1) and an adherent hepatoma cell line (Huh-7) and thereby demonstrated a higher sensitivity of both cell types in co-culture to troglitazone.<sup>43</sup> This former antidiabetic drug was withdrawn from the market by causing (*in vitro* undetected) hepatotoxicity.<sup>44</sup> Despite the benefits of *in vitro* co-culture models compared to monocultures, culturing cells on flat 2D surfaces remains problematic as cells interact with their surrounding non-cellular matrix in addition to intercellular signaling. Therefore, also the cell-matrix interactions are to be implemented in more advanced 3-dimensional (3D) *in vitro* models.<sup>45</sup>

## 1.2.2 Cell-matrix interactions

The biophysical microenvironment has a major impact on cellular differentiation and thus functionality.<sup>30</sup> In their natural environment, cells are arranged as 3D structures surrounded and supported by the tissue-dependent extracellular matrix (ECM).<sup>29</sup>

### 1.2.2.1 Structure and composition of the ECM

The ECM is a complex and dynamic hydrogel comprising a high content of water, with secreted and membrane-bound structuring components, including fibrous proteins (collagens, elastin), glycoproteins (laminins, fibronectins) as well as

glycosaminoglycans (GAGs), such as hyaluronan (HA) and heparan sulfate (HS).<sup>46</sup> It creates a functional network with narrow composition and mechanical properties, like stiffness and porosity, depending on its location.<sup>47</sup>

### 1.2.2.2 Cell-matrix interactions

Cells are able to sense and translate mechanical cues from the surrounding matrix to biochemical signals, which downstream affect various processes like proliferation, apoptosis, migration, adhesion and differentiation.<sup>46</sup> Therefore, cells need a mechanical connection to the surrounding substrate, which is mainly established by the formation of focal adhesions (FA). Initially, integrin heterodimers spanning the cell membrane interact with ECM proteins such as collagen, laminin and fibronectin. This interaction activates the integrins and initiates their clustering to form nascent adhesions.<sup>48</sup> Proteins like talin and vinculin connect cytoskeletal actin fibers to the integrin clusters and thereby allow cellular mechanosensing, which is a complex and multi-step process.<sup>49</sup> The sensing of *e.g.*, substrate stiffness can be illustrated as the cells pulling and dragging on their surrounding or underlying substrate through myosin-based contractility (Figure 1.2). Depending on the feedback, *i.e.* the deformability of the substrate, a complex signal cascade is set in motion.<sup>50</sup> In the human body, the elastic modulus of tissues is ranging from 0.1-1 kPa (brain) to 40 kPa (bone),<sup>51</sup> while polystyrene as the most commonly used cell culture substrate<sup>52</sup> resides in unphysiological ranges of substrate stiffness from 2 to 4 GPa.<sup>53</sup> Engler *et al.* demonstrated the influence of the substrate stiffness on the cell fate by showing a substrate elasticity-dependent neurogenic (brain), myogenic (muscle) and osteogenic (bone) differentiation of mesenchymal stem cells (MSCs) on collagen-coated polyacrylamide gels.<sup>51</sup> There are different approaches to implement materials with adjusted mechanical properties into *in vitro* models, including embedding the cells into a hydrogel or seeding them on pre-fabricated and shaped porous scaffolds.<sup>54</sup>

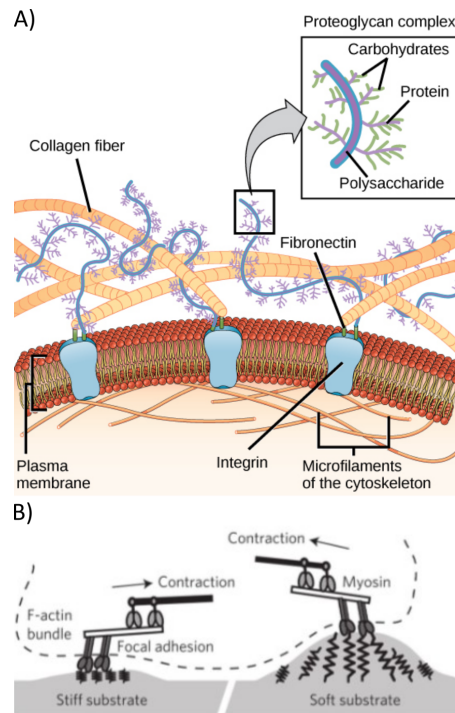


**Figure 1.2:** (a) Structure of extracellular matrix and (b) cellular sensing of substrate stiffness. (a) Reprinted under a Creative Common Licence (CC BY 4.0) from reference<sup>55</sup> and (b) adapted and reprinted with permission from reference.<sup>56</sup>

### 1.2.3 Hydrogels to proceed from 2D to 3D

In 1992, Petersen and Bissell were the first to report on human breast epithelial cells regaining their structural and functional phenotype when embedded into a 3D, ECM-based matrix.<sup>57,58</sup> Since then, a variety of materials including nature-derived biomaterials and synthetic materials have been developed to enable cell-cell and cell-matrix interactions through embedding (Figure 1.3).<sup>59</sup>

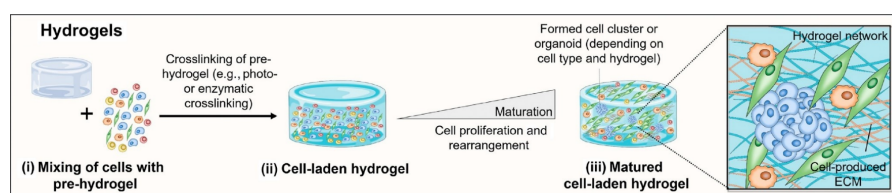


**Figure 1.3:** Illustration of cellular embedding to yield 3D hydrogel constructs. Adapted and reprinted under a Creative Common Licence (CC BY 4.0) from reference.<sup>54</sup>

### 1.2.3.1 Biomaterials

The most commonly used bio-derived hydrogel is Matrigel™. It is derived from a murine tumor that extensively produces ECM-proteins, with laminin and collagen IV as the main structuring components.<sup>60</sup> Due to its origin, the composition of Matrigel™ is complex, varies from batch to batch and comprises cancer-derived proteins with potential tumorigenicity.<sup>61</sup> Nevertheless, it is commonly used to maintain undifferentiated stem cells<sup>62</sup> and for *in vitro* tube-formation assays of human umbilical vein endothelial cells (HUVECs) to study angiogenesis.<sup>63</sup> Alternative biomaterials with more reliable compositions include purified ECM<sup>64</sup> or blood plasma proteins.<sup>65</sup> The advantages of biomaterials for 3D *in vitro* models reside in their intrinsic biocompatibility and cell-adhesiveness, while their compositional and mechanical variations and high costs limit their application.<sup>66,67</sup>

### 1.2.3.2 Synthetic hydrogels

Synthetic hydrogels used for *in vitro* models offer precise control of mechanical properties with defined structures and compositions.<sup>68-70</sup> One of the first synthetic materials for cell culture was polyacrylamide, which is commonly synthesized via free radical polymerization with bis-acrylamide and is still widely used today. The elasticity of polyacrylamide gels can be adjusted within a broad range (200 Pa-40 kPa), but cell-adhesion is only achieved via modification by *e.g.*, introducing RGD-peptides.<sup>71</sup> Polyethylene glycol (PEG) is another commonly used synthetic hydrogel, which also needs modification to enable cell adhesion. Nevertheless, its synthesis and post-modification are well established and defined and its low costs additionally contribute to its broad application in biomedical hydrogels.<sup>72,73</sup>

## 1.2.4 Scaffolds to generate *in vivo* inspired 3D structures

To provide cells with a biomimicking 3D environment, whole organs can be decellularized and recellularized to serve as scaffolds for the seeded cells. Detergents like sodium-dodecyl-sulfate (SDS) and Triton-X 100 are commonly used to remove cells from organs of different origins,<sup>74</sup> at best leaving behind a scaffold only

comprising native ECM-compounds. This scaffold can be then repopulated with cells of choice. The de- and recellularization approach is usually applied the field of regenerative medicine,<sup>75</sup> but has been also used to investigate drug delivery or as disease models to study pathogenesis.<sup>76–78</sup> However, due to restrictions in availability and scale of decellularized ECM (dECM) for high through-put studies, scaffolds for *in vitro* models are commonly manufactured from bio- or synthetic materials, populated with cells (Figure 1.4) and thus<sup>54</sup> implementing 3-dimensionality into *in vitro* models.<sup>79</sup>

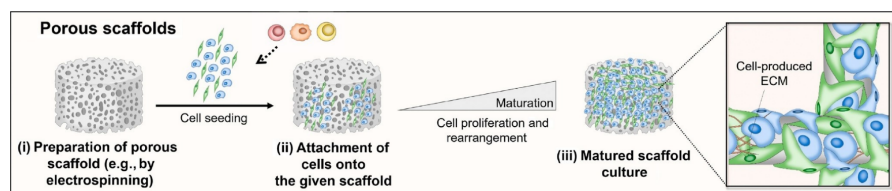


**Figure 1.4:** Illustration of porous scaffolds to enable shaped three-dimensionality to *in vitro* models. Adapted and reprinted under a Creative Common Licence (CC BY 4.0) from reference.<sup>54</sup>

#### 1.2.4.1 Manufacturing of scaffolds for tissue models

Scaffolds for the fabrication of *in vitro* models have certain requirements, including biocompatibility, narrow mechanical properties and a high porosity to enable nutrient diffusion as well as removal of metabolic waste.<sup>79–81</sup>

#### Conventional techniques

Conventional techniques to generate porous scaffolds from bio- or synthetic materials include *e.g.*, salt-leaching and freeze-drying methods.<sup>82</sup> In the salt-leaching, the solvent in a salt-containing polymer solution is evaporated, leaving behind a polymer/salt composite, from where the salt is further extracted with water. This method was successfully applied to generate scaffolds with up to 93% porosity.<sup>81</sup> In the freeze-drying (also called lyophilization), freezing of the polymer solution generates solvent crystals that are subsequently removed under vacuum via sublimation, leaving polymer scaffolds with up to 99% porosity.<sup>83</sup>

### Advanced techniques

Even though the conventional manufacturing techniques are simple and of low cost, they suffer from poor control over the pore architecture. With more advanced techniques, the pore size and shape can be better adjusted to result in well-defined scaffold structures. In the electrospinning process, an electric field between a nozzle and a collector is generated by subjection to high voltage. A polymer solution is dispensed through the nozzle, creating a fine jet that solidifies by solvent evaporation.<sup>84</sup> This results in a mesh-like anisotropic or isotropic structure with variable thickness and fiber-diameters ranging from nano- to micrometers.<sup>85,86</sup>

Another advanced and more recent way to manufacture well-defined porous scaffolds is 3D printing via different principles. For example, in fused deposition modeling, the filamented material is fed through a heated nozzle, forming pattern on a build platform in a layer-by-layer manner. In vat photopolymerization, including stereolithography (SLA) and digital light processing (DLP), liquid resins that contain photocrosslinkable monomers or polymers and a radical-forming photoinitiator form solid crosslinked layers upon light irradiation (Figure 1.5).<sup>87</sup>

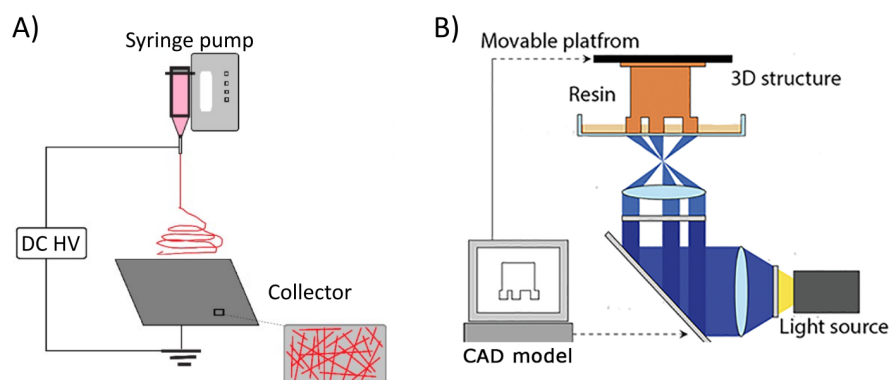


**Figure 1.5:** Manufacturing of scaffolds for *in vitro* models. Illustration of (a) electrospinning and (b) DLP-based 3D printing. (a) Adapted and reprinted under a Creative Common Licence (CC BY 4.0) from reference.<sup>88</sup>

### Materials

Like the conventional methods, all the advanced methods are able to generate scaffolds from both biological and synthetic materials as well as their blends. It is often

assumed that nature-derived biomaterials lack the necessary mechanical properties to yield well-defined scaffolds. A few studies have shown the feasibility of chemically modified biobased materials including alginate and HA,<sup>89</sup> as well as functionalized methacryloyl gelatin.<sup>90</sup> However, in direct comparison with synthetic polymers, lower shape integrities are observed.<sup>91</sup> The synthetic materials for hydrogels have the advantage of being tunable and well defined, but they commonly lack cell adhesive properties and therefore often require additional surface modification or functionalization. For hard tissue engineering, hydrophobic, mechanically stronger polymers, such as poly(*L*-lactic acid) (PLLA) and polycaprolactone (PCL) are commonly used instead of hydrogels.<sup>92,93</sup> The use of blends of two material types can eliminate the corresponding disadvantages of the other, as previously demonstrated ((dECM/PCL)<sup>90</sup> and (polysaccharide/PCL)<sup>94</sup> or (alginate/PEG)<sup>95</sup>).

With the aforementioned materials and fabrication methods, a wide range of 3D *in vitro* tissue models with varying structures and different levels of complexity can be generated. However, all of these models share a common feature: They are based on scaffolds that are populated with cells derived from single cell suspensions. The standard method to subculture and seed cells into the scaffolds relies on use of enzymes that via proteolytic activity disrupt cell-cell and cell-matrix junctions, including already produced ECM.<sup>96</sup> Non-enzymatic alternatives, such as a solution of chelating agents in combination with salts<sup>97,98</sup> and mechanical treatment by the application of acoustic pressure/ultrasound,<sup>99</sup> exist, but they are rarely applied and still disrupt the cell-cell junctions.

### 1.2.5 Thermoresponsive polymers for cell culture

Another enzyme-free and non-invasive approach to detach single cells as well as confluent cellular monolayers, known as cell sheets, is based on using surfaces coated with trigger-responsive polymers.<sup>100</sup> To facilitate cellular detachment, trigger-responsive systems need to switch from a cell-adherent to a cell-repellent state provoked by an external factor, which can be diverse and includes *e.g.*, the exposition to light<sup>101</sup> or a change in pH.<sup>102,103</sup> However, the most commonly used responsive

polymers to detach cells from surfaces are triggered via thermal changes, so-called thermoresponsive polymers.<sup>100,104</sup>

### 1.2.5.1 General aspects

The principle of thermoresponsive polymers lies in their solubility change upon changing temperature.<sup>105</sup> The homogeneous polymer/solvent system undergoes a transformation into a heterogeneous two-phase system by segregation of the polymer and solvent; the specific temperature at which this phase transition occurs is referred to as the phase transition or cloud point temperature (TCP) (Figure 1.6). The TCP of a thermoresponsive polymer can be defined by adjusting its composition and molecular weight, and it furthermore depends on its concentration (weight or volume fraction) and the solvent system.<sup>106</sup> To be applied in cell culture processes, the TCP needs to be in a physiological temperature range, ideally above room-temperature and below 37 °C.<sup>96</sup> Thermoresponsive surface coatings can be prepared in different ways, including grafting the polymer from the surface via polymerization (grafting-from) and grafting of synthesized polymers to the surface (grafting-to).<sup>107</sup>

### 1.2.5.2 Common thermoresponsive polymers for cell culture application

#### Poly(*N*-isopropylacrylamide)

The best characterized and most widely used polymer for cell detachment is poly(*N*-isopropylacrylamide) (PNIPAM) (Figure 1.6). First published by Yamada *et al.*,<sup>108</sup> it was successfully applied to detach cells from different origins, including endothelial cells<sup>109</sup> and epithelial cells<sup>110</sup> and is commercially distributed in various formats under the trademark Nunc™. The TCP of PNIPAM is approximately 32 °C, and remains mostly unaffected by molecular weight.<sup>111</sup> Thermoresponsive coatings of PNIPAM are usually generated from aqueous polymer solutions via electron beam irradiation, which results in the formation of polymer gels.<sup>112</sup> Besides the requirement of costly equipment,<sup>113</sup> this grafting-from approach is rather uncontrolled and leads to a gel-like polymerization with unpredictable configuration.<sup>114</sup> This, along with

biocompatibility concerns<sup>115</sup> and need for additional surface coatings with ECM-compounds,<sup>116</sup> has motivated the development of alternative thermoresponsive polymers for the use in cell culture.

### Poly(glycidyl ethers)

Thermoresponsive poly(glycidyl ethers) (PGE) copolymerized from glycidyl methyl ether (GME) and ethyl glycidyl ether (EGE) monomers were first described as surface coatings for cell culture by Weinhart *et al.* in 2010 (Figure 1.6).<sup>96</sup> By introducing a hydrophobic photoreactive anchor block including benzophenone, the polymer can be adsorbed to bare polystyrene, a process called physisorption, and immobilized via UV-irradiation.<sup>117</sup> This grafting-to approach yields highly reproducible and defined thermoresponsive coatings. The TCP as well as layer thickness and other parameters can be precisely controlled by *e.g.*, the polymers' molecular weight and co-monomer ratios.<sup>118</sup> PGE-coated surfaces have shown excellent cell-adhesive properties without additional precoating and have been successfully implemented to culture and detach cells of various origins, including fibroblasts, smooth muscle cells (SMCs) and endothelial cells.<sup>119</sup>

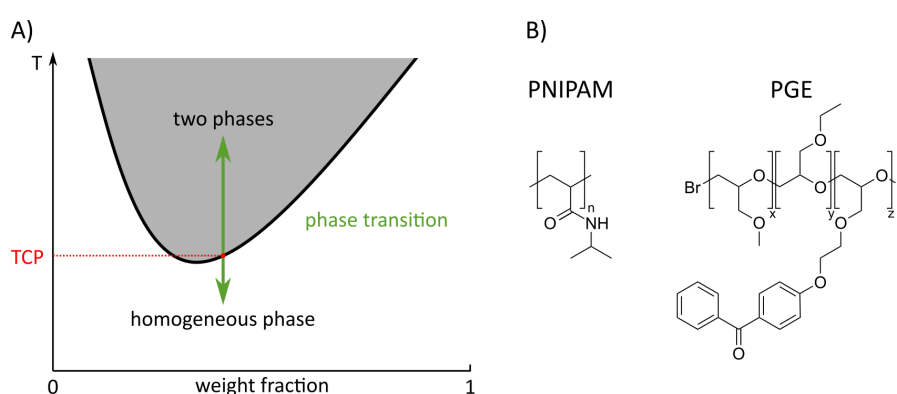


**Figure 1.6:** (a) Illustration of phase transition and TCP in a phase diagram and (b) examples of thermoresponsive polymers.

#### 1.2.5.3 Development of 3D *in vitro* models utilizing cell sheets

Intact cell sheets harvested from thermoresponsive polymers enable the construction of both scaffold-based and scaffold-free *in vitro* models.<sup>120,121</sup> Due to their fragility, the application of single cell sheets is mainly restricted to regenerative medicine

in the form of transplantation as shown with human corneal endothelial cells<sup>122</sup> and primary hepatocytes.<sup>123</sup> Only a few studies utilized single cell sheets for the construction of *in vitro* models. Sekine *et al.* investigated the differentiation of cell sheets obtained from human endometrial gland-derived mesenchymal stem cells (MSCs) into chondrocytes. Even though harvested as a single sheet, the cellular layers had a multilayered appearance due to cellular contraction.<sup>124</sup>

### **Stacking as a scaffold-free approach**

An increased stability of the cell sheets can be obtained by stacking several cell sheets to yield 3D models or by combining harvested cell sheets with a supporting scaffold. Tsuda *et al.* constructed a multilayered model including human dermal fibroblasts (HDFs) and HUVECs and demonstrated the formation of vessel-like vascular structures.<sup>125</sup> Additionally, the endothelial migration of HUVECs into multilayered human skeletal muscle myoblast constructs was investigated by Ngo *et al.*<sup>126</sup>

### **Wrapping as a scaffold-based approach**

The combination of cell sheets with scaffolds can be addressed by rolling or wrapping the sheets around a pre-shaped 3D construct. Kubo *et al.* reported on the construction of an advanced *in vitro* heart model by wrapping sheets of neonatal rat ventricular cardiomyocytes around a fibrinogen-based tubular scaffold and demonstrated dense cell layers with synchronized pulsation.<sup>127</sup> Furthermore, a blood vessel mimic comprising primary human aortic smooth muscle cells wrapped around an electrospun PCL-scaffold was proposed by Rayatpisheh *et al.*<sup>128</sup> The aforementioned methods demonstrate the capacity to generate advanced 3D *in vitro* models with higher functionality compared to conventional 2D models. Nevertheless, the implementation of external biophysical triggers remains to be included, providing *in vitro* tissue models with a further refinement.

## 1.3 The transition from static to dynamic cell culture

Cells in multicellular organisms are permanently exposed to external and internal mechanical forces and stress.<sup>30</sup> These external biophysical triggers influence cell fate and are essential for tissue functionality and development.<sup>129</sup> The mechanical stimuli can arise from various origins, including *e.g.*, the (cyclic) compression and tension of cellular substrate and fluid flow-derived shear stress as well as osmotic pressure gradients<sup>130</sup> or hydrostatic fluid pressure.<sup>131</sup> In addition, selected cells such as muscle cells<sup>132,133</sup> or contractile fibroblasts<sup>30,134</sup> are capable of generating intrinsic contractile forces.

### 1.3.1 General aspects of stress and strain

Stress is defined as the ratio of applied force to the cross-sectional area of the material and is usually reported in Pa ( $\text{N m}^{-2}$ ) or  $\text{dyn cm}^{-2}$  (equivalent to  $1 \times 10^{-1}$  Pa). Cells can experience two different types of stress, with the force acting perpendicular to the surface (normal stress) or parallel to it (shear stress). The latter occurs from fluid motions parallel to the cellular surface, causing a flow-derived wall shear stress (WSS). Strain, on the other hand, is defined as the change in length of an object relative to its initial state and is therefore dimensionless. Cells are facing strain by the compression and tension of their surrounding ECM/matrix (Figure 1.7).<sup>135</sup>

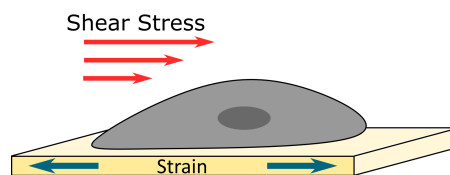


**Figure 1.7:** Illustration of stress and strain.

### 1.3.2 Stress and strain *in vivo*

Fluid flow-derived shear stress is often associated with blood flow in the vascular system, but also occurs in the lung, kidney, lymphatic system and the intestine with varying magnitudes. Endothelial cells lining all vascular vessels are subjected to

varying shear stress depending on their location and vessel-type, ranging from 1 up to 70 dyn cm<sup>-2</sup> in venous and arterial vascular networks, respectively.<sup>136</sup> Air-facing epithelial cells in the lung are exposed to approximately 0.5-3 dyn cm<sup>-2</sup>,<sup>137</sup> whereas epithelial cells in kidneys are facing approximately 0.1-1 dyn cm<sup>-2</sup> depending on the glomerular filtration rate.<sup>138</sup> Ingested and digested fluids cause even lower shear with dimensions about 0.002-0.08 dyn cm<sup>-2</sup>.<sup>139</sup> Furthermore, interstitial flow, which is slow travel of liquid through ECM is estimated to be in a range of several 10<sup>-3</sup> dyn cm<sup>-2</sup>.<sup>140</sup> Substrate strain primarily occurs in the lung and is estimated to range from 1-5% for alveolar epithelial cells at rest,<sup>141</sup> but it also appears in the gut<sup>142</sup> and to a small extent in blood vessels.<sup>143</sup> Besides stress and strain, cells are subjected to other physical cues, including hydrostatic pressure in capillaries<sup>144</sup> and the lymphatic system<sup>131</sup> as well as osmotic pressure in renal collecting tubules.<sup>145</sup>

### 1.3.3 Cellular mechanosensing of stress and strain

According to the mechanism of sensing mechanical properties of cell-matrices, the cellular mechanosensing of fluid flow involves complex processes and has not yet been fully deciphered. Glycocalyx components, directly or indirectly coupled with the cytoskeleton, were identified as mechanosensors of endothelial cells. The enzymatic removal of cellular HS or HA is causing a loss of shear-induced HUVEC alignment and elongation,<sup>146,147</sup> which typically protects the cells and maintains endothelial barrier function.<sup>136</sup> In contrast, kidney epithelial cells comprise hair-like projections of the cell surface, known as primary cilia, which sense external flow by bending.<sup>148,149</sup> Up to now, intestinal mechanosensing is barely understood and mechanisms as well as sensors remain unidentified.<sup>150</sup>

### 1.3.4 Implementation of dynamic culture conditions into *in vitro* models

#### 1.3.4.1 Early examples of stress and strain in cell culture

The culture of cells in the presence of physical stimuli has found its early application. Krueger *et al.* demonstrated the effect of fluid flow-derived shear stress (FFS) in a

parallel plate flow setup, applying  $10^{-3}$  to  $10 \text{ dyn cm}^{-2}$  on madin darby bovine kidney cells and by subsequently observing alterations in their morphology and migration.<sup>151</sup> In 1985, Banes *et al.* showed that cyclic stress by only 0.13% compression of plastic substrate generated with vacuum affected the actin and tubulin synthesis in primary cells from chicken tendons.<sup>152</sup> The vacuum principle to generate substrate strain is widely applied in various formats and models. The substrate can either be membranes comprising barrier functions or bulk materials without barrier function. For both, polydimethylsiloxane (PDMS) material is often applied, with thicknesses ranging from tens of micrometers up to millimeter-scale,<sup>153,154</sup> and stretching frequencies and resulting strains up to 5 Hz and 60%, respectively.<sup>155,156</sup>

#### 1.3.4.2 Pumps to generate fluid flow

The fluid flow in cell culture can be generated in different ways. Gravity-, surface tension- and osmosis-driven pumps are passive examples, which are easy to implement and of low costs, although they usually suffer from either low flow rates, short operating times or inconstant flow patterns.<sup>157</sup> For continuous cell culture under laminar flow conditions, active fluid transport is required. Syringe pumps are convenient in their implementation and operation, but they usually allow only open flow circuits without recirculation<sup>158</sup> and thus without conditioning of cell culture medium. Unlike the syringe pumps, peristaltic pumps allow recirculation of the media,<sup>159</sup> and their non-invasive pump principle prevents a direct contact of the pump with liquid to be transferred.<sup>160</sup>

#### 1.3.4.3 Microfluidic devices

Many groups have developed different microfluidic systems, commonly referred to as “lab-on-a-chip” or “organ-on-a-chip” systems with channel-dimension in micrometer-sizes.<sup>161</sup> There, the fluid flow is generated via syringe pumps<sup>158</sup> as well as external<sup>159,162</sup> and internal<sup>163</sup> (“on chip”) peristaltic pumps. The numerous advantages of microfluidic system include for example their small scale, low required cell number, precise control over the flow conditions and other process parameters, as well as advanced structural complexity by the implementation of different cell

compartments and additional physical cues.<sup>163–165</sup> However, the use of microfluidic systems is still difficult to standardize, and most platforms include or are even completely made of PDMS, which may interfere with study design due to its hydrophobic adsorption and absorption.<sup>166</sup> Additionally, manufacturing of microfluidic devices involves complex manufacturing procedures and requires expensive equipment.<sup>167</sup>

#### 1.3.4.4 Millifluidic devices

Millifluidic devices, which are typically easier to handle and allow rapid prototyping and manufacturing, are a valuable alternative to the microfluidics and enable the use of standard cell culture substrates. They provide an accessible and easily customizable system to apply shear forces to cells and thereby generate advanced *in vitro* tissue models.

#### Commercially available millifluidic devices

Quasi-Vivo is a commercially available system from Kirkstall (York, UK) comprising different designs of “bioreactor systems” for various applications, including dynamic culture of cell-populated scaffolds or single and double-circuit flow on or through.<sup>168</sup> Nithiananthan *et al.* studied physiological flow conditions ( $3.61 \times 10^{-5}$  dyn cm<sup>-2</sup>) on oral and dermal fibroblasts and demonstrated their enhanced differentiation as judged by immunofluorescent staining and mRNA-levels of selected markers.<sup>169</sup> Additionally, Miranda-Azpiazu *et al.* created a co-culture system including human brain primary endothelial cells, pericytes and astrocytes to investigate individual functionality of cells comprising the blood-brain barrier under flow conditions of  $2 \times 10^{-5}$  dyn cm<sup>-2</sup>.<sup>170</sup> Unfortunately, characterization of the system via computational fluid dynamic (CFD) simulation revealed rather inhomogeneous flow conditions<sup>171,172</sup> and the setup could be reused a maximum of 3 times, according to manufacturer. Ibidi (Gräfelfing, GER) offers various flow channels with well-defined geometries and flow conditions in a standard microscope slide format, traded as  $\mu$ -slides. This system can address various scientific questions and is widely used.<sup>173–175</sup> However, in addition to being solely for single use only, the chambers for high shear stress are usually completely closed and open channels allow applications of only low

shear stress, which limits their output. To overcome these limitations, convenient culture chambers in a millifluidic format that can be used to apply shear stresses on standard cell culture substrates are needed.

### **Material for the fabrication of millifluidic cell culture chambers and their requirements**

The main critical material properties for the fabrication of millifluidic cell culture chambers, including their biocompatibility and mechanical properties, are similar to those in the construction of 3D *in vitro* models, but must fulfill different requirements. Ideally, the cell culture chambers are reusable while withstanding repeated sterilization processes like autoclaving and therefore need high mechanical load capacity. Commonly used materials include glass and various plastics, such as polycarbonate (PC), polypropylene or nylon 66 (polyamide, PA).<sup>163,176,177</sup> In addition, to connect the culture chambers into a fluid flow circuit, materials for tubing must be carefully selected (Section 3.1). The requirements for hoses are diverse and mainly include abrasion resistance when operated in a peristaltic pump<sup>178</sup> and gas permeability to enable sufficient supply of cells with oxygen.<sup>179</sup> Silicone is the most commonly used tubing material in biomedical research.<sup>180</sup>

## **1.4 Where fluid flow meets cells**

Cells possess numerous protective mechanisms to avoid damage from external and internal factors. Epidermal melanin, for example, functions as a photoprotector in the skin by adsorbing harmful UV irradiation.<sup>181</sup> Accordingly, endothelial and epithelial cells comprising cellular barriers and interfacing FFS need protection.<sup>182,183</sup> Although this is widely known, these interfaces are often neglected in *in vitro* barrier models.<sup>184</sup> The following concluding section focuses on the cellular interfaces where shear forces meet cells, with emphasis on the gastrointestinal (GI) mucus and the endothelial glycocalyx.

### 1.4.1 Mucus

Mucus is a highly dynamic hydrogel with up to 95% water content, which can be found on every wet surface of epithelial cells in the human body,<sup>185</sup> including the eyes,<sup>186</sup> reproductive tract<sup>187</sup> as well as lung<sup>188</sup> and GI tract.<sup>182</sup> Dimension and composition of the GI mucus varies according to its location, with membrane-bound or secreted high molecular weight glycoproteins, mucins, representing its main structural element. For a long time, only mechanical protection of the underlying epithelium was functionally attributed to the GI mucus. Detailed investigations revealed a variety of additional functions, such as hosting commensal bacteria while simultaneously suppressing growth of pathogens.<sup>189</sup> *In vitro* models cultured under conventional static conditions are usually lacking mucus, or unphysiological mucus thicknesses are reported.<sup>190,191</sup> Especially intestinal *in vitro* models that are used to evaluate the adsorption and reabsorption as well as pharmacokinetics of drug candidates are usually comprising only Caco-2 cells that represent enterocytes without being able to generate mucus.<sup>192</sup> Even though it is known from literature that dynamic culture conditions enhance mucus production,<sup>190</sup> common mucus models are still suffering from low thicknesses or require complex equipment to achieve the desired mucus layer (Section 3.2).

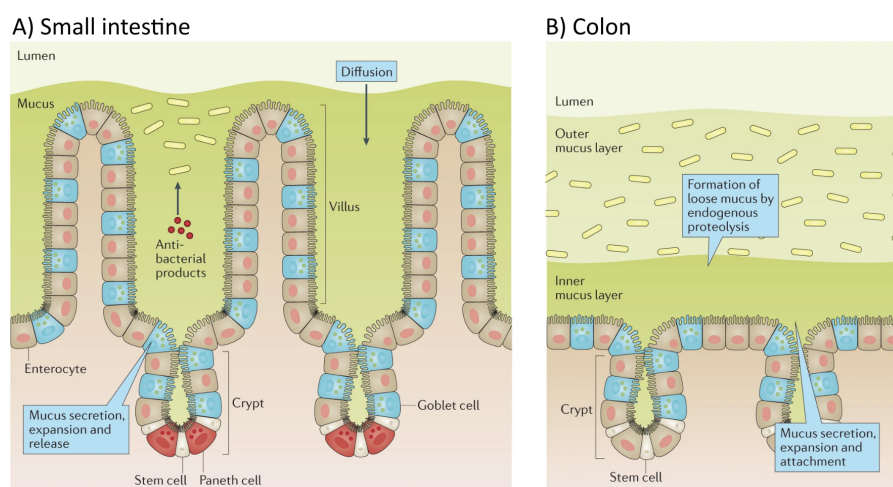


**Figure 1.8:** Illustration of the mucus structure in the (a) small intestine and (b) colon. Adapted and reprinted with permission from reference.<sup>193</sup>

### 1.4.2 Glycocalyx

The endothelial glycocalyx is a membrane bound, mesh-like hydrogel composed of different glycoproteins, proteoglycans and GAGs.<sup>183</sup> It interacts with circulating proteins like albumin<sup>194</sup> and is modulated by fluid flow-induced surface shear stress.<sup>195</sup> It comprises different vasculoprotective functions like the inhibition of coagulation<sup>196</sup> and leukocyte adhesion under physiological conditions.<sup>197</sup> A loss of glycocalyx, besides others, initiates the repair of damaged vascular vessels by enabling the interaction of leukocytes and platelets.<sup>198</sup> The glycocalyx regulates the vascular permeability by steric hinderance of substances as well as electrostatic repulsion through its net-negative charge,<sup>199</sup> and several glycocalyx components, such as HS and HA, are involved in mechanosensing.<sup>200–202</sup> Due to its various important functions, functional *in vitro* models mimicking the endothelial barrier require an intact glycocalyx layer with *in vivo* like dimensions and composition (Section 3.3).

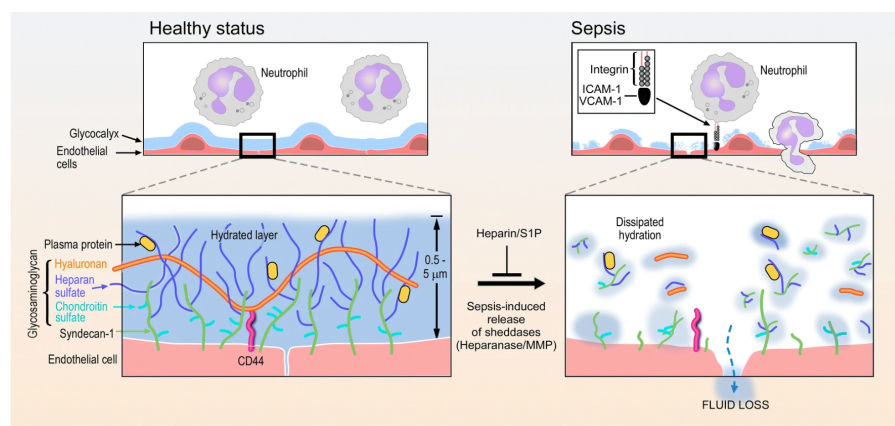


**Figure 1.9:** Illustration of endothelial glycocalyx under physiological and pathological conditions. Reprinted under a Creative Common Licence (CC BY 4.0) from reference.<sup>203</sup>



# 2

## Objectives

Conventional cell culture techniques, particularly 2D monoculture under static conditions, are limited in their ability to generate physiologically relevant *in vitro* models of endothelial and epithelial barriers.<sup>204</sup> In fact, there is a need for reproducible and easily accessible ways to implement fluid flow using commercial substrates which can enhance cellular functionality to overcome these limitations. A convenient technical setup as well as easy-to-use, well-characterized and adaptable cell culture chambers capable of applying native fluid shear stress would be highly needed to improve the physiological relevancy of *in vitro* cell culture studies. Therefore, the overall aim of this thesis was to

1. build a versatile system for the application of physiological fluid-derived shear stress to anchorage-dependent mammalian cells.
2. develop and characterize easy-to-use chambers for the dynamic culture of mammalian cells on various substrates.
3. examine the influence of shear stress on human endothelial and epithelial cells for the fabrication of advanced barrier models.

To achieve and implement these aims with meeting the aforementioned requirements, the first step includes the establishment of an economical and reliable circuit to apply fluid flow in place, *i.e.*, in the cell culture incubator. This involves the generation of the flow and in particular the design, manufacturing, and characterization of the cell culture chambers. For this purpose, suitability of conventional and advanced manufacturing techniques for the fabrication of cell

culture chambers for medium flow circuits will be compared in this thesis, including particularly CNC-milling and 3D printing. The comparison includes evaluation of the achievable chamber geometries and the processable materials. The requirements of the material are comprehensive and range from general aspects like biocompatibility to application-specific parameters, such as resistance to repeated sterilization or optical transparency for imaging. Accordingly, common materials, such as glass and thermoplastic polymers, as well as appropriate elastomeric materials for tubing require careful selection and validation. This goes along with the design of the culture chambers, which at best are reusable and allow cell culture on standardized solid and membrane-comprising substrates. Depending on the system to be modeled, the cell culture chambers can be evaluated in detail via mathematical approximations and computational fluid dynamics with respect to their flow conditions as well as the application of physiologically relevant shear forces. Iteratively, the chambers will be functionally evolved with respect to the implementable substrate as well as the biological output. Substrates could be, for example, simple microscope slides that allow the application of shear forces on cells on solid substrates as well as membrane-comprising cell-culture inserts for barrier models. From the biological perspective, cell lines that are easy to handle and extensively studied will be used to validate the selected materials and the whole circuit in ensemble. Demonstrating first the capacity of dynamic culture to enhance the functionality of these simple cell models will lay the foundation to proceed to more sophisticated cell types, including primary and stem cell-derived differentiated cells. The setup and consequently the models will successively be refined by enhancing the biological output and including cellular crosstalk. Likewise, the use of hydrogels as well as the combination of thermoresponsive surfaces with flow culture could be an interesting approach towards 3-dimensionality, which has not yet been implemented. For precise characterization of the dynamically grown cells, the establishment of appropriate quantitative and qualitative methods is necessary. These can be multifaceted and include, for example, immunofluorescence staining followed by high-resolution microscopy to visualize and evaluate the structure and composition

of cellular barrier layers as well as cell-cell and cell-matrix interactions. Appropriate assays for in-depth evaluation of critical parameters, such as proliferative capacity of cells and their differentiation and functionality, will be established. Quantitative methods for the investigation of metabolic activity and validation of the barrier function of the cells are also conceivable, but not limited to this. Overall, this work will provide a convenient basis to construct 3-dimensional, reliable, and functional *in vitro* models mimicking human endothelial and epithelial barriers.



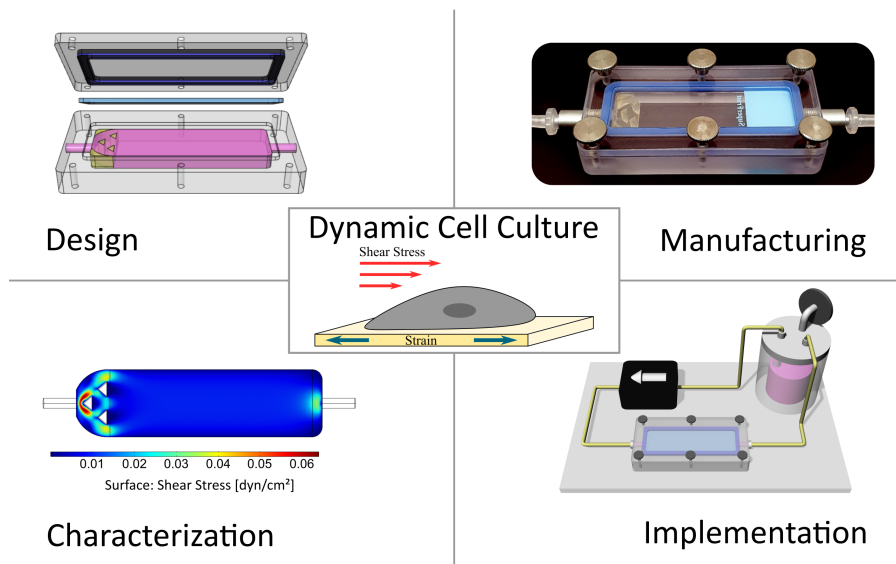
# 3

## Publications

This thesis and included publications deal with the establishment and characterization of a convenient system to implement physiological fluid-flow derived shear stresses to anchorage-dependent mammalian cells. Unless otherwise stated, the individual projects were conceptualized by the author and Prof. Dr. Marie Weinhart.

### 3.1 Step-by-step development of a toolbox for dynamic cell culture

This manuscript describes the technical establishment of a system for generating physiological shear forces and the design of culture chambers. Except for the CNC milling, which was done by the institutes' workshop, all practical tasks, CAD modelling and CFD simulation were carried out by the author. The manuscript was written by the author and reviewed and edited by Dr. Laura Elomaa and Dr. Anna Laporte.



# Step-by-Step Development of a Toolbox for Dynamic Cell Culture

## Abstract

To develop reliable *in vitro* models for varying applications, it is crucial to mimic physiological, *in vivo*-like conditions in cell culture, especially including various biomechanical cues. Particularly important is the application of relevant flow-induced shear stress that resembles the biophysical environment of cells. In this work, we provide step-by-step guidance for establishing dynamic culture conditions, starting from building an apparatus to generate flow and selecting materials to set up a flow circuit. Next, we introduce the design, characterization, and fabrication of millifluidic flow chambers for various cell culture substrates and applicable shear stresses. We herein focus on presenting essential points for all necessary steps, adding personal experiences on different issues and referring to appropriate literature for in depth exploration of the individual topics.

## 1. Introduction to Dynamic Cell Culture

Cells *in vivo* are exposed to a variety of internal and external mechanical forces, and their ability to respond and adapt to stress induced by, for example, breathing or muscle contraction is fundamental for their development and survival.<sup>[1]</sup> Besides the substrate compression and tension, one of the most important mechanical triggers is shear stress on surfaces generated by moving fluids in the body (**Figure 1**).<sup>[2]</sup>

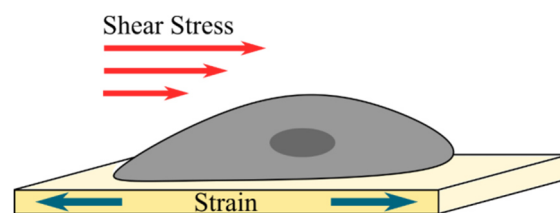


**Figure 1:** Illustration of shear stress caused by fluid flow and strain in connection to substrate compression and tension acting on a surface-attached cell.

In conventional two-dimensional *in vitro* culture of mammalian cells, it is evident that the mechanical input is limited by several factors, such as the underlying substrate of the cells,<sup>[3]</sup> intercellular forces between neighboring cells,<sup>[4]</sup> and the osmolarity of the medium.<sup>[5]</sup> The idea of including additional mechanical triggers into cell culture was introduced in the 70s, when cells were for the first time exposed to defined fluid flow and cyclic stretching of their substrate.<sup>[6-7]</sup> An easy way to apply fluid flow-derived shear stress in cell culture is the use of shakers. Besides the actual device, no further equipment is required in addition to the standard cell culture materials. However, this simplicity is also its major disadvantage, namely that the applied stress is inhomogeneous, unspecific and the flow is non-laminar, if not turbulent.<sup>[8-9]</sup>

In the following, we will focus on the use of liquid handling pumps that can be employed instead of the simple shakers<sup>1</sup>. These allow the generation of a constant or pulsatile medium flow under laminar conditions, applying a well-defined physical cue to the cell. However, the typical setup of such a dynamic cell culture system is more complex, consisting of a pump, one or more cell culture chambers,

---

<sup>1</sup>Other ways for liquid transports e.g., gravity or osmosis-driven, are comprehensively reviewed in ref.<sup>[11]</sup>

tubing and adapters. This circuit can be either open or closed, with the latter being characterized by the possibility of medium recirculation and can therefore be especially valuable for long-term dynamic culture.

In dynamic cell culture, the use of inexpensive and easy-to-operate syringe pumps is suitable for the application of very low shear stresses. Although technically feasible,<sup>[10]</sup> syringe pumps are mainly operated in open systems without recirculation, which limits their use in long-term application of shear stress. Therefore, peristaltic pumps are frequently employed to generate fluid flow over a prolonged period of time.<sup>[11]</sup> Commercially available devices that can be operated in the incubator are available, but they can be inconvenient in terms of size and bulkiness, and usually allow operation only at a single pump speed. Advanced systems, such as the ibidi® Pump System, are superior in terms of precision and versatility, as they allow uniform, oscillating, or pulsatile flow and can be based on an air-pressure pump. However, these systems are rather expensive to acquire (>10,000 €; [www.ibidi.com](http://www.ibidi.com)).

To provide alternatives to the current commercial systems, we will introduce the set-up and configuration of a simple and flexible controller that allows operation of up to four peristaltic pumps independently in the following section. The costs of this system amount to little more than the price of the individual pump heads. Furthermore, we describe in detail all necessary components including principles, production and materials for the construction of a dynamic culture circuit. This is complemented by an introduction to the design and manufacturing of culture chambers using CAD modeling and 3D printing as well as their final characterization using CFD simulation. In addition, four various culture chambers developed in our group will be portrayed, summarizing the rationale behind the design and their application.

## 2. Peristaltic Pumps: Principle and Operation

### *2.1 Basics of Peristaltic Pumps*

In the body, propulsive peristalsis is defined as wave-like contraction of muscles that moves the contents of hollow organs. It is often associated with the digestive tract (e.g. the esophagus, stomach, and intestine), but is also observed in urine transport from the kidney to the urinary bladder.<sup>[12-13]</sup> Similarly to the body, the peristaltic pumps, which belong to the category of positive displacement pumps, use this principle as illustrated in **Figure 2**. In a peristaltic pump, a flexible tube is pushed against a wall by a rotor with external rollers, which is the reason for these pumps commonly being referred to as roller pumps. The closing of the hose and the continuous movement recapitulates the peristaltic muscle contraction and results in liquid flow with negative pressure on the inlet side and positive pressure on the outlet.<sup>[14]</sup>

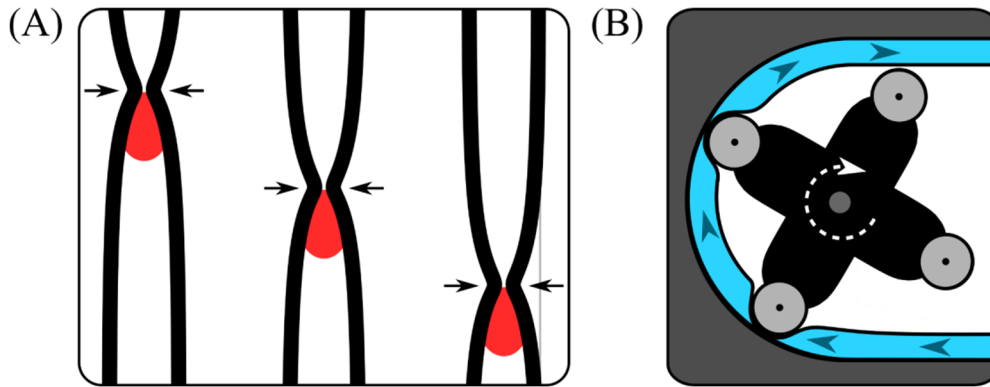


**Figure 2:** Illustration of (A) propulsive peristalsis in a hollow tube created by wave-like contractions and (B) basic principle of a peristaltic pump comprising a rotor with four connected rollers.

The principle of peristaltic pumps is their greatest advantage for the use in bioprocesses: The pump itself does not come into direct contact with the pumped liquid, which on the one hand protects components of the pump from corrosion and on the other hand prevents contamination of the liquid inside the tube.<sup>[11]</sup> Every peristaltic pump must be driven by a motor, the most common of which are conventional direct current (DC) motors and stepper motors. The former are relatively easy to control in constant pump speeds, but their disadvantage lies in their maintenance requirements and their tendency to fail especially at relative humidity >90%, which exists in cell culture incubators.<sup>[15]</sup> Contrary to the DC motors, the stepper motors need little maintenance and can be operated at temperatures of 40-60 °C under normal conditions, which counteracts condensation in the incubator<sup>2</sup>. Furthermore, they have the required torque at low pump speeds. The stepper motors work on the following principle: One revolution of the motor is divided into  $n$  steps, usually 200 or 400, and electromagnets are arranged circularly/radially around a permanent magnet to move it step by step with the help of a moving axis. The electromagnets are controlled with a special stepper motor driver.<sup>[16]</sup>

## 2.2 Construction of the pump control with the help of Arduino microcontroller

### Hardware/Material

The pump control in our circuit is based on the open-source hardware platform Arduino. It comprises a microcontroller (Arduino Uno Rev 3, Arduino S.r.l, Monza, Italy) that is extended with a pluggable computer numerical control (CNC) shield. This shield (CNC shield v3, SIMAC Electronics GmbH, Neukirchen-Vluyn, Germany) was originally developed for CNC milling and has the ability to control four stepper motors independently with plug-on motor drivers (A4988, Pololu Robotics and Electronics, Las Vegas, NV/USA). A separate LED driver (24V, 4.2A, MeanWell, New Taipei, Taiwan) was used to supply the stepper motors, and this setup was able to control different peristaltic pump models, including Model 114 ST (Watson Marlow, Falmouth, UK) as well as Model 15QQ (Stepper 24V, 4 Roller) and Model 9QS (Stepper 24V, 6 Roller) from Boxer GmbH, Ottobeuren, Germany<sup>3</sup>. Jumpers to configure the CNC shield (RM 2.54, BKL Electronic, Lüdenscheid, Germany) and the cables to connect the stepper motors to the board (4-PIN, female, Dupont) were purchased separately. The microcontroller itself can be powered via a normal USB cable (connected to a laptop or USB power adapter) or with a universal power supply (7-12 V, 1 A, plug: 5.5 x 2.1 mm).

<sup>2</sup> We did not observe any failure of pumps or motors during constant operation over 3 years.

<sup>3</sup> The operable stepper motors and thus peristaltic pumps are not limited to the specified models. The CNC shield can operate stepper motors with voltages between 12-36 V, whereby the supplying power supply must be adapted accordingly.

**Important: The assembly of the pump controller should only be carried out by a suitably trained person. When power is applied to the microcontroller, neither the stepper motor drivers nor the stepper motor may be removed or attached. This can lead to a defect of the driver and/or the entire board.**

### Assembly

The assembly of the device to control the stepper motors is shown in **Figure 3**. Basically, the microcontroller (A) is equipped with the shield (B), the jumpers on the board are placed to configure the shield (C), the motor drivers<sup>4</sup> are attached (D), and the stepper motors (E) and power supply are connected (not illustrated).

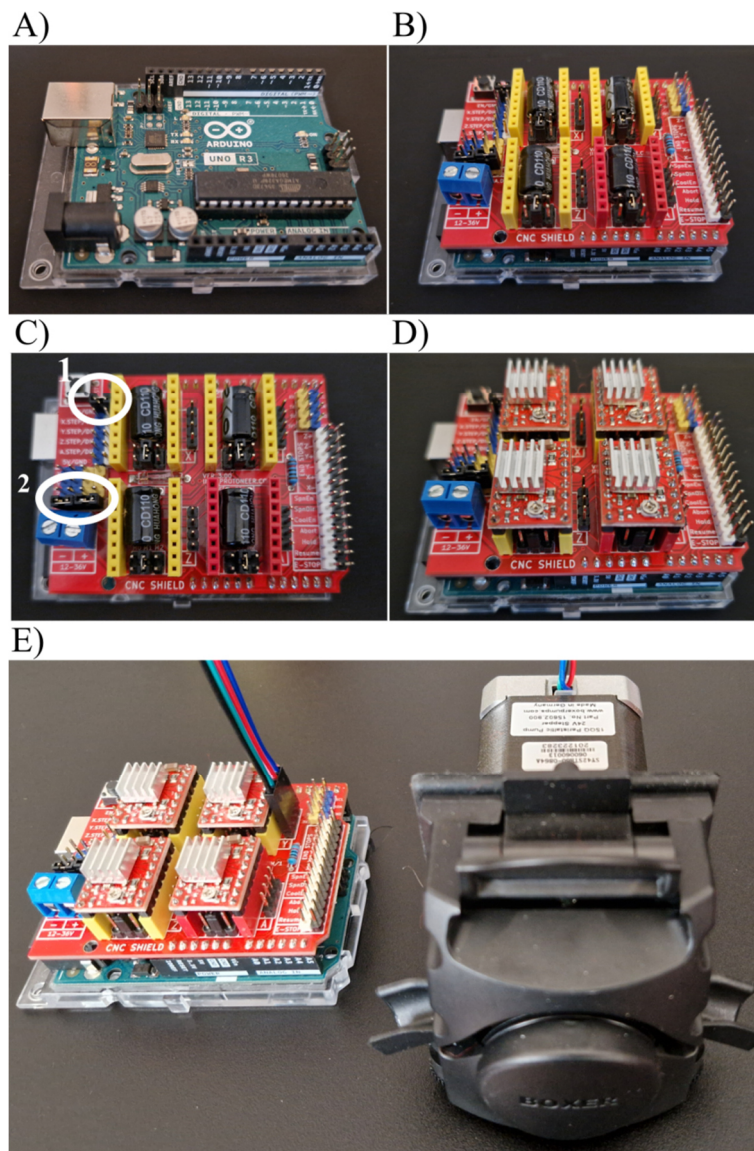


**Figure 3:** Photographs of (A) Arduino Uno Rev 3 microcontroller, (B) with pluggable CNC shield v3 and (C) positioned jumpers. (D) Fully equipped microcontroller after attaching motor drivers and (E) connecting a peristaltic pump.

<sup>4</sup> If not pre-mounted, the supplied heat sinks must be attached to the drivers. This is done with the already attached double-sided adhesive tape.

### Software and final adjustments

The free software of Arduino (v 1.8.9) was used to configure the microcontroller. Beginner tutorials up to professional explanations in dealing with Arduino can be found online ([www.arduino.cc](http://www.arduino.cc)). In brief, the software is installed, the microcontroller is connected to the computer and automatically detected via *Tools - Get Board Info*. Now sketches can be written in the programming interface and uploaded to the controller. In the following, a minimal example of using the *AccelStepper* library for controlling a single pump is shown and commented (**Figure 4**).<sup>[17]</sup> The library must be added in advance in the Arduino software via *Sketch - Include library – Manage libraries*.

```
#include <AccelStepper.h>
float RPMXaxis = 10.;
// Speed of pump connected to X-Axis in RPM, data type defined as float

AccelStepper Xaxis(1, 2, 5);
// assigns pins for CNC shield/driver

void setup() {

  Xaxis.setMaxSpeed(1000.0);
  // Sets the maximum permitted speed in steps/second
  Xaxis.setSpeed(RPMXaxis * 4 * (200. / 60.));
  // Defines running speed in steps/second. Includes quaterstep (4) and stepsize (200)
}

void loop() {
  Xaxis.runSpeed();
  //runs the motor at constant, pre-defined speed
}
```

**Figure 4:** A minimal source code to drive a stepper motor with 10 RPM connected to the X-axis of the CNC shield.

After uploading the sketch to the microcontroller, the program can be tested by enabling power to the LED power supply and the stepper motor-driven peristaltic pump should move<sup>5</sup>. Finally, the reference voltage  $V_{ref}$  of the motor driver, that regulates its electrical current, needs to be adjusted. If the  $V_{ref}$  is too low, the torque may not be sufficient to move the peristaltic pump with the hose clamped, whereas in case of too high  $V_{ref}$ , the motor may overheat and be damaged. According to the manufacturer's datasheet,  $V_{ref}$  can be calculated with Equation (1)

$$V_{ref} = I_{max} \times 8 \times R_s \quad (1)$$

where  $I_{max}$  is the rated current (specific for stepper motor) and  $R_s$  is sense resistor (specified by manufacturer of the stepper driver). The calculated voltage reflects its maximum value and should finally be reduced by 20-30%. An illustration of measuring and adjusting  $V_{ref}$ , as well as implementation of micro steps and an approach to realize a time-dependent, stepwise acceleration of the pump speed can be found in the supporting information (SI, Tables S1 and S2, Figures S1 and S2).

---

<sup>5</sup> When disconnecting the microcontroller from power it does not lose its configuration, but restarts after replugging.

### 3. Setting up a circuit for dynamic cell culture

After having established a device to generate fluid flow, we will now proceed with the setup of a minimal circuit for dynamic cell culture, which is shown schematically in **Figure 5**.

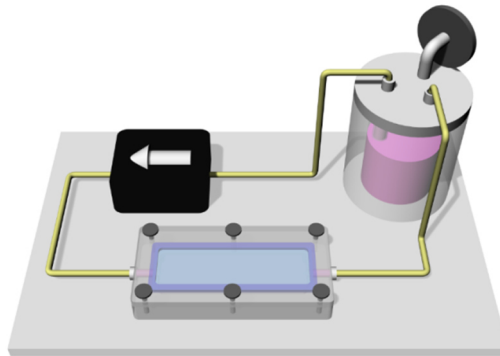


**Figure 5:** Schematic illustration of a minimal circuit for dynamic cell culture comprising a peristaltic pump, a slide culture chamber and a medium reservoir/bubble trap connected by tubes.

#### 3.1 Materials used in dynamic cell culture

##### *General requirements*

A variety of materials can be used in the construction of a circuit for dynamic cell culture, while their most important characteristic is cyto- and biocompatibility. Certifications such as FDA-approval, USP classification, or the biocompatibility test according to DIN EN ISO 10993 can provide suitable indications. However, because of the use of many proprietary materials, detailed specifications including their exact composition, molecular weight, and chemical structure, which are all affecting mechanical properties are rarely presented.<sup>[18]</sup> This is because the information is often kept confidential by manufacturers,<sup>[19]</sup> which further highlights the need to validate materials for their intended purpose. Polystyrene, as the most commonly used disposable substrate in cell culture<sup>[20]</sup> may contain plasticizers and other leachable substances, which may differ from batch-to-batch and can negatively influence the cultured cells.<sup>[21]</sup> This also emphasizes the need to be critical and validate the suitability of materials, despite appropriate certification and depending on the application. In the following, we will focus on the materials we have used in our circuits.

##### *Tubings*

The requirements for the hoses depend on their intended use, which can be either to simply connect individual components of the circuit or are used as a pump hose in the peristaltic pump<sup>6</sup>. The use of silicone tubing (polydimethylsiloxane, PDMS) is common for medical application and research purpose.<sup>[22]</sup> They are relatively inexpensive, autoclavable, and available in nearly any dimension. Despite its good biocompatibility, PDMS is highly hydrophobic and is susceptible to adsorption and absorption of small hydrophobic substances, and possibly needs to be avoided if interfering with the study design.<sup>[23]</sup> In addition, the mechanical strength of silicone, albeit dependent on its degree of

---

<sup>6</sup> Due to the principle of peristaltic pumps, the tubings must have a defined wall thickness in addition to the corresponding mechanical properties in order to function properly. The inner diameter can be varied to a limited extent and thus determines the volume/revision and consequently the flow rate. This depends on the model of the pump. In addition, pump designs determines if continuous tubing is operable or whether the hoses need so-called stoppers to keep them in place. A table with the corresponding requirements for the hoses and the resulting flow rates for our pump models can be found in the SI, Table S3.

crosslinking, is rather low, making the tubing susceptible to abrasion when used with peristaltic pumps for prolonged time.<sup>[24]</sup>

A variety of proprietary materials for pump tubing specially designed for use with peristaltic pumps exists, which are more robust and durable under mechanical load compared to conventional silicone tubing. As the exact composition of the hoses is mostly unknown, their specification ranges from a "polypropylene-based thermoplastic elastomer" (Pharmed BPT<sup>®</sup> from Cole Parmer, Wertheim, Germany), and "manufactured from virgin, FDA approved raw materials" (Innovaprene<sup>®</sup> P60 from Innovapure, Shanghai, China), to "made from medical grade thermoplastic elastomers" (Pharm-A-Line<sup>™</sup> from TBL Plastics, Sparta, NJ/USA). Although not quantified, we have seen significantly less tubing deformation and extended tubing life compared to conventional silicone tubing after continuous pumping<sup>7</sup>.

#### *Thermoplastics for culture chambers and adapters*

Bisphenol A (BPA)-carbonic acid copolymer (MakroClear<sup>®</sup>, Arla Plast, Borensberg, Sweden) was used as the bulk material for our conventionally produced culture chambers. It is an amorphous, thermoplastic polyester, which is usually referred to as "polycarbonate" (PC). The advantage of this material is its high impact strength, optical transparency, and high temperature resistance. Nevertheless, the use of BPA-derived polycarbonates should be critically questioned and validated depending on the study. BPA released from polycarbonate can be absorbed and has an endocrine, estrogen-analogous effect.<sup>[25]</sup> In addition to polycarbonate, luer-based adapters (introduced in the upcoming section) that were used to assemble the circuit were made mainly of polypropylene (PP, polyolefin) and nylon 66 (PA, polyamide), both of which are semi-crystalline thermoplastic elastomers. They are softer than polycarbonate (PP > PA),<sup>[26]</sup> which allows better sealing, with still retaining their shape integrity over several cycles of steam sterilization.

#### *Biocompatible resins for 3D printing of culture chambers*

Commercially available resins were used to manufacture culture chambers by means of 3D printing. Initially DentalSG was used (Surgical Guide, Formlabs, Somerville, MA/USA), which was later replaced by BioMed Amber (Formlabs) resin. Both resins are biologically evaluated for use in medical devices after processing, and they are non-cytotoxic, non-sensitizing and non-irritating. However, this certification is limited to short-term contact, such as dental procedures. A closer look at the safety data sheets of the two resins reveals that the DentalSG resin, but not BioMed Amber, contains  $\geq 75\%$  (w/w) of the BPA derivative bisphenol A glycol dimethacrylate (bisEMA). As the BPA has been seen to be released from printed resins in dental application,<sup>[27]</sup> the use of these materials in cell culture should be evaluated accordingly. In our experiments with cell lines (intestinal epithelial, HT29-MTX), as well as primary cells (human umbilical vein endothelial cells and dermal fibroblasts), no negative side effect could be detected when using components manufactured from these resins. However, careful post-processing after 3D printing is essential as non-crosslinked resin must be removed with a suitable solvent, such as isopropanol, and the printed parts should be fully crosslinked.<sup>[28]</sup> To further remove possible leachables, we extensively extracted the printed parts in deionized water and repeatedly autoclaved them under submerged conditions.

---

<sup>7</sup> A direct comparison was not possible, since the different hoses were used in different pumps and thus parameters like pump speed and wall thicknesses varied.

### 3.2 Adapters - Introducing the Luer system

The luer system refers to a standardized connection system (specified via DIN EN 1707:1996 and DIN EN 20594-1:1993) and is mainly used for syringes and needles, although it is applied also in numerous other medical and analytical devices. Originally, a simple conical press seal (also known as a *luer slip*) was used, which was later improved by the addition of a thread that counteracts self-loosening and thus provides additional security (hence referred to as *luer lock*). Adapters with an inner and outer cone are designated as female and male<sup>8</sup>, respectively. There are uncountable different variants and designs of adapters for this system. An overview of the adapters we used most frequently can be found in the SI (Table S4).

### 3.3 Bubble trap and medium reservoir

A bubble trap is a simple but essential part of the circuit system for dynamic cultivation of cells. It comprises a vessel containing the medium used for cell culture. Adapters in the lid allow tubes to be connected from the outside and inside. A minimum of three connectors are needed, namely the input, the output, and the filter adapter, which enables gas exchange. At the output, the medium is drawn bubble-free by the pump via a hose located below the filling level. **Figure 6** illustrates the principle and shows different variants of our bubble traps<sup>9</sup>.

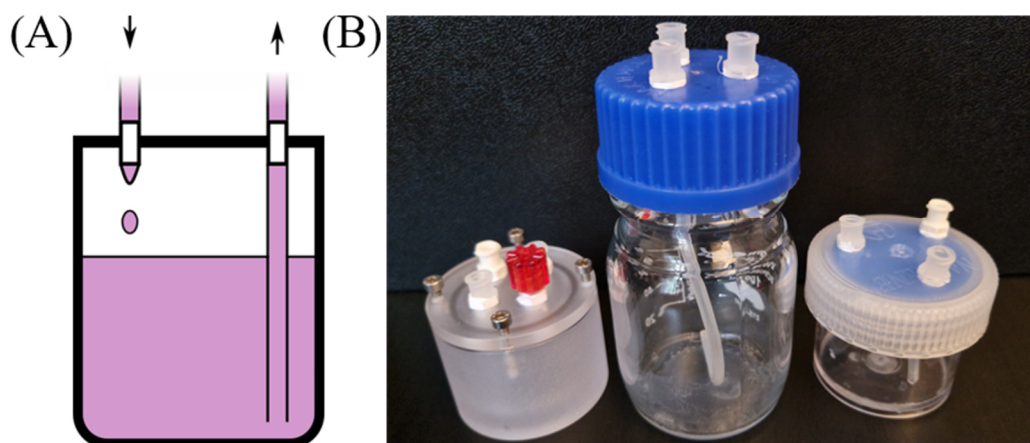


**Figure 6:** (A) Schematic illustration of a bubble trap showing the input and the output of medium and (B) photographs of bubbletraps made of polycarbonate, borosilicate and PP/PC (from left to right) all comprising the minimum of three outlets.

<sup>8</sup> Male luer lock adapters are available either as a single part with a fixed thread or as two-piece version with a rotating thread. The advantage of the latter is that during fastening, only the "nut" is tightened without twisting already connected hoses.

<sup>9</sup> Initially milled from polycarbonate, we switched to commercially available borosilicate bottles (Schott, Jena, Germany) and plastic-based wide-mouth jars (PP and PC, Nalgene, ThermoFisher, Waltham, MA/USA) due to easier fabrication. The use of commercially available vessels allowed us to fabricate the traps by ourself with minimal requirements, namely drilling a 5.5 mm core hole for the specified adapters and cutting a thread (1/4" 28 UNF) with a hand tap. Panel mount adapters sealed with poly(tetrafluoroethylene) (PTFE) thread tape were subsequently mounted.

## 4. Chamber design, manufacturing, and evaluation

In the following, we will address the design and manufacturing of culture chambers. The general requirements for all culture chambers comprise reliability, tightness, easy handling, and reusability if possible. More detailed design criteria are essentially determined by three factors:

- The cell culture format or substrate.
- The range of applicable shear stresses, which is determined by the cells' (patho)-physiological *in vivo* counterpart.
- The desired output.

### 4.1 Computer-aided design (CAD)

3-dimensional models created via CAD are required for using 3D printers as well as modern CNC milling machines.<sup>[29]</sup> Illustrations and descriptions of specific commands can be found in the SI and were generated using Rhinoceros® (Version 5.0, Robert McNeel & Associates, Seattle, WA/USA). There we limited the presentation to operators, which are available in the OpenSource software FreeCAD as well. Illustratively, the creation of 3D models is a combination of additive and subtractive manufacturing. Starting from simple geometries like cuboids or cylinders, structures are removed or added to generate the final model<sup>10</sup> mainly via Boolean operators (Difference, Intersection, Split, and Union)<sup>11</sup>.

### 4.2 Mathematical approximation of flow induced wall shear stresses

The aim of dynamic cultivation of cells is to apply shear stress to the respective cells and/or enable crosstalk by combination of different cell types. Depending on the scientific question, shear stresses need to be maintained in a specific (patho-)physiological range. When designing a new dynamic culture chamber, the applied shear stress can be roughly estimated with the help of mathematical equations<sup>12</sup>.

In rectangular flow channels, the wall shear stress under laminar conditions can be approximated with Equation (2)<sup>[30]</sup>

$$T = 6\mu Qw^{-1}h^{-2} \quad (2)$$

where  $\mu$  is dynamic viscosity,  $Q$  is volume flow rate,  $w$  is width and  $h$  is height of the flow channel.

As derived from Equation (2), the shear stress correlates positively with the flow rate, which is dependent on the speed of the pump and the internal hose diameter (and thus volume per revolution). The dynamic viscosity of the medium also has a positive correlation with applied shear stress. Water has a measured dynamic viscosity of  $\mu = 0.66$  mPa s at 37 °C, whereas  $\mu = 0.73$  mPa s for Dulbecco's Modified Eagle's Medium (DMEM, high glucose), and  $\mu = 0.93$  mPa s after supplementation of DMEM with 10% serum (fetal bovine serum, FBS).<sup>[31]</sup> The dynamic viscosity of a medium at constant temperature is thus determined, among other things, by the type and quantity of dissolved/contained substances. The addition of a biologically inert substance to increase the viscosity, such as dextran, is

---

<sup>10</sup> It is recommended to place the X and Y mirror axis of the model on the coordinate origin of the CAD software. This allows faster modeling of axis-symmetric objects.

<sup>11</sup> Especially when using corresponding operators, it is recommended to use layers in the CAD software. The source objects should be duplicated and kept in a layer, since (past) commands can partly not be undone. Any necessary adjustments can then be made more quickly.

<sup>12</sup> In addition to the SI unit of Pascal (Pa), shear stress is commonly found in literature as dyn cm<sup>-2</sup>. To convert from dyn cm<sup>-2</sup> to Pa, multiply by 10.

a common practice to modify the shear stress in flow experiments. Nevertheless, the supplementation may have undesired side effects on the cells, which should be evaluated upon application.<sup>[32]</sup> With reduced channel dimensions at a constant flow rate, the mean flow velocity in the channel and thus wall shear stress increases.

In tubular flow channels, the wall forces can be estimated with Equation (3),<sup>[33]</sup> with the adjustable parameters remaining the same.

$$T = 4\mu Q\pi^{-1}r^{-3} \quad (3)$$

### 4.3 Manufacturing of the chambers

The various techniques for the fabrication of culture chambers can be distinguished between subtractive and additive manufacturing, where in the subtractive manufacturing layers of material are removed to produce the object, whereas in additive manufacturing layers of material are added to achieve the same.<sup>[29]</sup>

#### *Conventional CNC milling*

Conventional manufacturing via CNC milling belongs to the subtractive manufacturing and is a well-established method that can be used to process a wide variety of materials, including plastics and metals. It is reproducible and may allow the production of prototypes and small series. On the other hand, production of complex structures may not be feasible and the required equipment is expensive, which is why service providers or in-house workshops are usually consulted for the fabrication<sup>13</sup>.

#### *3D printing via vat photopolymerization*

The advantage of 3D printing is that the required equipment is affordable even for home users. After appropriate training, it allows rapid prototyping and fast adaption to realize models with defined structures. A disadvantage is that materials for biomedical application are rare and the production on a larger scale is difficult. The advantages and disadvantages of various additive manufacturing techniques are discussed in more detail in several comprehensive review articles.<sup>[29, 34-35]</sup>

### 4.4 Vat photopolymerization in detail

#### *The principle*

In typical vat photopolymerization, a liquid, light-curable resin is placed in a container comprising a transparent bottom that can be irradiated from below with a UV or visible light source. The vat bottom usually consists of fluorocarbon-based polymer films made of fluorinated ethylene propylene (FEP) or PTFE, which are characterized by their low adhesiveness and chemical inertness.<sup>[36]</sup> To print the first layer of a 3D object, a Z-movable building platform is positioned in such a way that it leaves a small gap between the base and the building platform. The light source now irradiates the polymer from below, leading to crosslinking of the resin. The non-adhesive surface prevents attachment of the cured resin to the vat bottom and allows the building platform to be moved up and down, again leaving a gap between the previous layer and the bottom. This is repeated until the model is completed in a bottom-up manner. The simplest and most important adjustable parameter, besides layer thickness, is the exposure time, which needs to be adjusted depending on the printer (light source) and the photocrosslinkable resin.

---

<sup>13</sup> Internal corners are always rounded and comprise at least the radius of the milling head itself.

### *One way to determine the optimal exposure time*

Various platforms on the Internet allow the user-to-user exchange of 3D models, with *Thingiverse* ([www.thingiverse.com](http://www.thingiverse.com)) being the largest of these and the first place to go for finding existing 3D models.<sup>[37]</sup> Among these, one can find different models for validation of the exposure time and testing the printers' resolution. The 3D model "Resin XP2 Validation Matrix" is one versatile tool to optimize printing parameters (**Figure 7A**). To do so, the model is printed with different exposure times and subsequently analyzed for over- or underexposure. The interpretation is rather simple, and the following features indicate for good or optimized printing parameters: The number of intact countable pins and holes should be equal, the central square should measure 20 mm with 1 mm edges, and the enclosed "teardrops" should barely touch at the intersection point as illustrated in **Figure 7**. The remaining features can provide additional information about e.g., resolution, which also depends on the printer, the printing parameters, and the resin used.

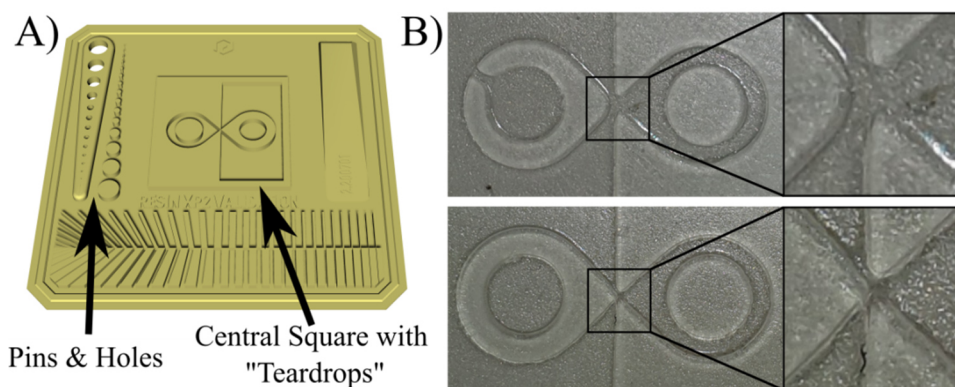


**Figure 7:** (A) 3D model of the "Resin XP2 Validation Matrix" with labelled features and (B) examples of printed models indicating for too low (top) and optimized exposure time (bottom).

### *Aspects to consider for biomedical resins*

In order to reduce the amount of material required and to reduce intersectional area<sup>14</sup> and thereby adhesion to the vat bottom, solid parts are hollowed if possible. Yet this requires special attention since uncured resin will be trapped in enclosed volumes and printing may fail. Holes for resin drainage are therefore cut in the model. The efficiency of resin removal depends mainly on the viscosity of the resin, the dimension of the drainage holes, and movement speed of the building platform. Compared to other commercially available resins, which we used for e.g., drafting, both the Dental SG and the BioMed Amber resin had relatively high viscosities. This may be due to the absence of solvents, which could possibly leach from printed models and impair their use for biomedical application.<sup>[38]</sup> With these resins, a lack of drainage for printing culture chambers, as illustrated in **Figure 8** by the areas marked in red, can therefore lead to defects in the printed parts.

<sup>14</sup> This can also be achieved via tilting of the structure and including support structures.

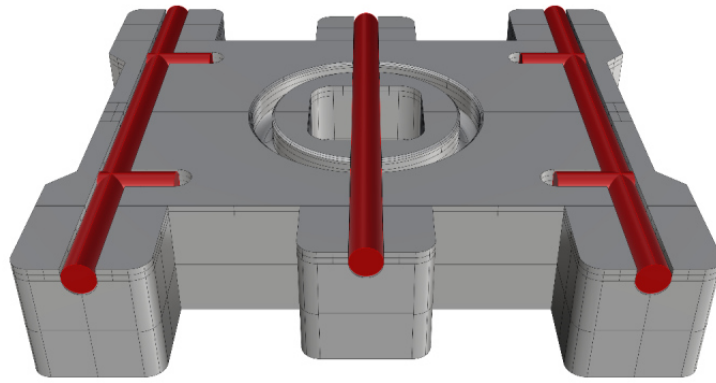


**Figure 8:** Implementation of holes (red structures) to enable drainage of trapped resin.

#### 4.5 Validation of chamber design - CFD simulations

The flow behavior of fluids can be simulated with computational fluid dynamics (CFD), which is particularly useful in case of physical problems in the cell culture chamber.<sup>[31]</sup> However, the programs for numerical analysis are not limited to solving only fluid flow problems, but can also address (bio)chemical problems such as metabolism and oxygen diffusion.<sup>[39]</sup> We will focus here on the general workflow and possible outputs, rather than any mathematical background, which is excellently reviewed in literature.<sup>[40]</sup> The CFD-simulations were conducted using the commercially available software COMSOL Multiphysics with the CFD module (v 6.0). The most frequently used CFD software is provided by ANSYS (commercial) and OpenFOAM (free).<sup>[41]</sup> Their general workflow for CFD-simulations is similar and includes the following steps, which are illustrated in **Figure 9**.

- Design of the fluid channel in the software or import from already existing CAD-models.
- Assignment and definition of the material.
- Definition of the physics and boundary conditions. This includes choosing the mathematical model (e.g., turbulent vs. laminar flow or stationary vs. time-dependent) and definition of boundaries and in-/outlet conditions.
- Dividing the geometry into finite subunits, called meshing. The subunits are usually tetrahedral or hexahedral<sup>15</sup>.
- Based on the defined conditions, the software tries to solve the problem<sup>16</sup>.
- If successful solved, obtained results can be validated quantitatively (surface shear stress) or qualitatively (streamlines).

<sup>15</sup> The quality of the mesh also conditions to a large extent the results obtained and is extensively discussed.<sup>[40]</sup>

<sup>16</sup> It should be mentioned, that the software will not find a discrete solution, rather than an approximation. A measure for how well the result is solving/approximating the problem is the "residual", which should converge to 0. It can happen that COMSOL is not able to solve a problem and therefore the residual error does not converge. This might be the case if the physic is out of range, e.g., the defined conditions are resulting in a turbulent flow but the software tries to solve under the mathematical assumption of laminar one.

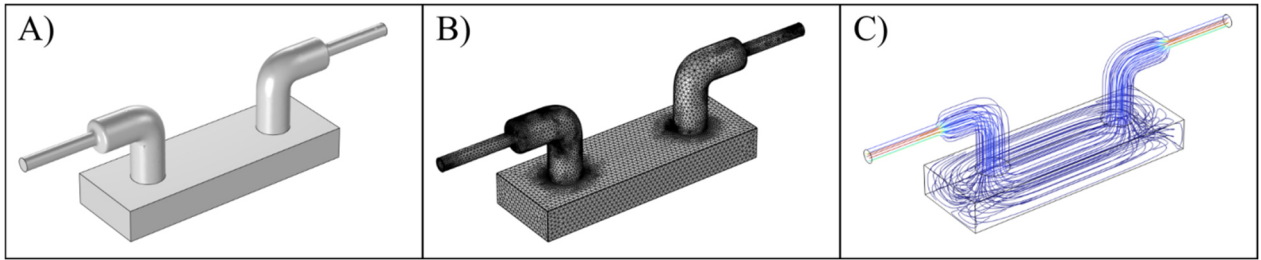
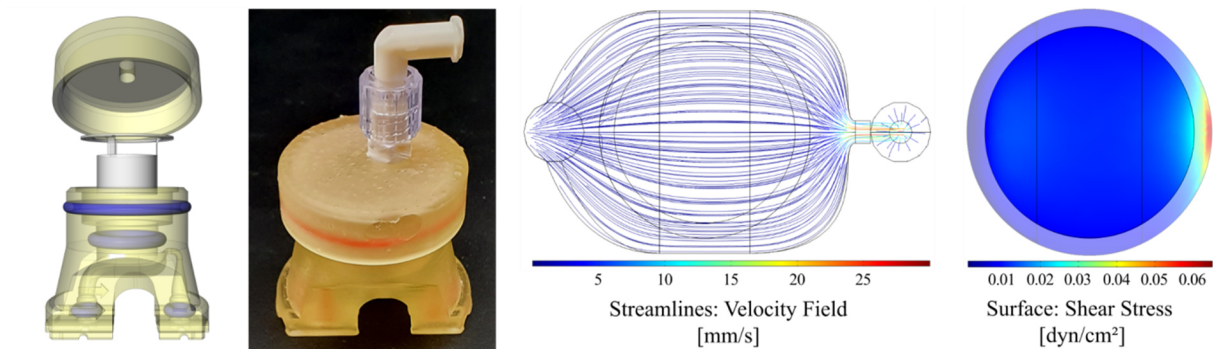


**Figure 9:** Workflow of CFD-Simulations including (A) the design of the flow channel, (B) meshing of the structure and (C) possible result expressed as velocity stream lines of the fluid flow.

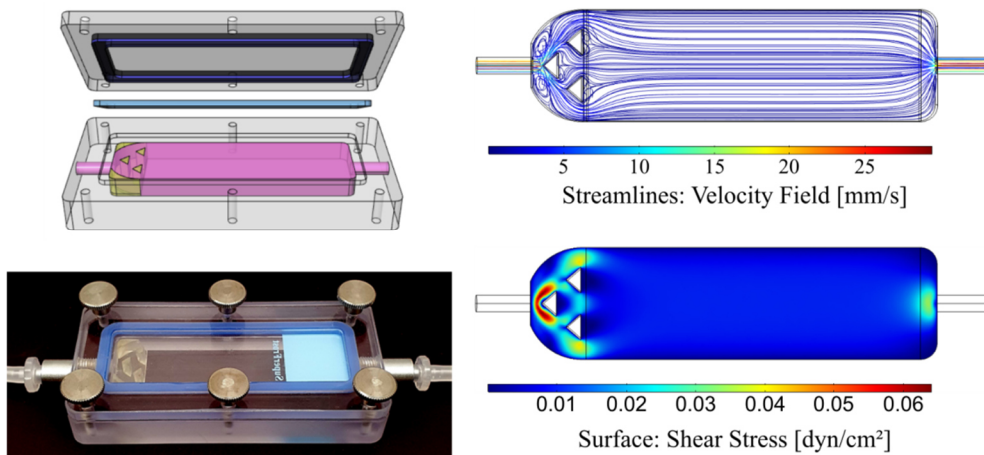
#### 4.6 Examples of chamber designs

##### Insert chamber



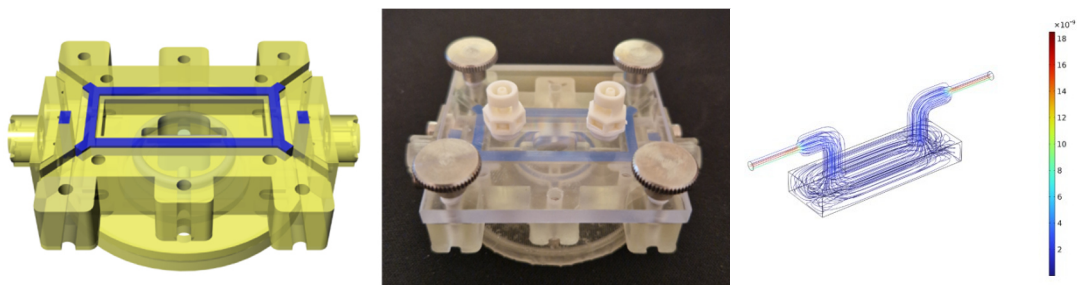
Substrate:	cell culture inserts (format: 12-Well)
Fabrication:	3D printing
Intended application:	barrier models (intestinal, <sup>[43]</sup> renal, dermal)
Features:	screwless handling, compatible for inserts from different manufacturers (Falcon®, Transwell®), removal of trapped bubbles via continuously rising flow channel

## Slide chamber



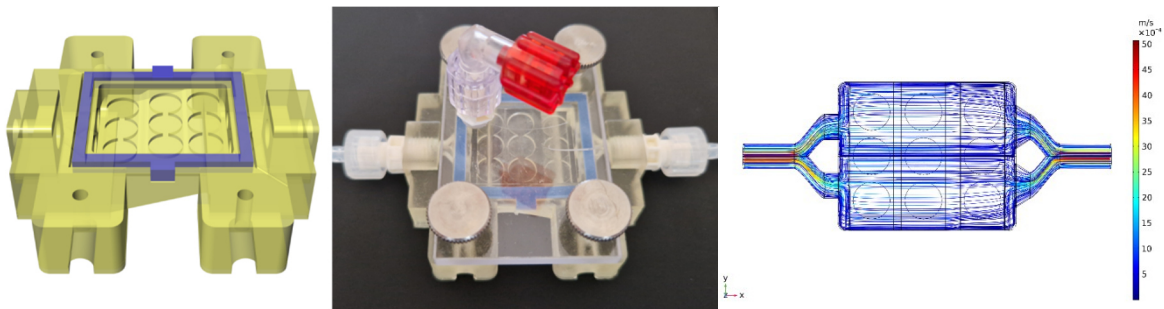
- Substrate: standard microscope slides (75 x 25 mm), various materials
- Fabrication: milling, 3D printing possible
- Intended application: generation of a wide range of shear stress depending on channel height (shear stress spanning four orders of magnitude from  $<0.004$  to  $>20 \text{ dyn cm}^{-2}$ )
- Features: compatible for different substrate thicknesses from 1.0-1.5 mm

## Tube chamber



- Substrate: tubular scaffolds, 3D printed, embedding/ECM possible
- Fabrication: 3D printing
- Intended application: vascularization, reconstruction of artificial blood vessels, crosstalk
- Features: optical (glass) bottom enable microscopy, two independent circuits for inner perfusion and crosstalk with separate cell type (Elomaa *et al.* 2022, manuscript in preparation for publication, section 3.4)

## Disc chamber



Substrate:	cylindrical, scaffolds based on decellularized extracellular matrix (dECM, $\varnothing$ 5-6 $\times$ 0.5 mm)
Fabrication:	3D printing
Intended application:	intestinal epithelial, influence of matrix stiffness and composition
Features:	Simultaneous application of different shear forces (differing with a factor of 5) to 3 sample replicates

## 5. Conclusion

The use of dynamic conditions in *in vitro* cell cultures significantly improves their physiological relevance as it allows the application of mechanical stress to the cells similar to *in vivo* conditions. Here, we provided the readers with guidance to design their own cell culture chambers and full dynamic culture circuits. To ensure a non-toxic, cytocompatible environment for cells in the dynamic culture, the selection of materials used in the culture chambers, tubings, and medium reservoirs requires special attention, which we aimed to discuss here in detail by sharing our own experience and know-how. When setting up a new dynamic culture system, 3D printing enables the design and adjustable prototyping of the cell culture chambers in a fast and feasible way and the Arduino microcontroller is an extremely useful tool to control several peristaltic pumps at the same time. To show the readers examples of the dynamic circuits, we introduced here the design and 3D printing of various perfusable cell culture chambers for use in development of *in vitro* epithelial barrier and vascularization models. As all the parts in the dynamic circuits introduced above are easily available with relatively low costs, we hope to provide a broader audience with an access to dynamic cell culture circuits without the need for high-cost investments in commercial bioreactors.

## References

- [1] J. Hohfeld, T. Benzing, W. Bloch, D. O. Furst, S. Gehlert, M. Hesse, B. Hoffmann, T. Hoppe, P. F. Huesgen, M. Kohn, W. Kolanus, R. Merkel, C. M. Niessen, W. Pokrzywa, M. M. Rinschen, D. Wachten, B. Warscheid, *EMBO Rep.* **2021**, *22*, e52507.
- [2] D. L. Butler, S. A. Goldstein, F. Guilak, *J. Biomech. Eng.* **2000**, *122*, 570-575.
- [3] D. E. Discher, P. Janmey, Y. L. Wang, *Science* **2005**, *310*, 1139-1143.
- [4] J. Zimmermann, B. A. Camley, W. J. Rappel, H. Levine, *Proc. Natl. Acad. Sci. U. S. A.* **2016**, *113*, 2660-2665.

- [5] K. Watanabe, K. Morishita, X. Zhou, S. Shiizaki, Y. Uchiyama, M. Koike, I. Naguro, H. Ichijo, *Nat. Commun.* **2021**, *12*, 1353.
- [6] J. W. Krueger, D. F. Young, N. R. Cholvin, *J. Biomech.* **1971**, *4*, 31-36.
- [7] A. J. Banes, J. Gilbert, D. Taylor, O. Monbureau, *J. Cell Sci.* **1985**, *75*, 35-42.
- [8] A. Dardik, L. Chen, J. Frattini, H. Asada, F. Aziz, F. A. Kudo, B. E. Sumpio, *J. Vasc. Surg.* **2005**, *41*, 869-880.
- [9] N. Filipovic, K. Ghimire, I. Saveljic, Z. Milosevic, C. Ruegg, *Comput. Methods Biomech. Biomed. Engin.* **2016**, *19*, 581-590.
- [10] M. Iannone, D. Caccavo, A. A. Barba, G. Lamberti, *HardwareX* **2022**, *11*, e00295.
- [11] C. K. Byun, K. Abi-Samra, Y. K. Cho, S. Takayama, *Electrophoresis* **2014**, *35*, 245-257.
- [12] J. Lapidus, *J. Urol.* **1948**, *59*, 501-533.
- [13] W. B. Cannon, *Am. J. Physiol.* **1912**, *30*, 114-128.
- [14] T. W. Latham, Fluid motions in a peristaltic pump, Doctoral dissertation, Massachusetts Institute of Technology, **1966**.
- [15] R. J. Hamilton, *IEEE Trans. Ind. Appl.* **2000**, *36*, 1682-1687.
- [16] S. Sharma, S. Harish, *Int. J. Innov. Res. Technol.* **2019**.
- [17] M. McCauley, "AccelStepper library for Arduino" can be found under <https://www.airspayce.com/mikem/arduino/AccelStepper/>, **2018**.
- [18] J. P. Mercier, J. J. Aklonis, M. Litt, A. V. Tobolsky, *J. Appl. Polym. Sci.* **1965**, *9*, 447-459.
- [19] K. Gunaalan, E. Fabbri, M. Capolupo, *Water Res.* **2020**, *184*, 116170.
- [20] M. J. Lerman, J. Lembong, S. Muramoto, G. Gillen, J. P. Fisher, *Tissue Eng. Part B Rev.* **2018**, *24*, 359-372.
- [21] N. Fekete, A. V. Beland, K. Campbell, S. L. Clark, C. A. Hoesli, *Transfusion* **2018**, *58*, 1800-1813.
- [22] M. Zare, E. R. Ghomi, P. D. Venkatraman, S. Ramakrishna, *J. Appl. Polym. Sci.* **2021**, *138*, 50969.
- [23] M. W. Toepke, D. J. Beebe, *Lab Chip* **2006**, *6*, 1484-1486.
- [24] V. Saller, J. Matilainen, U. Grauschopf, K. Bechtold-Peters, H. C. Mahler, W. Friess, *J. Pharm. Sci.* **2015**, *104*, 1440-1450.
- [25] P. Alonso-Magdalena, A. B. Ropero, S. Soriano, M. García-Arévalo, C. Ripoll, E. Fuentes, I. Quesada, Á. Nadal, *Mol. Cell. Endocrinol.* **2012**, *355*, 201-207.
- [26] A. Güllü, A. Özdemir, E. Özdemir, *Mater. Des.* **2006**, *27*, 316-323.
- [27] L. Lopes-Rocha, L. Ribeiro-Goncalves, B. Henriques, M. Ozcan, M. E. Tiritan, J. C. M. Souza, *J. Biomed. Mater. Res. - B Appl. Biomater.* **2021**, *109*, 1942-1952.
- [28] I. M. Barszczewska-Rybarek, *Materials (Basel)* **2019**, *12*.
- [29] O. Abdulhameed, A. Al-Ahmari, W. Ameen, S. H. Mian, *Adv. Mech. Eng.* **2019**, *11*, 1687814018822880.
- [30] H. Yamawaki, S. Pan, R. T. Lee, B. C. Berk, *J. Clin. Invest.* **2005**, *115*, 733-738.
- [31] C. Poon, *bioRxiv* **2020**, 2020.2008.2025.266221.
- [32] J. Gonzalez-Molina, J. Mendonça da Silva, B. Fuller, C. Selden, *Sci. Rep.* **2019**, *9*, 8505-8505.
- [33] B. Zhang, J. Gu, M. Qian, L. Niu, H. Zhou, D. Ghista, *Biomed. Eng. Online* **2017**, *16*, 137.
- [34] A. J. Capel, R. P. Rimington, M. P. Lewis, S. D. Christie, *Nat. Rev. Chem.* **2018**, *2*, 422-436.
- [35] N. Shahrubudin, T. C. Lee, R. Ramlan, *Procedia Manuf.* **2019**, *35*, 1286-1296.
- [36] X. Wu, Q. Lian, D. Li, Z. Jin, *J. Mater. Process. Technol.* **2017**, *243*, 184-196.
- [37] E. Buehler, S. Branham, A. Ali, J. J. Chang, M. K. Hofmann, A. Hurst, S. K. Kane, in *Proceedings of the 33rd Annual ACM Conference on Human Factors in Computing Systems*, **2015**, pp. 525-534.
- [38] M. Sandmeier, N. Paunović, R. Conti, L. Hofmann, J. Wang, Z. Luo, K. Masania, N. Wu, N. Kleger, F. B. Coulter, A. R. Studart, H. Grützmacher, J.-C. Leroux, Y. Bao, *Macromolecules* **2021**, *54*, 7830-7839.
- [39] H. Schmidt, M. Jirstrand, *Bioinformatics* **2006**, *22*, 514-515.
- [40] J. D. Anderson, J. Wendt, *Computational fluid dynamics, Vol. 206*, Springer, **1995**.
- [41] G. Nely, D. Sivelina, T. Petko, in *IOP Conference Series: Materials Science and Engineering, Vol. 1031*, IOP Publishing, **2021**, p. 012079.

- [42] A. Lintermann, in *Clinical and Biomedical Engineering in the Human Nose*, Springer, **2021**, pp. 85-115.
- [43] M. Lindner, A. Laporte, S. Block, L. Elomaa, M. Weinhart, *Cells* **2021**, *10*.

## Supporting Information regarding the setup for dynamic cell culture

### Pin assignment for all axes

**Table S1** shows the definitions of pins to enable the 4 available axes on the CNC shield in the Arduino software.

**Table S1:** Assignment of pins in the Arduino software respective to the axes on the CNC shield.

Axis	Definition (pins)
X	AccelStepper Xaxis(1, 2, 5)
Y	AccelStepper Yaxis(1, 3, 6)
Z	AccelStepper Zaxis(1, 4, 7)
A	AccelStepper Aaxis(1, 12, 13)

### Microstepping

As mentioned before, one revolution in a stepper motor is divided into a number of steps specific to the motor, and is usually 200 or 400. The motors can be operated in different modes. In full-step mode, the original number of steps of the motor is maintained. However, this can lead to vibrations and oscillation of the rotor, especially at low speeds. To smoothen the movement and reduce vibrations, microstepping is used, which further divides the steps and increases resolution of the motor (half-step doubles, quarter-step quadruples the number, etc.<sup>[1]</sup> However, this comes at the expense of the torque that can be applied and increases controller's complexity. In our experiments, motors were operated in quarter-step mode, which enabled smooth operation with still sufficient torque. The configuration is done via jumpers and is summarized in **Table S2** for the Pololu A4988 stepper motor driver. The adjacent **Figure S1** illustrates set jumpers for operating a stepper motor in quarter-step mode.

**Table S2:** Configuration of the Pololu A4988 stepper motor driver via jumpers.

Mode	MS1	MS2	MS3
Full step	Low	Low	Low
Half step	High	Low	Low
Quarter step	Low	High	Low
Eighth step	High	High	Low
Sixteenth step	High	High	High

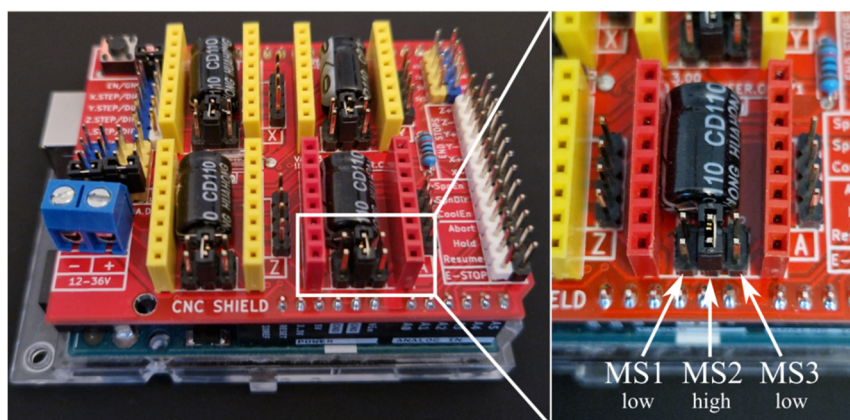


**Figure S1:** Positioned jumpers to operate stepper motor in quarter-step mode with *high* indicating presence and *low* absence of respective jumpers.

### Adjustment of the reference voltage

**Figure S2** illustrates measuring and adjusting the reference voltage  $V_{ref}$ . The bolt of the on-board potentiometer is screwed to increase (clockwise) or decrease (count-clockwise)  $V_{ref}$ .<sup>1</sup>

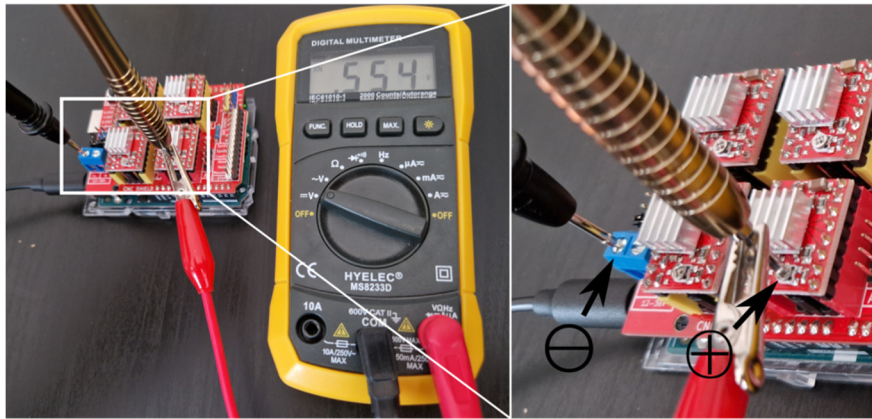


**Figure S2:** Adjustment of the stepper drivers' reference voltage.

### An approach to gradually increase the number of steps

Especially when applying shear stress to cells in high magnitudes ( $>1 \text{ dyn cm}^{-2}$ ), it is recommended not to run the culture instantly at maximum speed, rather than giving the cells time to adapt to shear stress by gradually increasing the pump speed. The approach for implementing this into Arduino is as following:

In addition to pump speed, parameters *step number* and *interval length* and *interval counter=0* are defined. The microcontroller compares the time when the pump started ( $t_{start}$ ) with the current time ( $t_{now}$ ). If the difference of both is greater than the specified interval length ( $t_{now} - t_{start} > \text{interval length}$ ), the *interval counter* is increased by 1 as long as it is smaller than the *step number*. The actual speed is now calculated according to Equation (S1).

$$\text{actual speed} = \text{final speed} \times \frac{1 + \text{interval counter}}{\text{step count}} \quad (\text{S1})$$

### Pump speed and tube requirements for used pumps:

**Table S3** shows required wall thicknesses (WT) for different pump models and volume flow rates for specified inner diameters (ID) of the tubing depending on the pump speed.

**Table S3:** Volume flow rates for 3 different peristaltic pumps in relation to wall thickness (WT) and inner diameter (ID) of pump tubing.

Modell (ID, WT, $\mu\text{l}$ revision <sup>-1</sup> )	Boxer 9QS (2.0 mm, 1.0mm, 120 <sup>a</sup> )	Boxer 15QQ (1.6 mm, 1.6 mm, 170 <sup>b</sup> )	Watson Marlow 114 ST (1.6 mm, 1.6 mm, 142 <sup>b</sup> )	Volume Flow Rate [ml min <sup>-1</sup> ]	
RPM	5	0,6	0,85		0,71
	10	1,2	1,7		1,42
	15	1,8	2,55		2,13
	20	2,4	3,4		2,84
	25	3,0	4,25		3,55
	30	3,6	5,1		4,26

<sup>a</sup> technical specification from manufacturer, <sup>b</sup> experimentally determined

<sup>1</sup> Touching other compartments than the potentiometer can easily short circuit and damage the board.

## Adapters for dynamic cell culture

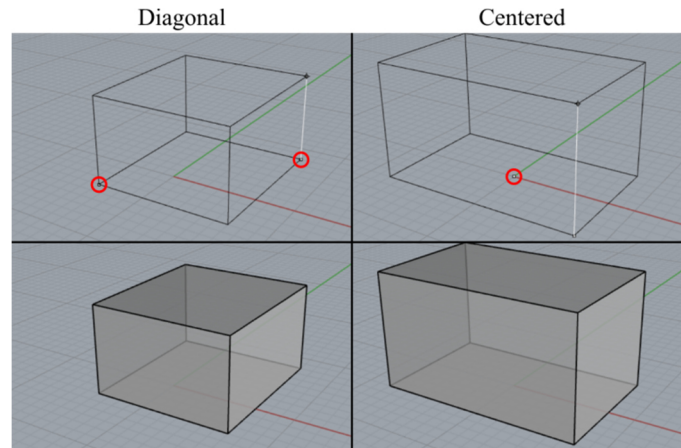
**Table S4** summarizes the adapters we used including article numbers from the distributor (Qosina), the material, and usage comments.

**Table S4:** Luer adapters implementable into dynamic cell culture circuits distributed by Qosina.

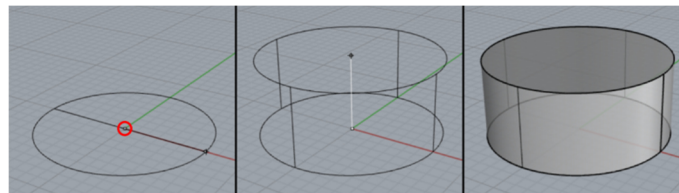
	<b>Name (article number)</b>	<b>Material</b>	<b>Comment</b>
	Male Luer lock to barb connector (11533, 11534)	PP	For connecting tubings
	Female Luer lock to barb connector (11532, 11534)	PP	For connecting tubings
	Female Luer Lock; Panel Mount (PMLF21, PMLF31)	PP	The thread allows mounting to lids or culture chambers. Especially useful for bubble trap.
	Female Luer Lock Connector, Threaded (40101)	PA	Threaded adapter for in- and output of culture chambers. Higher inner diameters are beneficial for flow distribution.
	Straight Connector, Barbed, White, Threaded (KS230)	PA	Threaded adapter for in- and output of culture chambers. Higher inner diameters are beneficial for flow distribution. Direct connection of thin silicon tubing (1.6 ID, 0.8 WT) possible, reduces risk of leakage via loosened adapters.
	Elbow Connector, Female Luer Lock, Male Luer Slip (11950, 11952, 11953) With Luer Lock Ring for Male Luer Slips (11955, 11959)	PC, PP, PA	The shape enables better structure and arrangement of components and tubings.
	Non-Vented Universal Luer Lock Cap (65812)	PC	Is used to close non-used ports while maintaining sterility.
	Male Luer Lock Injection Site (80029)	PC, Polyisoprene	Latex-free septum for needle-based sample taking.
	Duckbill Check Valve, Female Luer Lock Inlet (80065)	PC, Silicone	Limits medium flow to one direction.
	Rotating High Pressure Male Luer Lock Connector (20022)	PC, EPDM/Silicone	Can reduce twisting of tubings. Resistant to only a limit of sterilization cycles.
	T Connector, Barbed (11700, 11702)	PP	Can be used to split medium flow.
	T Connector with Swivel Male Luer and 2 Female Luer Locks (80061)	PC	Enables more connections to one port. In combination with injection site valuable for bubble trap.

## Important commands used for modelling culture chambers with Rhino

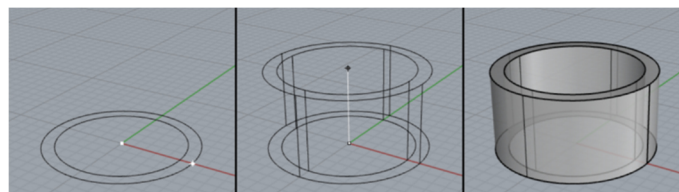
**Box:** Creates cubes and cuboids. Rhinoceros usually allows different alternatives for the execution of commands. A cube or a cuboid can be constructed by "Two points" (diagonal of the base and the height), or "Central" (center of the base, width, depth, height).



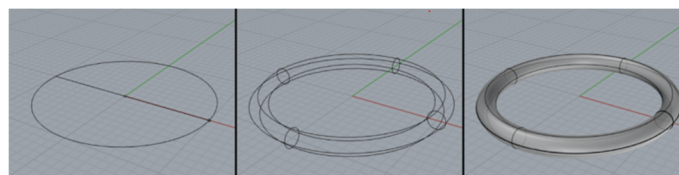
**Cylinder:** Defined by the center of the base, its radius and height.



**Tube:** Tubular hollow body defined by the center of the base, the inner and outer radius, and the height.



**Torus:** Mainly used to create cutouts for seals such as O-rings, defined by the center point, the inner diameter (with the *FixInnerDiameter* option) and the diameter or radius of the cross-section<sup>2</sup>.



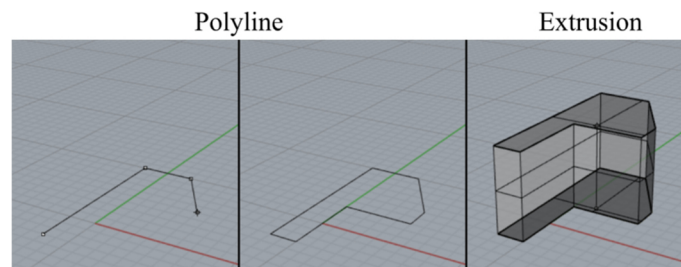
---

<sup>2</sup> The dimension of O-rings is standardized and (usually) indicated with two numbers,  $d_1 \times d_2$ .  $d_1$  corresponds to the inner diameter (mm) and  $d_2$  the diameter of the cross-section. An O-ring with the dimension 10 x 4.5 therefore has an outer diameter of 19 mm.

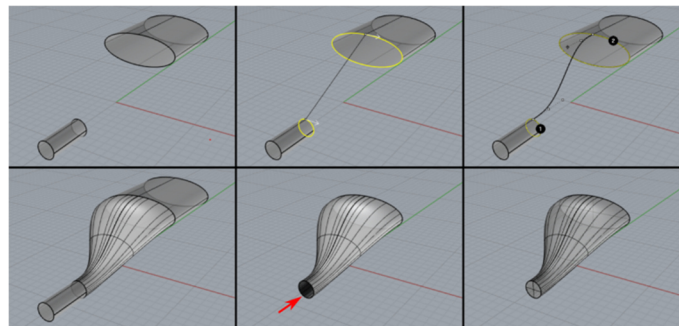
### *Irregular structures and smooth transitions*

This is particularly important for 3D printing, since structures cannot simply be printed “in the air” without having a support. One approach to solve this problem without the use of support structures is the implementation of smooth transitions, each of which is connected to the previous layer during printing. This was used for the insert chamber, which will be presented later.

**Polyline & ExtrudeCrv:** Creates a set of connected line or arc segments. After closing, the *ExtrudeCrv* command can be used to extrude the corresponding base surface and create a 3-dimensional object.



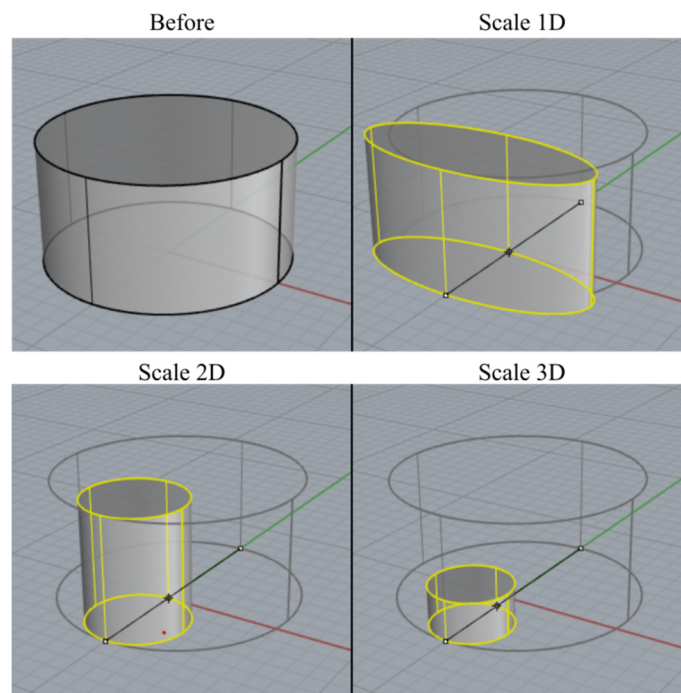
**BlendSrf:** This command is used to create a smooth transition between two surfaces<sup>3</sup>.



<sup>3</sup> Rhino creates a transition surface that must be closed for later processing using *\_Cap* (cap planar holes).

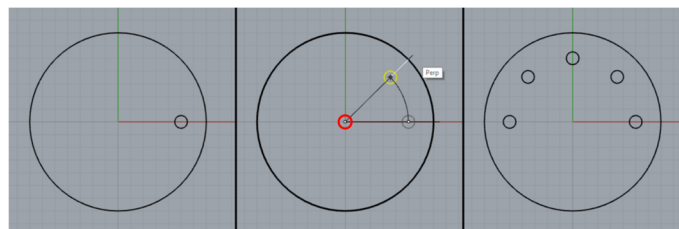
*Adjustment of already existing structures*

**Scale:** Depending on the command, the object is scaled according to a factor or starting point either in one (scale1D), two (scale2D), or three dimensions (scale).

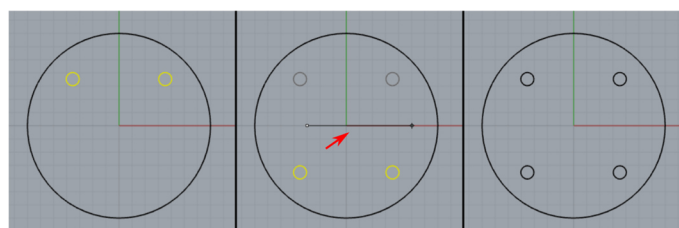


**Move** changes the position of the selected object(s).

**Rotate** turns the objects around a specific angle and center point.



**Mirror** flips the object either at a self-defined mirror axis, or the axes of the coordinate system (X, Y, or Z). This is especially useful for holes for symmetrical threads.



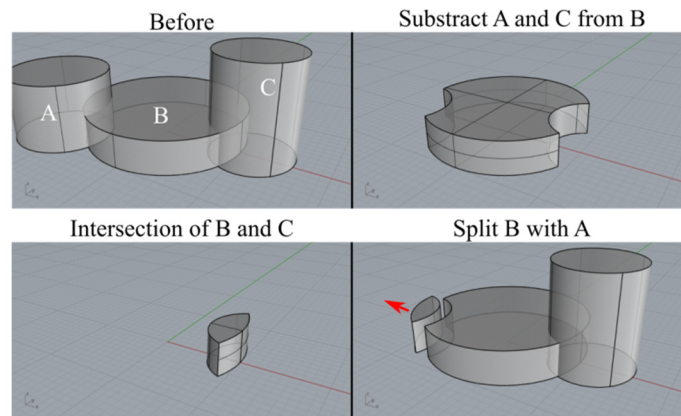
*Boolean operators*

**BooleanDifference** (=cut), Subtracts one (or more) object(s) from one (or more) other(s).

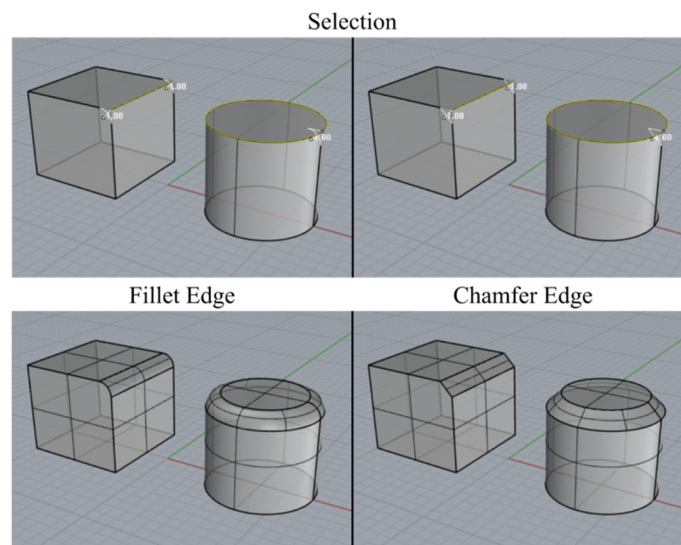
**BooleanIntersection** creates the intersection of two (or more) objects.

**BooleanSplit** divides object by, for example, outer surface or plane.

**BooleanUnion** combines two or more objects into a single one.



Refinements: **FilletEdge** and **ChamferEdge** rounds or chamfers selected corners with a specified radius/distance.



## Introducing a system for automated bioprocesses

Using a commercially available system (OSPIN, Berlin, Germany), we present the possibility of performing automated bioprocesses.

### Brief introduction of the device

The OSPIN Bioreactor System is a stand-alone device that works independently of conventional incubators. It enables (semi-) automated bioprocesses to be carried out, whereby important process parameters can be monitored online and partially controlled. The device requires a power and network connection and has inputs for compressed air and CO<sub>2</sub>.

### Design, components and controllable process parameters

**Figure S3** shows a possible configuration of the device.

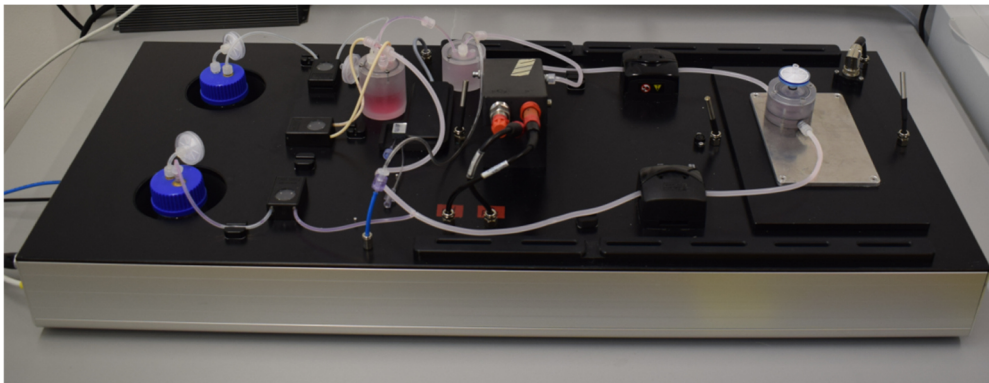


**Figure S3:** Representative photograph of a bioreactor system (OSPIN).

Similar to the minimum circuit for dynamic cultivation described in section 3, the bioreactor circuit requires a culture chamber, as well as the bubble trap/media reservoir which are connected via tubing and allows the application of medium flow via peristaltic pumps.

### Process controlling in general

A brief introduction to process control is necessary before additional components of the bioreactor and their principles are described (**Figure S4**).

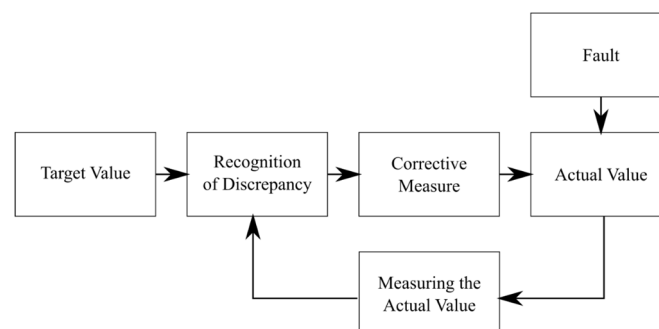


**Figure S4:** Illustration of a control loop.

The principle for controlling a parameter can be described as follows (examples): First, a measurable and controllable parameter (temperature) is required. The desired value of this parameter is defined for the process (37 °C, setpoint). The actual value is now determined via a suitable measuring method (20 °C), and a controller compares the setpoint and actual value and determines the corrective measure (switching on a heating element).

### *PID controller*

A variety of control concepts exist, with the PID controller still being the most common.<sup>[2]</sup> In the following, we will deal with the individual components of the controller in a simplified manner, whereby detailed descriptions of the concept and the adjustment of the controller are reviewed elsewhere.<sup>[3]</sup>

#### *Proportional term:*

The proportional term (P) of the controller is linear and reacts immediately to control deviation.

#### *Integral term:*

The integral term (I) accumulates the control deviation over time. It stabilizes the system and corrects possible offsets.

#### *Derivative term:*

The derivative term (D) does not consider the actual control deviation, but the change of the deviation over time and thus anticipates the control process ("negative feedback").

### *Temperature*

Two systems in the device enable temperature control:

#### *Ambient air:*

Air is permanently circulated within the device via fans. In combination with heating elements, the temperature can be kept constant at 37 °C (or more/less). Temperature sensors, which can be placed within a limited radius, monitor the temperature<sup>4</sup>.

#### *Heating plate:*

A heating plate below the culture chamber can be helpful especially for working with thermoresponsive surfaces and counteracts temperature drops e.g., when removing the cover/lid of the device.

### *Filling the circuit, perfusion, and media change*

The minimal required circuit is extended by additional vessels (*medium reservoir* and *waste*). This enables filling and (automatic) change of the medium. For this purpose, two additional pumps are added (*medium in* und *medium out*)<sup>5</sup>.

### *pH control*

In contrast to cell culture incubators, the pH value of the medium within the circuit is actively controlled. This is done in the gassing unit, where a defined air/CO<sub>2</sub> mixture is introduced and changes the pH value of the medium via diffusion through a thin-walled silicone tube<sup>6</sup>. The actual value is

---

<sup>4</sup> The heating system only works when the lid is closed. The time during which the unit is operated open (for example mounting/placing of the circuit) should be kept to a minimum.

<sup>5</sup> For initial filling, a two-step procedure has proven successful, whereby the bubble trap is first filled to about 50% and then perfusion is started. The medium is changed in two steps as well. First, as much as possible medium is removed from the circuit by means of the *medium out* pump and then refilled.

<sup>6</sup> The efficiency of the pH control not only depends on the CO<sub>2</sub> content of the gas mixture, but also on length and wall thickness of the tubing and the pumping speed for perfusion. Too low flow rates can lead to a high controlling-delay and consequently oscillation of the pH value. Likewise, repeated steam sterilization increases the permeability of the gas hose in the gassing unit and may require an adjustment of the pH control.

measured by a pH probe (InPro 3253i/SG/120<sup>7</sup>, Mettler-Toledo, Columbus, OH/USA) and according control deviations, the composition and volume flow of the gas mixture is adjusted. This allows, for example, the creation of physiological conditions for cells that are outside the norm *in vivo* (e.g., in the gastrointestinal tract)<sup>8, [4]</sup>

#### *Metabolic monitoring*

A biosensor (enzyme-based, Biosensor B.LV5, Jobst Technologies, Freiburg, Germany) can be integrated into the circuit to monitor the metabolic activity of the cells, especially glucose consumption and lactate production. This is particularly advantageous when establishing new bioprocesses, as it allows the medium change intervals to be determined<sup>9</sup>. A cheap and fast alternative to the semi-quantitative test for residual glucose in the medium can be the use of test strips to determine the glucose content in urine. Preliminary tests were promising (Medi-Test Glucose, range: 0 to  $\geq 55.5$  mmol L<sup>-1</sup>, MACHEREY-NAGEL, Düren, Germany), although further investigation is required determine whether media components have an influence on the test result.

#### *References*

- [1] W. Kim, D. Shin, Y. Lee, C. C. Chung, *Mechatronics* **2016**, *35*, 162-172.
- [2] H. O. Bansal, R. Sharma, P. Shreeraman, *J. Control Eng. Technol.* **2012**, *2*, 168-176.
- [3] R. A. Paz, in *Klipsch school of Electrical and Computer engineering, Vol. 8*, **2001**, pp. 1-23.
- [4] J. Fallingborg, *Dan. Med. Bull.* **1999**, *46*, 183-196.

---

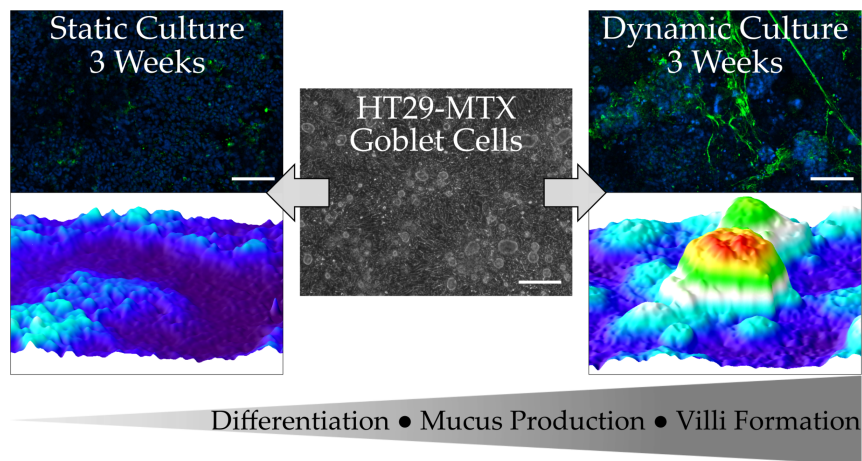
<sup>7</sup> The probe can be calibrated both internally in the device and externally via computer/cable. The probe is an autoclavable, closed probe that cannot be refilled and therefore needs periodic replacement.

<sup>8</sup> Depending on the placement and distance between the culture chamber and the pH probe, the pH value in the chamber may differ from the measured one and should be evaluated accordingly.

<sup>9</sup> Due to the limited capacity of the sensor (glucose = 1,200 mM × 24 h, lactate = 40-80 mM × 24 h), it is not operated permanently but in intervals. This interval is divided into four phases: the loading of the sensor, the measurement process, the rinsing of the sensor and a final pause. The sensor itself cannot be disinfected with solvent and must either be rinsed with antibiotic solutions or the recirculation of the medium is avoided.

### 3.2 Physiological shear stress enhances differentiation, mucus-formation and structural 3D organization of intestinal epithelial cells *in vitro*

In this study, the influence of physiological shear stress on a mucus-producing intestinal epithelial cell line was investigated. All experiments were carried out by the author except for the TEER measurements with inserts which were performed by Dr. Laura Elomaa. The initial idea and support to establish the mucus thickness measurement was given by Dr. Stephan Block. The manuscript was drafted including literature research by the author with assistance from Dr. Anna Laporte and Prof. Dr. Marie Weinhart. The final write-up was performed by the author together with Dr. Anna Laporte who also participated in the conceptualization of the study. Prof. Dr. Marie Weinhart and Dr. Laura Elomaa reviewed and edited the manuscript.



Lindner, M.; Laporte, A.; Block, S.; Elomaa, L.; Weinhart, M. Physiological Shear Stress Enhances Differentiation, Mucus-Formation and Structural 3D Organization of Intestinal Epithelial Cells In Vitro. *Cells* **2021**, *10*, 2062.

DOI: 10.3390/cells10082062

## Article

# Physiological Shear Stress Enhances Differentiation, Mucus-Formation and Structural 3D Organization of Intestinal Epithelial Cells In Vitro

Marcus Lindner<sup>1</sup>, Anna Laporte<sup>2</sup>, Stephan Block<sup>1</sup>, Laura Elomaa<sup>1</sup> and Marie Weinhart<sup>1,2,\*</sup>

<sup>1</sup> Institute of Chemistry and Biochemistry, Freie Universität Berlin, 14195 Berlin, Germany; m.lindner@fu-berlin.de (M.L.); stephan.block@fu-berlin.de (S.B.); laura.elomaa@fu-berlin.de (L.E.)

<sup>2</sup> Institute of Physical Chemistry and Electrochemistry, Leibniz Universität Hannover, 30167 Hannover, Germany; anna.laporte@pci.uni-hannover.de

\* Correspondence: marie.weinhart@pci.uni-hannover.de or marie.weinhart@fu-berlin.de; Tel.: +49-511-7621-4938 or +49-30-8387-5050

**Abstract:** Gastrointestinal (GI) mucus plays a pivotal role in the tissue homeostasis and functionality of the gut. However, due to the shortage of affordable, realistic in vitro GI models with a physiologically relevant mucus layer, studies with deeper insights into structural and compositional changes upon chemical or physical manipulation of the system are rare. To obtain an improved mucus-containing cell model, we developed easy-to-use, reusable culture chambers that facilitated the application of GI shear stresses (0.002–0.08 dyn·cm<sup>-2</sup>) to cells on solid surfaces or membranes of cell culture inserts in bioreactor systems, thus making them readily accessible for subsequent analyses, e.g., by confocal microscopy or transepithelial electrical resistance (TEER) measurement. The human mucus-producing epithelial HT29-MTX cell-line exhibited superior reorganization into 3-dimensional villi-like structures with highly proliferative tips under dynamic culture conditions when compared to static culture (up to 180 vs. 80 μm in height). Additionally, the median mucus layer thickness was significantly increased under flow (50 ± 24 vs. 29 ± 14 μm (static)), with a simultaneous accelerated maturation of the cells into a goblet-like phenotype. We demonstrated the strong impact of culture conditions on the differentiation and reorganization of HT29-MTX cells. The results comprise valuable advances towards the improvement of existing GI and mucus models or the development of novel systems using our newly designed culture chambers.

**Keywords:** 3D-printed insert chamber; bioreactor; cell-based mucus model; cellular self-organization; CFD simulation; goblet cell differentiation; native mucus thickness; physiological fluid flow; reverse cell culture



**Citation:** Lindner, M.; Laporte, A.; Block, S.; Elomaa, L.; Weinhart, M. Physiological Shear Stress Enhances Differentiation, Mucus-Formation and Structural 3D Organization of Intestinal Epithelial Cells In Vitro. *Cells* **2021**, *10*, 2062. <https://doi.org/10.3390/cells10082062>

Academic Editor: Alexander E. Kalyuzhny

Received: 15 July 2021

Accepted: 10 August 2021

Published: 12 August 2021

**Publisher's Note:** MDPI stays neutral with regard to jurisdictional claims in published maps and institutional affiliations.



**Copyright:** © 2021 by the authors. Licensee MDPI, Basel, Switzerland. This article is an open access article distributed under the terms and conditions of the Creative Commons Attribution (CC BY) license (<https://creativecommons.org/licenses/by/4.0/>).

## 1. Introduction

The luminal surface of the gastrointestinal (GI) tract is a highly dynamic barrier consisting of a constantly renewing epithelial layer covered by mucus [1]. For a long time, the mucus was solely attributed to the protection against shear-induced damage and the invasion of pathogens. In recent years, this view has changed, and it was identified to be in a symbiotic relationship with the commensal microbiome; for example, by supporting the growth of indigenous bacteria, which, in exchange, deliver nutrients to the host [2]. For in vitro models, focusing on these host–microbiome interactions, a physiological mucus layer is fundamental [3,4]. Additionally, changes in the structure and composition of mucus are related to serious illnesses such as inflammatory bowel disease, although it is not yet clear whether they are the cause or consequence [5]. Therefore, an improved understanding of the dynamic mucus architecture is needed.

In general, mucus is a complex biological hydrogel, consisting mostly of water (~95%), proteins, salts, nucleic acids and cell debris. Depending on the location within the human GI tract, the thickness of the adherent mucus layer varies between 16 ± 5 μm and

$155 \pm 54 \mu\text{m}$  in the duodenum and rectum, respectively [6]. Its properties and structure change according to variations in pH-value, the concentration of calcium ions, and the action of DNases and pancreatic enzymes [7–9]. The structuring components are mucins, a family of highly O-glycosylated proteins, of which 21 members are known up to now. Mucins are divided into two groups: membrane-bound and secreted mucins. The latter are mainly represented by gel-forming mucins, which are able to form complex networks via multimerization through covalent and non-covalent interactions. The main gel-forming mucin in the stomach is MUC5AC, whereas MUC2 is predominant in the intestine [1]. To study the underestimated influence of mucus in health and disease, there is an urgent need for improved, reproducible cell-based mucus models.

Various mucus models have been published in the past, including ex vivo human and in/ex vivo animal models as well as diverging in vitro models. Even though the in vivo and ex vivo models are physiologically highly relevant due to their high degree of complexity, they suffer from intra- and inter-species variations, limited availability and ethical concerns [10]. These restrictions also apply to the use of raw mucus, for which not only batch-to-batch variations but also the involved isolation process cause high heterogeneity. Additionally, trapped enzymes in the isolated mucus can cause a degradation and aging over time [11]. Although the homogeneity of raw mucus can be increased by purification, it is time intensive and results in irreversible alterations of its native structure, composition and physical properties [12]. Alternatively, defined mucus biosimilars are under development, which is yet complicated by the high complexity of the natural example [13]. Instead of using the intricate in vivo models or raw mucus samples, the use of models based on mucus-producing cells circumvents most of the aforementioned limitations.

Notwithstanding the extensive developments in the culture of primary intestinal cells as organoids or monolayers, intestinal models based on immortalized cells currently remain the most commonly used systems for routine applications due to their robustness, scalability, reproducibility and cost-effectiveness, with Caco-2 cells being the most widely used cell line [14,15]. These cells are derived from a human colorectal adenocarcinoma and exhibit several properties of enterocytes, including the formation of tight junctions and the expression of drug transporters as well as typical metabolic enzymes [16]. However, their use for permeability studies suffers from several unphysiological factors, including an overly strong barrier formation with high transepithelial electrical resistance (TEER) values [17] and a lack of mucus production [18,19], which is accomplished in vivo by highly specialized goblet cells. Therefore, Caco-2 cells are commonly co-cultured with the human cell line HT29, also originating from a colorectal adenocarcinoma and differentiating into a constitutive mucus-forming phenotype in the presence of methotrexate (MTX) [20]. These co-cultures are extensively applied in in vitro models of the intestinal barrier [15,21], mimicking the physiological features somewhat more closely than monocultures. Nevertheless, studies focusing on the characterization of the resulting mucus layer, which is known to play an essential role in the reliability of these models [22,23], are scarce. When closer analysis was conducted, unphysiologically low mucus thicknesses, mostly in the range of a few micrometers, were found [17,24]. Accordingly, an increase in mucus production, and thus mucus thickness, could further improve the relevance of these models. Previously, the presence of biologically active molecules, such as prostaglandin E<sub>2</sub>, ATP or vasoactive intestinal peptide, as well as bacteria have been detected to induce elevated mucus generation and secretion [24–26]. Aside from that, the mucus formation can be increased by an underlying substrate or by culture under semi-wet or air-liquid-interface conditions [24,27]. Furthermore, several groups have reported the shear-induced mucus production of primary and Caco-2 cells in organ-on-a-chip systems [26,28–30]. These microfluidic devices are highly sophisticated, allowing, for example, other mechanical stresses in addition to the application of fluid flow, and were recently reviewed [31,32]. Despite all of the aforementioned benefits, these culture variants are still limited either by

low mucus thicknesses, unphysiological culture conditions, costly supplementation or the requirement for complex equipment.

To overcome these restraints, we aimed to develop a simple millifluidic setup for the culture of cells under laminar flow conditions to thereby improve the mucus layer in a cell-based model without the need for further stimulation, making it easily accessible for deeper characterization of the mucus thickness and composition. Therefore, we developed a complementary set of reusable culture chambers that allow the application of physiological shear stress to cells on microscope slides or on membranes of commercially available cell culture inserts. Designed for this set of conventional solid and porous cell culture substrates, our chambers are intended to augment and refine state of the art microfluidic devices by providing the opportunity to apply homogenous shear stress in varying magnitudes on the entire macroscopic cellular seeding area. This versatility makes it possible to address a multitude of diverse scientific questions. We herein solely focused on the mucus-producing HT29-MTX cell line, hypothesizing that the applied mechanical influence is sufficient to promote their maturation into goblet-like cells and consequently increase mucus production. The obtained results could further improve its significance as a simple and readily available human mucus model or as component in future cell line-based GI models with higher physiological relevance. Thus, HT29-MTX cells were cultured under defined dynamic conditions and analyzed in terms of proliferation, differentiation, 3D reorganization, mucus generation and barrier formation. The composition of the adherent mucus layer was further characterized via immunofluorescent staining and its thickness was determined by confocal microscopy.

## 2. Materials and Methods

### 2.1. Materials

Dulbecco's Modified Eagle's Medium (DMEM, high glucose, GlutaMAX™ supplemented), trypsin-ethylenediamine tetraacetic acid (Trypsin-EDTA), Dulbecco's phosphate-buffered saline (PBS), proliferation assay (Click-iT™ EdU Cell Proliferation Kit, Alexa Fluor™ 488), DNA-intercalating dye (Hoechst 33342), proteinase K powder (from Engyodontium album), 96 well plates (Black/Clear Bottom), amine-modified fluorescent latex beads (FluoSpheres™, 0.2 µm, yellow-green), MUC5AC-antibody (mouse, monoclonal), radioimmunoprecipitation assay buffer (RIPA, Lysis and Extraction Buffer), protease inhibitor (Halt™, EDTA-free) and ZO-1-antibody (rabbit, polyclonal) were purchased from Thermo Fisher Scientific (Waltham, MA, USA). Fetal bovine serum (FBS, Superior), non-essential amino acids (MEM-NEAA), octoxynol 9 (Triton™ X-100), alcian blue solution (1% in 3% acetic acid, pH 2.5), periodic acid Schiff (PAS) staining kit, MUC5B-antibody (rabbit, polyclonal), *p*-nitrophenyl phosphate solution (pNPP, Alkaline Phosphatase Yellow Liquid Substrate) and phalloidin-Atto® 647N were obtained from Sigma-Aldrich (St. Louis, MO, USA). Microscope slides (Superfrost®), 4% paraformaldehyde (PFA, ROTI® Histofix 4%), tris-(hydroxymethyl)-amino methane (Tris, ≥99.3%, PUFFERAN®), EDTA (≥99), albumin fraction V (BSA, biotin-free) and sodium hydroxide (NaOH, ≥98%) were ordered from Carl Roth (Karlsruhe, Germany). Glacial acetic acid (>99.7) and hydrochloric acid (HCl, 37%) were purchased from Fisher Scientific (Loughborough, UK), 6-well tissue culture plates and rectangular cell culture dishes (quadriPERM®) from Sarstedt (Nümbrecht, Germany) and syringe filters (Minisart®, PTFE, 0.2 µm) from Sartorius (Göttingen, Germany). MUC1-antibody (rabbit, polyclonal) was obtained from Abcam (Cambridge, UK), polycarbonate (Makroclear®) from Arla Plast (Borensberg, Sweden), mounting medium (ProTaq® Mount Flour) from Biocyc (Luckenwalde, Germany), DNA-quantitation kit (AccuBlue® Broad Range) from Biotium (Hayward, CA, USA) and antibiotic-antimycotic solution from Biowest (Nuaille, France). Silicone tubings (Puri-Flex L/S 14®) were purchased from Cole Parmer (Vernon Hills, IL, USA), 12-well cell culture inserts (Transwell®, PET, 0.4 µm) from Corning (Corning, NY, USA), HT29-MTX-E12 from ECACC (Porton Down, Wiltshire, UK), thumbscrews (M3 × 10, DIN 646, stainless steel) from ERIKS Deutschland (Halle, Germany), 3D-printable resin (Dental SG Resin) from Formlabs (Somerville, MA, USA),

round coverslips ( $\varnothing$  18 mm No.1) from Glaswarenfabrik Karl Hecht (Sondheim v.d. Rhön, Germany), 35 mm dishes (high, glass bottom) from ibidi (Martinsried, Germany). Luer lock to M5 thread adapters (stainless steel) were obtained from Key Surgical (Lensahn, Germany), Luer lock to barb connectors (polypropylene) from QOSINA (Ronkonkoma, NY, USA), MUC2-antibody (mouse, monoclonal) from Santa Cruz Biotechnology (Dallas, TX, USA), duplicating silicone (REPLISIL 22 N) from SILCONIC® (Lonsee, Germany), 3-[(3-Cholamidopropyl)dimethylammonio]-1-propanesulfonat (CHAPS, VWR International, Darmstadt, Germany) and heat-seal sterilization bags (400 mm  $\times$  250 mm) from SÜDPACK Medica (Baar, Switzerland).

## 2.2. Chamber Design and Fabrication

### 2.2.1. Slide Chamber for Dynamic Culture on Solid Substrates

The culture chambers were computer-aided designed (CAD) with Rhinoceros (Version 5.0, Robert McNeel & Associates, Seattle, WA, USA). The chambers consist of a body, which fits and holds a standard 26 mm  $\times$  76 mm  $\times$  1 mm microscope slide in its cavity and forms a flow channel of defined height when closed with a lid (Figure 1a). Fluid tight sealing of the chambers was accomplished by the insertion of casted gaskets made from medical grade silicone in between the body and the lid, and the closing of the chambers with six knurled thumb screws. The applicable wall shear stress  $\tau$  was estimated using the following Equation (1):

$$\tau = 6\mu Qw^{-1}h^{-2}, \quad (1)$$

with the dynamic viscosity  $\mu$ , the volume flow rate  $Q$  as well as the width  $w$  and height  $h$  of the fluidic channel, which was varied from 0.15 to 6 mm (Table S1). The chambers were fabricated from bulk polycarbonate by conventional CNC-milling. A homogenizing triangular structure was 3D-printed from a commercially available, biocompatible and autoclavable ink for the chamber with a 6 mm channel height (see Supplementary Materials for detailed information on 3D-printing, CFD-simulation and material biocompatibility assessment). This chamber, with a homogenizing structure implemented, was used for dynamic culture on solid substrates. After fabrication, threads were cut and steel adapters were mounted to connect hoses. All materials remained inherently stable after autoclaving for at least 10 cycles.

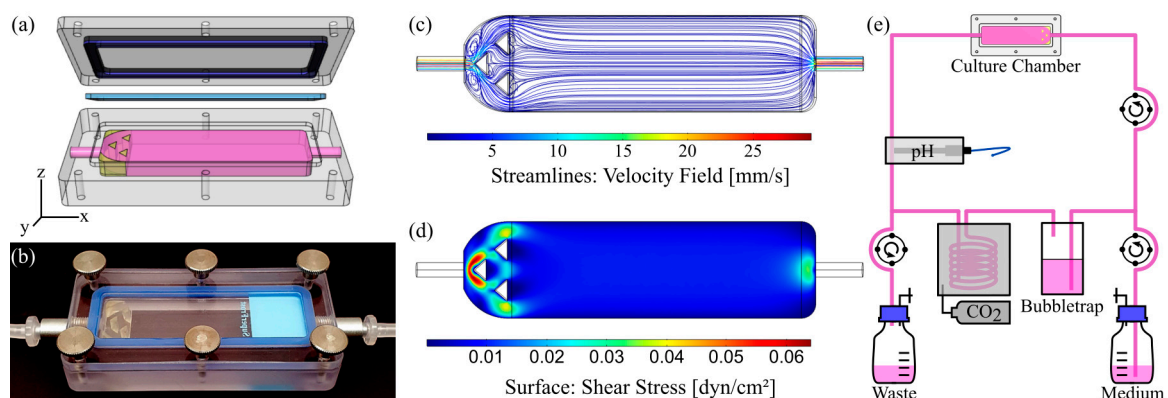


**Figure 1.** Chamber design, evaluation of flow properties and bioreactor setup for dynamic culture of cells on solid substrates. (a) CAD model (exploded view) and (b) photograph of the assembled culture chamber with 6 mm channel height and flow homogenizing insert. (c) Corresponding velocity streamline profile within the fluid channel and (d) surface shear stress obtained by CFD simulation at a volume flow rate of  $6.4 \text{ mL} \cdot \text{min}^{-1}$ . (e) Schematic illustration of the bioreactor circuit.

### 2.2.2. Insert Chamber for Dynamic Culture on Membranes

The insert chamber was completely CAD-modeled and subsequently printed with the aforementioned resin. The chamber fits a 12-well Transwell® cell culture insert and exhibits a flow channel with 3 mm height. The channel was designed to rise from the inlet

to the outlet, allowing potential air bubbles in the circuit to be removed by the fluid flow. Silicone O-rings were used to seal the lid and Luer adapters were used to connect the fluid in- and outlet. An illustration and the realization of the chamber are shown in Figure 7a,b.

### 2.2.3. Computational Fluid Dynamics (CFD)

The numerical analysis of flow conditions within the designed culture chambers was carried out with COMSOL Multiphysics (v5.5, including the CFD-module, COMSOL, Stockholm, Sweden). The inlet flow properties were set to  $6.4 \text{ mL}\cdot\text{min}^{-1}$  and  $1.42 \text{ mL}\cdot\text{min}^{-1}$  for the slide and insert chamber, respectively. Zero pressure was defined as outlet condition. Gravity was included and the dynamic viscosity  $\mu$  of the fluid was set to  $0.93 \text{ cP}$  [33]. Meshing was performed using the “physics-controlled”-mesh option as free tetrahedral elements and the mesh-quality was judged based on COMSOL’s minimum element quality.

## 2.3. Cell Culture

Human intestinal HT29-MTX cells (ECACC, Porton Down, UK) were cultured in DMEM High Glucose medium, supplemented with 10% FBS,  $1\times$  MEM-NEAA and  $1\times$  antibiotic-antimycotic solution at  $37^\circ\text{C}$  and 5%  $\text{CO}_2$  in a humidified atmosphere. Trypsin-EDTA (0.05%) was used to passage cells once a confluency of 60–80% was reached. The seeding density for all experiments was  $2 \times 10^5 \text{ cells}\cdot\text{cm}^{-2}$ . The passage number of cells used in experiments ranged from 24 up to 36.

### 2.3.1. Solid Substrates

For static experiments, cells were seeded on 6-well plates, on 35 mm dishes with glass coverslip bottom for microscopy or on glass coverslips for the determination of thickness. Medium exchange was performed every two to three days. Prior to dynamic culture, cells were seeded on sterilized glass coverslips for the determination of thickness, or on glass microscope slides in rectangular cell culture dishes with the aid of silicone casted cell separators to define a growth area of  $2 \times 3 \text{ cm}^2$  per slide. Separators were removed 24 h after cell seeding and cells were cultured for two more days under static conditions to reach confluency.

### 2.3.2. Membranes

Cells were seeded either conventionally into the Transwell® inserts on the top of the membranes, or on the bottom of the membrane, which will be referred to as “normal” and “reverse” culture below. For reverse culture, cell culture inserts were flipped, equipped with sterile cast silicone rings and transferred into 6-well plates. After overnight adhesion, the inserts were transferred into the corresponding 12-well plate. The medium volume was 0.5 mL in the upper and 1.5 mL in the lower compartment.

## 2.4. Dynamic Cell Culture

### 2.4.1. Bioreactor Setup for Dynamic Culture on Solid Substrates

The stand-alone bioreactor system (OSPIN, Berlin, Germany) for dynamic culture comprises peristaltic pumps for medium exchange and perfusion, a pH sensor to monitor and adjust the pH-value, and temperature control via the circulation of heated air. The mounted peristaltic pumps enable a constant perfusion rate of  $2.84$  to  $14.2 \text{ mL}\cdot\text{min}^{-1}$  when operated at 20 to 100 RPM with silicone hoses with an inner diameter of 1.6 mm. A schematic illustration as well as a photograph can be found in Figure 1e and Figure S3a, respectively.

For sterilization of all parts, the assembled culture circuit was transferred into sterilization pouches, which were sealed and autoclaved for 20 min at  $121^\circ\text{C}$  and 2 bar. Afterwards, the reservoir flask of the assembled circuit was filled with fresh medium under sterile conditions and sealed with sterile filters for gas exchange. The circuit was integrated into the bioreactor and equilibrated for 24 h at a constant fluid flow rate of  $6.4 \text{ mL}\cdot\text{min}^{-1}$  (45 RPM). Subsequently, confluent cells on microscope slides or glass coverslips were transferred into the chamber with 6 mm channel height and cultured under the aforementioned

conditions. A complete medium exchange of approximately 40 mL was performed every four to five days. The applied flow rate generates a physiological surface shear stress of  $0.009 \text{ dyn}\cdot\text{cm}^{-2}$  ( $9 \times 10^{-4} \text{ Pa}$ ) on the cellular monolayer. The described conditions are referred to as “dynamic culture conditions”.

#### 2.4.2. Bioreactor Setup for Dynamic Culture on Membranes

The dynamic culture of cells on inserts was carried out using a peristaltic pump (Model 114 ST, Watson Marlow, Falmouth, UK) in a cell culture incubator under standard conditions ( $37 \text{ }^\circ\text{C}$ ,  $5\% \text{ CO}_2$ ). The mounted stepper motor was operated with an Arduino UNO R3 microcontroller with the use of the AccelStepper library v1.61. The circuit consisted of four series-connected chambers and a bubble trap, shown in Figure S3b. Sterilization was performed as described above. The pump was operated at 10 RPM, generating a constant fluid flow of  $1.42 \text{ mL}\cdot\text{min}^{-1}$ , which results in an average surface shear stress of  $0.012 \text{ dyn}\cdot\text{cm}^{-2}$  ( $12 \times 10^{-4} \text{ Pa}$ ). The entire culture medium of 12 mL was exchanged every four days.

#### 2.5. Cell Proliferation Assay

The proliferation of cells was detected via 5-Ethynyl-2'-deoxyuridine (EdU) incorporation according to the manufacturer's instructions. Briefly, cells were incubated with  $10 \text{ }\mu\text{M}$  EdU in cell culture medium for 2 h under static or dynamic conditions. Cells were fixed with 4% PFA for 10 min, permeabilized with 0.5% Triton-X 100 for 20 min and afterwards incubated with the EdU-Click-It™ reaction cocktail for 20 min. Nuclei were counterstained with  $1 \text{ }\mu\text{g}\cdot\text{mL}^{-1}$  Hoechst 33342 in PBS for 15 min in the dark. Finally, cells were mounted and analyzed via confocal microscopy (LSM800, Carl Zeiss, Jena, Germany) or via epifluorescence microscopy (Axio Observer Z1, Carl Zeiss) equipped with a black and white camera (AxioCam MR R3, Carl Zeiss). All steps were conducted at room temperature.

#### 2.6. Mucus Staining and Quantification

To visualize acidic mucins, samples from dynamic and static culture were fixed using PFA, washed with PBS and incubated with Alcian Blue G8x Solution (1% in 3% acetic acid) for 15 min at room temperature. Subsequently, the solution was removed and samples were washed with distilled water, followed by washing steps with 3% acetic acid and water to remove residual staining solution. To stain neutral mucins, fixed samples were incubated for 2 min with 0.5% periodic acid, washed and treated for 10 min with Schiff's reagent, followed by three washing steps with PBS. Stained samples in PBS were imaged using an inverted microscope (Axio Observer Z1, Carl Zeiss) equipped with a color camera (AxioCam 105 color, Carl Zeiss).

To quantify neutral mucins, cells and adherent mucus were removed from the culture substrate using a cell scraper, vigorously resuspended in PBS (1 mL), snap frozen in liquid nitrogen and stored at  $80 \text{ }^\circ\text{C}$  until further analysis. The cell suspension ( $100 \text{ }\mu\text{L}$ ) and 2% *w/v* CHAPS ( $100 \text{ }\mu\text{L}$ ) were mixed and diluted with PBS ( $800 \text{ }\mu\text{L}$ ). The resulting suspension was sequentially incubated with periodic acid ( $20 \text{ }\mu\text{L}$ ) and Schiff's reagent ( $100 \text{ }\mu\text{L}$ ) for 2 and 1 h, respectively, at  $37 \text{ }^\circ\text{C}$  in a thermal shaker. The absorbance  $A_{555}$  of the resulting solution ( $100 \text{ }\mu\text{L}$ ) was measured in 96-well plates using a microplate reader (Infinite™ M200 PRO, Tecan, Männedorf, Switzerland).

For normalization, DNA content was determined using AccuBlue® assay according to the manufacturer's instructions. In brief, the cell suspension ( $100 \text{ }\mu\text{L}$ ) was resuspended in  $2\times$  digestion buffer (20 mM Tris, 2 mM EDTA, 0.2% Triton X-100 and  $1 \text{ mg}\cdot\text{mL}^{-1}$  proteinase K) and incubated overnight at  $37 \text{ }^\circ\text{C}$ . AccuBlue® reagent was diluted 1:100 in reaction buffer, mixed with the sample at a ratio of 10:1 and incubated for 15 min in the dark. Samples were excited at 480 nm and emission  $E_{520}$  was measured in 96-well plates using a microplate plate reader in reference to a standard calibration curve.

### 2.7. Thickness-Determination of the Adherent Mucus Layer

The thickness of the adherent mucus layer was determined as previously described in the literature using fluorescent particles and confocal microscopy [34,35]. In brief, HT29-MTX cells, on coverslips, were incubated with amine-modified, fluorescent latex beads ( $\varnothing$  200 nm, 1:500) and Hoechst 33342 ( $5 \mu\text{g}\cdot\text{mL}^{-1}$ ) in medium for 20 min under cell culture conditions. Samples were gently washed twice with warm PBS and afterwards analyzed in cell culture medium via confocal microscopy. The ImageJ based software package Fiji v1.52 [26] was used for image processing and analysis to estimate the median mucus thickness ( $\pm$  median absolute deviation, MAD,  $n = 5$ ) of the adherent hydrated mucus layer. Detailed information about image processing and data acquisition can be found in the Supplementary Materials (Figure S4).

### 2.8. Alkaline Phosphatase (ALP) Activity Assay

To determine intracellular ALP activity, HT29-MTX cells were removed from their substrate using a cell scraper, washed with PBS and centrifuged for 10 min at  $5000 \times g$ . PBS was aspirated, cells were resuspended in cold RIPA buffer ( $60 \mu\text{L}$ ), containing  $1 \times$  EDTA-free protease inhibitor and incubated for 40 min on ice. Reaction tubes were briefly vortexed every 10 min to ensure complete cell lysis. After incubation, the lysates were centrifuged for 5 min at maximum speed to sediment insoluble cell debris. The supernatant and ALP working reagent were mixed at a 1:1 ratio in a 96-well plate. The ALP-catalyzed formation of *p*-nitrophenol was colorimetrically monitored over a period of 60 min by measuring the change of absorbance as  $\Delta(A_{405} - A_{660}) \cdot \text{min}^{-1}$  with a microplate reader.

### 2.9. Immunostaining and Direct Labelling

Cells were fixed with 4% PFA for 20 min, permeabilized with 0.1% Triton X-100 for 10 min, blocked using 5% BSA in PBS for 90 min and afterwards incubated with primary antibodies against MUC1, MUC2, MUC5AC, MUC5B or ZO-1 for 4 h. Primary antibodies were detected via incubation with fluorophore-coupled secondary antibodies for 90 min (see Table S3 for further information). All samples were counterstained with Hoechst 33342 ( $10 \text{ ng}\cdot\text{mL}^{-1}$ ) in PBS, and selected samples were counterstained using phalloidin-Atto<sup>®</sup>647, for 15 min in the dark. All steps were performed at room temperature, samples were analyzed via confocal microscopy and images were processed with the Zen Blue software (v2.3).

### 2.10. Transepithelial Electrical Resistance (TEER)

The electrical resistance of HT29-MTX cells seeded on Transwell<sup>®</sup> inserts was measured using the Millicell<sup>®</sup> ERS-2 unit equipped with an STX1 electrode (Millipore, Bedford, MA, USA) to assess their barrier function. To ensure accurate measurements, apical and basolateral medium was replaced by pre-warmed, fresh medium and inserts were kept on a  $37 \text{ }^\circ\text{C}$  heating plate (HP062, AgnThos, Lidingö, Sweden) for 10 min prior to and during the measurement. Cell culture inserts without cells were measured as reference.

### 2.11. Statistics

All experiments were conducted at least in triplicate with a minimum of two technical replicates. Statistical significance between two groups was evaluated using the Wilcoxon/Mann–Whitney test, whereas statistical significance between more than two groups was evaluated using the Kruskal–Wallis test, followed by Dunn’s post-hoc test with OriginPro 2020b (v9.7.5.184, OriginLab, Northampton, MA, USA). Significances are indicated as \*  $p \leq 0.05$ ; \*\*  $p \leq 0.005$  and \*\*\*  $p \leq 0.0005$ .

## 3. Results and Discussion

### 3.1. Characterization of Flow Chamber for Solid Substrates

To culture cells on standard microscope slides under defined dynamic conditions, an easy to reproduce, reusable flow chamber was designed and manufactured (Figure 1a,b). It allows implementation into a stand-alone bioreactor system, as illustrated in Figure 1e and

Figure S3a. All materials remained inherently stable after repeated cycles of autoclaving. Additionally, the chamber was operable in a common CO<sub>2</sub> incubator with a peristaltic pump that was similar to the setup of the flow chambers for culture of cells on membranes shown below (Figure S3b).

The geometry of the chamber was shaped to generate homogenous laminar flow on the cell surface with adjustable physiological shear stresses. By varying the height of the flow channel from 0.15 to 6 mm, we mathematically approximated an applicable range of wall shear stresses from 0.004 to 29.7 dyn·cm<sup>-2</sup> ( $4 \cdot 10^{-4}$  to 2.97 Pa; Equation (1)), which resembles the physiological shear stresses of a variety of human organs and blood vessels [36], opening up the opportunity to cultivate cells from various origins under their respective physiological flow conditions to generate more realistic tissue mimicking models [37]. The obtained values were further validated and the fluid flow behavior within the chambers was characterized via CFD-simulations, which revealed differences between simulated and calculated values, with the latter being slightly overestimated (Table S1). Chambers with channel heights of up to 1.5 mm already exhibited laminar flow conditions due to a construction-dependent threshold (Figures S1a and S2). As it can be seen from Figure S1b, homogenous laminar flow necessitated the implementation of homogenizing structures for chambers with 6 mm channel height, which were designed on the basis of the conducted CFD simulations (Figure S1c). A representative example, including the velocity profile and surface shear stress, is shown in Figure 1c,d for a corresponding chamber with 6 mm channel height and 3D-printed homogenizing triangular features at a volume flow rate of 6.4 mL·min<sup>-1</sup>. The estimated and simulated surface shear stresses were 0.008 and 0.009 dyn·cm<sup>-2</sup> ( $8$  and  $9 \times 10^{-4}$  Pa), thus matching with physiological shear stresses in the human small intestine [28]. Similar shear stresses could be applied using convenient ibidi® chambers (μ-Slide I, 0.8 mm channel height), which in preliminary experiments unfortunately resulted in a marked pH-gradient from the inlet to the outlet with the HT29-MTX cells under physiological flow conditions (data not shown). Overcoming these limitations, our newly designed flow chamber was the better choice for the dynamic culture of HT29-MTX cells when aiming to develop a more realistic in vitro mucus model of the human GI tract.

### 3.2. Design of Experiments

The human cell line HT29-MTX generally requires 21 days to fully differentiate into an intestinal epithelial, mucus-producing cell layer under static conditions [38]. Their ongoing maturation into functional goblet-like cells is macroscopically visible, since the mucus layer, accumulated on top of the cell layer, progressively reduces its transparency. It was previously shown that the mucus production of HT29-MTX cells cultured on membranes at the liquid–air interface is enhanced under mechanical stimulation [24,39]. Preliminary experiments revealed a markedly faster and stronger development of the aforementioned visual turbidity of the cultures under flow conditions using our chamber, which suggests a reduced culture time of only 14 days under dynamic conditions to yield a mucus-producing epithelial cell layer (data not shown). Hence, the maturation of HT29-MTX cells in terms of proliferation, differentiation and mucus production under static and dynamic conditions was further characterized at different time points up to three weeks of culture.

### 3.3. Morphology and Proliferation of HT29-MTX Cells under Static and Dynamic Conditions

To monitor differences in the development of integrity and morphology of HT29-MTX cells under static and dynamic culture conditions, the conformation of the cell layer was first monitored at different time points via phase contrast microscopy (Figure 2a). The cell layers were confluent at all times and conditions without any recognizable defects. Additionally, we observed a time-dependent formation of darker regions that are hard to bring into focus during microscopic imaging. This phenomenon developed faster and was distinctly more pronounced under dynamic conditions, which was in agreement with the macroscopic observation of turbidity when compared to samples from static

conditions at the same or even advanced time points. It was previously reported in the literature that HT29-MTX monolayers are able to expand three-dimensionally (3D) [27]. The presence of multilayered regions and the accumulation of mucus seem to decrease the light transmission in the respective areas and hinder optimal focus adjustment.

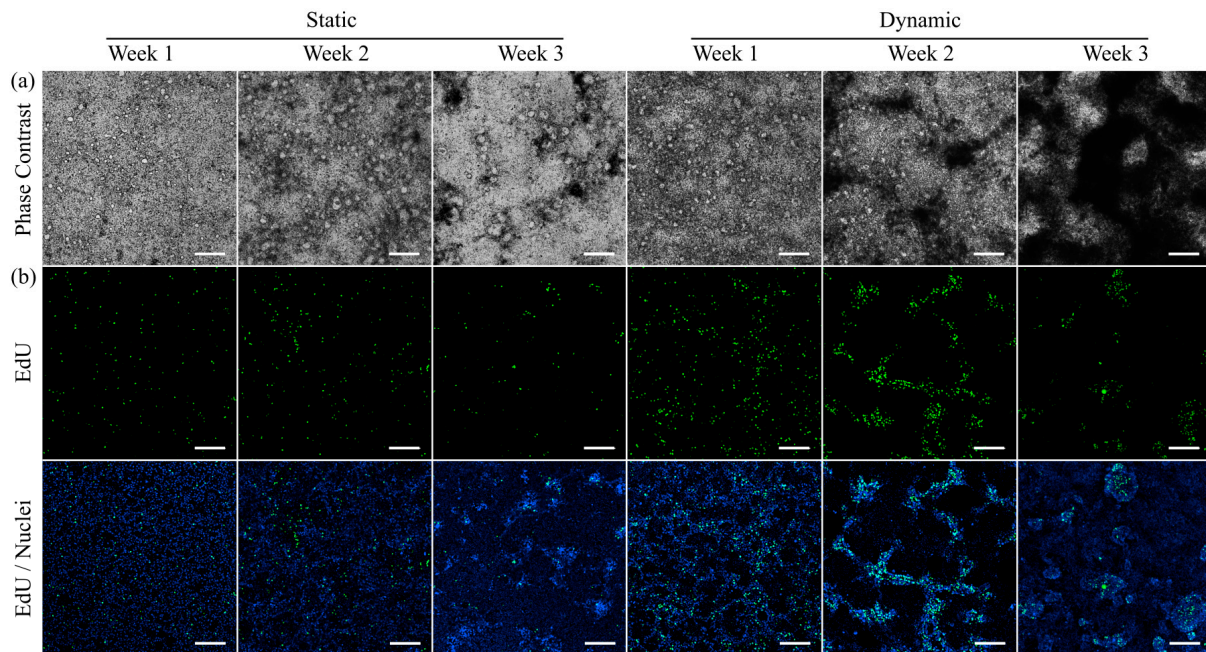


**Figure 2.** Morphology and proliferation of HT29-MTX cells under static and dynamic culture conditions at various time points. (a) Morphology was assessed via phase contrast microscopy and (b) newly synthesized DNA was visualized with EdU-Alexa<sup>®</sup> 488 (green) and imaged using confocal microscopy. Nuclei were counterstained with Hoechst 33342 (blue). (a,b) show independent samples. (Scale bars: 200  $\mu$ m).

To further examine this effect, the influence of culture conditions on the proliferative capacity of HT29-MTX cells was detected via incorporation of the thymidine analogue EdU into the newly synthesized DNA of daughter cells, and subsequent labelling (Figure 2b). Regardless of their cancerous origin, the proliferative capacity of HT29-MTX cells is known to disappear once cells reach confluency [40]. However, a larger number of proliferating cells was detected at all analyzed time points under dynamic conditions compared to samples from static culture. These results are consistent with the observed increased proliferation of Caco-2 cells, when cultured under flow conditions [41]. Furthermore, the simultaneous visualization of nuclei via Hoechst-staining revealed HT29-MTX clusters with a higher fluorescence intensity, which were particularly defined after two and three weeks of dynamic culture when compared to the status after three weeks of static culture. The clusters share structural similarities with the dark spots on the cell layer detected via phase contrast microscopy and can be attributed to multiple layers of highly proliferative cells and their 3D rearrangement beyond cellular monolayers. Proof of the colocalization of the darker regions and proliferative cells is shown in Figure S5 using epifluorescence microscopy. To exclude a potential influence of the larger medium volume, and thus, constant and high nutrient supply present in dynamic culture, control experiments using equally high medium volumes in static culture were conducted, revealing no effect on the proliferation of the HT29-MTX cells (Figure S7). The improved proliferation and 3D organization under dynamic culture conditions seem to be solely induced by the applied physiological shear stress.

### 3.4. Villi Formation

The presence of intestinal micro- and macrovilli and the accompanying increase in overall surface area determines the high absorptive capacity of the small intestine [42].

Based on the previous data on morphology and proliferation, we further examined the cellular reorganization via visualization of the cytoskeleton. The 3D expansion of HT29-MTX cells under static and dynamic conditions can be seen in Figure 3a. For both culture conditions, hollow structures are visible in the lower regions of the epithelial layer, which are covered by cells on the top. In the literature, such structures within the HT29-MTX cell layer were previously described as arch morphology or mucus-containing vacuoles without attribution of a function [24,27]. In our hands, these structures did not contain mucins, but increased over time in number and size, merged to form larger entities and were overgrown by cell layers, resulting in a 3D expansion of the cellular monolayer. Although not yet completed, this 3D reorganization was more pronounced after two weeks of dynamic culture, with the villi-like structures having a height of up to 120  $\mu\text{m}$  [43], when compared to the situation after three weeks of static culture, in which there was a height of only up to 80  $\mu\text{m}$ . After three weeks of dynamic culture, the villi-like structures were even more defined and completely singularized, reaching up to 180  $\mu\text{m}$  in height (Figure 3a). These results validate the faster and much more sufficient maturation and reorganization of the cellular layer under minimal flow conditions.

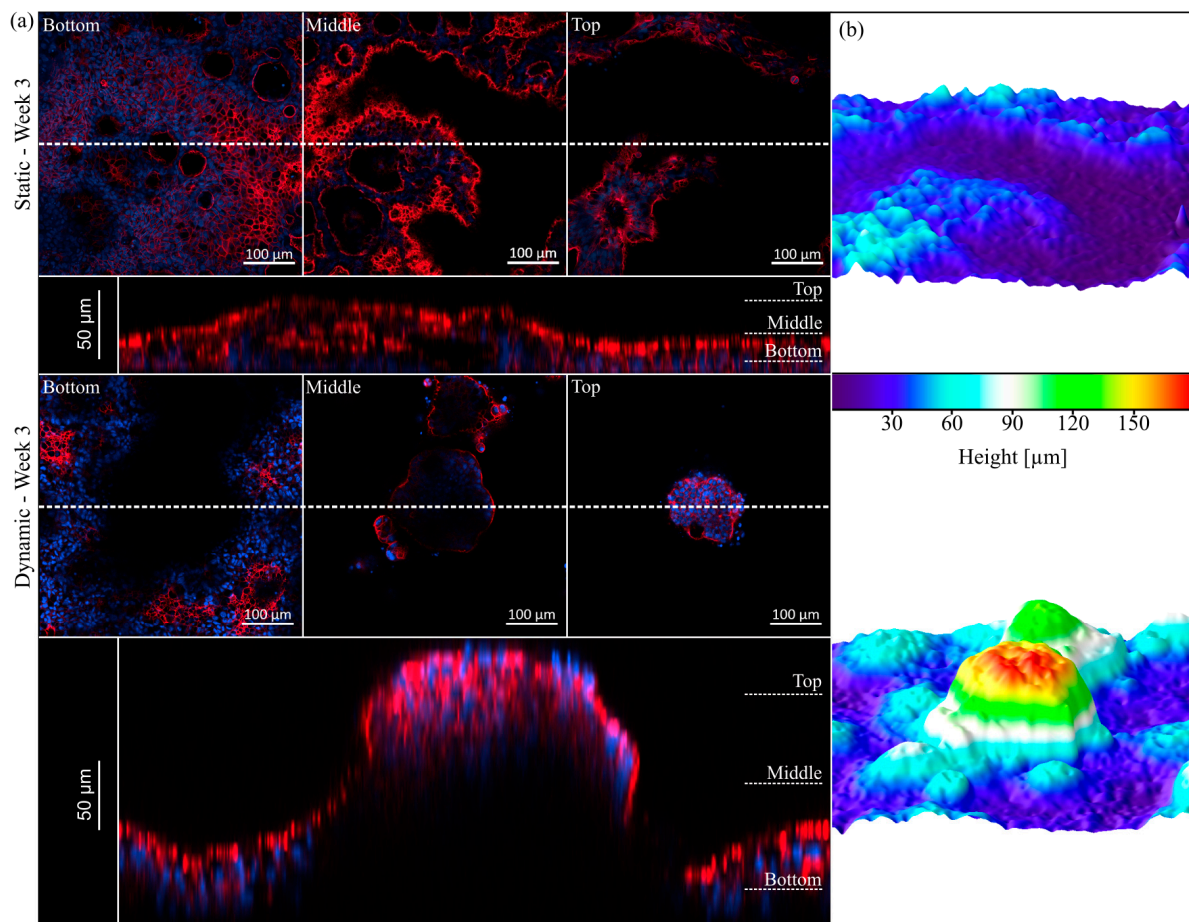


**Figure 3.** Topography of HT29-MTX cells under static and dynamic conditions after three weeks of culture. (a) Confocal images of F-actin (red) and nuclei (blue) staining at different z-positions (Bottom, Middle, Top) and representative orthogonal views below (the dotted line indicates the cutting plane). (b) Corresponding 3D surface reconstructions of z-stacks of the epithelium, modelled by ImageJ.

### 3.5. Mucus Characterization

Mucus synthesis and secretion, a major function of the intestinal epithelium [1], was examined for both culture conditions. Staining of acidic and neutral mucins revealed a time-dependent and ongoing increase in the respective mucins under static and dynamic culture

conditions (Figure 4a,b). The staining intensified more rapidly under dynamic conditions, which was not due to the higher medium volume and, therefore, better nutrition of the cells in this culture system. According to Wang et al., an increased mucus formation and thickness could be the result of a reduced dilution of mucin molecules in a smaller medium volume [25]. In our hands, the higher dilution in dynamic culture nevertheless resulted in increased mucus formation, whereas the same medium amount applied to static culture conditions revealed a dilution of mucins compared to the conventional static conditions (see Figure S8a). The higher amount of mucus per cell in dynamic culture can, therefore, be solely related to the applied fluid flow. To achieve the thickest possible mucus layers under static conditions, we recommend a reduction in medium volume (by as much as practically feasible) and particularly careful media changes.

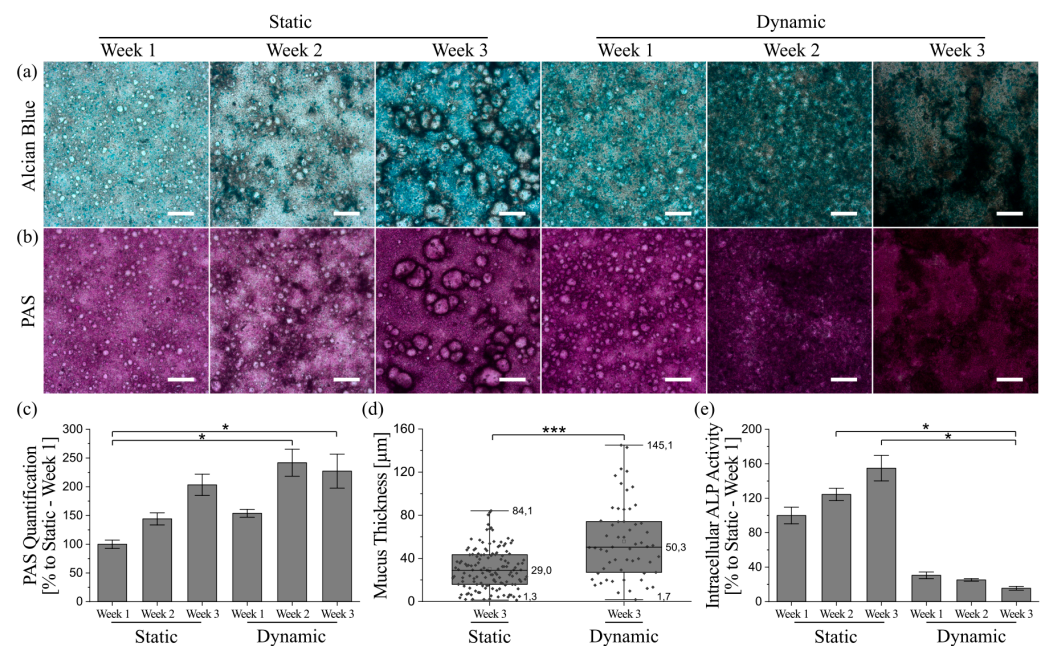


**Figure 4.** Qualitative and quantitative characterization of mucus produced by HT29-MTX cells under static and dynamic culture conditions at various time points. Microscopy images of (a) Alcian blue and (b) PAS-stained cells showing acidic mucins in blue and neutral mucins in purple, respectively. (Scale bars: 200 µm). (c) Photometrically quantified amounts of neutral mucins after PAS-incubation. Data presented as mean ± SEM with respect to week 1 under static conditions (n = 3–5). (d) Adherent mucus layer thickness determined under native conditions via confocal imaging data, shown as box plot, including data points, median and full range (n = 5). (e) Intracellular activity of ALP as enterocyte marker. Data presented as mean ± SEM with respect to week 1 under static conditions (n = 3–8). Statistical significance indicated by \*  $p \leq 0.05$  and \*\*\*  $p \leq 0.0005$ .

Furthermore, both acidic and neutral mucins seem to be located preferentially close to the aforementioned villi-like structures, which becomes most obvious under static conditions. Because the presence of multicellular layers is also accompanied by a reduction in visible light transparency, the color images of the stained samples might misleadingly suggest higher amounts of mucins at cell dense positions with 3D villi-like structures. Thus, we additionally determined the amount of neutral mucins per cell and were able to confirm the time-dependent increase in mucus production under both culture conditions (Figure 4c). The only significant increases in mucin amount were detectable after two and three weeks of dynamic culture when compared to static conditions after week 1. The 2.4-fold increase in mucin generation after two weeks of dynamic culture was already higher than the 2-fold increase after three weeks of static culture, clearly demonstrating the accelerated differentiation of HT29-MTX cells into goblet-like mucus-producing cells induced by shear stress. After week 2, the mucin amount in dynamic culture remained relatively stable.

This indicates the completion of differentiation into a mucus-producing phenotype after two weeks of physiological fluid flow, followed by a more defined 3D-restructuring of the cellular layers, as shown previously.

Adherent mucus is commonly analyzed after fixation of the respective samples, which causes the lack of data on mucus characteristics under native conditions. Unfortunately, common fixation methods lead to dehydration, and thus, a collapse of the adherent mucus, which does not represent its native structure. Consequently, the conventional fixation decreases the mucus thickness, resulting in thickness values in the range of a few micrometers for fixed HT29-MTX cells [17,24,27]. Even though there are some fixatives used that supposedly preserve its native structure, this is mutually dependent on the sample origin as the adherent mucus may be altered by multiple washing steps and further processing [44]. To overcome this obstacle, we incubated the native cultures with amine-modified fluorescent beads, which stick to the charged mucus via electrostatic interactions, and counterstained the cell nuclei with Hoechst. Confocal imaging and further image processing of z-stacks made it possible to measure the average distance between nuclei and beads sticking to the mucus surface (Figure 4d). We observed native mucus thicknesses reaching up to 84  $\mu\text{m}$  after three weeks under static conditions, and 145  $\mu\text{m}$  after three weeks under dynamic conditions. Thus, culture under physiological shear stress yielded an increase in maximum mucus thickness by 72%. The corresponding averaged thicknesses after three weeks of static or dynamic culture were  $29 \pm 14 \mu\text{m}$  and  $50 \pm 24 \mu\text{m}$ , respectively, indicating a significant average mucus thickness increase of 72% for flow conditions. Along with the accelerated development of mucus amounts in dynamic compared to static culture discussed above, a maximal mucus thickness of 148  $\mu\text{m}$  and an average thickness of  $41 \pm 14 \mu\text{m}$  measured after only two weeks of culture under flow [43] confirm the assumption of a faster differentiation of HT29-MTX cells into a goblet-like cell type under physiological shear stress.

Additionally, the intracellular activity of the enterocyte marker enzyme alkaline phosphatase (ALP) was measured to evaluate the differentiation status of the cells under different culture conditions in greater detail [45]. As illustrated in Figure 4e, the ALP activity increases time-dependently in samples obtained from static culture. Cells derived from dynamic culture, on the other hand, show a drastic reduction in ALP activity from week 1 onwards. Static control experiments with media volumes comparable to dynamic culture also revealed a decrease in intracellular ALP activity after three weeks when compared to conventional static culture (Figure S8b). However, the ALP activity in samples from dynamic culture was still reduced by a factor of two, supporting the hypothesis of a better maturation of the cells towards a goblet-like phenotype under flow.

### 3.6. Immunofluorescent Staining of Selected Mucins

To investigate the distribution and localization of selected mucins, the best characterized transmembrane mucin MUC1 and the two main GI secreted mucins MUC2 and MUC5AC were visualized via immunofluorescence (Figure 5). In general, all examined mucins were expressed at higher levels after culture of the cells under dynamic conditions and they were mainly located at the tips of the 3D villi-like structures, as can be concluded from the images showing the counterstaining of the nuclei. An enhanced shear-induced polarization was shown previously for various cell types, including epithelial and endothelial cells of different origins [24,46]. Furthermore, mucins are known to protect the underlying epithelium from mechanical stress [1], which is expected to be highest at the tip of the villi-like structures under dynamic conditions. MUC1 was hardly detectable under static conditions, whereas the tips of the villi-like structures of dynamically cultured cells were apically covered by MUC1. The stress-induced production of MUC2 was shown previously for HT29-MTX cells [27], and also for Caco-2 cells, which usually do not express MUC2 [47]. In our experiments, MUC2 seemed to be mainly stored intracellularly (Figure 5). MUC5AC is known to be highly expressed in the stomach and the respiratory tract [48] and it is the main secreted mucin of HT29-MTX cells [34]. It can multimerize by forming disulfide

bonds and contributes to the formation of a dense mucus network [49]. As can be seen in Figure 5, under dynamic culture conditions, the secreted MUC5AC forms a heavily branched network, which seems to span the tips of the villi-structures and as such may contribute to an increased robustness of the formed mucus layer. The immunofluorescent staining allows the observation of an increased mucus coverage of the cellular layer after culture under flow conditions. Additionally, the increased generation of secreted mucins after culture of the cells for only two weeks under dynamic conditions, compared to a culture spanning three weeks under static conditions, confirms the accelerated maturation of the HT29-MTX cells in the direction of the goblet cell phenotype. The respective images of the staining from all of the various time points, including week 2 of dynamic culture, as well as a further immunofluorescent staining for MUC5B can be found in Figure S6. Again, a control experiment using the medium volume of dynamic culture in a static approach resulted in a dilution of mucins even when compared to static culture (Figure S9). All effects seen under dynamic culture conditions can, therefore, be attributed to the influence of the fluid flow applied to the cell surface.

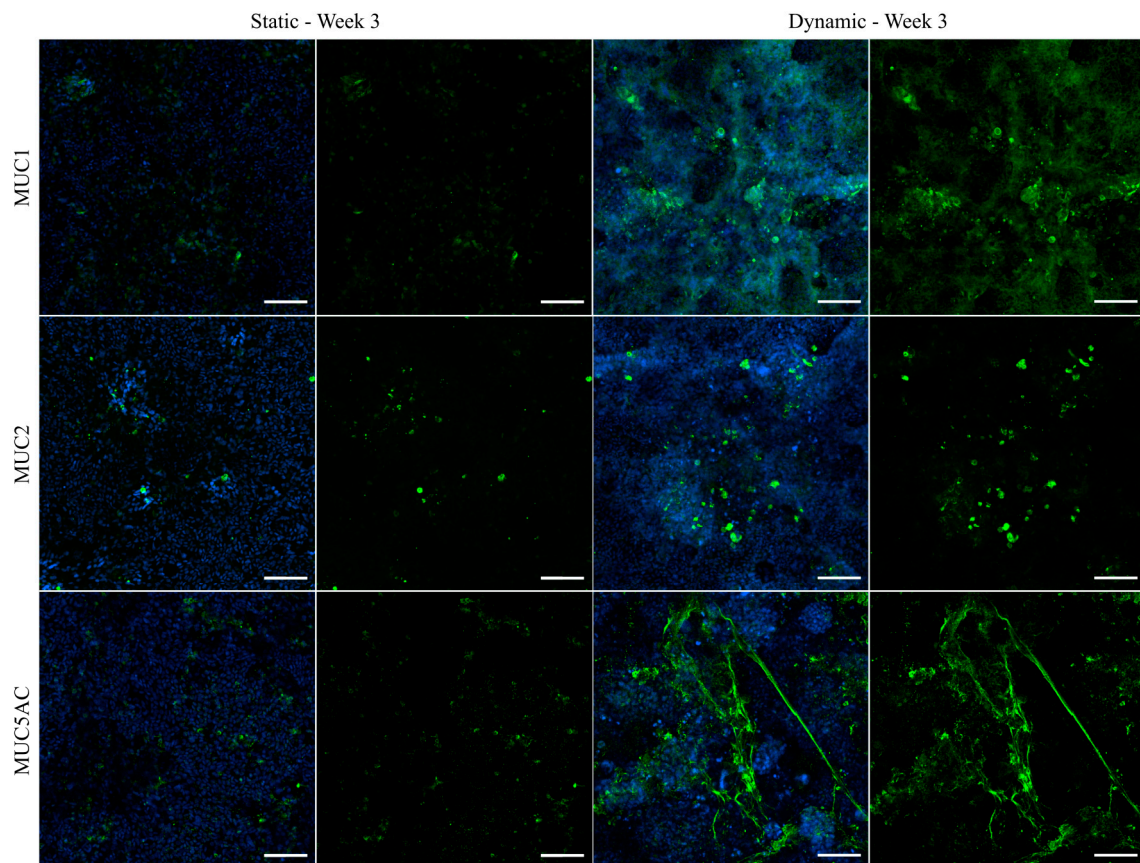


**Figure 5.** Confocal immunofluorescence images of HT29-MTX cells under static and dynamic conditions after three weeks. Samples were stained with antibodies for the membrane-bound mucin MUC1 and secreted mucins MUC2 and MUC5AC (green). Nuclei were counterstained with Hoechst 33342 (blue). (Scale bars: 100  $\mu$ m).

Since the immunofluorescent staining of MUC5AC showed high similarities to mucus networks found on the surface of airway epithelia, previously reported by Sheehan et al., we conducted a co-staining of MUC5AC and the main secreted airway mucin 5B (Figure 6) [50]. Interestingly, both mucins were colocalized in the previously observed branched networks and, to a lesser extent, in secretory vesicles, as indicated by the white arrow. Imaging at higher magnifications revealed diameters for these single fibers as small as 200 nm. A similar colocalization of fibrous MUC5AC and MUC5B in mucus networks is commonly observed in lung-derived mucus samples [51]. To the best of our knowledge, our results

are the first to show a fibrous and heavily entangled network of MUC5AC and MUC5B strands produced and secreted by the intestinal HT29-MTX cell line.

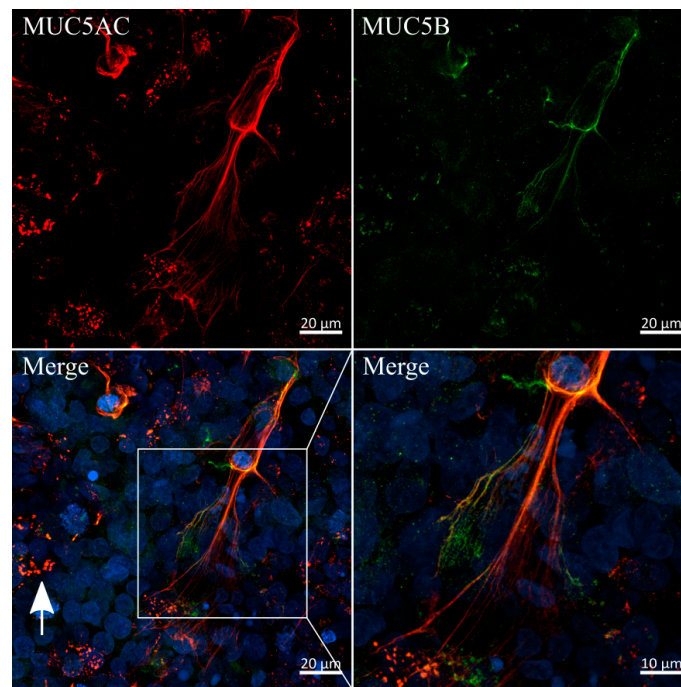


**Figure 6.** Colocalization and fiber-formation of secreted mucins MUC5AC and MUC5B. Confocal immunofluorescence images of HT29-MTX cells after two weeks of dynamic culture stained with antibodies for MUC5AC (red) and MUC5B (green). Nuclei were counterstained with Hoechst 33342 (blue). White arrow indicates an example of colocalization of both mucins in secretory vesicles.

### 3.7. Transfer of the Model System from Solid Substrates to Membranes

In order to transfer the established well-defined dynamic cell culture conditions for the fast maturation and differentiation of HT29-MTX cells from the microscopic slides to commercial cell culture inserts, we developed a fully 3D-printed insert culture chamber that enables the culture of cells on membranes under flow conditions. A similar setup is commercially available, comprising a silicone-based chamber that allows the application of apical and basal shear stress. However, silicone is known to adsorb hydrophobic drugs and applicable shear stresses are restricted to a relatively low maximum flow rate ( $\leq 500 \mu\text{L}/\text{min}$ ) with this system [52]. Furthermore, CFD simulations revealed that rather non-homogenous shear stresses were applied to the cellular surface, originating from the chamber design [53]. The CAD-model of our design and the printed and assembled chamber are shown in Figure 7a,b. CFD simulation at a volume flow rate of  $1.42 \text{ mL}\cdot\text{min}^{-1}$  (corresponding to 10 RPM) demonstrated a homogenous flow distribution, as illustrated by the velocity field, which applies a physiological shear stress of  $0.012 \text{ dyn}\cdot\text{cm}^{-2}$  ( $12 \times 10^{-4} \text{ Pa}$ ) to the cell surface of the cell culture insert (Figure 7c,d). The Dental SG Resin (Formlabs) used for 3D-printing of the insert chamber is specified as biocompatible. Nevertheless, a leaching assay was performed, which revealed no influence on the viability and no increase in cell death of HT29-MTX cells induced by contact of the cell culture medium with the printed resin for up to three weeks (Figure S10).

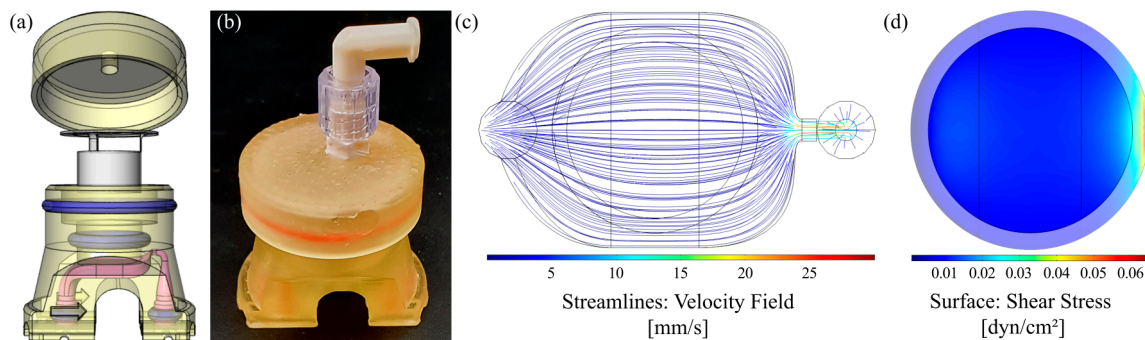


**Figure 7.** Chamber design for dynamic culture of cells on membranes and evaluation of flow properties. (a) CAD model (exploded view) and (b) photograph of the assembled 3D-printed culture chamber. (c) Corresponding velocity streamline profile within the fluid channel and (d) surface shear stress highlighted for the membrane area obtained by CFD simulation at a volume flow rate of  $1.42 \text{ mL} \cdot \text{min}^{-1}$ .

To ensure that cells cultured on conventional inserts are accessible to shear stress in the chamber, they must be seeded in a reverse manner onto the bottom of the insert membrane, as illustrated in Figure 8a. Among others, this method offers the advantage of improved optical access to the mucus layer and the mucus–cell interface and, thus, enhances the imaging quality in immunofluorescence experiments [54]. For a characterization of the epithelial barrier function of differently cultured HT29-MTX cell layers, we aimed at TEER measurements. In contrast to Caco-2 cells, which are the most commonly used model to mimic the intestinal barrier, HT29-MTX cells only form weak barriers, as indicated by low TEER values [55]. Beduneau et al. reported a time-dependent barrier formation of HT29-MTX cells developing from approximately  $20$  to  $60 \text{ } \Omega \cdot \text{cm}^2$  from day 7 to 14 in static culture [17]. These values were comparable to our TEER-measurements, and also showed a time-dependent increase in the barrier strength, reaching  $62.8 \pm 2.2 \text{ } \Omega \cdot \text{cm}^2$  after three weeks of normal static culture (Figure 8b). Notably, an additional increase in the barrier function of HT29-MTX cell layers under reverse static conditions was observed, with a 2-fold increase in the TEER value up to  $128.1 \pm 5.6 \text{ } \Omega \cdot \text{cm}^2$  after three weeks of inverted culture. It is reported, with Caco-2 cells, that static, reverse, upside-down culture on inserts had a qualitatively similar effect on differentiation and cellular reorganization as the application of fluid flow [56]. Moreover, upon application of defined shear stress of  $0.012 \text{ dyn} \cdot \text{cm}^{-2}$  ( $12 \times 10^{-4} \text{ Pa}$ ) to reversely cultured HT29-MTX cells, the maturation of the barrier was further accelerated compared to static cultures, resulting in significantly increased TEER values of  $37.3 \pm 2.1 \text{ } \Omega \cdot \text{cm}^2$  after one week followed by a more than 2-fold increase in the value, reaching  $84.0 \pm 3.6 \text{ } \Omega \cdot \text{cm}^2$  after only two weeks of dynamic culture (Figure 8b). At first glance, this increase seems to stagnate from two to three weeks of inverse dynamic culture (see dashed bar in Figure 8b). However, immunofluorescent stainings of the cytoskeleton via phalloidin revealed a similar formation of the villi-like structures detected on solid substrates when cultured under dynamic conditions (Figure 9a). The concomitant drastic increase in surface area under flow conditions thus resulted in TEER values that underestimated the reality. Therefore, we performed a correction of the value measured after three weeks of dynamic culture for the increased surface area (see Figure S13 for details). The resulting TEER value of  $121.5 \pm 8.1 \text{ } \Omega \cdot \text{cm}^2$  shows a clear increase after two weeks of dynamic culture and is in the same range as the one measured in static reverse conditions (Figure 8b).

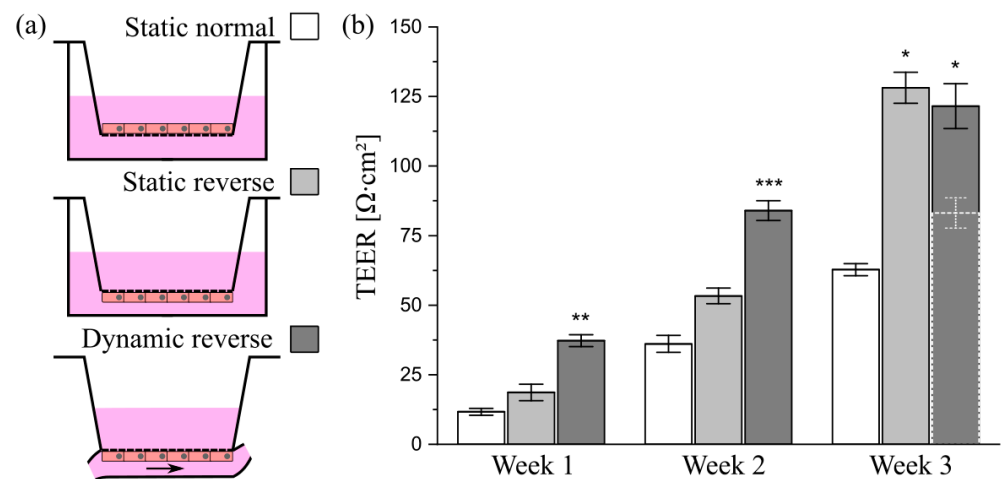


**Figure 8.** Influence of culture conditions on the barrier function of HT29-MTX cells. (a) Illustration of culture conditions with cells seeded either onto the top or bottom of Transwell®-insert membranes, termed as “normal” and “reverse”, and cultured under static or dynamic conditions. (b) Barrier function of HT29-MTX cells cultured under “Static normal” (white), “Static reverse” (light gray) and “Dynamic reverse” (dark gray) condition as quantified by TEER measurements at various time points. Data presented as mean ± SEM ( $n = 4–12$ ). Dotted bar (Dynamic reverse—Week 3) represents raw data prior to correction of the value for the surface area. \*  $p \leq 0.05$ ; \*\*  $p \leq 0.005$  and \*\*\*  $p \leq 0.0005$  compared to corresponding “Static normal”.

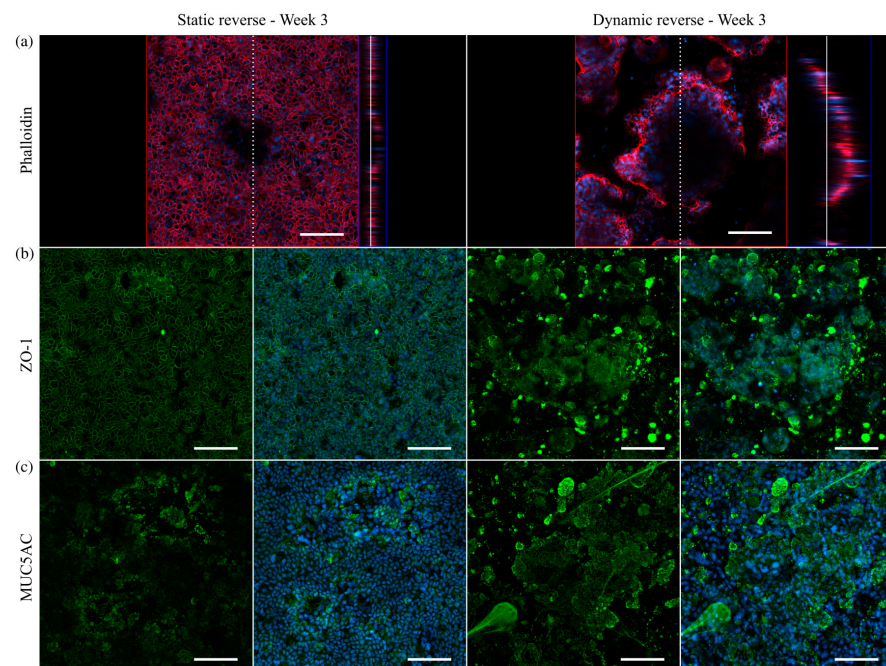


**Figure 9.** Confocal immunofluorescence images of HT29-MTX cells on Transwell®-insert membranes under static and dynamic conditions after three weeks. (a) Confocal image and corresponding orthogonal view of F-actin stained with phalloidin (red). Dotted and straight white line indicate the cutting plane and the position within the z-stack, respectively. Nuclei were counterstained with Hoechst 33342 (blue). Orthogonal projections of samples stained with antibodies for (b) ZO-1 as an integral part of tight junctions (green) and (c) the secreted mucin MUC5AC (green). (Scale bars: 100 μm).

To further investigate the epithelial barrier maturation, staining was conducted for the tight junction protein-1 (ZO-1), revealing a similar formation of tight junctions after

three weeks of static reverse and dynamic reverse culture (Figure 9b). Beyond that, the amount of the main mucin MUC5AC produced by HT29-MTX cells was markedly increased after three weeks of culture under physiological flow, with comparable structural features as seen previously under dynamic conditions on solid substrates (Figure 9c). Additional control experiments again confirmed the biocompatibility of the 3D-printed resin, showing no influence of potential leaching on barrier function and mucus production (Figures S11 and S12). Overall, we were able to transfer the improved HT29-MTX-based mucus model, established in dynamic culture on solid substrates, to membranes as culture substrate, thus allowing additional measurements of the barrier function.

#### 4. Conclusions

Reusable and sterilizable flow chambers were designed to apply physiologically relevant mechanical stress to intestinal HT29-MTX cells seeded on conventional microscopy slides or on membrane inserts. These conditions triggered the reorganization of the initial cellular monolayer, in the absence of cell-instructive gel matrices, towards a 3D structure that more closely resembles the physiological intestinal shape, with an increased surface area, via villi-like structure formation. Additionally, the required culture time for sufficient maturation towards a goblet-like phenotype was drastically reduced and a thick mucus layer could be detected, which was adherent to the cells. If singularized villi-like structures are desired in the model, a dynamic culture time of three weeks is recommended, while if only the produced mucus layer on the model is of interest, two weeks of dynamic culture are sufficient. Detailed analysis of the mucus revealed heavily branched networks of various mucins. We herein demonstrated the high impact of the application of physiological shear stresses of approximately  $0.01 \text{ dyn}\cdot\text{cm}^{-2}$  ( $1 \times 10^{-3} \text{ Pa}$ ) on the cellular differentiation, mucus production, barrier formation and 3D reorganization of the cellular layer without further need for expensive culture supplements or equipment. In the future, by transferring this technique to the culture of intestinal monolayers derived from organoids or stem cells, their physiological behavior in terms of villi-like structure formation and especially mucus production could be enhanced. Therefore, the obtained results are an important contribution to the future development of advanced human mucus or improved intestinal models to mimic the intestinal barrier in vitro.

**Supplementary Materials:** The following are available online at <https://www.mdpi.com/article/10.3390/cells10082062/s1>, Figure S1: Evaluation of flow properties in slide chambers, Figure S2: Surface shear stresses and velocity streamline profiles in slide chambers with varying channel heights, Figure S3: Setup for dynamic cell culture, Figure S4: Image processing and analysis to determine the native thickness of mucus produced by HT29-MTX cells, Figure S5: Colocalization of 3D self-organized and proliferative HT29-MTX cells, Figure S6: Confocal immunofluorescence images of HT29-MTX cells after static and dynamic culture at various time points, Figure S7: Influence of medium volume on cellular proliferation, Figure S8: Influence of medium volume on mucus production and intracellular ALP activity, Figure S9: Influence of medium volume on mucus structure, Figure S10: Biocompatibility of the 3D-printed resin, Figure S11: Influence of the 3D-printed resin on cellular barrier function, Figure S12: Influence of the 3D-printed resin on mucin expression and tight junction formation, Figure S13: Illustration of the surface area determination using ImageJ and Origin, Table S1: Calculated and simulated wall shear stress values, Table S2: Printing parameters for Dental SG Resin with LONGER Orange 30 printer, Table S3: Primary and secondary antibodies for immunofluorescent staining.

**Author Contributions:** Conceptualization, M.L. and M.W.; methodology, M.L. and S.B.; writing—original draft preparation, A.L. and M.L.; writing—review and editing, M.W. and L.E.; supervision, project administration and funding acquisition, M.W. All authors have read and agreed to the published version of the manuscript.

**Funding:** This research was funded by HZG Graduate School of Macromolecular Bioscience, the Federal Ministry of Education and Research, Germany (BMBF; grant number: 13N13523), and the collaborative research center CRC 1449 which was funded by the German Research Foundation (DFG).

**Institutional Review Board Statement:** Not applicable.

**Informed Consent Statement:** Not applicable.

**Data Availability Statement:** Data are reported within the article and in the Supplementary Materials.

**Acknowledgments:** We acknowledge the support of the OpenAccess Publication Fund of Freie Universität Berlin.

**Conflicts of Interest:** The authors declare no conflict of interest.

## References

- Johansson, M.E.; Sjovall, H.; Hansson, G.C. The gastrointestinal mucus system in health and disease. *Nat. Rev. Gastroenterol. Hepatol.* **2013**, *10*, 352–361. [[CrossRef](#)] [[PubMed](#)]
- Schroeder, B.O. Fight them or feed them: How the intestinal mucus layer manages the gut microbiota. *Gastroenterol. Rep.* **2019**, *7*, 3–12. [[CrossRef](#)] [[PubMed](#)]
- Prakash, S.; Rodes, L.; Coussa-Charley, M.; Tomaro-Duchesneau, C. Gut microbiota: Next frontier in understanding human health and development of biotherapeutics. *Biologics* **2011**, *5*, 71–86. [[CrossRef](#)] [[PubMed](#)]
- Maurer, M.; Gresnigt, M.S.; Last, A.; Wollny, T.; Berlinghof, F.; Pospich, R.; Cseresnyes, Z.; Medyukhina, A.; Graf, K.; Groger, M.; et al. A three-dimensional immunocompetent intestine-on-chip model as in vitro platform for functional and microbial interaction studies. *Biomaterials* **2019**, *220*, 119396. [[CrossRef](#)] [[PubMed](#)]
- Schultsz, C.; Van Den Berg, F.M.; Ten Kate, F.W.; Tytgat, G.N.; Dankert, J. The intestinal mucus layer from patients with inflammatory bowel disease harbors high numbers of bacteria compared with controls. *Gastroenterology* **1999**, *117*, 1089–1097. [[CrossRef](#)]
- Corfield, A.P.; Carroll, D.; Myerscough, N.; Probert, C.S. Mucins in the gastrointestinal tract in health and disease. *Front. Biosci.* **2001**, *6*, D1321–D1357. [[CrossRef](#)]
- Yildiz, H.M.; Speciner, L.; Ozdemir, C.; Cohen, D.E.; Carrier, R.L. Food-associated stimuli enhance barrier properties of gastrointestinal mucus. *Biomaterials* **2015**, *54*, 1–8. [[CrossRef](#)]
- Macierzanka, A.; Mackie, A.R.; Bajka, B.H.; Rigby, N.M.; Nau, F.; Dupont, D. Transport of particles in intestinal mucus under simulated infant and adult physiological conditions: Impact of mucus structure and extracellular DNA. *PLoS ONE* **2014**, *9*, e95274. [[CrossRef](#)]
- Müller, C.; Leithner, K.; Hauptstein, S.; Hintzen, F.; Salvenmoser, W.; Bernkop-Schnürch, A. Preparation and characterization of mucus-penetrating papain/poly(acrylic acid) nanoparticles for oral drug delivery applications. *J. Nanopart. Res.* **2012**, *15*, 1353. [[CrossRef](#)]
- Carlson, T.L.; Lock, J.Y.; Carrier, R.L. Engineering the Mucus Barrier. *Annu. Rev. Biomed. Eng.* **2018**, *20*, 197–220. [[CrossRef](#)]
- Harding, S.E. Trends in muco-adhesive analysis. *Trends Food Sci. Technol.* **2006**, *17*, 255–262. [[CrossRef](#)]
- Groo, A.C.; Saulnier, P.; Gimel, J.C.; Gravier, J.; Ailhaas, C.; Benoit, J.P.; Lagarce, F. Fate of paclitaxel lipid nanocapsules in intestinal mucus in view of their oral delivery. *Int. J. Nanomed.* **2013**, *8*, 4291–4302. [[CrossRef](#)]
- Boegh, M.; Baldursdottir, S.G.; Mullertz, A.; Nielsen, H.M. Property profiling of biosimilar mucus in a novel mucus-containing in vitro model for assessment of intestinal drug absorption. *Eur. J. Pharm. Biopharm.* **2014**, *87*, 227–235. [[CrossRef](#)] [[PubMed](#)]
- Youhanna, S.; Lauschke, V.M. The Past, Present and Future of Intestinal In Vitro Cell Systems for Drug Absorption Studies. *J. Pharm. Sci.* **2021**, *110*, 50–65. [[CrossRef](#)]
- Darling, N.J.; Mobbs, C.L.; Gonzalez-Hau, A.L.; Freer, M.; Przyborski, S. Bioengineering Novel in vitro Co-culture Models That Represent the Human Intestinal Mucosa With Improved Caco-2 Structure and Barrier Function. *Front. Bioeng. Biotechnol.* **2020**, *8*, 992. [[CrossRef](#)]
- Dosh, R.H.; Jordan-Mahy, N.; Sammon, C.; Le Maitre, C.L. Tissue Engineering Laboratory Models of the Small Intestine. *Tissue Eng. Part B Rev.* **2018**, *24*, 98–111. [[CrossRef](#)] [[PubMed](#)]
- Beduneau, A.; Tempesta, C.; Fimbel, S.; Pellequer, Y.; Jannin, V.; Demarne, F.; Lamprecht, A. A tunable Caco-2/HT29-MTX co-culture model mimicking variable permeabilities of the human intestine obtained by an original seeding procedure. *Eur. J. Pharm. Biopharm.* **2014**, *87*, 290–298. [[CrossRef](#)] [[PubMed](#)]
- Gagnon, M.; Zihler Berner, A.; Chervet, N.; Chassard, C.; Lacroix, C. Comparison of the Caco-2, HT-29 and the mucus-secreting HT29-MTX intestinal cell models to investigate Salmonella adhesion and invasion. *J. Microbiol. Methods* **2013**, *94*, 274–279. [[CrossRef](#)]
- van Klinken, B.J.; Oussoren, E.; Weenink, J.J.; Strous, G.J.; Buller, H.A.; Dekker, J.; Einerhand, A.W. The human intestinal cell lines Caco-2 and LS174T as models to study cell-type specific mucin expression. *Glycoconj. J.* **1996**, *13*, 757–768. [[CrossRef](#)]
- Lesuffleur, T.; Barbat, A.; Dussaulx, E.; Zweibaum, A. Growth adaptation to methotrexate of HT-29 human colon carcinoma cells is associated with their ability to differentiate into columnar absorptive and mucus-secreting cells. *Cancer Res.* **1990**, *50*, 6334–6343. [[PubMed](#)]
- Schultz, I.; Keita, A.V. The Intestinal Barrier and Current Techniques for the Assessment of Gut Permeability. *Cells* **2020**, *9*, 1909. [[CrossRef](#)]

22. Walter, E.; Janich, S.; Roessler, B.J.; Hilfinger, J.M.; Amidon, G.L. HT29-MTX/Caco-2 cocultures as an in vitro model for the intestinal epithelium: In vitro-in vivo correlation with permeability data from rats and humans. *J. Pharm. Sci.* **1996**, *85*, 1070–1076. [[CrossRef](#)] [[PubMed](#)]
23. Behrens, I.; Stenberg, P.; Artursson, P.; Kissel, T. Transport of lipophilic drug molecules in a new mucus-secreting cell culture model based on HT29-MTX cells. *Pharm. Res.* **2001**, *18*, 1138–1145. [[CrossRef](#)]
24. Navabi, N.; McGuckin, M.A.; Linden, S.K. Gastrointestinal cell lines form polarized epithelia with an adherent mucus layer when cultured in semi-wet interfaces with mechanical stimulation. *PLoS ONE* **2013**, *8*, e68761. [[CrossRef](#)]
25. Wang, Y.; Kim, R.; Sims, C.E.; Allbritton, N.L. Building a Thick Mucus Hydrogel Layer to Improve the Physiological Relevance of In Vitro Primary Colonic Epithelial Models. *Cell. Mol. Gastroenterol. Hepatol.* **2019**, *8*, 653–655.e655. [[CrossRef](#)] [[PubMed](#)]
26. Sontheimer-Phelps, A.; Chou, D.B.; Tovaglieri, A.; Ferrante, T.C.; Duckworth, T.; Fadel, C.; Frimantas, V.; Sutherland, A.D.; Jalili-Firoozinezhad, S.; Kasendra, M.; et al. Human Colon-on-a-Chip Enables Continuous In Vitro Analysis of Colon Mucus Layer Accumulation and Physiology. *Cell. Mol. Gastroenterol. Hepatol.* **2020**, *9*, 507–526. [[CrossRef](#)]
27. Reuter, C.; Alzheimer, M.; Walles, H.; Oelschlaeger, T.A. An adherent mucus layer attenuates the genotoxic effect of colibactin. *Cell. Microbiol.* **2018**, *20*, e12812. [[CrossRef](#)]
28. Kim, H.J.; Huh, D.; Hamilton, G.; Ingber, D.E. Human gut-on-a-chip inhabited by microbial flora that experiences intestinal peristalsis-like motions and flow. *Lab Chip.* **2012**, *12*, 2165–2174. [[CrossRef](#)] [[PubMed](#)]
29. Mahler, G.J.; Esch, M.B.; Glahn, R.P.; Shuler, M.L. Characterization of a gastrointestinal tract microscale cell culture analog used to predict drug toxicity. *Biotechnol. Bioeng.* **2009**, *104*, 193–205. [[CrossRef](#)]
30. Chi, M.; Yi, B.; Oh, S.; Park, D.J.; Sung, J.H.; Park, S. A microfluidic cell culture device (muFCCD) to culture epithelial cells with physiological and morphological properties that mimic those of the human intestine. *Biomed. Microdevices* **2015**, *17*, 9966. [[CrossRef](#)] [[PubMed](#)]
31. Zhao, Q.; Cole, T.; Zhang, Y.; Tang, S.Y. Mechanical Strain-Enabled Reconstitution of Dynamic Environment in Organ-on-a-Chip Platforms: A Review. *Micromachines* **2021**, *12*, 765. [[CrossRef](#)] [[PubMed](#)]
32. Ashammakhi, N.; Nasiri, R.; Barros, N.R.; Tebon, P.; Thakor, J.; Goudie, M.; Shamloo, A.; Martin, M.G.; Khademhosseini, A. Gut-on-a-chip: Current progress and future opportunities. *Biomaterials* **2020**, *255*, 120196. [[CrossRef](#)]
33. Poon, C. Measuring the density and viscosity of culture media for optimized computational fluid dynamics analysis of in vitro devices. *bioRxiv* **2020**. [[CrossRef](#)]
34. Furter, M.; Sellin, M.E.; Hansson, G.C.; Hardt, W.D. Mucus Architecture and Near-Surface Swimming Affect Distinct Salmonella Typhimurium Infection Patterns along the Murine Intestinal Tract. *Cell Rep.* **2019**, *27*, 2665–2678.e2663. [[CrossRef](#)]
35. Johansson, M.E.; Gustafsson, J.K.; Holmen-Larsson, J.; Jabbar, K.S.; Xia, L.; Xu, H.; Ghishan, F.K.; Carvalho, F.A.; Gewirtz, A.T.; Sjovall, H.; et al. Bacteria penetrate the normally impenetrable inner colon mucus layer in both murine colitis models and patients with ulcerative colitis. *Gut* **2014**, *63*, 281–291. [[CrossRef](#)] [[PubMed](#)]
36. Shemesh, J.; Jalilian, I.; Shi, A.; Heng Yeoh, G.; Knothe Tate, M.L.; Ebrahimi Warkiani, M. Flow-induced stress on adherent cells in microfluidic devices. *Lab Chip.* **2015**, *15*, 4114–4127. [[CrossRef](#)]
37. Wong, T.Y.; Chang, S.N.; Jhong, R.C.; Tseng, C.J.; Sun, G.C.; Cheng, P.W. Closer to Nature Through Dynamic Culture Systems. *Cells* **2019**, *8*, 942. [[CrossRef](#)]
38. Lesuffleur, T.; Porchet, N.; Aubert, J.P.; Swallow, D.; Gum, J.R.; Kim, Y.S.; Real, F.X.; Zweibaum, A. Differential expression of the human mucin genes MUC1 to MUC5 in relation to growth and differentiation of different mucus-secreting HT-29 cell subpopulations. *J. Cell Sci.* **1993**, *106 Pt 3*, 771–783. [[CrossRef](#)]
39. Reuter, C.; Oelschlaeger, T.A. Enhancement of Mucus Production in Eukaryotic Cells and Quantification of Adherent Mucus by ELISA. *Bio-Protocol* **2018**, *8*. [[CrossRef](#)]
40. Berger, E.; Nassra, M.; Atgie, C.; Plaisancie, P.; Geloan, A. Oleic Acid Uptake Reveals the Rescued Enterocyte Phenotype of Colon Cancer Caco-2 by HT29-MTX Cells in Co-Culture Mode. *Int. J. Mol. Sci.* **2017**, *18*, 1573. [[CrossRef](#)] [[PubMed](#)]
41. Costello, C.M.; Phillipsen, M.B.; Hartmanis, L.M.; Kwasnica, M.A.; Chen, V.; Hackam, D.; Chang, M.W.; Bentley, W.E.; March, J.C. Microscale Bioreactors for in situ characterization of GI epithelial cell physiology. *Sci. Rep.* **2017**, *7*, 12515. [[CrossRef](#)]
42. Helander, H.F.; Fandriks, L. Surface area of the digestive tract—Revisited. *Scand. J. Gastroenterol.* **2014**, *49*, 681–689. [[CrossRef](#)]
43. Lindner, M.; Laporte, A.; Block, S.; Elomaa, L.; Weinhart, M. Physiological shear stress enhances differentiation and mucus-formation of intestinal epithelial cells in vitro. *Authorea Prepr.* **2020**. [[CrossRef](#)]
44. Rohe, I.; Huttner, F.J.; Plendl, J.; Drewes, B.; Zentek, J. Comparison of different histological protocols for the preservation and quantification of the intestinal mucus layer in pigs. *Eur. J. Histochem.* **2018**, *62*, 2874. [[CrossRef](#)]
45. Goldberg, R.F.; Austen, W.G., Jr.; Zhang, X.; Munene, G.; Mostafa, G.; Biswas, S.; McCormack, M.; Eberlin, K.R.; Nguyen, J.T.; Tatlidede, H.S.; et al. Intestinal alkaline phosphatase is a gut mucosal defense factor maintained by enteral nutrition. *Proc. Natl. Acad. Sci. USA* **2008**, *105*, 3551–3556. [[CrossRef](#)] [[PubMed](#)]
46. Wojciak-Stothard, B.; Ridley, A.J. Shear stress-induced endothelial cell polarization is mediated by Rho and Rac but not Cdc42 or PI 3-kinases. *J. Cell Biol.* **2003**, *161*, 429–439. [[CrossRef](#)]
47. Kim, H.J.; Ingber, D.E. Gut-on-a-Chip microenvironment induces human intestinal cells to undergo villus differentiation. *Integr. Biol.* **2013**, *5*, 1130–1140. [[CrossRef](#)]
48. Johansson, M.E.; Hansson, G.C. Immunological aspects of intestinal mucus and mucins. *Nat. Rev. Immunol.* **2016**, *16*, 639–649. [[CrossRef](#)]

49. Sheehan, J.K.; Kirkham, S.; Howard, M.; Woodman, P.; Kutay, S.; Brazeau, C.; Buckley, J.; Thornton, D.J. Identification of molecular intermediates in the assembly pathway of the MUC5AC mucin. *J. Biol. Chem.* **2004**, *279*, 15698–15705. [[CrossRef](#)] [[PubMed](#)]
50. Sheehan, J.K.; Brazeau, C.; Kutay, S.; Pigeon, H.; Kirkham, S.; Howard, M.; Thornton, D.J. Physical characterization of the MUC5AC mucin: A highly oligomeric glycoprotein whether isolated from cell culture or in vivo from respiratory mucous secretions. *Biochem. J.* **2000**, *347 Pt 1*, 37–44. [[CrossRef](#)]
51. Fischer, A.J.; Pino-Argumedo, M.I.; Hilkin, B.M.; Shanrock, C.R.; Gansemer, N.D.; Chaly, A.L.; Zarei, K.; Allen, P.D.; Ostedgaard, L.S.; Hoffman, E.A.; et al. Mucus strands from submucosal glands initiate mucociliary transport of large particles. *JCI Insight* **2019**, *4*, e124863. [[CrossRef](#)]
52. IVTech Srl Home Page of LiveBox2 Bioreactor. Available online: [https://www.ivtech.it/Products/LiveBox2-\(LB2\)](https://www.ivtech.it/Products/LiveBox2-(LB2)) (accessed on 5 August 2021).
53. Cacopardo, L.; Costa, J.; Giusti, S.; Buoncompagni, L.; Meucci, S.; Corti, A.; Mattei, G.; Ahluwalia, A. Real-time cellular impedance monitoring and imaging of biological barriers in a dual-flow membrane bioreactor. *Biosens. Bioelectron.* **2019**, *140*, 111340. [[CrossRef](#)] [[PubMed](#)]
54. Zaderer, V.; Hermann, M.; Lass-Florl, C.; Posch, W.; Wilflingseder, D. Turning the World Upside-Down in Cellulose for Improved Culturing and Imaging of Respiratory Challenges within a Human 3D Model. *Cells* **2019**, *8*, 1292. [[CrossRef](#)]
55. Schimpel, C.; Teubl, B.; Absenger, M.; Meindl, C.; Frohlich, E.; Leitinger, G.; Zimmer, A.; Roblegg, E. Development of an advanced intestinal in vitro triple culture permeability model to study transport of nanoparticles. *Mol. Pharm.* **2014**, *11*, 808–818. [[CrossRef](#)] [[PubMed](#)]
56. Shen, C.; Meng, Q.; Zhang, G. Design of 3D printed insert for hanging culture of Caco-2 cells. *Biofabrication* **2014**, *7*, 015003. [[CrossRef](#)]

# Supplementary Information to the Manuscript “Physiological Shear Stress Enhances Differentiation, Mucus-Formation and Structural 3D Organization of Intestinal Epithelial Cells *in vitro*.”

Marcus Lindner <sup>1</sup>, Anna Laporte <sup>2</sup>, Stephan Block <sup>1</sup>, Laura Elomaa <sup>1</sup> and Marie Weinhart <sup>1,2\*</sup>

<sup>1</sup> Institute of Chemistry and Biochemistry, Freie Universität Berlin, Berlin, Germany

<sup>2</sup> Institute of Physical Chemistry and Electrochemistry, Leibniz Universität Hannover, Hannover, Germany

\* Correspondence: marie.weinhart@pci.uni-hannover.de; Tel.: +49 511 76214938

## Outline

1. Chamber Design and Evaluation .....	2
2. 3D-Printing .....	3
3. Setup for Dynamic Cell Culture .....	4
4. Thickness-determination of the Adherent Mucus Layer .....	5
5. Colocalization of Proliferative and 3D Self-organized Cells .....	6
6. Immunofluorescent Staining .....	6
7. Control Experiments – Medium Volume Adaption in Static Culture .....	7
8. Control Experiments – Material Leaching Assay to Assess Biocompatibility .....	9
9. Cellular Area Determination .....	11
10. References .....	12

## 1. Chamber Design and Evaluation

The range of applicable wall shear stresses was determined via mathematical approximation and validated by CFD simulation. Channel heights of the culture chamber and applied flow rates were varied from 0.15 to 6 mm and 2.84 to 14.2 mL/min, respectively (Table S1).

**Table S1.** Calculated and simulated wall shear stress values.

Channel Height [mm]	Homogenizer	Average surface shear stress [dyn/cm <sup>2</sup> ] (CFD / calculated <sup>†</sup> )		
		2.84 mL/min (20 RPM) ‡	6.4 mL/min (45 RPM) ‡	14.2 mL/min (100 RPM) ‡
0.15	Threshold	4.6 / 5.9	10.4 / 13.2	23.1 / 29.7
0.35	Threshold	0.86 / 1.08	1.93 / 2.43	4.29 / 5.39
1.5	Threshold	0.055 / 0.059	0.124 / 0.132	0.277 / 0.294
6	Triangular	0.0039 / 0.0037	0.0088 / 0.0083	0.0196 / 0.0183

<sup>†</sup> mathematical approximation:  $\tau=6\mu Qw^{-1}h^{-2}$  with  $\mu=0.93$  cP

<sup>‡</sup> valid for the OSPIN bioreactor system, using silicone tubings with an inner diameter of 1.6 mm.

CFD simulations were conducted to evaluate the fluid flow behavior within different channel geometries. Homogenous flow is enabled by a construction-dependent threshold for channel heights up to 1.5 mm, whereas a channel height of 6 mm necessitates the implementation of homogenizing structures (Figure S1).

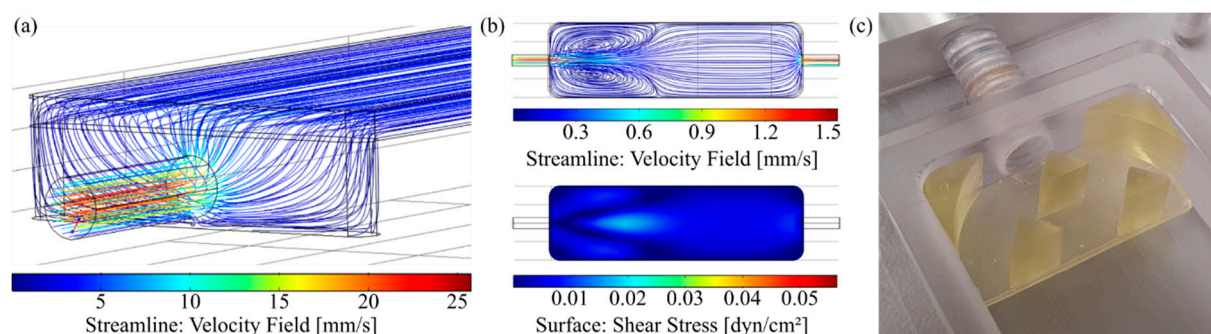


**Figure S1.** Evaluation of flow properties in slide chambers. (a) Fluid flow behaviour (velocity streamline profile) in a chamber with 1.5 mm channel height including a homogenizing threshold at a volume flow rate of 6.4 mL·min<sup>-1</sup>. (b) Velocity streamline profile and surface shear stress in culture chambers without homogenizing structures with a channel height of 6 mm and a 6.4 mL·min<sup>-1</sup> volume flow rate. (c) Photograph of a 3D-printed homogenizing insert (triangular) in a culture chamber.

Surface shear stress and velocity streamline profiles of all chambers at  $6.4 \text{ mL min}^{-1}$  (45 RPM) are shown in Figure S2.

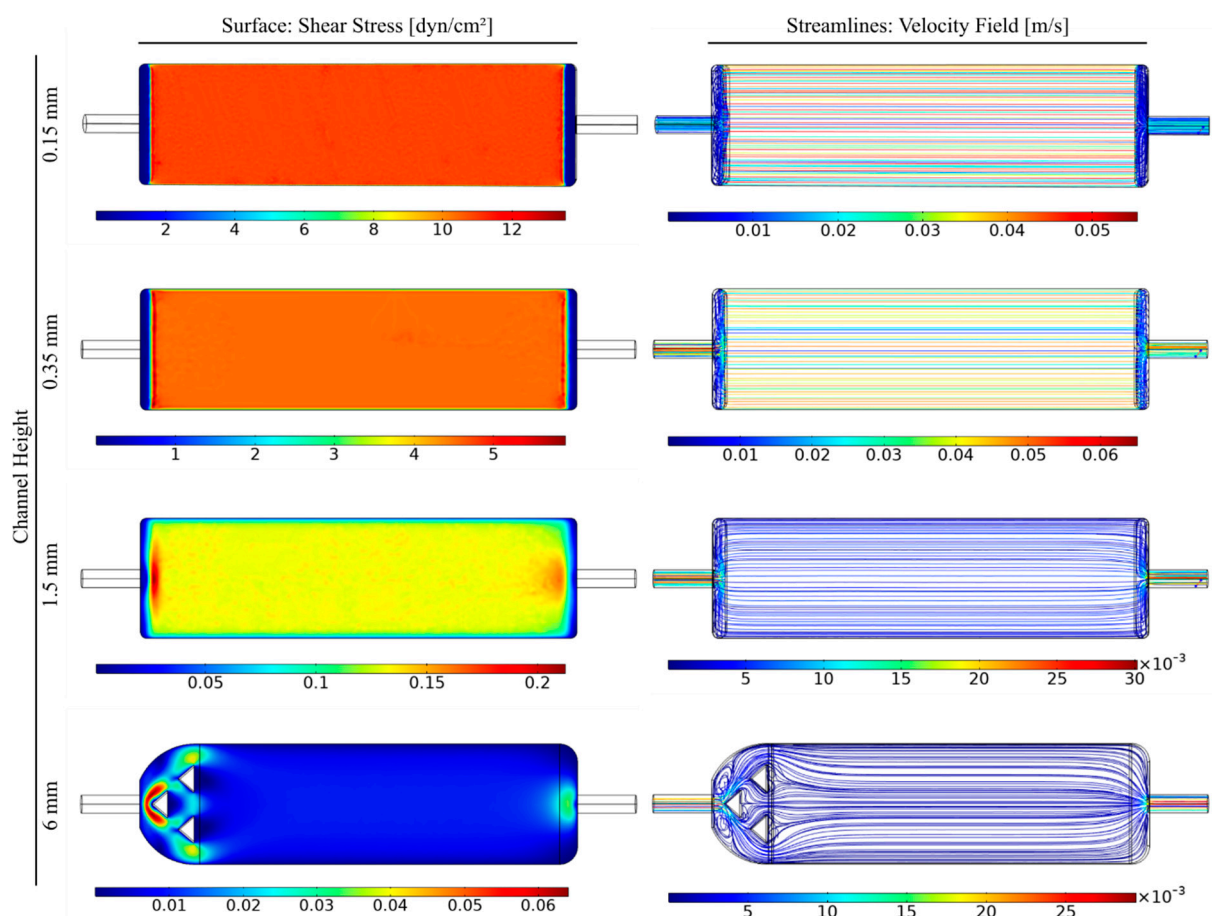


**Figure S2.** Surface shear stresses and velocity streamline profiles in slide chambers with varying channel heights from 0.15 to 6 mm including homogenizing structures at a volume flow rate of  $6.4 \text{ mL} \cdot \text{min}^{-1}$ .

## 2. 3D-Printing

Homogenizing structures and chambers for dynamic insert culture were CAD-modelled with *Rhinoceros* (Version 5.0, Robert McNeel & Associates, Seattle, WA/USA) and exported as an stl-file. We used a LONGER Orange 30 printer (Shenzhen, China) and Formlabs Dental SG resin (Somerville, MA/USA), which is classified as biocompatible according to EN-ISO 10993-1:2009/AC:2010 to print the models. The stl-file was imported into the printer's own slicing software *LongerWare* v1.32. The models were manually aligned in x- and y-position and tilted, if necessary. Supporting structures were added with default specifications and the model was sliced with a layer thickness of  $50 \mu\text{m}$ . The resin-specific printing parameters can be found in Table S2. After exporting the lgs-file and printing, the parts were removed from the building platform and washed twice in 99% isopropyl alcohol or ethanol, followed by a post-curing step in a self-made chamber using a 30 W UV-A LED lamp ( $\lambda = 385\text{-}400 \text{ nm}$ ) for 60 seconds each (top & bottom). The models were finally washed excessively with warm tap water and extracted in deionized water at  $37 \text{ }^\circ\text{C}$  for at least 24 h.

**Table S2.** Printing parameters for Dental SG Resin with LONGER Orange 30 printer.

Parameter	Value
Burn-In Time [ms]	: 60000
Burn-In Range [mm]	: 0.3
Curing Time [ms]	: 7500
Stable Time [ms]	: 1000
Lift Distance 1 [mm]	: 2
Lift Speed 1 [mm/min]	: 48
Lift Distance 2 [mm]	: 2
Lift Speed 2 [mm/min]	: 300

### 3. Setup for Dynamic Cell Culture

The dynamic culture of cells on solid surfaces was performed using OSPIN's bioreactor system. A photo of the setup without the closing lid is shown in Figure S3a. Peristaltic pumps provide perfusion of the circuit and enable an automatic media exchange. The pH-value is monitored on-line and controlled via passive diffusion of CO<sub>2</sub> through a silicone tubing in the gassing unit. With the system closed, a temperature of 37 °C is maintained. A simpler system was used for cultivation of cells on cell culture inserts, with a peristaltic pump directly operated in a cell culture incubator under standard conditions (37 °C, 5% CO<sub>2</sub>), shown in Figure S3b. A bubble trap and four culture chambers were mounted in line as a circuit.

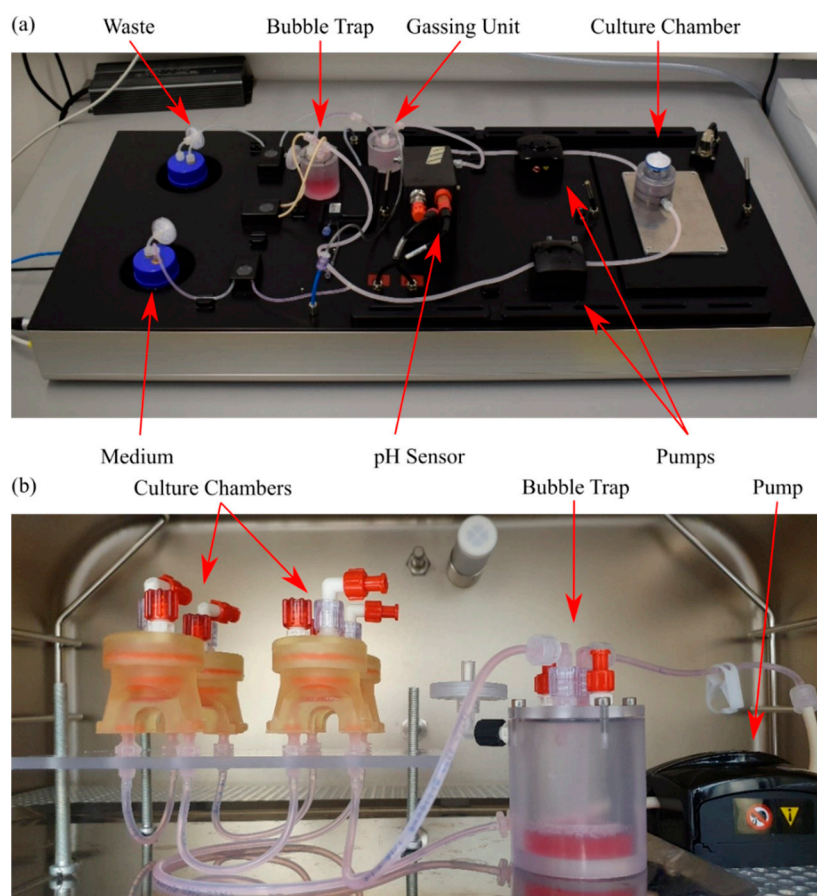


**Figure S3.** Setup for dynamic cell culture. A labeled photograph of (a) the bioreactor system and (b) a peristaltic pump, operated in a cell culture incubator, including the circuits for the dynamic culture of cells on solid substrates and cell culture inserts, respectively.

#### 4. Thickness-determination of the Adherent Mucus Layer

To determine mucus thickness, unfixed samples were incubated with fluorescence-labelled particles as well as Hoechst and subsequently analyzed using confocal microscopy [1, 2]. Multiple frame averaging (4x) is essential during data acquisition. The raw data (Z-stacks, 8-bit grayscale) is converted into binary images via manual thresholding in *ImageJ*. Frame averaging allows the exclusion of unbound particles via their reduced intensity. Particle analysis is then performed using *BoneJ* plugin, applying a size filter of 500-2500 and 5-150  $\mu\text{m}^3$  for nuclei and beads, respectively (Figure S4a). The obtained coordinates (X, Y and Z position) were verified (exemplified in Figure S4b) and allotted to groups in a 10x10 heatmap with *Origin* to prevent areas with high bead-density from falsifying the results (Figure S4c). Finally, corresponding clustered data points were subtracted from each other (beads minus nuclei). The slight overestimation of thickness due to the distance from nucleus center to cell surface was deliberately ignored since nuclei had an average radius of approximately  $6 \pm 2 \mu\text{m}$  and were thus within the margin of error.

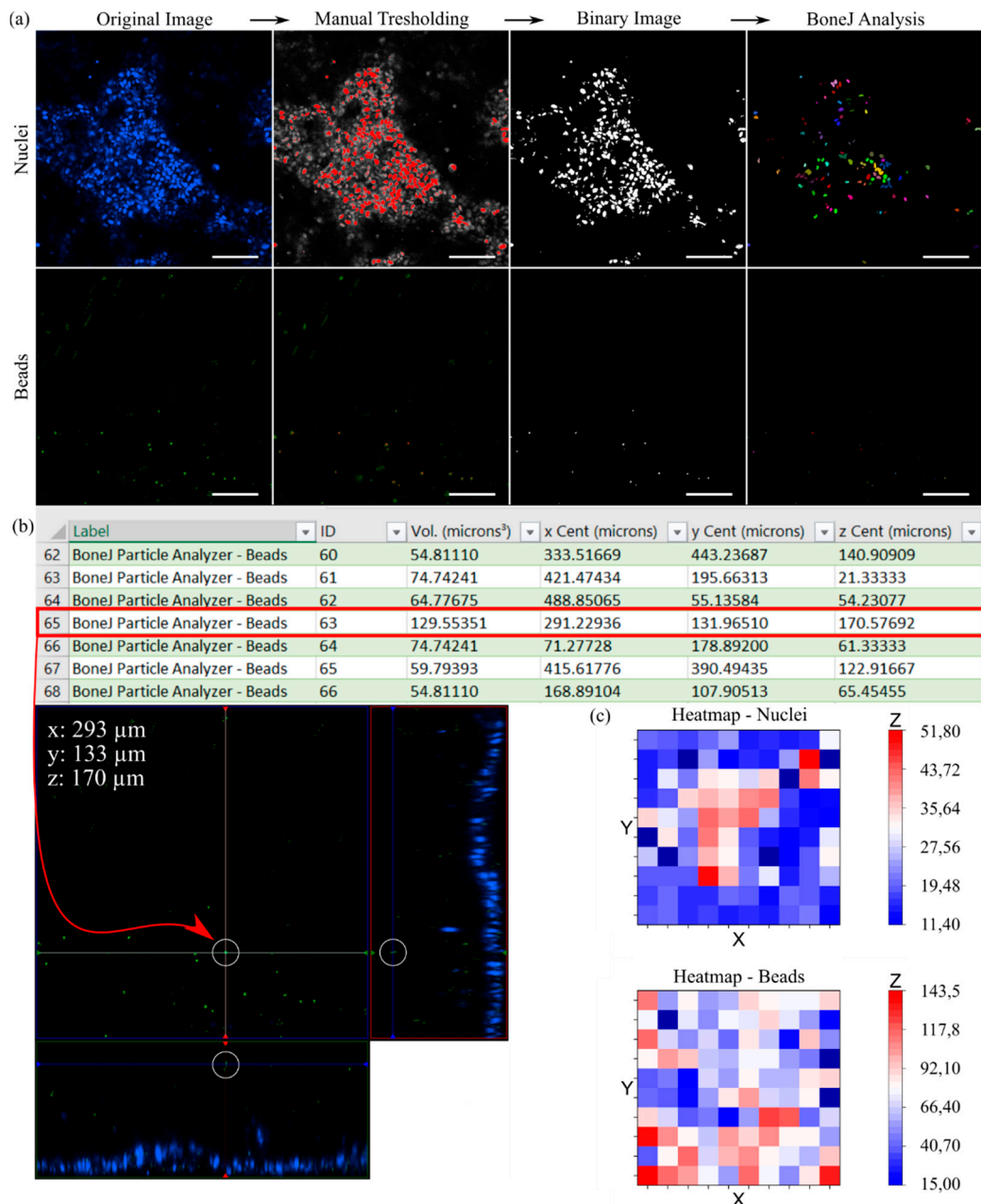


**Figure S4.** Image processing and analysis to determine the native thickness of mucus produced by HT29-MTX cells. (a) The raw data is converted into a binary image via manual thresholding and analyzed via *BoneJ*'s particle analyzer. The results were verified, as illustrated exemplary in (b). All data points were plotted in *Origin* as a 10x10 matrix and finally subtracted (beads - nuclei; (c)). (scale bar 100  $\mu\text{m}$ )

## 5. Colocalization of Proliferative and 3D Self-organized Cells.

As the confocal microscope used for acquisition of fluorescence images shown in the main manuscript is not equipped with a camera for brightfield imaging, we examined HT29-MTX cells after 3 weeks of dynamic culture on a normal inverted epifluorescence microscope, after staining with Hoechst and EdU for nuclei and proliferative cells, respectively. The dark areas, which are pronounced after dynamic culture, show a clear colocalization with proliferating cells, illustrated by the merged images in Figure S5.

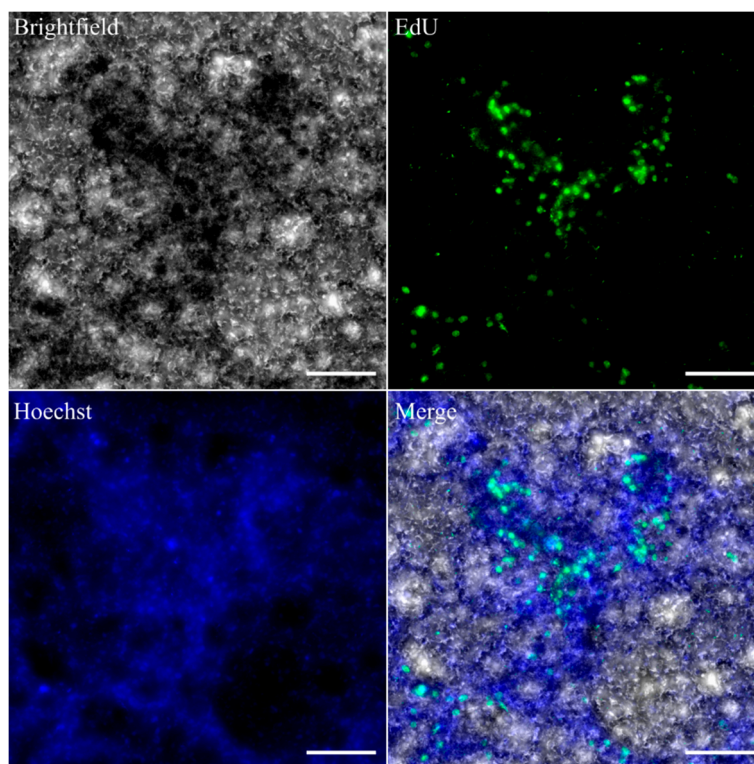


**Figure S5.** Colocalization of 3D self-organized (dark areas, brightfield) and proliferative HT29-MTX cells (green, EdU), obtained via brightfield and epifluorescence microscopy, respectively. Nuclei were counterstained with Hoechst 33342 (blue). (scale bar 100  $\mu$ m)

## 6. Immunofluorescent Staining

For immunofluorescent staining of selected mucins and ZO-1, the following antibodies and dilutions were used.

**Table S3.** Primary and secondary antibodies for immunofluorescent staining.

Target	Species	Dilution	2 <sup>nd</sup> Antibody (1:500)
MUC1	Rabbit (polyclonal)	1:200	Goat- $\alpha$ -rabbit (H+L) Alexa-488 <sup>®</sup>
MUC2	Mouse (monoclonal)	1:100	Goat- $\alpha$ -mouse (IgG1) Alexa-488 <sup>®</sup>
			(counterstained with Phalloidin-Atto647 <sup>®#</sup> )
MUC5AC	Mouse (monoclonal)	1:250	Goat- $\alpha$ -mouse (IgG1) Alexa-488 <sup>®</sup>
MUC5B	Rabbit (polyclonal)	1:100	Goat- $\alpha$ -rabbit (H+L) Alexa-488 <sup>®</sup>
ZO-1	Rabbit (polyclonal)	1:250	Goat- $\alpha$ -rabbit (H+L) Alexa-647 <sup>®</sup>
Co-Staining			
MUC5AC	Mouse (monoclonal)	1:250	Goat- $\alpha$ -mouse (IgG1) Alexa-647 <sup>®</sup>
MUC5B	Rabbit (polyclonal)	1:100	Goat- $\alpha$ -rabbit (H+L) Alexa-488 <sup>®</sup>

<sup>#</sup> diluted 1:200 in PBS, incubation for 1 h at room temperature

Confocal images of immunofluorescent stainings of HT29-MTX cells after dynamic and static culture for up to three weeks on solid substrates are shown in Figure S6.

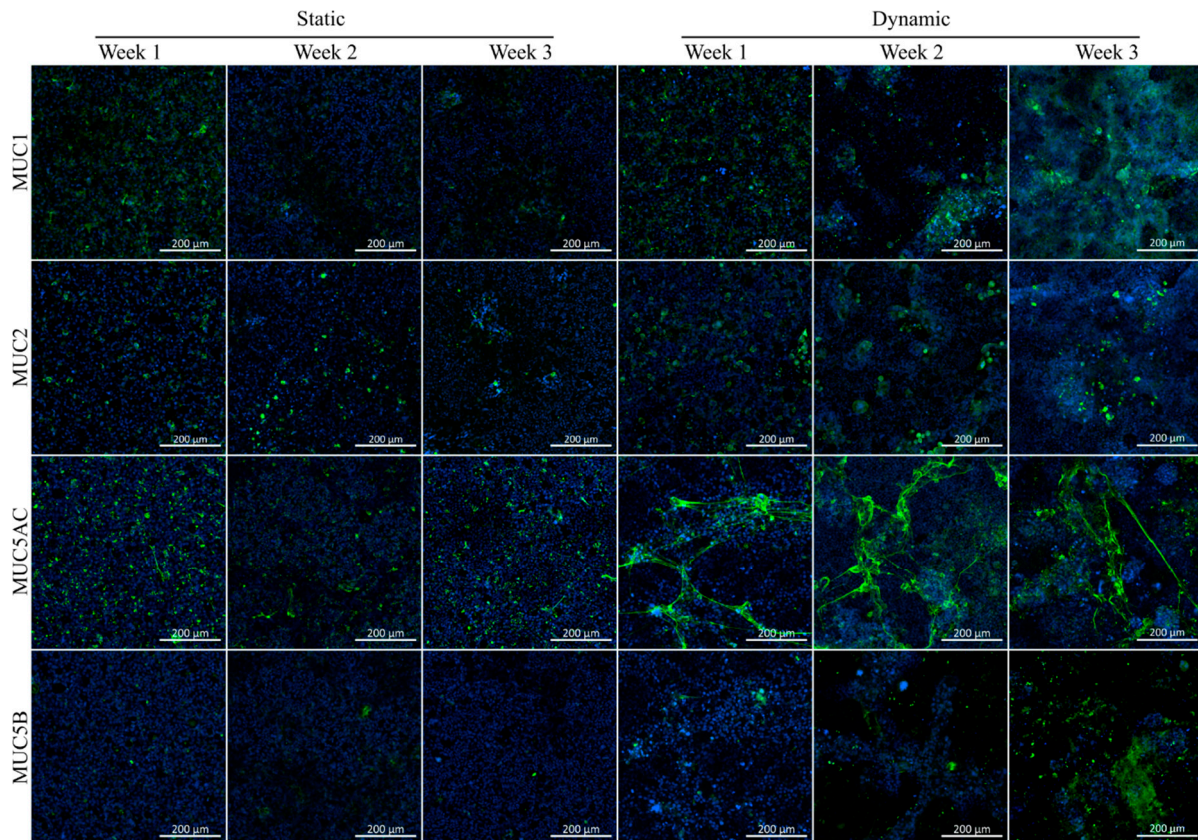


**Figure S6.** Confocal immunofluorescence images of HT29-MTX cells after static and dynamic culture at various time points stained with antibodies for the membrane-bound mucin MUC1 and secreted mucins MUC2, MUC5AC and MUC5B (green). Nuclei were counterstained with Hoechst 33342 (blue).

## 7. Control Experiments – Medium Volume Adaption in Static Culture

Since the bioreactor circuit contains a higher volume of cell culture medium compared to static culture on solid substrates, control experiments were performed to ensure that the observed effects were caused by the shear stress in dynamic culture only and were not related to the higher medium volume. Cells were either cultured under standard conditions (Static Culture), dynamic conditions (Dynamic Culture) or static conditions with similar ratio of medium volume to cell seeding area as in the dynamic culture (Medium control). Changes in proliferation (Figure S7), mucus production (Figure S8a), ALP activity (Figure S8b) and mucus structure (Figure S9) induced by higher medium volume were not comparable to the ones seen in dynamic culture. The cell proliferation was even weaker than in conventional static culture after three weeks and mucin amounts tended to be much lower due to the higher dilution of mucins under static conditions with high medium volume [3].

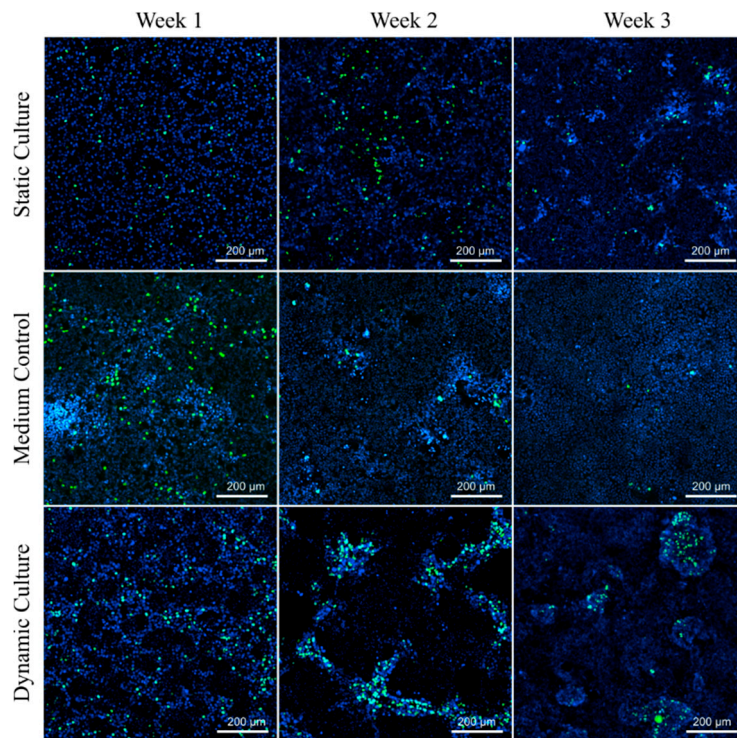


**Figure S7.** Influence of medium volume on cellular proliferation. HT29-MTX cells were cultured for up to three weeks under conventional conditions (Static Culture), dynamic conditions (Dynamic Culture), and static conditions with media volumes comparable to dynamic culture (Medium Control). n=2

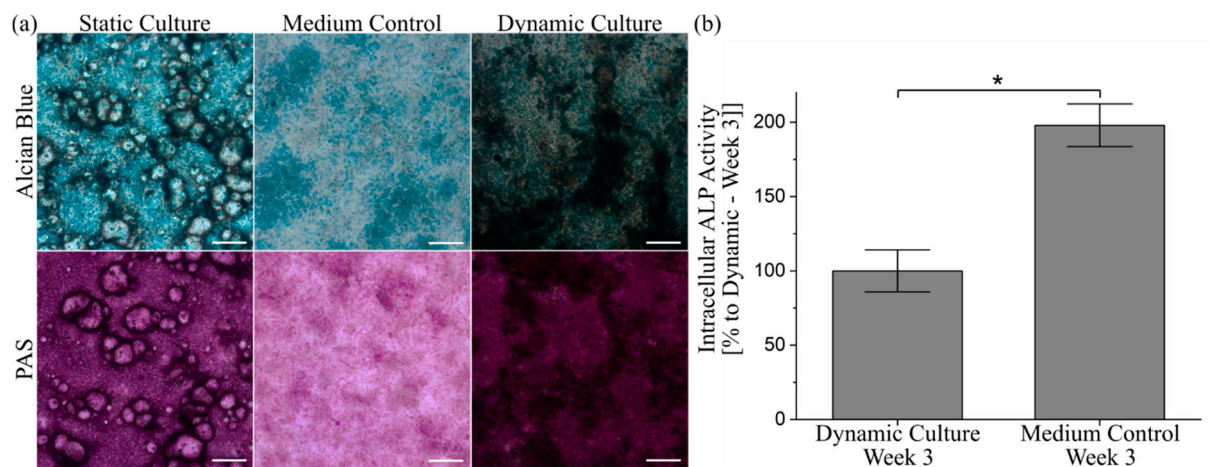


**Figure S8.** Influence of medium volume on mucus production and intracellular ALP activity. (a) Alcian blue and PAS staining of HT29-MTX after three weeks of culture under conventional conditions (Static Culture), dynamic conditions (Dynamic Culture), and static conditions with media volumes comparable to dynamic culture (Medium Control) n=2. (b) Intracellular ALP activity after three weeks of culture under dynamic conditions and static conditions with media volumes comparable to dynamic culture (Medium Control). Data presented as mean  $\pm$  SEM with respect to week 3 under dynamic conditions. n=4-8

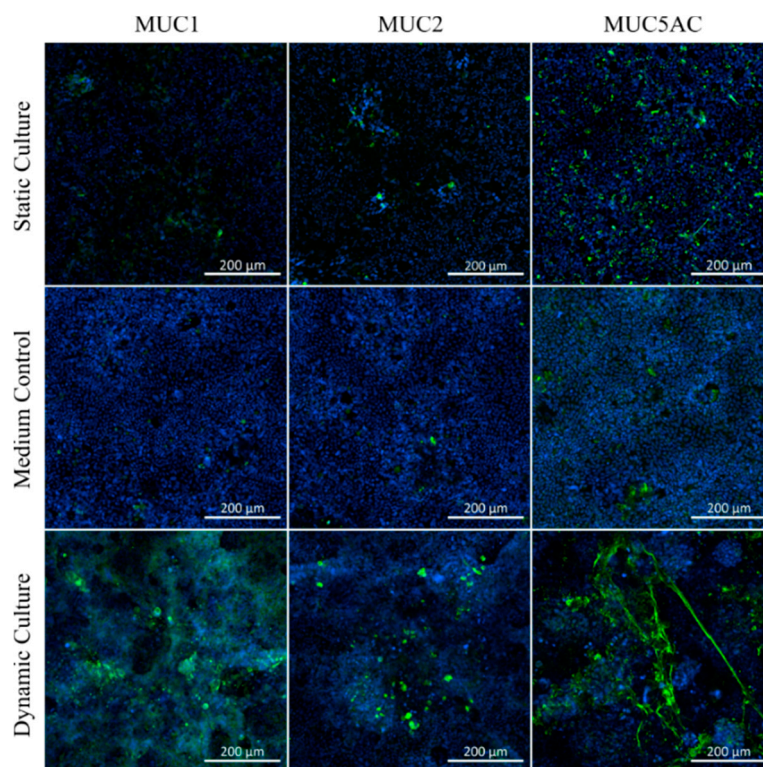


**Figure S9.** Influence of medium volume on mucus structure determined by immunofluorescent staining with antibodies for MUC1, MUC2 and MUC5AC. HT29-MTX cells were cultured for three weeks under conventional conditions (Static Culture), dynamic conditions (Dynamic Culture), and static conditions with media volumes comparable to dynamic culture (Medium Control). n=2

## 8. Control Experiments – Material Leaching Assay to Assess Biocompatibility

To evaluate the biocompatibility of the printed resin, we statically cultured HT29-MTX cells on inserts for three weeks either conventionally in 12-well plates (Static Culture) or in 3D-printed wells (Leaching Control), with similar ratio of medium volume to contact area to the material as in the chamber for dynamic culture. Subsequently a live/dead staining using fluorescein diacetate and propidium iodide was conducted and samples were analyzed via confocal microscopy, shown in Figure S10.

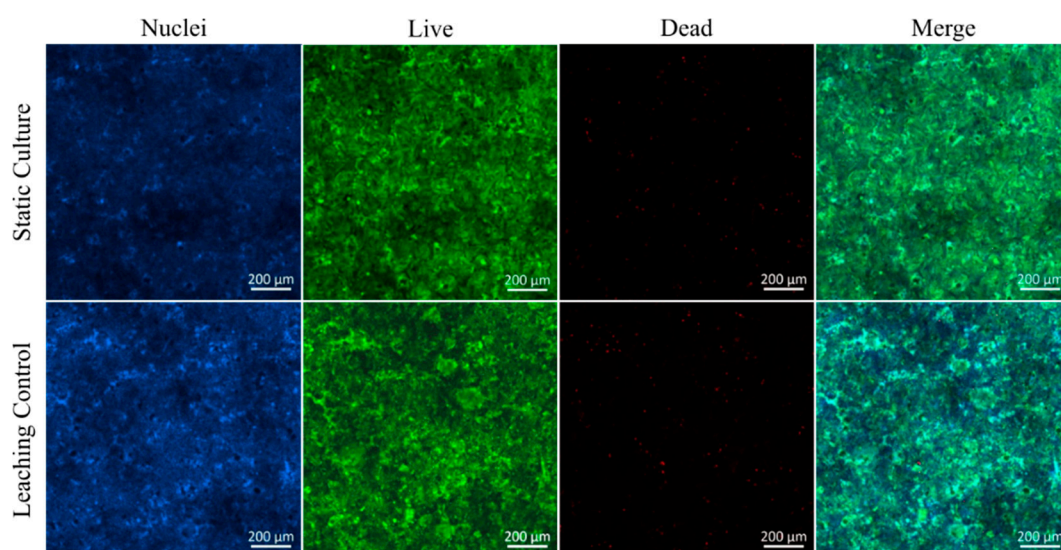


**Figure S10.** Biocompatibility of the 3D-printed resin. HT29-MTX cells were cultured for three weeks in conventional (Static Culture) and 3D-printed (Leaching Control) wells and subsequently incubated with fluorescein diacetate (green) and propidium iodide (red) to identify living and dead cells, respectively. Nuclei were counterstained with Hoechst 33342 (blue). n=2

The same culture setup was used to exclude an influence of the crosslinked resin on barrier function, mucus production and tight junction formation, as shown in Figures S11 and S12.

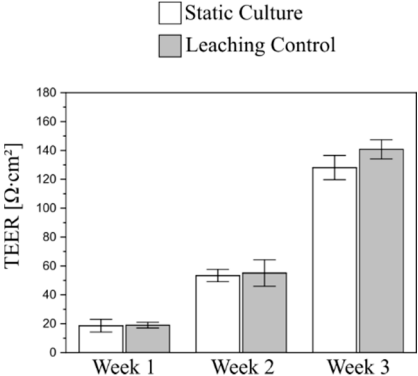


**Figure S11.** Influence of the 3D-printed resin on cellular barrier function. HT29-MTX cells were cultured for three weeks in conventional (Static Culture) and 3D-printed (Leaching Control) wells. TEER values were measured every 7 days. Data presented as mean ± SEM. n=4-12

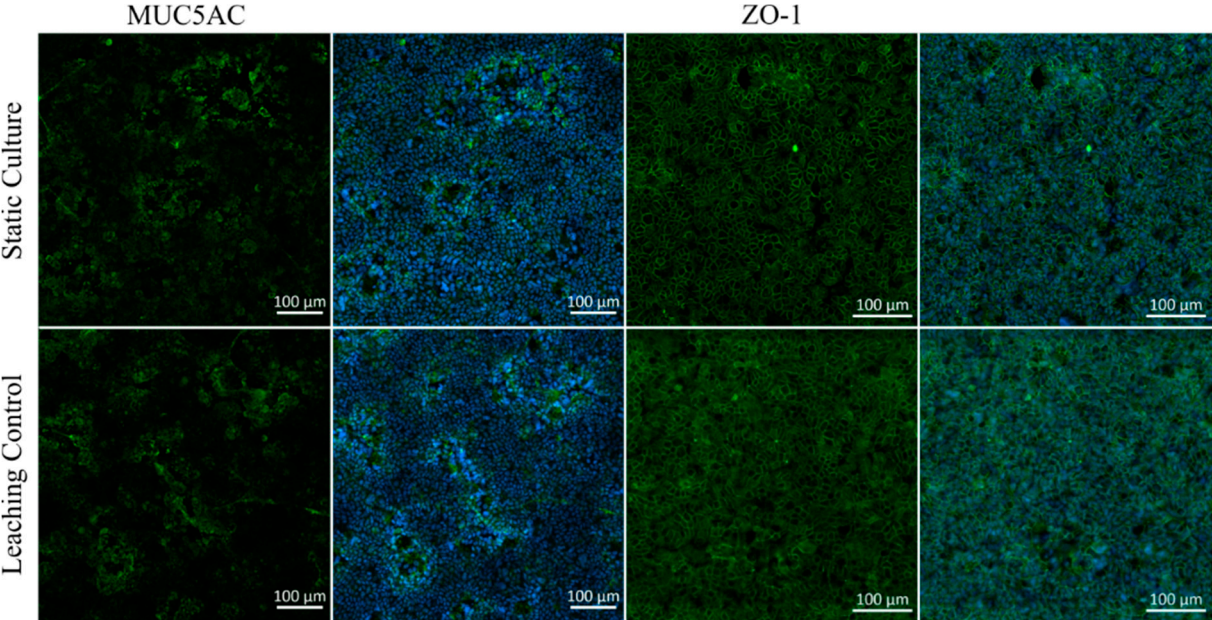


**Figure S12.** Influence of the 3D-printed resin on mucin expression and tight junction formation. HT29-MTX cells were cultured for three weeks in conventional (Static Culture) and 3D-printed (Leaching Control) wells and stained for the secreted mucin MUC5AC and for ZO-1 as an integral part of tight junctions. n=2

## 9. Cellular Area Determination

To determine the respective surface area of cells cultured statically and dynamically on membrane inserts, we analyzed confocal images of cell layers stained using phalloidin after three weeks under both culture conditions with *ImageJ* and *Origin*. To evaluate the method, a hemisphere with a radius of 125  $\mu\text{m}$  on a 500  $\times$  500  $\mu\text{m}$  flat surface was CAD-modelled, sliced with a layer thickness of 5  $\mu\text{m}$  and imported in *ImageJ*. The topography was computed with *TopoJ*-plugin, resulting in a 2-dimensional image, which was subsequently smoothed by applying a gaussian filter. The image was exported as a text file, imported into *Origin* and 3D-plotted. The surface area of the plot can be calculated via the *xyzarea* command and resulted in a reasonable area of 0.295  $\text{mm}^2$ , with a deviation of only 1.3% to the theoretical value: base area (0.25  $\text{mm}^2$ ) minus circular area (0.049  $\text{mm}^2$ ) plus area of hemisphere (0.098  $\text{mm}^2$ ). Cellular surface areas were determined identically (Figure S13).

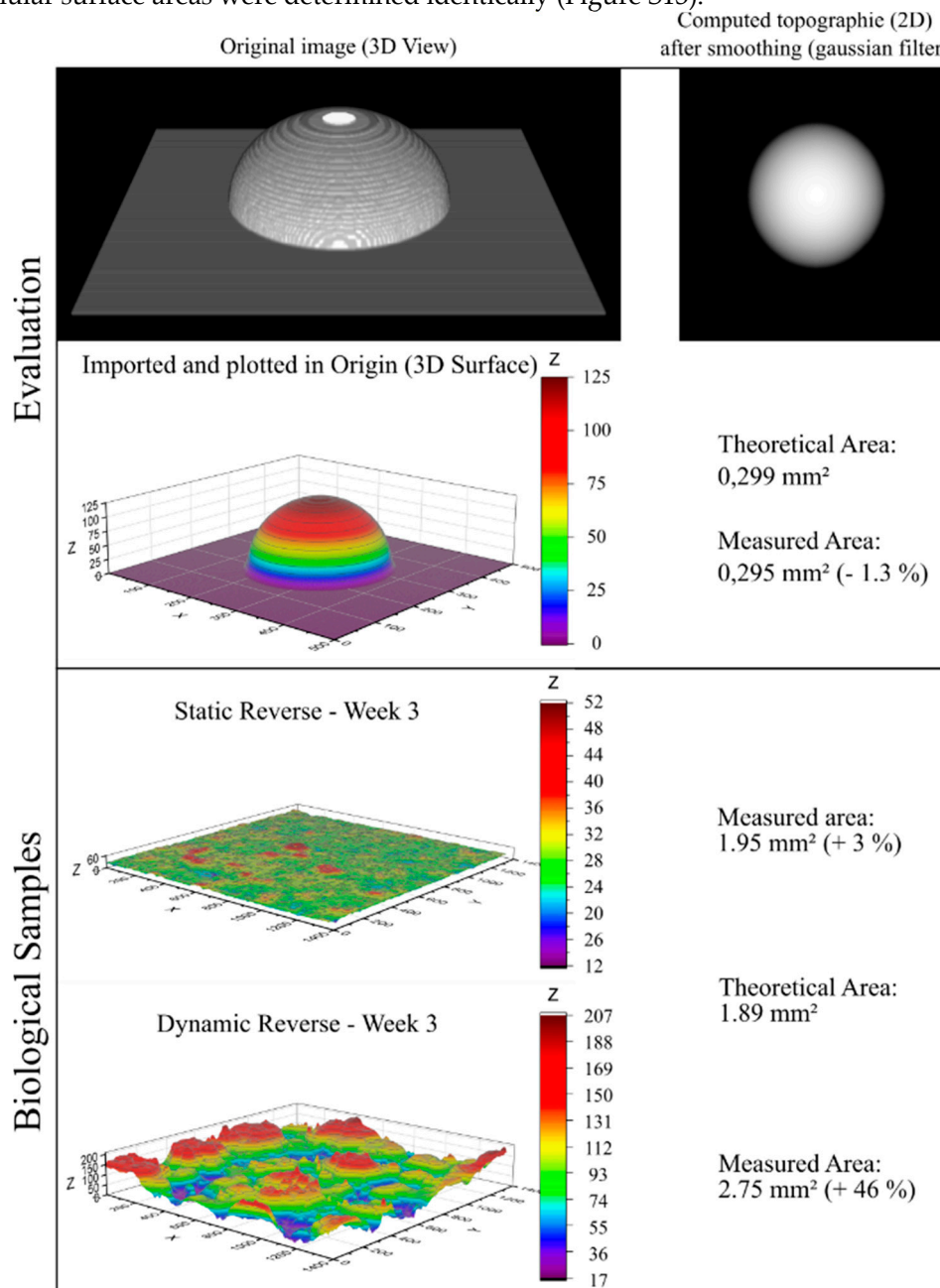


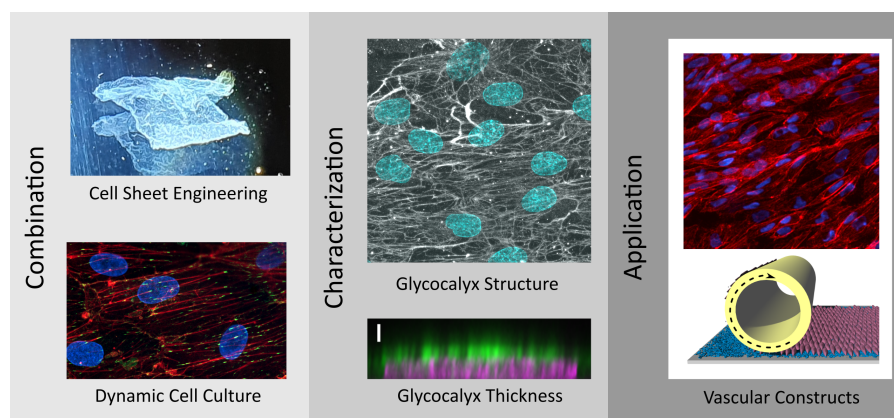
**Figure S13.** Illustration of the surface area determination using *ImageJ* and *Origin*. For the evaluation, a 3D model of a hemisphere was CAD-modelled, sliced and imported into *ImageJ*. The topography was computed with the *TopoJ*-plugin and a gaussian filter was applied to smoothen the surface. The file was exported as a text file, imported into *Origin*, plotted as a 3D-surface and the surface area was determined. The same procedure was performed for confocal images of cells stained with phalloidin.

## 10. References

1. Johansson, M.E.; Gustafsson, J.K.; Holmen-Larsson, J.; Jabbar, K.S.; Xia, L.; Xu, H.; Ghishan, F.K.; Carvalho, F.A.; Gewirtz, A.T.; Sjovall, H.; et al. Bacteria penetrate the normally impenetrable inner colon mucus layer in both murine colitis models and patients with ulcerative colitis. *Gut* **2014**, *63*, 281-291; DOI:10.1136/gutjnl-2012-303207.
2. Furter, M.; Sellin, M.E.; Hansson, G.C.; Hardt, W.D. Mucus Architecture and Near-Surface Swimming Affect Distinct Salmonella Typhimurium Infection Patterns along the Murine Intestinal Tract. *Cell Rep.* **2019**, *27*, 2665-2678 e2663; DOI:10.1016/j.celrep.2019.04.106.
3. Wang, Y.; Kim, R.; Sims, C.E.; Allbritton, N.L. Building a Thick Mucus Hydrogel Layer to Improve the Physiological Relevance of In Vitro Primary Colonic Epithelial Models. *Cell. Mol. Gastroenterol. Hepatol.* **2019**, *8*, 653-655 e655; DOI:10.1016/j.jcmgh.2019.07.009.

### 3.3 Flow-induced glycocalyx formation and cell alignment of HUVECs compared to iPSC-derived ECs for tissue engineering applications

The comparative study on the impact of shear stress on endothelial cells of different origins was conceptualized by the author, Dr. Anna Laporte and Prof. Dr. Marie Weinhart. Dr. Daniel Stöbener kindly provided the thermoresponsive PGEs and surface coating was conducted by Dr. Laura Elomaa. All other experimental tasks were accomplished by the author, with initial support to establish the iPSC-culture from Dr. Ruth Olmer. The manuscript was drafted by the author under assistance of Dr. Anna Laporte and Prof. Dr. Marie Weinhart. General literature on the background of the scientific question and state of the art as well as main parts of the literature for the discussion of the results in the context of current literature was provided by the author while the final write-up was performed by Dr. Anna Laporte. Final reviewing and editing were done by Dr. Laura Elomaa, Prof. Dr. Cornelia Lee-Thedieck, Dr. Ruth Olmer and Prof. Dr. Marie Weinhart.



Lindner, M.; Laporte, A.; Elomaa, L.; Lee-Thedieck, C.; Olmer, R.; Weinhart, M. Flow-induced glycocalyx formation and cell alignment of HUVECs compared to iPSC-derived ECs for tissue engineering applications. *Manuscript in submission.*

1 **Flow-induced glycocalyx formation and cell alignment of HUVECs compared to**  
2 **iPSC-derived ECs for tissue engineering applications**

3 **Marcus Lindner<sup>1</sup>, Anna Laporte<sup>2</sup>, Laura Elomaa<sup>1</sup>, Cornelia Lee-Thedieck<sup>3</sup>, Ruth Olmer<sup>4,5</sup>,**  
4 **Marie Weinhart<sup>1,2\*</sup>**

5 <sup>1</sup> Institute of Chemistry and Biochemistry, Freie Universität Berlin, Berlin, Germany

6 <sup>2</sup> Institute of Physical Chemistry and Electrochemistry, Leibniz Universität Hannover, Hannover,  
7 Germany

8 <sup>3</sup> Institute of Cell Biology and Biophysics, Leibniz Universität Hannover, Hannover, Germany

9 <sup>4</sup> Leibniz Research Laboratories for Biotechnology and Artificial Organs (LEBAO), Department of  
10 Cardiothoracic, Transplantation and Vascular Surgery, Hannover Medical School, 30625 Hannover,  
11 Germany. Biomedical Research in Endstage and Obstructive Lung Disease (BREATH), Member of  
12 the German Center for Lung Research (DZL)

13 <sup>5</sup> REBIRTH - Research Center for Translational Regenerative Medicine, Hannover Medical School,  
14 30625 Hannover, Germany

15 **\* Correspondence:**

16 Marie Weinhart: [marie.weinhart@fu-berlin.de](mailto:marie.weinhart@fu-berlin.de) or [marie.weinhart@pci.uni-hannover.de](mailto:marie.weinhart@pci.uni-hannover.de)

17 **Keywords:** Cell-based glycocalyx model, homogeneous surface shear stress, laminar flow,  
18 mechanotransduction, cellular directionality, peripheral blood mononuclear cell adhesion assay,  
19 thermoresponsive poly(glycidyl methyl ether-*co*-ethyl glycidyl ether) coating, cell sheet engineering

20 **Abstract**

21 The relevance of cellular *in vitro* models highly depends on their ability to mimic the physiological  
22 environment of the respective tissue or cell niche. Static culture conditions are often unsuitable,  
23 especially for endothelial models, since they completely neglect the physiological surface shear stress  
24 and corresponding reactions of endothelial cells (ECs) such as alignment in the direction of flow.  
25 Furthermore, formation and maturation of the glycocalyx, the essential polysaccharide layer covering  
26 all endothelial surfaces and regulating diverse processes, is highly dependent on applied fluid flow.  
27 This fragile but utterly important macromolecular layer is hard to analyze, its importance is often  
28 underestimated and accordingly neglected in many endothelial models. Therefore, we exposed  
29 human umbilical vein ECs (HUVECs) and human induced pluripotent stem cell-derived ECs (iPSC-  
30 ECs) as two relevant EC models in a side-by-side comparison to static and physiological dynamic  
31 (6.6 dyn cm<sup>-2</sup>) culture conditions. Both cell types demonstrated an elongation and alignment along  
32 the flow direction, some distinct changes in glycocalyx composition on the surface regarding the  
33 main glycosaminoglycan components heparan sulfate, chondroitin sulfate or hyaluronic acid as well

## Shear-induced changes in EC-glycocalyx

34 as an increased and thereby improved glycocalyx thickness and functionality when cultured under  
35 homogeneous fluid flow. Thus, we were able to demonstrate the maturity of the employed iPSC-EC  
36 model regarding its ability to sense fluid flow along with the general importance of physiological  
37 shear stress for glycocalyx formation. Additionally, we investigated EC monolayer integrity with and  
38 without application of surface shear stress, revealing a comparable existence of tight junctions for all  
39 conditions and a reorganization of the cytoskeleton upon dynamic culture leading to an increased  
40 formation of focal adhesions. We then fabricated cell sheets of EC monolayers after static and  
41 dynamic culture via non-enzymatic detachment using thermoresponsive polymer coatings as culture  
42 substrates. In a first proof-of-concept we were able to transfer an aligned iPSC-EC sheet to a 3D-  
43 printed scaffold thereby making a step in the direction of vascular modelling. We envision these  
44 results to be a valuable contribution to improvements of *in vitro* endothelial models and vascular  
45 engineering in the future.

### 46 1 Introduction

47 Mimicking the physiological cellular niche by translation and adaption of chemical and physical cues  
48 has become a valuable tool in *in vitro* primary and stem cell culture as well as tissue engineering  
49 (Metallo et al., 2008; Barthes et al., 2014; Chatterjee et al., 2021). In the engineering and  
50 biofabrication of blood vessels, functional endothelial cells (ECs) are of utmost importance as they  
51 form the inner lining of all blood vessel walls (Devillard and Marquette, 2021). In addition to tight  
52 junctions, the lumenally expressed, dense macromolecular layer consisting of glycoproteins,  
53 proteoglycans (PGs), glycosaminoglycans (GAGs) as well as soluble plasma factors, known as the  
54 glycocalyx, contributes significantly to the endothelial barrier function. This net negatively charged  
55 polysaccharide-rich layer is linked to the EC surface on the one hand via glycoproteins such as  
56 selectins, integrins and immunoglobulins and on the other hand by some types of PGs which are  
57 anchored in the EC membrane. The main structural feature of membrane-bound as well as secreted  
58 PGs is the presentation of GAG side-chains along the PG core protein. Within the glycocalyx the  
59 most abundant PG-bound GAG is heparan sulfate (HS) with 50-90% frequency, followed by  
60 chondroitin sulfate/dermatan sulfate (CS/DS) and the non-PG-bound GAG hyaluronic acid (HA)  
61 (Oohira et al., 1983; Ihrcke et al., 1993; Reitsma et al., 2007; Cosgun et al., 2020). Glycocalyx  
62 thickness varies between species as well as different types of blood vessels and is strongly dependent  
63 on the applied fluid-flow induced surface shear stress, ranging from ~0.5  $\mu\text{m}$  in capillaries up to 4-5  
64  $\mu\text{m}$  in carotid arteries (Gouverneur et al., 2006a; Gouverneur et al., 2006b; Reitsma et al., 2007;  
65 Tarbell et al., 2014). From a functional point of view, the glycocalyx plays a major role in regulating  
66 the vascular permeability, controlling the endothelial interactions with blood cells as well as  
67 signaling. Additionally, it acts as a protective barrier for the endothelium against blood flow-induced  
68 shear stress, while simultaneously sensing mechanical forces at the cell surface communicating it into  
69 the interior (Reitsma et al., 2007; Weinbaum et al., 2007; Curry and Adamson, 2012; Fels and  
70 Kusche-Vihrog, 2020). Important mechanotransducers on the cell surface are sialic acids as end  
71 groups of glycoprotein polysaccharide side chains (Psefteli et al., 2021), HS (Florian et al., 2003;  
72 Ebong et al., 2014) and HA (Mochizuki et al., 2003). As a result, ECs elongate and align along the  
73 flow direction *in vivo* as well as *in vitro* (Thoumine et al., 1995; Steward et al., 2015).

74 The importance of the glycocalyx for endothelial function has long been underestimated and  
75 quantitative studies are challenging due to its highly dynamic and fragile nature (Schött et al., 2016;  
76 Möckl, 2020). Especially *in vitro* cultivation conditions can have a major impact on its status, with

77 conventional static cell culture leading to unphysiological glycocalyx thicknesses and compositions  
78 (Potter and Damiano, 2008; Chappell et al., 2009).

79 A commonly used cellular model for *in vitro* studies of the endothelial barrier are human umbilical  
80 vein endothelial cells (HUVECs). As robust and accessible primary cells they hold several  
81 advantages over immortalized cell lines such as contact inhibition upon reaching confluency and  
82 especially physiological characteristics of the human vascular endothelium including *in vivo*-like  
83 responses to a variety of stimuli. However, the donor-to-donor variability as well as a strongly  
84 limited culture time urge the need for alternatives (Jaffe et al., 1973; Cao et al., 2017; Medina-Leyte  
85 et al., 2020). Particularly ECs derived from human induced pluripotent stem cells (iPSC-ECs) are a  
86 promising candidate to fill this gap. Several successful protocols for differentiation have been  
87 established so far (Orlova et al., 2014a; Patsch et al., 2015; Olmer et al., 2018), generating iPSC-ECs  
88 featuring various properties of a vascular endothelium, for example, regarding marker expression,  
89 phenotype or response to mechanical or chemical stimuli, representing a potential cell source for  
90 biologization of blood contacting surfaces (Pflaum et al., 2021). Furthermore, use of iPSC-ECs yields  
91 the potential to generate patient-specific or disease-related vascular lineages and of unlimited cell  
92 supply originating from the same donor (Jang et al., 2019; Kennedy et al., 2021). However, the  
93 evaluation of iPSC-ECs' eligibility as an alternative to primary cells in models of the vascular  
94 endothelium appears incomplete. Studies suggest that iPSC-derived cells could be less mature than  
95 primary cells, exemplary in being shear-naïve (Sivarapatna et al., 2015; Tiemeier et al., 2019;  
96 Kennedy et al., 2021). Moreover, detailed analyses on the glycocalyx condition in iPSC-ECs are  
97 needed.

98 As side-by-side comparisons between HUVECs and iPSC-ECs under different culture conditions are  
99 still rare, in the present study we cultured these EC types under static as well as dynamic conditions  
100 with particular focus on the glycocalyx. Under dynamic conditions a homogenous defined shear  
101 stress ( $6.6 \text{ dyn cm}^{-2}$ ) was applied to the cell surface, thereby mimicking physiological fluid flow in  
102 veins and capillaries (Ballermann et al., 1998; Paszkowiak and Dardik, 2003). The effects on cellular  
103 elongation and alignment as well as glycocalyx composition and thickness were subsequently  
104 analyzed. In a first proof-of-concept we utilized the aligned EC monolayers as a tool for cell sheet  
105 engineering toward 3-dimensional (3D) modelling of vascular structures. The endothelial barrier and  
106 cell-matrix interactions were evaluated by fluorescent staining of tight junctions and focal adhesions.

107

108 **2 Materials and Methods**

109 **2.1 Materials**

110 5-Chlormethylfluoresceindiacetat (CMFDA), anti-chondroitin sulfate antibody (mouse, clone CS-  
 111 56), anti-vinculin antibody (mouse, Alexa Fluor® 488-conjugated, clone 7F9), anti-ZO-1 antibody  
 112 (rabbit, polyclonal), DNA-intercalating dye (Hoechst 33342), goat anti-mouse IgG (H+L) (cross-  
 113 adsorbed, Alexa Fluor® 488-conjugated), goat anti-mouse IgG (H+L) (cross-adsorbed, Alexa Fluor®  
 114 647-conjugated), goat anti-mouse IgM (Heavy Chain) (Alexa Fluor® 647-conjugated), goat anti-  
 115 rabbit IgG (H+L) (Alexa Fluor® 488-conjugated), labelled streptavidin (DyLight™ 488-conjugated),  
 116 tumor necrosis factor-alpha (TNF- $\alpha$ , human, recombinant protein) and wheat-germ-agglutinin  
 117 (WGA, Alexa Fluor® 555-conjugated) were purchased from ThermoFisher (Waltham, MA/USA).  
 118 Cell dissociation buffer (Accutase®), Dulbecco's phosphate-buffered saline (PBS, with and without  
 119 Ca<sup>2+</sup> and Mg<sup>2+</sup>), hyaluronic acid binding protein (bovine nasal, biotinylated), octoxynol 9 (Triton™  
 120 X-100) and phalloidin (Atto647N-conjugated) were received from Sigma-Aldrich (St. Louis,  
 121 Missouri/USA). Luer adapters for dynamic culture, namely elbow connector (male to female,  
 122 polypropylene (PP)), luer-lock to barb (male and female, PP), luer-lock to thread (female to 1/4 28  
 123 UNF, PP) and panel mount (female to barb with thread (1/4 28 UNF), PP) were ordered from  
 124 QOSINA (Ronkonkoma, NY/USA). Bovine serum albumin (BSA, fraction V), methanol (>99%),  
 125 paraformaldehyde (PFA, ROTI®Histofix 4%) and polyoxyethylene(20)sorbitan monolaurate (Tween  
 126 20®) were obtained from Carl Roth (Karlsruhe, Germany). Antibiotic/antimycotic solution  
 127 (gentamicin and amphotericin B), endothelial cell growth medium (VascuLife® VEGF) and human  
 128 umbilical vein endothelial cells (HUVECs) were purchased from Lifeline® Cell Technology  
 129 (Frederick, MD/USA) and 6-well plates (tissue culture treated), cell culture flasks (T25, T75 and  
 130 T175) and rectangular cell culture dishes (quadriPERM®) from Sarstedt (Nümbrecht, Germany).  
 131 Anti-CD31 antibody (mouse, Alexa Fluor™ 488-conjugated, clone JC/70A) and delimiting pen  
 132 (Dako Pen) were from Agilent Technologies (Santa Clara, CA/USA), hematopoietic cell medium (X-  
 133 VIVO™ 15, serum-free) and peripheral blood mononuclear cells (PBMCs, human) were from Lonza  
 134 (Basel, Switzerland). Human fibronectin (FN, lyophilized) was received from Advanced BioMatrix  
 135 (Carlsbad, CA/USA), polycarbonate (Makroclear®) from Arla Plast (Borensberg, Sweden), sterile  
 136 water for injection from B. Braun (Melsungen, Germany), ethanol (>99%) from Berkel  
 137 (Ludwigshafen, Germany), mounting medium (ProTaq® Mount Flour) from Biocyc (Luckenwalde,  
 138 Germany), rectangular cover glasses (60 × 22 mm) from Glaswarenfabrik Karl Hecht (Sondheim vor  
 139 der Rhön, Germany), 8-well chamber slides ( $\mu$ -Slide, ibiTreat bottom) from ibidi (Gräfelfing,

140 Germany) and peristaltic pump tubing (Innovaprene® P60) from Innovapure (Shanghai, China).  
141 Polystyrene slides (PS, 1.5 mm thickness, transparent) were ordered from Vink König Deutschland  
142 (Gilching, Germany) and milled to microscope slide format (76.5 mm, 25.8 mm, 1.5 mm) to fit the  
143 slide culture chamber, fetal bovine serum (FBS, Standard) from PAN-Biotech (Aidenbach,  
144 Germany), endothelial cell growth medium (EGM-2) from PromoCell (Heidelberg, Germany),  
145 collagen solution (type I, rat tail) from R & D Systems (Minneapolis, MN/USA), platinum-cured  
146 silicon tubing (Tygon® 3350) from Saint-Gobain (Courbevoie, France) and anti-VE-Cadherin  
147 antibody (mouse, clone BV9) from Santa Cruz Biotechnology (Dallas, Texas). Syringe filters  
148 (Minisart®, PTFE, 0.2 µm) were obtained from Sartorius (Göttingen, Germany), duplicating silicone  
149 (REPLISIL 22 N) from SILCONIC® (Lonsee, Germany) and anti-heparan sulfate antibody (mouse,  
150 clone 8.S.087) from US Biological (Salem, MA/USA).

### 151 **2.2 Ethics statement**

152 Human tissue was obtained after approval by the local Ethics Committee (Hannover Medical School,  
153 Ethical approval No.: 844-2010) and following the donor's written informed consent, or in the case  
154 of newborns, following informed consent of the parents.

### 155 **2.3 Cell culture**

156 HUVECs (passage 2-6) were cultured in VascuLife VEGF medium supplemented with 30 µg mL<sup>-1</sup>  
157 gentamicin, 15 ng mL<sup>-1</sup> amphotericin B and 2% FBS. iPSCs (MHHi001-A) were maintained under  
158 standard culture conditions (Haase et al., 2017) and differentiated toward iPSC-ECs according to  
159 Olmer *et al.* (Olmer et al., 2018). iPSC-ECs (passage 2-4) were maintained in EGM-2 medium  
160 supplemented with 30 µg mL<sup>-1</sup> gentamicin, 15 ng mL<sup>-1</sup> amphotericin B and 2% FBS. All cell culture  
161 substrates for iPSC-ECs were coated with 2.5 µg cm<sup>-2</sup> human fibronectin in PBS<sup>+</sup> for 30 minutes  
162 under standard conditions (5% CO<sub>2</sub>, 37 °C) and washed once with sterile water prior to cell seeding.  
163 ECs were sub-cultured using Accutase® cell dissociation reagent once reaching a confluency of 70-  
164 80%.

165 Unless otherwise mentioned, cell culture experiments were performed on thermoresponsive  
166 poly(glycidyl methyl ether-*co*-ethyl glycidyl ether)-coated (PGE-coated) polystyrene slides prepared  
167 as described before (Stöbener et al., 2018; Stöbener and Weinhart, 2020). After coating, slides were  
168 transferred to rectangular cell culture plates, disinfected with 70% ethanol for 10 minutes at room  
169 temperature (RT) and washed twice with cold (4 °C) PBS<sup>+</sup>. Sterilized cast silicone cell separators  
170 with a seeding area of 3 cm<sup>2</sup> were placed onto slides and cells were seeded with a density of 42,500

171 cells  $\text{cm}^{-2}$  in 300  $\mu\text{L cm}^{-2}$  VascuLife VEGF medium containing 2% FBS. After 24 h the cell culture  
172 medium was replaced with medium containing 10% FBS and the cells were kept for two more days  
173 under standard conditions to reach confluency. Cells were now either maintained under static  
174 conditions or transferred to dynamic culture for additional 96 h, which is referred to as "static 96 h"  
175 and "dynamic 96 h" throughout the manuscript.

### 176 **2.4 Dynamic culture: setup and flow characterization**

177 Cells were cultured under fluid flow conditions in parallel plate flow chambers as described before  
178 (Lindner et al., 2021). In brief, culture chambers fabricated from polycarbonate which can  
179 accommodate a standard microscopy slide are used to apply a homogenous shear stress onto the cell  
180 surface (**Figure 1A**). The chamber is included into a simple circuit comprising a bubble trap/medium  
181 reservoir and a peristaltic pump is used to generate a constant fluid flow (**Figure 1B**). With a channel  
182 height of 0.15 mm and a volume flow rate of 3.4  $\text{mL min}^{-1}$ , the applied shear stress is approximately  
183 6.6  $\text{dyn cm}^{-2}$  (Lindner et al., 2021). The final pump speed was gradually increased in three steps with  
184 an interval of 45 minutes to initially allow cells to adapt to the shear stress. CFD simulations were  
185 performed as previously published (Lindner et al., 2021), confirming laminar flow and homogenous  
186 surface shear stress (**Figure 1C,D**).

### 187 **2.5 Directionality analysis**

188 Phase-contrast images of ECs after static and dynamic culture were acquired using an inverted  
189 microscope (Axio Vert.A1, Carl Zeiss, Jena, Germany) equipped with a monochrome camera  
190 (Axiocam MRm, Carl Zeiss). Subsequently, the directionality of cells was analyzed either  
191 qualitatively by adding an angle-dependent color to cell borders or quantitatively by determining the  
192 main orientation angle of individual cells. Both analyses were carried out using *Fiji*, an *ImageJ*  
193 distribution for scientific image analysis (Schindelin et al., 2012). The processing is described in  
194 detail in section 2 of the Supplementary Material.

### 195 **2.6 Immunofluorescent staining**

196 For immunofluorescent staining, cells were rinsed with  $\text{PBS}^+$  after static and dynamic culture and  
197 fixed in cold methanol ( $-20\text{ }^\circ\text{C}$ ) or 4% PFA for 10 minutes at  $4\text{ }^\circ\text{C}$  or RT, respectively. PFA-fixed  
198 samples were permeabilized with 0.1% (v/v) Triton-X 100 in  $\text{PBS}^+$  for 5 minutes at RT and both  
199 types of samples were blocked with 5% BSA (w/v) in  $\text{PBS}^+$  containing 0.05% (v/v) Tween (PBST)  
200 for 90 minutes at RT. The endothelial marker CD31, glycocalyx components heparan sulfate (HS),

201 chondroitin sulfate (CS) and hyaluronic acid (HA), as well as proteins of tight junctions (zonula  
 202 occludens protein 1 (ZO-1) and vascular endothelial cadherin (VE-cadherin)) were detected via  
 203 indirect immunofluorescence, whereas the actin cytoskeleton and focal adhesions were stained  
 204 directly via phalloidin and labeled vinculin antibodies, respectively. Staining conditions are listed in  
 205 **Table 1**. After staining, the samples were mounted with mounting medium and glass coverslips.  
 206 Confocal microscopy was performed using Zeiss LSM800 equipped with an Airyscan detector (Carl  
 207 Zeiss).

208 **Table 1.** Conditions for immunofluorescence staining.

Primary antibody/protein	Secondary antibody/protein
Mouse- $\alpha$ -CD31 <sup>a</sup> , IgG1, 1:100	Goat- $\alpha$ -mouse IgG (H+L) Alexa Fluor® 488, 1:500
Mouse- $\alpha$ -chondroitin sulfate <sup>a</sup> , IgM, 1:100	Goat- $\alpha$ -mouse IgM Alexa Fluor® 647, 1:500
Mouse- $\alpha$ -heparan sulfate <sup>b</sup> , IgM, 1:100	Goat- $\alpha$ -mouse IgM Alexa Fluor® 647, 1:500
Hyaluronic acid binding protein <sup>b</sup> , biotinylated, (5 $\mu$ g mL <sup>-1</sup> )	Streptavidin DyLight™ 488, 1:250
Mouse- $\alpha$ -vinculin <sup>a</sup> , Alexa Fluor® 488, 1:50 <sup>d</sup>	-
Mouse- $\alpha$ -VE-cadherin <sup>b,c</sup> , IgG2a, 1:100	Goat- $\alpha$ -mouse IgM Alexa Fluor® 647, 1:500
Rabbit- $\alpha$ -ZO 1 <sup>b,c</sup> , polyclonal, 1:250	Goat- $\alpha$ -rabbit IgG (H+L) Alexa Fluor® 488, 1:500

209 *samples were fixed with <sup>a</sup> PFA or <sup>b</sup> methanol, <sup>c</sup> indicates co-staining, <sup>d</sup> counter staining using Phalloidin, Atto647N, 1:250*

## 210 **2.7 Glycocalyx thickness determination**

211 To measure the glycocalyx thickness after fixation and staining, confocal *Z*-stacks of CS stained  
 212 samples were acquired under Airyscan super-resolution mode, processed with *ZenBlue* software and  
 213 analyzed with *ImageJ* as described previously (Tiemeier et al., 2019). In brief, *Z*-stacks were resliced  
 214 to yield orthogonal projections. Subsequently, intensity profiles (*Z*-direction) for nucleus and CS  
 215 staining were plotted and a gaussian fit was added. The thickness was calculated as the difference  
 216 between apical full width half maximum of nucleus to CS signal. A minimum of seven spots per cell  
 217 and four cells per cell type and culture condition were analyzed. Airyscan processing strength was  
 218 kept constant for all images to allow comparison between single conditions and imaging was done  
 219 considering optical limitations.

220

221

### 222 **2.8 Peripheral blood mononuclear cell adhesion assay**

#### 223 **2.8.1 Labelling**

224 The adhesion of peripheral blood mononuclear cells (PBMCs) to ECs after static and dynamic  
225 conditions was quantified to assess glycocalyx functionality. For every experiment, one vial  
226 containing  $10 \times 10^6$  PBMCs was thawed in a water bath ( $37^\circ\text{C}$ ), transferred to 9 mL prewarmed X-  
227 Vivo medium and gently mixed via pipetting. Cells were centrifuged for 10 minutes at  $300 \times g$  and  
228 the supernatant was aspirated. Cells were then resuspended in 5 mL prewarmed medium with  
229 CMFDA ( $10 \mu\text{M}$ ) and labelled for 5-10 minutes in a cell culture incubator. After two repeated  
230 centrifugation ( $10'$ ,  $300 \times g$ ) and resuspensions steps, cells were resuspended in 1 mL medium,  
231 counted and further diluted to a final concentration of  $5 \times 10^5$  cells  $\text{mL}^{-1}$ .

#### 232 **2.8.2 Incubation and data acquisition**

233 PS-slides with ECs were carefully rinsed once with X-Vivo medium and  $300 \mu\text{L cm}^{-2}$  of the PBMC-  
234 suspension were added. After incubation for 60 minutes in an incubator, slides were washed with  
235 prewarmed  $\text{PBS}^+$  and fixed with PFA for 10 minutes at RT. The samples were finally imaged via  
236 confocal microscopy and data was analyzed using *ImageJ*. Details about the assay validation, image  
237 processing and analysis can be found in section 4 of the Supplementary Material.

### 238 **2.9 Cell sheet engineering**

239 To harvest confluent HUVEC or iPSC-EC sheets, slides with adherent cells were transferred to RT-  
240  $\text{PBS}^-$  after application of different culture conditions and incubated for 10-15 minutes. Cell sheet  
241 detachment started spontaneously at the edge of the cell layer and was monitored via phase contrast  
242 microscopy. To fully detach sheets from the substrate, gentle flushing with a small-volume pipette  
243 was necessary.

#### 244 **2.10 Cell sheet rolling**

245 In a preliminary experiment, dynamically cultured iPSC-ECs were wrapped around a 3D-printed  
246 tubular scaffold as recently reported for statically cultured HUVECs (Elomaa et al., 2022). In brief, a  
247 custom-made rolling device (OSPIN, Berlin, Germany) was used to transfer the EC sheets onto a 3D  
248 printed tubular scaffold while detaching from the substrate. Subsequently, the tubular construct was  
249 transferred to an 8-well slide and embedded into a collagen hydrogel. For this,  $500 \mu\text{L}$  acidic rat tail  
250 collagen solution ( $5 \text{ mg mL}^{-2}$ ) were mixed with  $110 \mu\text{L}$  0.1 M NaOH,  $100 \mu\text{L}$  10x PBS and  $290 \mu\text{L}$   
251 cell culture grade water. The solution was added to the well containing the tube and solidified for 30

252 minutes at 37 °C. Then, the cytoskeleton and nuclei were stained with phalloidin (1:250) and Hoechst  
253 33342 (1:1000) in PBS<sup>-</sup> for 3 h at RT, respectively. After 5 washing steps for 30 minutes each with  
254 PBS<sup>-</sup>, the samples were imaged via confocal microscopy to estimate coverage of the scaffold and cell  
255 directionality after the rolling process.

### 256 2.11 Statistics

257 Statistical analysis was performed with the software package *Origin Pro*. In case of normally  
258 distributed data, comparison was done using two-way ANOVA followed by Bonferroni post hoc test,  
259 whereas non-normally distributed data was compared via Mann-Whitney Test. Statistical significance  
260 is indicated with *p*-values \* < 0.05 and \*\*\* < 0.0005.

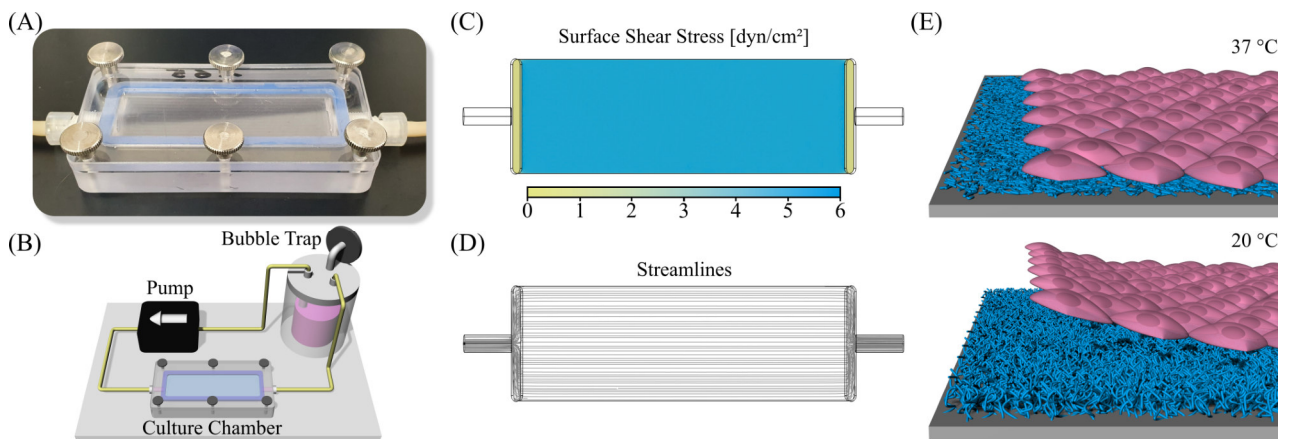
261

## 262 3 Results

### 263 3.1 Cellular orientation of HUVECs and iPSC-ECs in flow direction

264 To comparatively analyze the effect of shear stress applied to the apical surface of HUVEC or iPSC-  
265 EC monolayers on cellular orientation as well as glycocalyx composition and thickness a previously  
266 established reusable slide cultivation chamber was deployed for the culture of cells under flow on  
267 conventional microscopy slides (**Figure 1A**) (Lindner et al., 2021). This chamber can be  
268 implemented into a simple circuit further comprising a peristaltic pump and a medium reservoir  
269 simultaneously working as a bubble trap (**Figure 1B**). Operation of the circuit inside a customary cell  
270 culture incubator allows control of temperature and pH value. The setup enables the application of  
271 homogenous surface shear stress and laminar flow of the medium to adherent cells (**Figure 1C, D**).  
272 To facilitate the generation of confluent monolayers comprising a flow-induced cellular orientation  
273 for potential tissue engineering applications the ECs were cultured on thermoresponsive surfaces.  
274 These surfaces reversibly respond to temperature and are cell adhesive at a temperature of 37 °C but  
275 become cell repellent after a temperature switch to 20 °C which initiates the enzyme-free detachment  
276 of single cells or confluent cell sheets (**Figure 1E**). To prepare such substrates, untreated polystyrene  
277 (PS) slides were modified with a 5 nm thin, thermoresponsive poly(glycidyl ether) (PGE) brush  
278 coating (Stöbener et al., 2018; Stöbener and Weinhart, 2020).

## Shear-induced changes in EC-glycocalyx



279

280 **Figure 1.** Setup for dynamic cell culture and cell sheet fabrication. (A) Photography of the slide culture chamber (channel  
 281 height 150  $\mu\text{m}$ ) and (B) illustration of the circuit for dynamic cell culture including medium reservoir/bubble trap,  
 282 peristaltic pump and culture chamber. Characterization of the comprised flow channel via Computational Fluid Dynamics  
 283 (CFD) simulation showing (C) surface shear stress and (D) flow streamlines. (E) Schematic illustration of cell sheet  
 284 fabrication using a thermoresponsive PGE-coating on polystyrene (PS). The polymer coating is cell adhesive at a  
 285 temperature of 37  $^{\circ}\text{C}$  while changing to a cell repellent state at 20  $^{\circ}\text{C}$ , therefore initiating the enzyme-free detachment of  
 286 confluent cell sheets after the temperature switch.

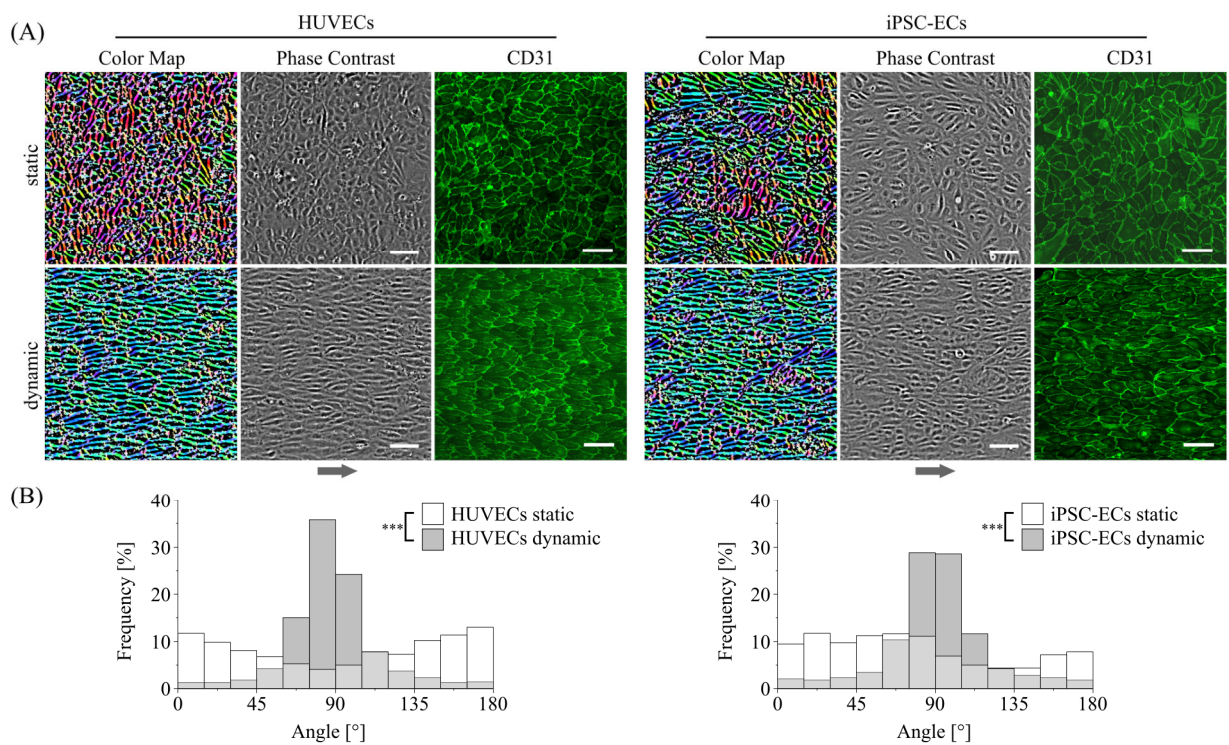
287 It is well known, that ECs undergo elongation as well as alignment in the direction of fluid flow after  
 288 application of shear stress to the cell surface (Thoumine et al., 1995; Steward et al., 2015). To obtain  
 289 information about intensities of shear stress and time periods needed to induce flow-alignment of  
 290 HUVECs in comparison to iPSC-ECs in our *in vitro* setup, a preliminary analysis was performed on  
 291 conventional tissue culture PS culture (TCPS) substrates applying physiological shear stresses  
 292 between 0 and 10  $\text{dyn cm}^{-2}$  to monolayers. Results indicate a dependency of HUVEC alignment on  
 293 both time and shear force (**Supplementary Figure S1**). While there was no directionality of both cell  
 294 types after static culture, HUVECs showed an alignment after 48 h for shear stresses of 6.6-10  $\text{dyn}$   
 295  $\text{cm}^{-2}$ , after 72 h for 3.3-5  $\text{dyn cm}^{-2}$  and after 96 h for 1.7-2.5  $\text{dyn cm}^{-2}$ . iPSC-ECs on the other hand  
 296 were already fully aligned after 24 h of culture with a shear force as little as 1.7  $\text{dyn cm}^{-2}$ . For the  
 297 highest shear stress of 10  $\text{dyn cm}^{-2}$  we observed a reduction of confluency of the HUVEC monolayer  
 298 at 96 h compared to earlier time points (**Supplementary Figure S1**). To allow a comparison between  
 299 the effects of continuous fluid flow on both cell types we decided to stick to a shear stress of 6.6  $\text{dyn}$   
 300  $\text{cm}^{-2}$  and a time span of 96 h for further experiments to enable fast alignment of cells without causing  
 301 defects in the monolayer during the 96 h culture time. This flow condition applied to cells cultured on  
 302 thermoresponsive PGE-modified PS substrates will from now on be referred to as ‘dynamic culture’.

303 *In vitro* ECs generally show a cobblestone-like phenotype when cultured as a monolayer without  
 304 fluid flow (Baudin et al., 2007; Adams et al., 2013). This was also found for HUVECs as well as  
 305 iPSC-ECs cultured under static conditions on PGE-coated surfaces as it can be seen in **Figure 2A**

11

## Shear-induced changes in EC-glycocalyx

306 from phase contrast and color-coded images. The latter were obtained via image processing as  
 307 described in the Supplementary material (**Supplementary Figure S2**). Regarding the coloration of  
 308 the image a higher uniformity of the color indicates a higher amount of orientation of the cells. This  
 309 was observed for dynamic culture for both types of ECs which are aligned in the direction of the fluid  
 310 flow (**Figure 2A**). Quantitative analysis of cellular directionality (**Supplementary Figure S3**)  
 311 validated these results as shown in distribution plots in **Figure 2B**. For both HUVECs and iPSC-ECs  
 312 there was a significant difference in main orientation between a more or less homogeneous  
 313 distribution of cellular directionality after static and a narrower distribution after dynamic culture  
 314 (**Figure 2B**). A CD31-staining revealed preservation of the EC status of both cell types under static  
 315 as well as dynamic conditions on thermoresponsive polymer coatings (**Figure 2A**).

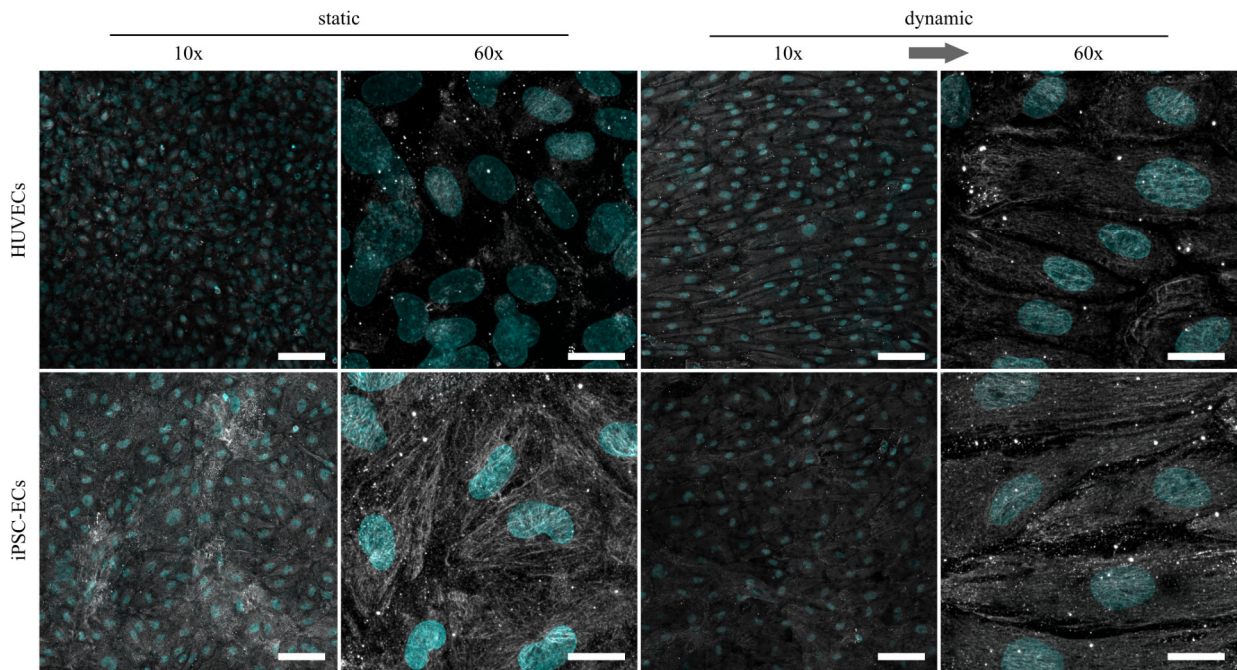


316

317 **Figure 2.** Directionality and differentiation analysis of HUVECs and iPSC-ECs on PGE-coated PS after culture with or  
 318 without flow. **(A)** Qualitative cellular alignment after static and dynamic culture of HUVECs and iPSC-ECs (96 h),  
 319 shown by phase contrast and corresponding color-coded images indicating cellular orientation by uniformity of  
 320 coloration. Differentiation status was confirmed by confocal imaging of CD31 (green) as endothelial marker (independent  
 321 sample). (Arrow indicates flow direction. Scale bars: 100  $\mu$ m). **(B)** Quantitative orientation analyses determined from  
 322 brightfield images after static and dynamic culture of HUVECs and iPSC-ECs (96 h) shown as histograms. Significant  
 323 differences were found between each dynamic and the respective static condition for both cell types, respectively (n=3,  
 324 Mann-Whitney Test, \*\*\*  $p < 0.0005$ ).

325 **3.2 Effects of shear stress on HUVEC and iPSC-EC glycocalyx composition and thickness**

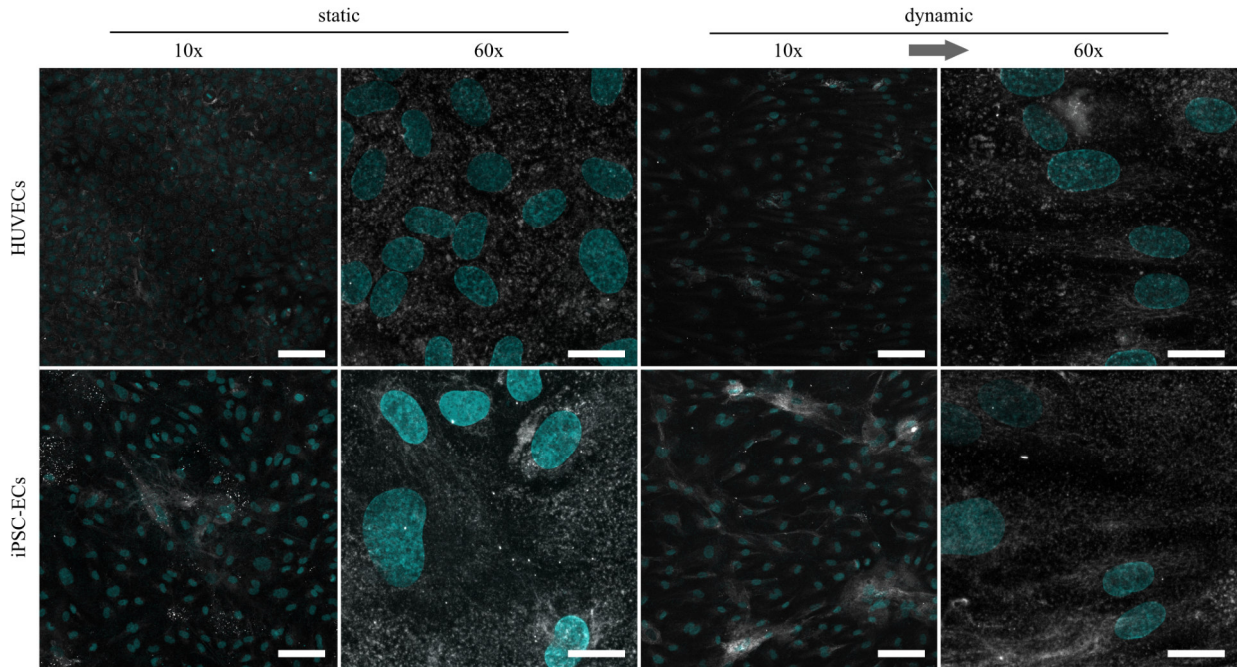
326 As previously shown, the glycocalyx composition as well as thickness in ECs changes depending on  
 327 the applied shear stress (Gouverneur et al., 2006a; Potter and Damiano, 2008). To further investigate  
 328 possible changes in HUVEC and iPSC-EC glycocalyx composition, staining of the three main  
 329 glycosaminoglycans (GAGs), namely chondroitin sulfate (CS), hyaluronic acid (HA) and heparan  
 330 sulfate (HS), were performed after static and dynamic culture (**Figures 3-5**). Under static conditions  
 331 the amount of CS on the cell surface turned out to be distinctly higher in iPSC-ECs compared to  
 332 HUVECs, while this difference dissipated after dynamic culture particularly due to an increase in CS  
 333 on the surface of HUVECs. Considering structural features, the CS formed a dense mesh-like pattern  
 334 uniformly covering the cell surfaces, that also aligned with the fluid flow after dynamic culture  
 335 (**Figure 3**, 60x magnification).



336  
 337 **Figure 3.** Representative confocal immunofluorescence images of a chondroitin sulfate staining (grey) of HUVECs and  
 338 iPSC-ECs after 96 h of static and dynamic culture. Nuclei were counterstained with Hoechst 33342 (cyan). (Arrow  
 339 indicates flow direction. Scale bars: 10x 100  $\mu$ m, 60x 20  $\mu$ m).

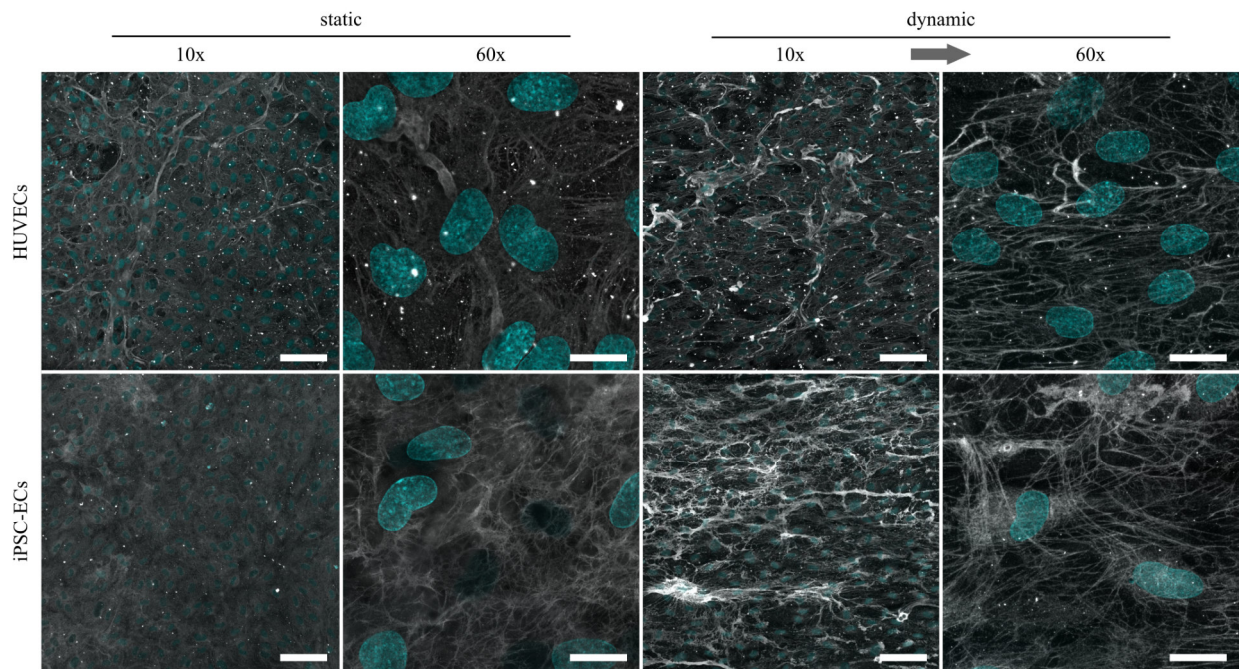
340 Regarding the amount of HA, there were no marked differences between HUVECs and iPSC-ECs  
 341 after static culture (**Figure 4**). Structurally the HA seemed to be more condensed in some spots,  
 342 especially in the case of iPSC-ECs, and not as homogeneously distributed as CS described before.  
 343 For iPSC-ECs the amount of HA comprised in the clusters increased after dynamic culture, while this  
 344 trend was not observed to this extent in the case of HUVECs cultured under flow (**Figure 4**, 10x

345 magnification). Evaluation of the images acquired at a magnification of 60x revealed a relatively  
 346 uniform HA distribution with no mesh or fiber formation (**Figure 4**, 60x magnification).



347  
 348 **Figure 4.** Representative confocal immunofluorescence images of a hyaluronic acid staining (grey) of HUVECs and  
 349 iPSC-ECs after 96 h of static and dynamic culture. Nuclei were counterstained with Hoechst 33342 (cyan). (Arrow  
 350 indicates flow direction. Scale bars: 10x 100  $\mu$ m, 60x 20  $\mu$ m).

351 Being the most abundant GAG component of the glycocalyx and also known as mechanosensor  
 352 (Oohira et al., 1983; Ihrcke et al., 1993; Ebong et al., 2014), HS revealed the most expressive  
 353 changes due to culture conditions. While in both culture conditions there was no drastic difference in  
 354 the amount of HS on HUVECs compared to iPSC-ECs, there was a clear increase in the HS amount  
 355 after dynamic culture for both cell types compared to static culture (**Figure 5**). Regarding the  
 356 phenotype, HS formed a dense outstretched mesh across the cellular monolayer with generation of  
 357 some thicker fibers in the case of HUVECs after static culture. Application of shear stress induced  
 358 the formation of thicker HS fibers which were still arranged as a dense network but additionally  
 359 aligned with the flow direction (**Figure 5**).



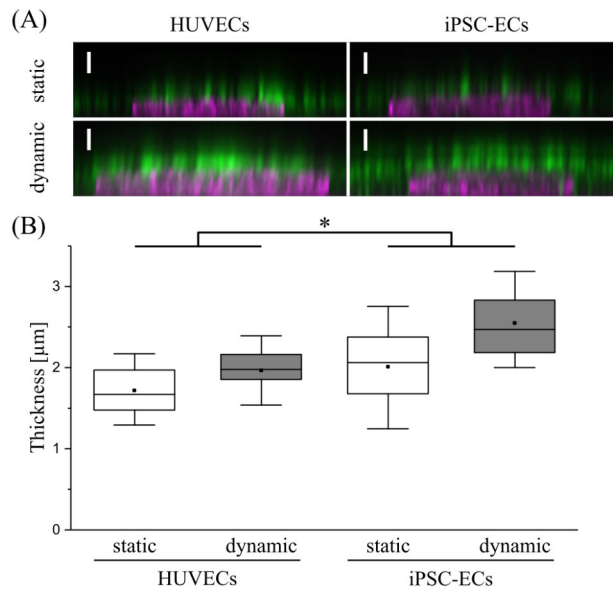
360

361 **Figure 5.** Representative confocal immunofluorescence images of a heparan sulfate staining (grey) of HUVECs and  
 362 iPSC-ECs after 96 h of static and dynamic culture. Nuclei were counterstained with Hoechst 33342 (cyan). (Arrow  
 363 indicates flow direction. Scale bars: 10x 100  $\mu\text{m}$ , 60x 20  $\mu\text{m}$ ).

364 For analysis of the influence of surface shear stress on glycocalyx thickness confocal images of the  
 365 homogeneously distributed CS staining with Hoechst counterstaining were employed (**Figure 6A**) as  
 366 previously performed elsewhere (Tiemeier et al., 2019). To estimate the glycocalyx thickness the  
 367 distance between the half-maximal signal of the nuclear staining representing the apical cell surface  
 368 and the half-maximal signal of the luminal end of the CS staining was determined for both cell types  
 369 and culture conditions. Comparing layer thicknesses on the surface of HUVECs and iPSC-ECs, there  
 370 was a significantly thicker glycocalyx observed for the iPSC-ECs (**Figure 6B**). Additionally, the  
 371 measurement revealed a significant difference between static and dynamic culture conditions with a  
 372 higher glycocalyx thickness for dynamic culture, ranging between  $2.0 \pm 0.3 \mu\text{m}$  for HUVECs and  
 373 around  $2.5 \pm 0.5 \mu\text{m}$  for iPSC-ECs (**Figure 6B**). As this analysis was conducted after fixation of cells,  
 374 which potentially causes a collapse of the glycocalyx and thereby underestimates the thickness, we  
 375 additionally performed a live-cell staining using wheat germ agglutinin (WGA) to verify the obtained  
 376 results (**Supplementary Figures S4, S5**). Lacking the fixation, it was necessary to switch the culture  
 377 substrate from the thermoresponsive polymer coating toward a non-responsive TCPS surface, thereby  
 378 preventing unintended, spontaneous detachment of cells during image acquisition. First a lectin  
 379 staining of cells cultured under static conditions on both substrates was conducted for HUVECs and  
 380 iPSC-ECs, respectively (**Supplementary Figure S4A**), demonstrating no influence of the culture

15

381 substrate on glycocalyx expression (**Supplementary Figure S4B**). Imaging of native WGA staining  
 382 together with cytosolically located CMF-DA showed a glycocalyx thickness of around 1.5-2.5  $\mu\text{m}$   
 383 after static culture of HUVECs and iPSC-ECs and thereby verified the results obtained from CS  
 384 staining after fixation (**Supplementary Figure S5**).



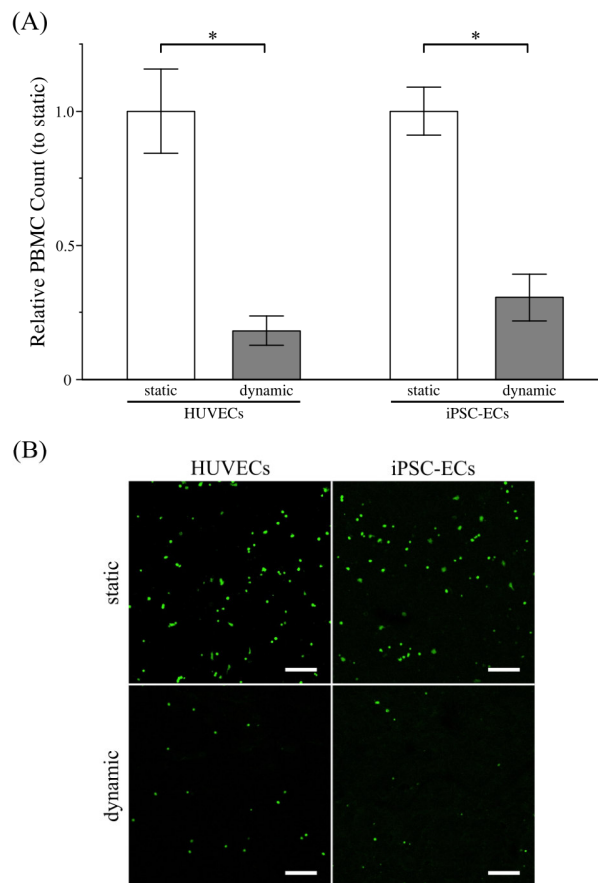
385  
 386 **Figure 6.** Determination of glycocalyx thickness on HUVECs and iPSC-ECs after 96 h of static and dynamic culture. **(A)**  
 387 Representative confocal images of chondroitin sulfate (green) and nuclear staining (magenta) shown as orthogonal  
 388 projection (Scale bars: 2.5  $\mu\text{m}$ ) to determine **(B)** the glycocalyx layer thickness. Data are presented as box plots including  
 389 mean, median and 90% confidence interval. Significant differences were found between the two cell types as well as  
 390 between the culture conditions, respectively (n=4, two-way ANOVA: main factors, \*  $p < 0.05$ ).

### 391 3.3 Effects of shear stress on glycocalyx functionality

392 To evaluate the functionality of the glycocalyx formed on HUVECs and iPSC-ECs under static as  
 393 well as dynamic culture conditions a peripheral blood mononuclear cell (PBMC) adhesion assay was  
 394 performed. In general, PBMCs are blood cells exhibiting a single round nucleus, for example  
 395 lymphocytes, monocytes, natural killer cells and dendritic cells. As integral parts of the immune  
 396 system these cell types are able to interact with the luminal endothelium for example in the case of  
 397 inflammation, undergoing the well-known steps of capture, rolling, adhesion and transmigration  
 398 through the endothelial layer. This complex mechanism is controlled by a myriad of factors and  
 399 processes, one being the decline in glycocalyx thickness by macromolecular shedding granting access  
 400 to shorter membrane bound glycoproteins like selectins and adhesion molecules (ICAM, VCAM) on  
 401 the EC surface (Kalucka et al., 2017). Therefore, the PBMC adhesion assay can be used as a simple  
 402 method to evaluate glycocalyx functionality *in vitro* giving a lower count of adhering PBMCs with  
 403 higher glycocalyx integrity and thickness.

## Shear-induced changes in EC-glycocalyx

404 For establishment of the assay, we performed PBMC adhesion using HUVEC monolayers with  
405 different concentrations of CMFDA-labelled PBMCs as well as potent positive controls  
406 (**Supplementary Figure S6**). The adhered PBMC counts increased with increasing cell numbers  
407 used in the assay (**Supplementary Figure S6C**). Additionally, mechanical and especially cytokine-  
408 induced glycocalyx shedding led to a drastic increase in PBMC adhesion, thereby proofing the  
409 functionality of the assay (**Supplementary Figure S6B,C**). When analyzing the influence of culture  
410 conditions on PBMC adhesion to HUVECs or iPSC-ECs we found a significant decrease in PBMC  
411 adhesion after dynamic culture for both cell types compared to static culture (**Figure 7A,B**), arguing  
412 for a better glycocalyx functionality/integrity after application of shear stress. This goes in line with  
413 the finding of higher amounts of HS on the EC surfaces and increased glycocalyx thicknesses after  
414 dynamic culture. Comparison of leucocyte adhesion to HUVECs and iPSC-ECs revealed no  
415 significant difference regarding the cell type (**Supplementary Figure S7**).

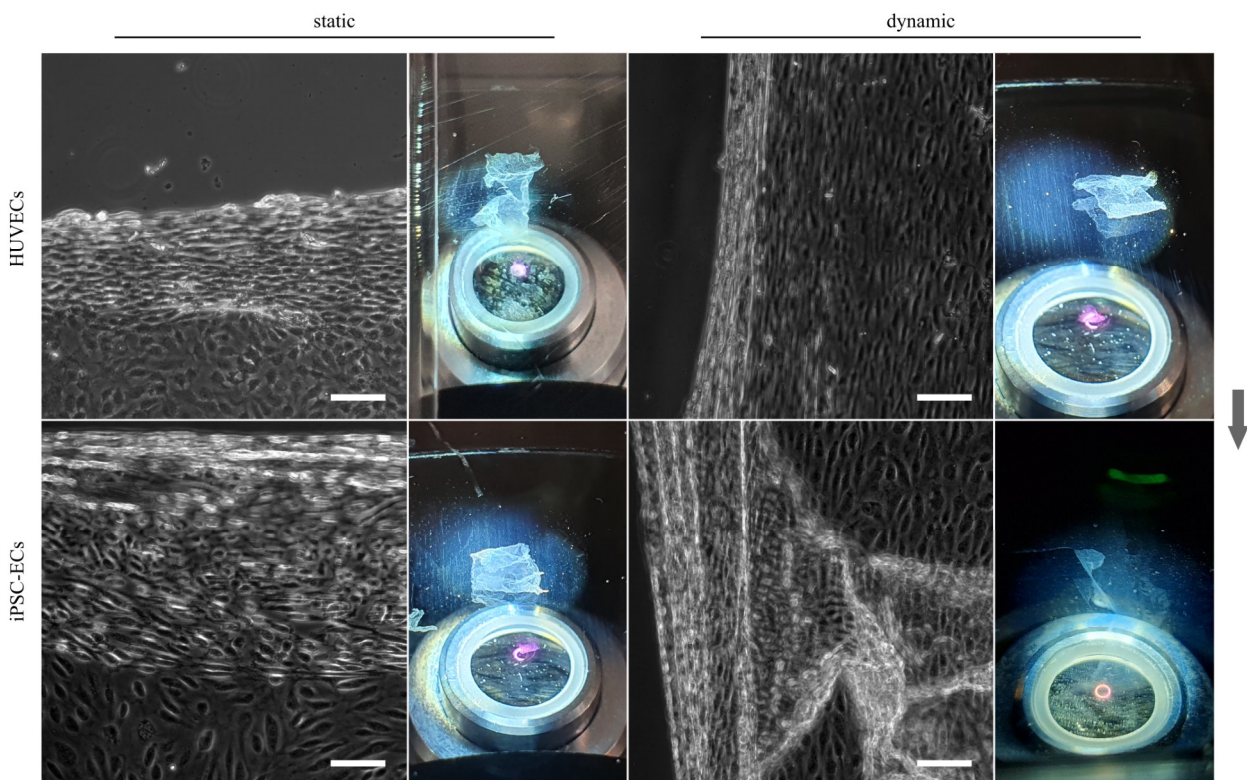


416

417 **Figure 7.** Assessment of glycocalyx functionality of HUVECs and iPSC-ECs after 96 h of static and dynamic culture via  
418 PBMC adhesion assay. **(A)** Relative PBMC count determined from confocal images (for details on image processing  
419 refer to **Supplemental Figure S6A**). Data are presented as mean  $\pm$  SEM with respect to “static” (n=4, Mann-Whitney  
420 Test, \*  $p < 0.05$ ). **(B)** Representative unprocessed confocal images of adherent PBMCs labelled with CMFDA on the  
421 surface of confluent HUVEC and iPSC-EC monolayers. (Scale Bars: 200  $\mu$ m).

422 **3.4 Detachment of aligned HUVEC and iPSC-EC sheets from thermoresponsive polymer**  
 423 **coatings**

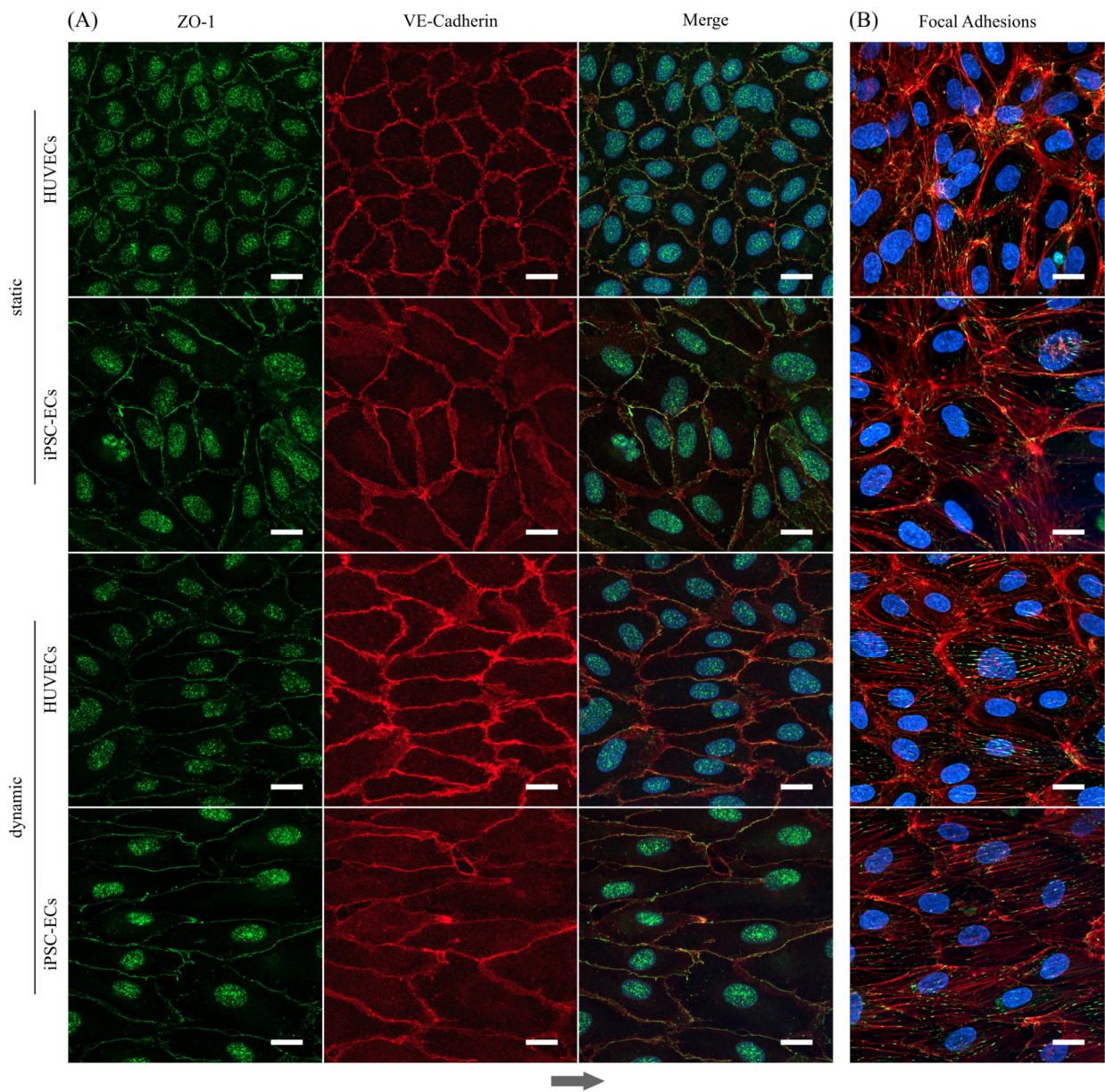
424 In addition to the analysis of cellular alignment under flow conditions and the study of glycocalyx  
 425 alterations due to shear stress, one objective of this study was the generation of polarized, confluent  
 426 HUVEC and iPSC-EC cell sheets, preferably with cells in an aligned state after dynamic culture for  
 427 tissue engineering applications. A first attempt to detach confluent cellular monolayers from  
 428 thermoresponsive PGE-coated surfaces after 48 h, which is the time point sufficient for cellular  
 429 alignment at the applied shear stress, resulted in singularization or partial sheet detachment of  
 430 HUVECs and iPSC-ECs after both static or dynamic culture (**Supplementary Figure S8**). Extending  
 431 the culture time to 72 h improved the integrity of detached sheets, yet it was still not possible to  
 432 harvest fully intact cell sheets from any of the conditions (data not shown). For both HUVECs and  
 433 iPSCs, cell sheet fabrication was possible after 96 h of culture without flow as shown by phase  
 434 contrast images and photographs in **Figure 8**. Intact aligned HUVEC cell sheets also detached after  
 435 96 h of shear application, whereas the iPSC-EC layer indeed separated from the thermoresponsive  
 436 surface but lost its integrity resulting in a disrupted sheet (**Figure 8**). It was evident that aligned cell  
 437 sheets tended to detach first from the sides parallel to the applied fluid flow.



438 **Figure 8.** Enzyme-free harvest of HUVEC and iPSC-EC cell sheets from PGE-coated PS substrates triggered by a short  
 439 temperature switch after static and dynamic culture for 96 h. Detachment of cell sheets is shown for each condition by a  
 440 representative phase contrast image as well as a photograph (Arrow indicates flow direction. Scale bars: 100  $\mu$ m, n=3).  
 441

## Shear-induced changes in EC-glycocalyx

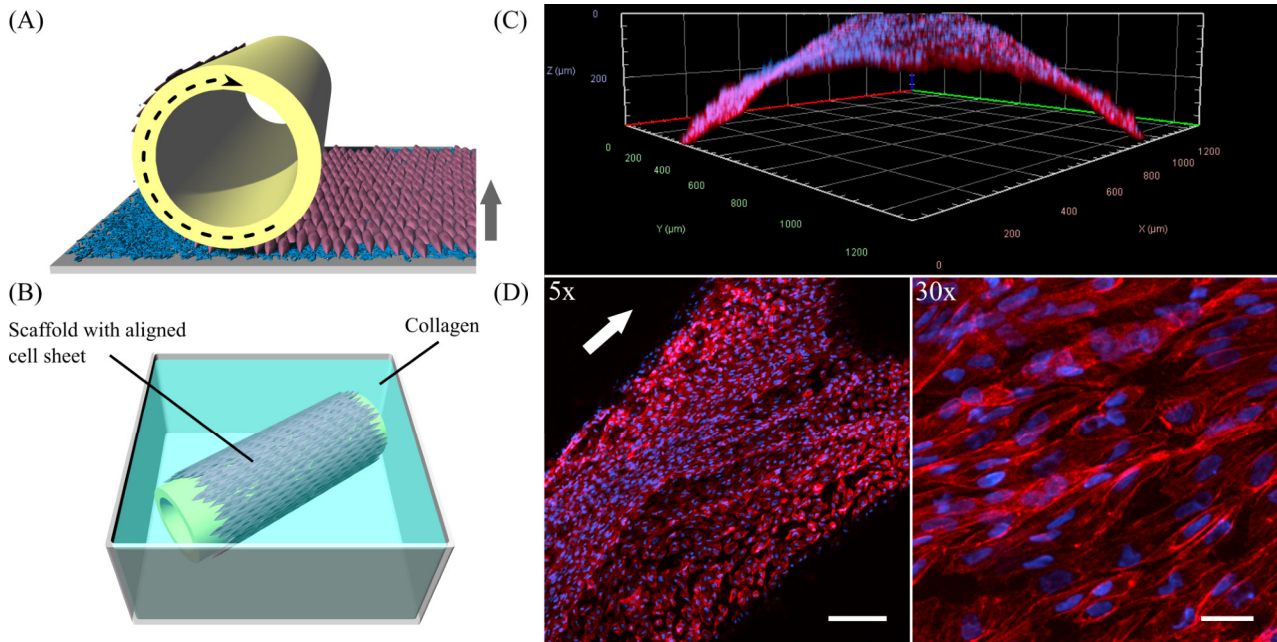
442 Searching for a reason for the differential behavior of aligned iPSC-ECs regarding the cell sheet  
443 detachment, we decided to conduct staining verifying the expression of essential components that  
444 ensure the integrity of endothelial layers. After 96 h of both static and dynamic culture ZO-1 as a  
445 protein associated with tight junctions is present in HUVECs as well as iPSC-ECs (**Figure 9A**).  
446 Same is true for VE-cadherin which is an indicator for EC junction integrity. Both proteins co-  
447 localize at the cell-cell interface and for cells cultured under dynamic conditions the alignment of  
448 cells along the flow is evident in the microscopic images (**Figure 9A**). As there were no differences  
449 in occurrence of cell-cell contacts we additionally stained the cells for F-actin and vinculin  
450 investigating the formation of stress fibers and focal adhesions. Indeed, the staining revealed an  
451 increased formation of stress fibers in the direction of flow in aligned cells after application of shear  
452 stress with a pronounced formation of focal adhesions (**Figure 9B, Supplementary Figure S9**).  
453 Since this was determined for both HUVECs and iPSC-ECs this finding does not explain the  
454 difficulties in intact, self-detached cell sheet fabrication observed for iPSC-ECs.



455  
 456 **Figure 9.** Formation of tight junctions and appearance of focal adhesion after static and dynamic culture of HUVECs and  
 457 iPSC-ECs for 96 h. **(A)** Representative confocal images of ZO-1 (green) and VE-Cadherin staining (red). Nuclei were  
 458 counterstained with Hoechst 33342 (blue). **(B)** Confocal images of phalloidin (red) and vinculin staining (green)  
 459 representing the focal adhesions. Nuclei were counterstained with Hoechst 33342 (blue). (Arrow indicates flow direction.  
 460 Scale bars: 20  $\mu$ m).

461 With vascular tissue engineering applications in mind, which largely benefit from a polarized,  
 462 aligned EC sheet, we tackled the issue of the incomplete self-detachment of the iPSC-EC sheets by  
 463 immediately transferring it onto a 3D printed tubular scaffold during the detachment process. This  
 464 was accomplished by a recently developed procedure in our group using a custom-made rolling  
 465 device (Elomaa et al., 2022) as illustrated in **Figure 10A**. The biofabricated vessel mimic made from  
 466 a dynamically cultured iPSC-EC sheet in this preliminary proof-of-concept study was embedded into

467 a collagen hydrogel (**Figure 10B**). The coverage of the tubular scaffold is shown by a 3D-  
 468 reconstruction indicating the curvature of the 3D-printed structure (**Figure 10C**) as well as by a Z-  
 469 projection of confocal stacks (**Figure 10D**). The latter not only proves the continuous coverage of the  
 470 rod but also shows the intact alignment of the cells after detachment and rolling of the sheet.



471

472 **Figure 10.** Generation of vessel-like constructs by transferring a detaching aligned endothelial sheet from a PGE-coated  
 473 thermoresponsive substrate onto a tubular 3D-printed scaffold. (A) Illustration of wrapping process and (B) rolled sheet  
 474 on scaffold embedded in a collagen gel. (C) 3-dimensional reconstruction and (D) Z-projection of confocal stacks of the  
 475 phalloidin-stained (red) iPSC-EC sheet at different magnifications. Nuclei were counterstained with Hoechst 33342  
 476 (blue). Cell sheet was detached and rolled after 96 h of dynamic culture. (Arrows indicate flow direction. Scale bars: 5x  
 477 200  $\mu\text{m}$ , 30x 30  $\mu\text{m}$ ).

478 **4 Discussion**

479 In this study we investigated the influence of physiological shear stress on cellular alignment and  
480 glycocalyx formation of HUVECs compared to iPSC-ECs. In order to apply homogenous laminar  
481 flow to the cellular monolayers our recently reported slide chamber system (Lindner et al., 2021) was  
482 used, which can reproducibly be operated in a simple flow circuit without the need for a complex  
483 bioreactor system (**Figure 1A-D**).

484 In a preliminary experiment shear stresses in the range of 1.7-10 dyn cm<sup>-2</sup>, mimicking shear in  
485 capillaries and veins as well as low arterial shear stress (Ballermann et al., 1998; Paszkowiak and  
486 Dardik, 2003), were applied to monolayers cultured on TCPS, inducing the alignment of both  
487 HUVECs and iPSC-ECs toward the flow direction (**Supplementary Figure S1**). In general, this  
488 behavior is well known for ECs (Thoumine et al., 1995; Steward et al., 2015) and has been shown  
489 previously by several groups for HUVECs cultured under different surface shear stresses (Koo et al.,  
490 2013; Li and Wang, 2018; Wang et al., 2020). Additionally, in our hands HUVECs showed a shear  
491 and time dependent reaction to flow, as seen by a faster elongation and alignment with higher surface  
492 shear. However, the application of 10 dyn cm<sup>-2</sup> led to a disruption in the cellular monolayer after  
493 96 h. As this level of shear corresponds to arterial conditions, our results imply a limited suitability of  
494 vein-originating HUVECs as a model for arterial ECs, at least for dynamic long-term studies. A  
495 previous result hinting in this direction was obtained by Gouverneur *et al.* who reported a reduction  
496 of HUVEC number already after 24 h of culture with a surface shear stress of 10 dyn cm<sup>-2</sup>  
497 (Gouverneur et al., 2006b).

498 A review of literature data on the flow-induced alignment of iPSC-ECs reveals contrary results as  
499 several groups found a reaction of iPSC-EC orientation to flow (Sivarapatna et al., 2015; Wang et al.,  
500 2016; Ingram et al., 2018; Arora et al., 2019; Ciampi et al., 2019; Rosa et al., 2019), while others did  
501 not see any effect comparable to primary ECs (Tiemeier et al., 2019). Comparing HUVEC behavior  
502 under flow to iPSC-ECs in our setup, we not only observed a flow-induced alignment of the latter but  
503 also a markedly faster response as regardless of applied shear strength, cells were fully aligned after  
504 24 h (**Supplementary Figure S1**). This could be explained by iPSC-ECs being in a less mature  
505 cellular state without previous contact to fluid flow. The shear naivety makes the cells potentially  
506 more susceptible toward dynamic culture conditions (Sivarapatna et al., 2015; Arora et al., 2019).  
507 Additionally, the employed iPSC-ECs were slightly larger in size compared to HUVECs. The larger

508 surface area exposed to the mechanical influence of flow might add to the shortened time needed for  
509 cellular alignment.

510 For the following comparative glycocalyx study we decided on using a physiologically relevant  
511 surface shear stress of  $6.6 \text{ dyn cm}^{-2}$  applied to monolayers, as this condition allows for a fast  
512 alignment of not only iPSC-ECs but also HUVECs without negative influence on cellular monolayer  
513 integrity. As a study by Koo *et al.* demonstrated, the time scale for glycocalyx formation on  
514 HUVECs is in the range of 2-3 days (Koo et al., 2013). Therefore, we decided on a culture time of  
515 96 h to ensure full maturation of the polysaccharide surface layer. HUVECs and iPSC-ECs cultured  
516 on PGE-coated PS surfaces, with prospect of planned cell sheet engineering experiments, showed  
517 similar flow-alignment after 96 h as seen before on TCPS, and endothelial differentiation status was  
518 preserved for all conditions (**Figure 2**). Subsequent staining of the glycocalyx components CS, HA  
519 and HS revealed some differences between cell types but even more with respect to the culture  
520 condition (**Figure 3-5**). Compared to HUVECs, we found more CS on the surface of the iPSC-EC  
521 monolayer under static conditions (**Figure 3**) as well as a slightly increased amount of HA after static  
522 and dynamic culture of iPSC-ECs (**Figure 4**) while there was no difference in the HS amount  
523 between both cell types (**Figure 5**). Additionally, the glycocalyx thickness was significantly higher in  
524 iPSC-ECs compared to HUVECs, although the difference was small as all measured values ranged  
525 between  $\sim 1.5\text{-}2.5 \mu\text{m}$  (**Figure 6**). These findings are contrary to findings by Tiemeier *et al.*, who  
526 presented a significantly reduced amount of HA and HS as well as a  $\sim 50\%$  reduced glycocalyx  
527 thickness on iPSC-ECs compared to primary ECs after 96 h application of laminar shear stress ( $5 \text{ dyn}$   
528  $\text{cm}^{-2}$ ) (Tiemeier et al., 2019). An explanation could be the fact that the iPSC-ECs used in their  
529 experiments were generated according to a different protocol (Orlova et al., 2014b) than the cells in  
530 our study (Olmer et al., 2018). As described by Jang *et al.* iPSC-ECs from different origins and  
531 differentiation protocols are often hard to compare as their characteristics are heterogeneous (Jang et  
532 al., 2019). Given that endothelial function relies strongly on glycocalyx functionality, analysis of this  
533 important cellular characteristic should find its way into the standard evaluation of iPSC-ECs used as  
534 endothelial models. Our findings on glycocalyx properties of the used iPSC-ECs suggest their  
535 superior maturity regarding glycocalyx formation.

536 Furthermore, the comparison of glycocalyx status after static and dynamic culture is important, as it  
537 has been shown before that, for example, glycocalyx thickness is highly dependent on applied fluid  
538 flow in *in vitro* studies (Ueda et al., 2004; Gouverneur et al., 2006b; Siren et al., 2021). In our present

539 study we also found a significantly higher glycocalyx layer thickness after dynamic culture with ~2  
540  $\mu\text{m}$  for HUVECs and ~2.5  $\mu\text{m}$  for iPSC-ECs (**Figure 6**). These established thicknesses fit with  
541 values in the range of 1.7-3  $\mu\text{m}$  obtained for diverse types of ECs in previous *in vitro* studies (Barker  
542 et al., 2004; Stevens et al., 2007; Zeng et al., 2013; Tiemeier et al., 2019) and with thicknesses  
543 established *in vivo* between 0.5-4.5  $\mu\text{m}$  (Reitsma et al., 2007). However, some studies reported  
544 unphysiological glycocalyx thicknesses in the range of ~30 nm (Potter and Damiano, 2008; Chappell  
545 et al., 2009). Moreover, thickness determinations after fixation were questioned because of  
546 alterations to the glycocalyx via dehydration (Curry and Adamson, 2012). Therefore, we additionally  
547 performed a native thickness determination using WGA, verifying our aforementioned results  
548 (**Supplementary Figures S4, S5**). When analyzing the glycocalyx composition and potential  
549 changes induced by fluid flow we found a slightly increased amount of uniformly distributed CS on  
550 HUVECs after dynamic culture (**Figure 3**), which is somewhat surprising as CS is not a typical  
551 mechanosensor (Pahakis et al., 2007; Siren et al., 2021). Nevertheless, also Zeng *et al.* found an  
552 upregulation of CS after dynamic culture of bovine aortic ECs with a uniform CS distribution (Zeng  
553 and Tarbell, 2014). HS and HA on the other hand have previously been described as important  
554 mechanosensors of the glycocalyx (Florian et al., 2003; Mochizuki et al., 2003; Ebong et al., 2014).  
555 For HA we only saw a reaction to flow in iPSC-ECs, while there was no difference in the amount of  
556 HA on the HUVEC surface (**Figure 4**). However, the increase of HA in HUVECs has been shown by  
557 Gouverneur *et al.* as well as Wang *et al.* (Gouverneur et al., 2006b; Wang et al., 2020). For HS we  
558 found the expected strong increase in amount on the surface of the endothelial layer after application  
559 of flow (**Figure 5**), which was also described by Giantsos-Adams *et al.* for HUVECs (Giantsos-  
560 Adams et al., 2013) and by several groups for bovine aorta endothelial cells (Florian et al., 2003;  
561 Pahakis et al., 2007; Ebong et al., 2014). HS generally shows the strongest reaction of the three  
562 important GAGs contained in the glycocalyx toward flow as it is, amongst other binding partners,  
563 attached to syndecans. These are transmembrane proteins comprising several functions, for example  
564 the transduction of mechanical influences on the cell surface into the interior by interaction with the  
565 cytoskeleton via their cytoplasmic tail region (Giantsos-Adams et al., 2013; Tarbell et al., 2014). The  
566 dense outstretched mesh structure with formation of thicker HS fibers shown in **Figure 5** is in line  
567 with the appearance of HS layers on rat fat pad endothelial cells (Zeng and Tarbell, 2014) and human  
568 umbilical vein smooth muscle cells (Kang et al., 2017).

569 To assess the functional integrity of the glycocalyx we employed a leucocyte adhesion assay as for a  
570 mature glycocalyx in the physiological state the polysaccharide moiety sufficiently covers cellular

## Shear-induced changes in EC-glycocalyx

571 adhesion molecules, thereby preventing the adhesion and subsequent extravasation of blood cells.  
572 After glycocalyx shedding or in the case of a thin immature glycocalyx, leukocytes are able to  
573 interact with the endothelial cell layer and subsequently adhere (Kalucka et al., 2017). Performing a  
574 simple static leucocyte adhesion assay, we could show a significant reduction in PBMC binding to  
575 the endothelial surface after dynamic culture for both cell types, arguing for a more mature  
576 glycocalyx layer compared to their status after static culture. This is in line with the thickness  
577 improvement identified after application of fluid flow and demonstrates functionality. Similar results  
578 were obtained by Delgadillo *et al.* for HUVECs and neutrophils, showing higher immune cell  
579 adhesion for lower surface shear stresses (Delgadillo et al., 2020).

580 Subsequent to the extensive analysis of cellular directionality and glycocalyx properties we aimed to  
581 utilize the aligned cellular monolayers comprising a functional glycocalyx for cell sheet engineering  
582 with the prospect of fabricating 3D vessel structures. As one of the mayor obstacles of 3D tissue  
583 engineering is the inefficient vascularization of fabricated constructs, vascular tissue engineering has  
584 been in the focus for decades (Devillard and Marquette, 2021). Several advances have been made  
585 toward perfusable 3D vessel formation, ranging from the inner lining of tubular constructs using ECs  
586 (Weinberg and Bell, 1986; Villalona et al., 2010) to promising advances employing cell sheet  
587 engineering to form 3D vascular grafts (L'Heureux et al., 1998; Kubo et al., 2007; Rayatpisheh et al.,  
588 2014; Othman et al., 2015). In a first proof-of-concept, we aimed to translate the advantages of EC  
589 culture under physiological flow toward tissue engineering applications of blood vessel mimics.  
590 Therefore, we cultured HUVECs and iPSC-ECs under static and dynamic conditions on  
591 thermoresponsive cell culture substrates (Stöbener et al., 2018; Stöbener and Weinhart, 2020) and at  
592 first successfully detached intact monolayers after a static culture time of 96 h simply by temperature  
593 reduction. To our knowledge, this is the first generation of a human iPSC-EC cell sheet, as this  
594 technique has only yet been employed using mouse iPSC-ECs (Hibino et al., 2012). For dynamically  
595 cultured cells, we observed aligned HUVEC sheet detachment but no complete self-detachment of  
596 iPSC-EC sheets (**Figure 8**). Looking for an explanation of sheet disruption, we verified the integrity  
597 of cell-cell-contacts within the confluent monolayers for all conditions and found ZO-1 and VE-  
598 cadherin homogenously distributed to cell-cell-contact sites (**Figure 9A**), as shown before for  
599 example for iPSC-ECs and VE-cadherin (Olmer et al., 2018) or HUVECs and ZO-1 (Bartosova et al.,  
600 2021). The observed nuclear staining of ZO-1 for all conditions can be explained by the still dynamic  
601 remodeling of cell-cell-contacts after 96 h of culture, leading to a nuclear localization of ZO-1  
602 (Gottardi et al., 1996). Furthermore, staining of actin and vinculin revealed a pronounced generation

603 of stress fibers and focal adhesions after application of fluid flow in HUVECs and iPSC-ECs (**Figure**  
604 **9B, Supplementary Figures S9**), which is a typical EC reaction to surface shear stress (Franke et al.,  
605 1984; Thi et al., 2004; Katoh et al., 2008). As both cell types showed a similar reorganization of the  
606 cytoskeleton upon dynamic culture, we conclude, consistent with data shown on cellular alignment  
607 and glycocalyx formation, that the iPSC-ECs are comparably mature as the primary HUVECs in  
608 terms of mechanosensing. However, the findings on cell-cell-interactions as well as state of  
609 cytoskeleton and focal adhesion cannot explain the deficit in self-detachment of iPSC-ECs as  
610 confluent layer. One difference to HUVEC culture is the pre-coating using fibronectin in the case of  
611 iPSC-ECs. Potentially, increased presence of this extracellular matrix glycoprotein can mediate  
612 stronger interaction of focal adhesions with the underlying substrate, thereby impeding self-  
613 detachment of the monolayer.

614 To increase the chance of intact detachment of an aligned iPSC-EC sheet, we delivered mechanical  
615 support by simultaneous transfer of the sheet during detachment to a tubular 3D-printed scaffold  
616 (**Figure 10**). By this preliminary experiment we could show that rolling of a flow-aligned iPSC-EC  
617 sheet onto a tube with preservation of cellular orientation is possible. Some groups have previously  
618 reported the wrapping of aligned HUVEC sheets (Rayatpisheh et al., 2014; Othman et al., 2015) after  
619 thermally triggered sheet detachment from micropatterned surfaces, which induced the cellular  
620 alignment. However, there have not been any studies so far on 3D vessel engineering of flow-aligned  
621 HUVEC or iPSC-EC sheets comprising functional mature glycocalyx. After these promising initial  
622 results, future studies will focus on the implementation of an aligned tubular sheet construct into a  
623 dynamic flow circuit as described by Elomaa *et al.* (Elomaa et al., 2022).

624 In conclusion, we were able to demonstrate the capability of HUVECs and iPSC-ECs to respond to  
625 physiological fluid flow and show its beneficial effect on glycocalyx formation and integrity  
626 compared to static culture. With the help of thermoresponsive substrates, we were able to generate  
627 either self-detached cell sheets or a 3D construct comprising a rolled sheet with preservation of the  
628 flow induced cellular alignment. We envision our results to be valuable contributions for the  
629 improvement of endothelial *in vitro* models in the future.

630

631 **5 Conflict of Interest**

632 The authors declare that the research was conducted in the absence of any commercial or financial  
633 relationships that could be construed as a potential conflict of interest.

634 **6 Author Contributions**

635 Conceptualization, M.L., A.L. and M.W.; methodology, M.L., L.E. and R.O.; writing - original draft  
636 preparation, A.L. and M.L.; writing - review and editing, M.W., C.L., R.O. and L.E.; supervision,  
637 project administration and funding acquisition, M.W., C.L., and R.O.. All authors have read and  
638 agreed to the published version of the manuscript.

639 **7 Funding**

640 This work was funded by the Deutsche Forschungsgemeinschaft (DFG, German Research  
641 Foundation) – 434130070 (MW) and DFG OL 653/2-1 (RO). We would like to acknowledge further  
642 financial support from the Federal Ministry of Education and Research Germany (BMBF) through  
643 grant: 13N13523 (MW) and from the Ministry for Science and Culture of Lower Saxony  
644 (Niedersächsisches Vorab MW, CLT, RO). We kindly acknowledge support by the Open Access  
645 Publication Initiative of Freie Universität Berlin.

646 **8 Acknowledgments**

647 We thank Julian Braun and Julia Dahmann for providing iPSC-ECs.

648 **9 Data Availability Statement**

649 The datasets for this study will be made available by the authors upon reasonable request.

650 **10 References**

- 651 Adams, W.J., Zhang, Y., Cloutier, J., Kuchimanchi, P., Newton, G., Sehwat, S., Aird, W.C.,  
652 Mayadas, T.N., Lusinskas, F.W., and García-Cardeña, G. (2013). Functional Vascular  
653 Endothelium Derived from Human Induced Pluripotent Stem Cells. *Stem Cell Reports* 1 (2),  
654 105-113. doi:10.1016/j.stemcr.2013.06.007.
- 655 Arora, S., Lam, A.J.Y., Cheung, C., Yim, E.K.F., and Toh, Y.C. (2019). Determination of Critical  
656 Shear Stress for Maturation of Human Pluripotent Stem Cell-Derived Endothelial Cells  
657 Towards an Arterial Subtype. *Biotechnol. Bioeng.* 116 (5), 1164-1175. doi:10.1002/bit.26910.
- 658 Ballermann, B.J., Dardik, A., Eng, E., and Liu, A. (1998). Shear Stress and the Endothelium. *Kidney*  
659 *Int. Suppl.* 67, S100-S108. doi:10.1046/j.1523-1755.1998.06720.x.
- 660 Barker, A.L., Konopatskaya, O., Neal, C.R., Macpherson, J.V., Whatmore, J.L., Winlove, C.P.,  
661 Unwin, P.R., and Shore, A.C. (2004). Observation and Characterisation of the Glycocalyx of  
662 Viable Human Endothelial Cells Using Confocal Laser Scanning Microscopy. *Phys. Chem.*  
663 *Chem. Phys.* 6 (5), 1006-1011. doi:10.1039/b312189e.
- 664 Barthes, J., Özçelik, H., Hindié, M., Ndreu-Halili, A., Hasan, A., and Vrana, N.E. (2014). Cell  
665 Microenvironment Engineering and Monitoring for Tissue Engineering and Regenerative  
666 Medicine: The Recent Advances. *Biomed. Res. Int.* 2014, 921905. doi:10.1155/2014/921905.

- 667 Bartosova, M., Ridinger, D., Marinovic, I., Heigwer, J., Zhang, C., Levai, E., Westhoff, J.H.,  
 668 Schaefer, F., Terjung, S., Hildenbrand, G., Kronic, D., Bestvater, F., Hausmann, M., Schmitt,  
 669 C.P., and Zarogiannis, S.G. (2021). An Experimental Workflow for Studying Barrier  
 670 Integrity, Permeability, and Tight Junction Composition and Localization in a Single  
 671 Endothelial Cell Monolayer: Proof of Concept. *Int. J. Mol. Sci.* 22 (15), 8178.  
 672 doi:10.3390/ijms22158178.
- 673 Baudin, B., Bruneel, A., Bosselut, N., and Vaubourdolle, M. (2007). A Protocol for Isolation and  
 674 Culture of Human Umbilical Vein Endothelial Cells. *Nat. Protoc.* 2 (3), 481-485.  
 675 doi:10.1038/nprot.2007.54.
- 676 Cao, Y., Gong, Y., Liu, L., Zhou, Y., Fang, X., Zhang, C., Li, Y., and Li, J. (2017). The Use of  
 677 Human Umbilical Vein Endothelial Cells (Huvecs) as an in Vitro Model to Assess the  
 678 Toxicity of Nanoparticles to Endothelium: A Review. *J. Appl. Toxicol.* 37 (12), 1359-1369.  
 679 doi:10.1002/jat.3470.
- 680 Chappell, D., Jacob, M., Paul, O., Rehm, M., Welsch, U., Stoeckelhuber, M., Conzen, P., and  
 681 Becker, B.F. (2009). The Glycocalyx of the Human Umbilical Vein Endothelial Cell: An  
 682 Impressive Structure Ex Vivo but Not in Culture. *Circ. Res.* 104 (11), 1313-1317.  
 683 doi:10.1161/CIRCRESAHA.108.187831.
- 684 Chatterjee, C., Schertl, P., Frommer, M., Ludwig-Husemann, A., Mohra, A., Dilger, N., Naolou, T.,  
 685 Meermeyer, S., Bergmann, T.C., Alonso Calleja, A., and Lee-Thedieck, C. (2021).  
 686 Rebuilding the Hematopoietic Stem Cell Niche: Recent Developments and Future Prospects.  
 687 *Acta Biomater.* 132, 129-148. doi:10.1016/j.actbio.2021.03.061.
- 688 Ciampi, O., Bonandrini, B., Derosas, M., Conti, S., Rizzo, P., Benedetti, V., Figliuzzi, M., Remuzzi,  
 689 A., Benigni, A., Remuzzi, G., and Tomasoni, S. (2019). Engineering the Vasculature of  
 690 Decellularized Rat Kidney Scaffolds Using Human Induced Pluripotent Stem Cell-Derived  
 691 Endothelial Cells. *Sci. Rep.* 9 (1), 8001. doi:10.1038/s41598-019-44393-y.
- 692 Cosgun, Z.C., Fels, B., and Kusche-Vihrog, K. (2020). Nanomechanics of the Endothelial  
 693 Glycocalyx: From Structure to Function. *Am. J. Pathol.* 190 (4), 732-741.  
 694 doi:10.1016/j.ajpath.2019.07.021.
- 695 Curry, F.E., and Adamson, R.H. (2012). Endothelial Glycocalyx: Permeability Barrier and  
 696 Mechanosensor. *Ann. Biomed. Eng.* 40 (4), 828-839. doi:10.1007/s10439-011-0429-8.
- 697 Delgadillo, L.F., Marsh, G.A., and Waugh, R.E. (2020). Endothelial Glycocalyx Layer Properties and  
 698 Its Ability to Limit Leukocyte Adhesion. *Biophys. J.* 118 (7), 1564-1575.  
 699 doi:10.1016/j.bpj.2020.02.010.
- 700 Devillard, C.D., and Marquette, C.A. (2021). Vascular Tissue Engineering: Challenges and  
 701 Requirements for an Ideal Large Scale Blood Vessel. *Front. Bioeng. Biotechnol.* 9, 721843.  
 702 doi:10.3389/fbioe.2021.721843.
- 703 Ebong, E.E., Lopez-Quintero, S.V., Rizzo, V., Spray, D.C., and Tarbell, J.M. (2014). Shear-Induced  
 704 Endothelial Nos Activation and Remodeling Via Heparan Sulfate, Glypican-1, and Syndecan-  
 705 1. *Integr. Biol. (Camb.)* 6 (3), 338-347. doi:10.1039/c3ib40199e.
- 706 Elomaa, L., Lindner, M., Leben, R., Niesner, R., and Weinhart, M. (2022). In Vitro Vascularization  
 707 of Hydrogel-Based Tissue Constructs Via a Combined Approach of Cell Sheet Engineering  
 708 and a Dynamic Perfusion Cell Culture. *In preparation for submission.*

- 709 Fels, B., and Kusche-Vihrog, K. (2020). It Takes More Than Two to Tango: Mechanosignaling of the  
710 Endothelial Surface. *Pflugers Arch.* 472 (4), 419-433. doi:10.1007/s00424-020-02369-2.
- 711 Florian, J.A., Kosky, J.R., Ainslie, K., Pang, Z., Dull, R.O., and Tarbell, J.M. (2003). Heparan  
712 Sulfate Proteoglycan Is a Mechanosensor on Endothelial Cells. *Circ. Res.* 93 (10), e136-142.  
713 doi:10.1161/01.RES.0000101744.47866.D5.
- 714 Franke, R.P., Gräfe, M., Schnittler, H., Siffge, D., Mittermayer, C., and Drenckhahn, D. (1984).  
715 Induction of Human Vascular Endothelial Stress Fibres by Fluid Shear Stress. *Nature* 307  
716 (5952), 648-649. doi:10.1038/307648a0
- 717 Giantsos-Adams, K.M., Koo, A.J., Song, S., Sakai, J., Sankaran, J., Shin, J.H., García-Cardena, G.,  
718 and Dewey, C.F., Jr. (2013). Heparan Sulfate Regrowth Profiles under Laminar Shear Flow  
719 Following Enzymatic Degradation. *Cell. Mol. Bioeng.* 6 (2), 160-174. doi:10.1007/s12195-  
720 013-0273-z.
- 721 Gottardi, C.J., Arpin, M., Fanning, A.S., and Louvard, D. (1996). The Junction-Associated Protein,  
722 Zonula Occludens-1, Localizes to the Nucleus before the Maturation and During the  
723 Remodeling of Cell-Cell Contacts. *Proc. Natl. Acad. Sci. USA.* 93 (20), 10779-10784.  
724 doi:10.1073/pnas.93.20.10779
- 725 Gouverneur, M., Berg, B., Nieuwdorp, M., Stroes, E., and Vink, H. (2006a). Vasculoprotective  
726 Properties of the Endothelial Glycocalyx: Effects of Fluid Shear Stress. *J. Intern. Med.* 259  
727 (4), 393-400. doi:10.1111/j.1365-2796.2006.01625.x.
- 728 Gouverneur, M., Spaan, J.a.E., Pannekoek, H., Fontijn, R.D., and Vink, H. (2006b). Fluid Shear  
729 Stress Stimulates Incorporation of Hyaluronan into Endothelial Cell Glycocalyx. *Am. J.*  
730 *Physiol. Heart Circ. Physiol.* 290 (1), H458-H462. doi:10.1152/ajpheart.00592.2005.
- 731 Haase, A., Göhring, G., and Martin, U. (2017). Generation of Non-Transgenic Ips Cells from Human  
732 Cord Blood Cd34(+) Cells under Animal Component-Free Conditions. *Stem Cell Res.* 21, 71-  
733 73. doi:10.1016/j.scr.2017.03.022.
- 734 Hibino, N., Duncan, D.R., Nalbandian, A., Yi, T., Qyang, Y., Shinoka, T., and Breuer, C.K. (2012).  
735 Evaluation of the Use of an Induced Pluripotent Stem Cell Sheet for the Construction of  
736 Tissue-Engineered Vascular Grafts. *J. Thorac. Cardiovasc. Surg.* 143 (3), 696-703.  
737 doi:10.1016/j.jtcvs.2011.06.046.
- 738 Ihrcke, N.S., Wrenshall, L.E., Lindman, B.J., and Platt, J.L. (1993). Role of Heparan Sulfate in  
739 Immun-System Blood Vessel Interactions. *Immunol. Today* 14 (10), 500-505.  
740 doi:10.1016/0167-5699(93)90265-M.
- 741 Ingram, P.N., Hind, L.E., Jiminez-Torres, J.A., Huttenlocher, A., and Beebe, D.J. (2018). An  
742 Accessible Organotypic Microvessel Model Using Ipsc-Derived Endothelium. *Adv. Healthc.*  
743 *Mater.* 7 (2), 1700497. doi:10.1002/adhm.201700497.
- 744 Jaffe, E.A., Nachman, R.L., Becker, C.G., and Minick, C.R. (1973). Culture of Human Endothelial  
745 Cells Derived from Umbilical Veins. Identification by Morphologic and Immunologic  
746 Criteria. *J. Clin. Invest.* 52 (11), 2745-2756. doi:10.1172/JCI107470.
- 747 Jang, S., Collin De L'hortet, A., and Soto-Gutierrez, A. (2019). Induced Pluripotent Stem Cell-  
748 Derived Endothelial Cells: Overview, Current Advances, Applications, and Future Directions.  
749 *Am. J. Pathol.* 189 (3), 502-512. doi:10.1016/j.ajpath.2018.12.004.

## Shear-induced changes in EC-glycocalyx

- 750 Kalucka, J., Bierhansl, L., Wielockx, B., Carmeliet, P., and Eelen, G. (2017). Interaction of  
751 Endothelial Cells with Macrophages-Linking Molecular and Metabolic Signaling. *Pflugers*  
752 *Arch.* 469 (3-4), 473-483. doi:10.1007/s00424-017-1946-6.
- 753 Kang, H., Liu, J., Sun, A., Liu, X., Fan, Y., and Deng, X. (2017). Vascular Smooth Muscle Cell  
754 Glycocalyx Mediates Shear Stress-Induced Contractile Responses Via a Rho Kinase (Rock)-  
755 Myosin Light Chain Phosphatase (Mlcp) Pathway. *Sci. Rep.* 7, 42092.  
756 doi:10.1038/srep42092.
- 757 Katoh, K., Kano, Y., and Ookawara, S. (2008). Role of Stress Fibers and Focal Adhesions as a  
758 Mediator for Mechano-Signal Transduction in Endothelial Cells in Situ. *Vasc. Health Risk*  
759 *Manag.* 4 (6), 1273–1282. doi:10.2147/vhrm.s3933.
- 760 Kennedy, C.C., Brown, E.E., Abutaleb, N.O., and Truskey, G.A. (2021). Development and  
761 Application of Endothelial Cells Derived from Pluripotent Stem Cells in Microphysiological  
762 Systems Models. *Front. Cardiovasc. Med.* 8, 625016. doi:10.3389/fcvm.2021.625016.
- 763 Koo, A., Dewey, C.F., Jr., and García-Cardeña, G. (2013). Hemodynamic Shear Stress Characteristic  
764 of Atherosclerosis-Resistant Regions Promotes Glycocalyx Formation in Cultured  
765 Endothelial Cells. *Am. J. Physiol. Cell Physiol.* 304 (2), C137–C146.  
766 doi:10.1152/ajpcell.00187.2012.
- 767 Kubo, H., Shimizu, T., Yamato, M., Fujimoto, T., and Okano, T. (2007). Creation of Myocardial  
768 Tubes Using Cardiomyocyte Sheets and an in Vitro Cell Sheet-Wrapping Device.  
769 *Biomaterials* 28 (24), 3508-3516. doi:10.1016/j.biomaterials.2007.04.016.
- 770 L'heureux, N., Pâquet, S., Labbé, R., Germain, L., and Auger, F.A. (1998). A Completely Biological  
771 Tissue-Engineered Human Blood Vessel. *FASEB J.* 12 (1), 47-56. doi:10.1096/fasebj.12.1.47.
- 772 Li, W., and Wang, W. (2018). Structural Alteration of the Endothelial Glycocalyx: Contribution of  
773 the Actin Cytoskeleton. *Biomech. Model. Mechanobiol.* 17 (1), 147-158. doi:10.1007/s10237-  
774 017-0950-2.
- 775 Lindner, M., Laporte, A., Block, S., Elomaa, L., and Weinhart, M. (2021). Physiological Shear Stress  
776 Enhances Differentiation, Mucus-Formation and Structural 3d Organization of Intestinal  
777 Epithelial Cells in Vitro. *Cells* 10 (8), 2062. doi:10.3390/cells10082062.
- 778 Medina-Leyte, D.J., Domínguez-Pérez, M., Mercado, I., Villarreal-Molina, M.T., and Jacobo-  
779 Albavera, L. (2020). Use of Human Umbilical Vein Endothelial Cells (Huvec) as a Model to  
780 Study Cardiovascular Disease: A Review. *Appl. Sci.* 10 (3), 938. doi:10.3390/app10030938.
- 781 Metallo, C.M., Mohr, J.C., Detzel, C.J., De Pablo, J.J., Van Wie, B.J., and Palecek, S.P. (2008).  
782 Engineering the Stem Cell Microenvironment. *Biotechnol. Prog.* 23 (1), 18-23.  
783 doi:10.1021/bp060350a.
- 784 Mochizuki, S., Vink, H., Hiramatsu, O., Kajita, T., Shigeto, F., Spaan, J.a.E., and Kajiya, F. (2003).  
785 Role of Hyaluronic Acid Glycosaminoglycans in Shear-Induced Endothelium-Derived Nitric  
786 Oxide Release. *Am. J. Physiol. Heart Circ. Physiol.* 285 (2), H722–H726.  
787 doi:10.1152/ajpheart.00691.2002.
- 788 Möckl, L. (2020). The Emerging Role of the Mammalian Glycocalyx in Functional Membrane  
789 Organization and Immune System Regulation. *Front. Cell. Dev. Biol.* 8, 253.  
790 doi:10.3389/fcell.2020.00253.
- 791 Olmer, R., Engels, L., Usman, A., Menke, S., Malik, M.N.H., Pessler, F., Göhring, G., Bornhorst, D.,  
792 Bolten, S., Abdelilah-Seyfried, S., Scheper, T., Kempf, H., Zweigerdt, R., and Martin, U.

- 793 (2018). Differentiation of Human Pluripotent Stem Cells into Functional Endothelial Cells in  
794 Scalable Suspension Culture. *Stem Cell Reports* 10 (5), 1657-1672.  
795 doi:10.1016/j.stemcr.2018.03.017.
- 796 Oohira, A., Wight, T.N., and Bornstein, P. (1983). Sulfated Proteoglycans Synthesized by Vascular  
797 Endothelial Cells in Culture. *J. Biol. Chem.* 258 (3), 2014-2021. doi:10.1016/s0021-  
798 9258(18)33090-4.
- 799 Orlova, V.V., Drabsch, Y., Freund, C., Petrus-Reurer, S., Van Den Hil, F.E., Muenthaisong, S., Ten  
800 Dijke, P., and Mummery, C.L. (2014a). Functionality of Endothelial Cells and Pericytes from  
801 Human Pluripotent Stem Cells Demonstrated in Cultured Vascular Plexus and Zebrafish  
802 Xenografts. *Arterioscler. Thromb. Vasc. Biol.* 34 (1), 177-186.  
803 doi:10.1161/atvbaha.113.302598.
- 804 Orlova, V.V., Van Den Hil, F.E., Petrus-Reurer, S., Drabsch, Y., Ten Dijke, P., and Mummery, C.L.  
805 (2014b). Generation, Expansion and Functional Analysis of Endothelial Cells and Pericytes  
806 Derived from Human Pluripotent Stem Cells. *Nat. Protoc.* 9 (6), 1514-1531.  
807 doi:10.1038/nprot.2014.102.
- 808 Othman, R., Morris, G.E., Shah, D.A., Hall, S., Hall, G., Wells, K., Shakesheff, K.M., and Dixon,  
809 J.E. (2015). An Automated Fabrication Strategy to Create Patterned Tubular Architectures at  
810 Cell and Tissue Scales. *Biofabrication* 7 (2), 025003. doi:10.1088/1758-5090/7/2/025003.
- 811 Pahakis, M.Y., Kosky, J.R., Dull, R.O., and Tarbell, J.M. (2007). The Role of Endothelial  
812 Glycocalyx Components in Mechanotransduction of Fluid Shear Stress. *Biochem. Biophys.*  
813 *Res. Commun.* 355 (1), 228-233. doi:10.1016/j.bbrc.2007.01.137.
- 814 Paszkowiak, J.J., and Dardik, A. (2003). Arterial Wall Shear Stress: Observations from the Bench to  
815 the Bedside. *Vasc. Endovascular Surg.* 37 (1), 47-57. doi: 10.1177/153857440303700107.
- 816 Patsch, C., Challet-Meylan, L., Thoma, E.C., Urich, E., Heckel, T., O'sullivan, J.F., Grainger, S.J.,  
817 Kapp, F.G., Sun, L., Christensen, K., Xia, Y., Florido, M.H., He, W., Pan, W., Prummer, M.,  
818 Warren, C.R., Jakob-Roetne, R., Certa, U., Jagasia, R., Freskgård, P.O., Adatto, I., Kling, D.,  
819 Huang, P., Zon, L.I., Chaikof, E.L., Gerszten, R.E., Graf, M., Iacone, R., and Cowan, C.A.  
820 (2015). Generation of Vascular Endothelial and Smooth Muscle Cells from Human  
821 Pluripotent Stem Cells. *Nat. Cell Biol.* 17 (8), 994-1003. doi:10.1038/ncb3205.
- 822 Pflaum, M., Dahlmann, J., Engels, L., Naghilouy-Hidaji, H., Adam, D., Zollner, J., Otto, A.,  
823 Schmeckeber, S., Martin, U., Haverich, A., Olmer, R., and Wiegmann, B. (2021). Towards  
824 Biohybrid Lung: Induced Pluripotent Stem Cell Derived Endothelial Cells as Clinically  
825 Relevant Cell Source for Biologization. *Micromachines (Basel)* 12 (8).  
826 doi:10.3390/mi12080981.
- 827 Potter, D.R., and Damiano, E.R. (2008). The Hydrodynamically Relevant Endothelial Cell  
828 Glycocalyx Observed in Vivo Is Absent in Vitro. *Circ. Res.* 102 (7), 770-776.  
829 doi:10.1161/CIRCRESAHA.107.160226.
- 830 Psefteli, P.M., Kitscha, P., Vizcay, G., Fleck, R., Chapple, S.J., Mann, G.E., Fowler, M., and Siow,  
831 R.C. (2021). Glycocalyx Sialic Acids Regulate Nrf2-Mediated Signaling by Fluid Shear  
832 Stress in Human Endothelial Cells. *Redox Biol.* 38, 101816.  
833 doi:10.1016/j.redox.2020.101816.
- 834 Rayatpisheh, S., Heath, D.E., Shakouri, A., Rujitanaroj, P.-O., Chew, S.Y., and Chan-Park, M.B.  
835 (2014). Combining Cell Sheet Technology and Electrospun Scaffolding for Engineered

- 836 Tubular, Aligned, and Contractile Blood Vessels. *Biomaterials* 35 (9), 2713-2719.  
837 doi:10.1016/j.biomaterials.2013.12.035.
- 838 Reitsma, S., Slaaf, D.W., Vink, H., Van Zandvoort, M.a.M.J., and Oude Egbrink, M.G.A. (2007).  
839 The Endothelial Glycocalyx: Composition, Functions, and Visualization. *Pflugers Arch.* 454  
840 (3), 345-359. doi:10.1007/s00424-007-0212-8.
- 841 Rosa, S., Praça, C., Pitrez, P.R., Gouveia, P.J., Aranguren, X.L., Ricotti, L., and Ferreira, L.S. (2019).  
842 Functional Characterization of Ipsc-Derived Arterial- and Venous-Like Endothelial Cells. *Sci.*  
843 *Rep.* 9 (1), 3826. doi:10.1038/s41598-019-40417-9.
- 844 Schindelin, J., Arganda-Carreras, I., Frise, E., Kaynig, V., Longair, M., Pietzsch, T., Preibisch, S.,  
845 Rueden, C., Saalfeld, S., Schmid, B., Tinevez, J.Y., White, D.J., Hartenstein, V., Eliceiri, K.,  
846 Tomancak, P., and Cardona, A. (2012). Fiji: An Open-Source Platform for Biological-Image  
847 Analysis. *Nat. Methods* 9 (7), 676-682. doi:10.1038/nmeth.2019.
- 848 Schött, U., Solomon, C., Fries, D., and Bentzer, P. (2016). The Endothelial Glycocalyx and Its  
849 Disruption, Protection and Regeneration: A Narrative Review. *Scand. J. Trauma Resusc.*  
850 *Emerg. Med.* 24, 48. doi:10.1186/s13049-016-0239-y.
- 851 Siren, E.M.J., Luo, H.D., Bajaj, S., Mackenzie, J., Daneshi, M., Martinez, D.M., Conway, E.M.,  
852 Cheung, K.C., and Kizhakkedathu, J.N. (2021). An Improved in Vitro Model for Studying the  
853 Structural and Functional Properties of the Endothelial Glycocalyx in Arteries, Capillaries  
854 and Veins. *FASEB* . 35 (6), e21643. doi:10.1096/fj.201802376RRRR.
- 855 Sivarapatna, A., Ghaedi, M., Le, A.V., Mendez, J.J., Qyang, Y., and Niklason, L.E. (2015). Arterial  
856 Specification of Endothelial Cells Derived from Human Induced Pluripotent Stem Cells in a  
857 Biomimetic Flow Bioreactor. *Biomaterials* 53, 621-633.  
858 doi:10.1016/j.biomaterials.2015.02.121.
- 859 Stevens, A.P., Hlady, V., and Dull, R.O. (2007). Fluorescence Correlation Spectroscopy Can Probe  
860 Albumin Dynamics inside Lung Endothelial Glycocalyx. *Am. J. Physiol. Lung Cell. Mol.*  
861 *Physiol.* 293 (2), L328-335. doi:10.1152/ajplung.00390.2006.
- 862 Steward, R.J., Tambe, D., Hardin, C.C., Krishnan, R., and Fredberg, J.J. (2015). Fluid Shear,  
863 Intercellular Stress, and Endothelial Cell Alignment. *Am. J. Physiol. Cell Physiol.* 308 (8),  
864 C657-664. doi:10.1152/ajpcell.00363.2014.
- 865 Stöbener, D.D., Hoppensack, A., Scholz, J., and Weinhart, M. (2018). Endothelial, Smooth Muscle  
866 and Fibroblast Cell Sheet Fabrication from Self-Assembled Thermoresponsive Poly(Glycidyl  
867 Ether) Brushes. *Soft Matter* 14 (41), 8333-8343. doi:10.1039/c8sm01099d.
- 868 Stöbener, D.D., and Weinhart, M. (2020). Thermoresponsive Poly(Glycidyl Ether) Brush Coatings  
869 on Various Tissue Culture Substrates-How Block Copolymer Design and Substrate Material  
870 Govern Self-Assembly and Phase Transition. *Polymers (Basel)* 12 (9), 1899.  
871 doi:10.3390/polym12091899.
- 872 Tarbell, J.M., Simon, S.I., and Curry, F.R. (2014). Mechanosensing at the Vascular Interface. *Annu.*  
873 *Rev. Biomed. Eng.* 16, 505-532. doi:10.1146/annurev-bioeng-071813-104908.
- 874 Thi, M.M., Tarbell, J.M., Weinbaum, S., and Spray, D.C. (2004). The Role of the Glycocalyx in  
875 Reorganization of the Actin Cytoskeleton under Fluid Shear Stress: A "Bumper-Car" Model.  
876 *Proc. Natl. Acad. Sci. USA* 101 (47), 16483-16488. doi:10.1073/pnas.0407474101.

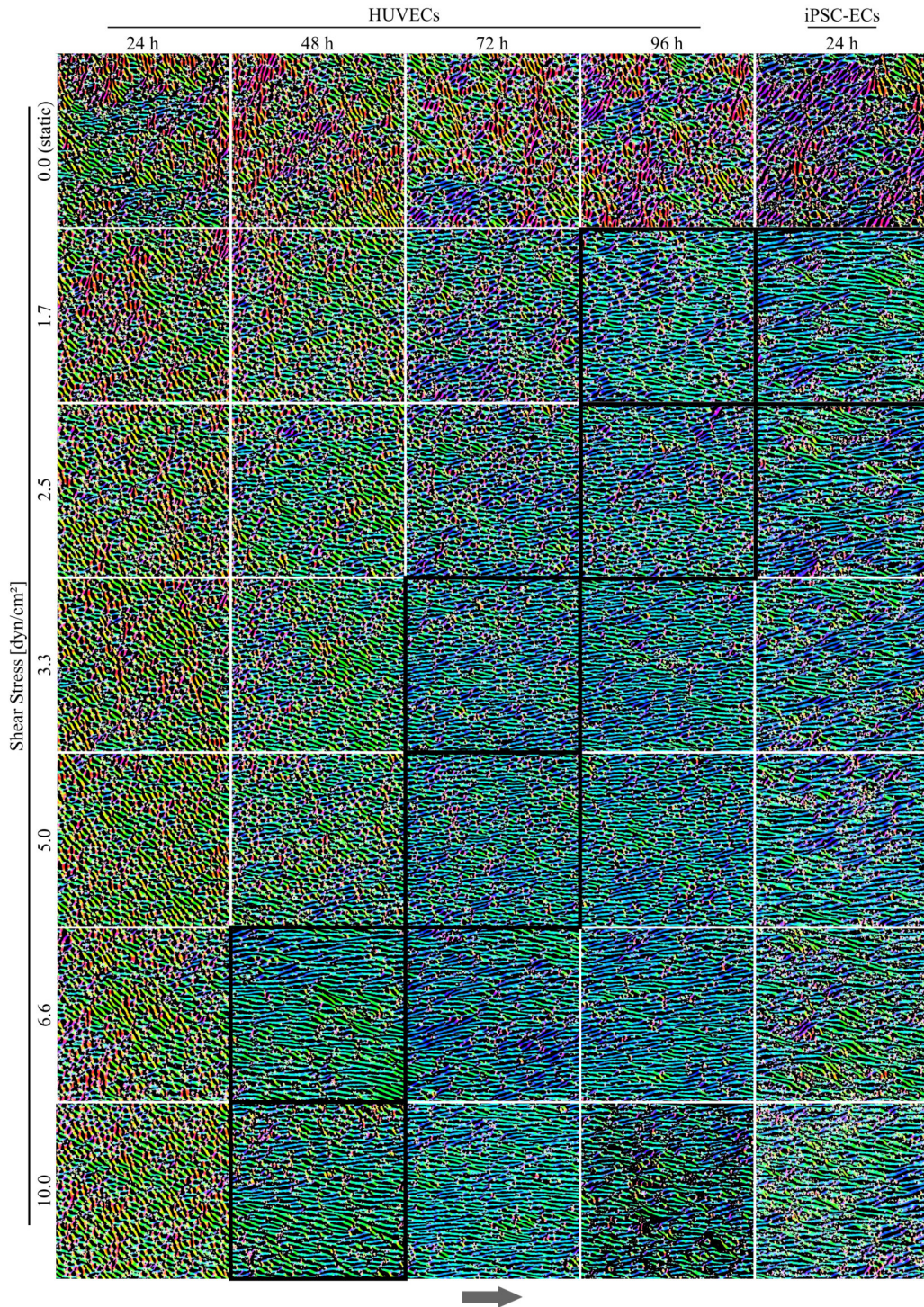
- 877 Thoumine, O., Ziegler, T., R., G.P., and M., N.R. (1995). Elongation of Confluent Endothelial Cells  
 878 in Culture: The Importance of Fields of Force in the Associated Alterations of Their  
 879 Cytoskeletal Structure. *Exp. Cell Res.* 219 (2), 427-441. doi:10.1006/excr.1995.1249.
- 880 Tiemeier, G.L., Wang, G., Dumas, S.J., Sol, W.M.P.J., Avramut, M.C., Karakach, T., Orlova, V.V.,  
 881 Van Den Berg, C.W., Mummery, C.L., Carmeliet, P., Van Den Berg, B.M., and Rabelink,  
 882 T.J. (2019). Closing the Mitochondrial Permeability Transition Pore in Hpsc-Derived  
 883 Endothelial Cells Induces Glycocalyx Formation and Functional Maturation. *Stem Cell*  
 884 *Reports* 13 (5), 803-816. doi:10.1016/j.stemcr.2019.10.005.
- 885 Ueda, A., Shimomura, M., Ikeda, M., Yamaguchi, R., and Tanishita, K. (2004). Effect of Glycocalyx  
 886 on Shear-Dependent Albumin Uptake in Endothelial Cells. *Am. J. Physiol. Heart Circ.*  
 887 *Physiol.* 287 (5), H2287–H2294. doi:10.1152/ajpheart.00808.2003.
- 888 Villalona, G.A., Udelsman, B., Duncan, D.R., Mcgillicuddy, E., Sawh-Martinez, R.F., Hibino, N.,  
 889 Painter, C., Mirensky, T., Erickson, B., Shinoka, T., and Breuer, C.K. (2010). Cell-Seeding  
 890 Techniques in Vascular Tissue Engineering. *Tissue Eng. Part B Rev.* 16 (3), 341-350.  
 891 doi:10.1089/ten.TEB.2009.0527.
- 892 Wang, G., Kostidis, S., Tiemeier, G.L., Sol, W.M.P.J., De Vries, M.R., Giera, M., Carmeliet, P., Van  
 893 Den Berg, B.M., and Rabelink, T.J. (2020). Shear Stress Regulation of Endothelial  
 894 Glycocalyx Structure Is Determined by Glucobiosynthesis. *Arterioscler. Thromb. Vasc. Biol.*  
 895 40 (2), 350-364. doi:10.1161/ATVBAHA.119.313399.
- 896 Wang, L., Xiang, M., Liu, Y., Sun, N., Lu, M., Shi, Y., Wang, X., Meng, D., Chen, S., and Qin, J.  
 897 (2016). Human Induced Pluripotent Stem Cells Derived Endothelial Cells Mimicking  
 898 Vascular Inflammatory Response under Flow. *Biomicrofluidics* 10 (1), 014106.  
 899 doi:10.1063/1.4940041.
- 900 Weinbaum, S., Tarbell, J.M., and Damiano, E.R. (2007). The Structure and Function of the  
 901 Endothelial Glycocalyx Layer. *Annu. Rev. Biomed. Eng.* 9, 121-167.  
 902 doi:10.1146/annurev.bioeng.9.060906.151959.
- 903 Weinberg, C.B., and Bell, E. (1986). A Blood Vessel Model Constructed from Collagen and Cultured  
 904 Vascular Cells. *Science* 231 (4736), 397-400. doi:10.1126/science.2934816.
- 905 Zeng, Y., and Tarbell, J.M. (2014). The Adaptive Remodeling of Endothelial Glycocalyx in  
 906 Response to Fluid Shear Stress. *PLoS ONE* 9 (1), e86249. doi:10.1371/journal.pone.0086249.
- 907 Zeng, Y., Waters, M., Andrews, A., Honarmandi, P., Ebong, E.E., Rizzo, V., and Tarbell, J.M.  
 908 (2013). Fluid Shear Stress Induces the Clustering of Heparan Sulfate Via Mobility of  
 909 Glypican-1 in Lipid Rafts. *Am. J. Physiol. Heart Circ. Physiol.* 305 (6), H811–H820.  
 910 doi:10.1152/ajpheart.00764.2012.

## ***Supplementary Material – Lindner et al. 2022***

### **Outline**

1 Correlation of shear stress and orientation of the cells	2
2 Directionality analysis	4
3 Evaluation of native glycocalyx thickness	6
4 Evaluation of the PBMC adhesion assay	8
5 Cell sheet detachment after 48 h	10
6 Formation of stress fibers due to fluid flow	11
7 References	12

1 Correlation of shear stress and orientation of the cells

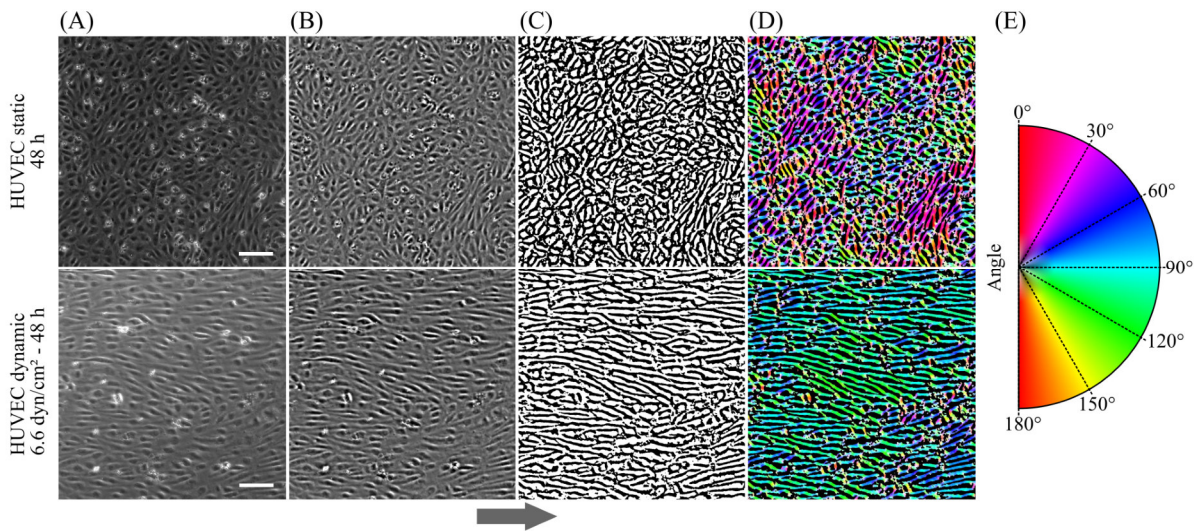


**Supplementary Figure S1.** Time and shear stress dependent orientation of HUVECs and iPSC-ECs displayed as color maps. Black frames highlight the first timepoint comprising an apparent orientation and elongation of the respective cells with the fluid flow. (Arrow indicates flow direction. Image size: 670x670  $\mu\text{m}$ , n=1).

To define optimal parameters for alignment and elongation of endothelial cells (ECs) under flow conditions, HUVECs were seeded on ibidi  $\mu$ -slides (channel heights 0.2 and 0.4 mm) and cultured under different volume flow rates. Various shear stresses in a physiological range from 0 (static culture) to 10 dyn cm<sup>-2</sup> were applied in a preliminary screening for up to 96 h. After 48 h, cellular alignment and elongation was already observed for  $\geq 6.6$  dyn cm<sup>-2</sup>, whereas cells cultured with 3.3 to 5 dyn cm<sup>-2</sup> required 72 h for alignment. Alignment and elongation were observed at  $\geq 1.7$  dyn/cm<sup>2</sup> after 96 h. High shear stress conditions (10 dyn cm<sup>-2</sup>) resulted in a reduction of cellular confluency after 96 h, as indicated by black areas. Based on these results, we finally decided to apply 6.6 dyn cm<sup>-2</sup> throughout the remaining experiments, which at the same time yields a fast alignment without being apparently harmful to cells for  $\geq 96$  h. Adaption of the experiment to iPSC-ECs demonstrated their high capacity for alignment and elongation, as the cells were (already) aligned after 24 h under all flow conditions.

## 2 Directionality analysis

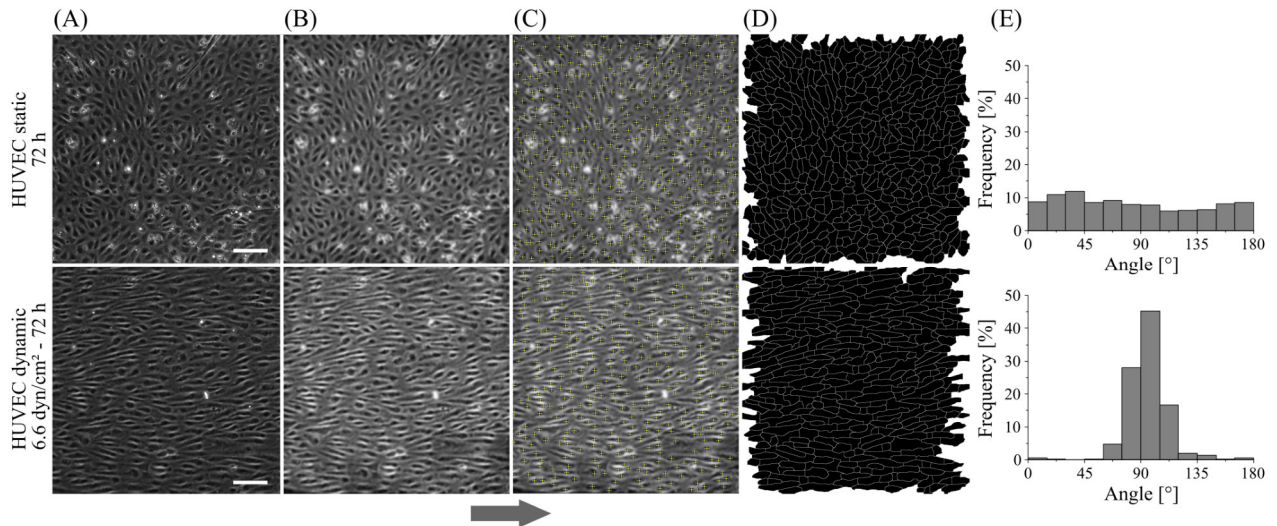
To qualitatively analyze and visually highlight the influence of varying culture conditions on the orientation of ECs as already shown in section 1 of this supplementary material, phase contrast images of ECs after static and dynamic culture were pre-processed using *ImageJ* and subsequently an orientation/angle-specific color coding was added using the *OrientationJ* plugin [1]. For pre-processing, the background was subtracted from the raw phase contrast images (rolling ball, radius 100 px), a Gaussian filter ( $\sigma = 1 \mu\text{m}$ , scaled), and a bandpass filter (down to  $20 \mu\text{m}$ , no lower limit) were applied to compensate for inhomogeneous illumination and smoothen the image [2]. The image is binarized via (auto)-thresholding according to Huang *et al.* [3], and finally processed/colored using the *OrientationJ* plugin (local window:  $\sigma = 3$  pixel). Color map is showing hue: orientation, saturation: coherency and lightness of the original image.



**Supplementary Figure S2.** Image processing steps for qualitative directionality analysis. **(A)** Original phase contrast images from HUVECs cultured under static and dynamic conditions for 48 h. **(B)** Preprocessing of the images by background subtraction as well as addition of gaussian blur and bandpass filters to remove uneven illumination and smoothen the image. **(C)** Thresholding to create a binary image. **(D)** Generation of color-map using the *OrientationJ*-plugin in *ImageJ*, adding an angle-dependent color to cell borders illustrated in **(E)**. (Arrow indicates flow direction. Scale bars:  $100 \mu\text{m}$ ).

*ImageJ* was further used to quantify the effect of culture conditions on cellular alignment/orientation. Initially, the background of phase contrast images was subtracted (rolling ball, radius = 100 pixels) and the contrast of images was increased via gamma correction ( $\gamma = 0.8$ ) and contrast stretching (*ImageJ*'s *enhance contrast* function, cutoff parameter = 0.7% saturated pixels). Using the *find maxima* function (prominence = 25, excluded on edges, light background), the cell centers were determined and the image was segmented into single cell areas accordingly. The *Extended Particle*

*Analyzer* of the *BioVoxxel* toolbox was used to determine/measure the main orientation of single cells<sup>1</sup> [4].

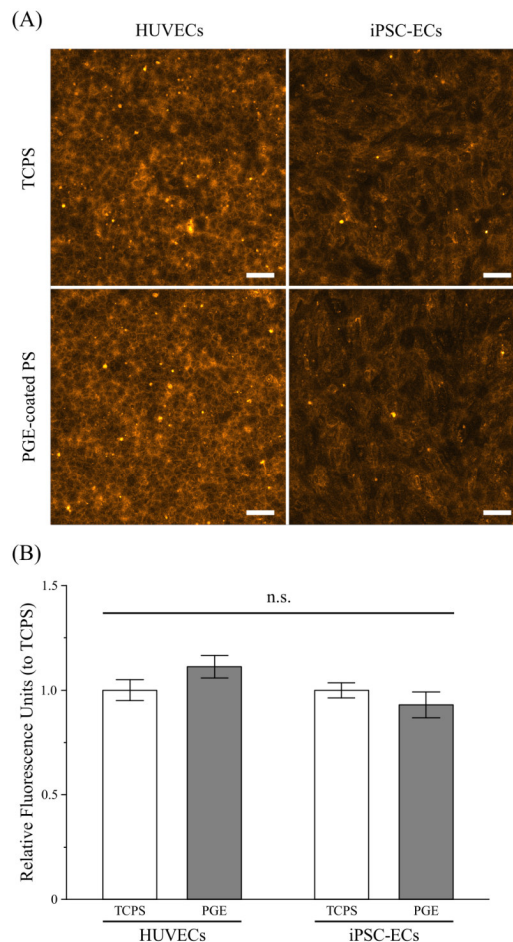


**Supplementary Figure S3.** Image processing steps for quantitative directionality analysis. (A) Original phase contrast images from HUVECs cultured under static and dynamic conditions for 72 h. (B) Preprocessing of the images by background subtraction and gamma/brightness adjustment to enhance contrast. (C) Application of the 'Find maxima' function in *ImageJ* and (D) segmentation of the images to create a mask of single cells. (E) Histogram of main orientation of single cells obtained using the extended particle analyzer in *ImageJ*. (Arrow indicates flow direction. Scale bars: 100 μm).

<sup>1</sup> These parameters were determined empirically and were valid/applicable for all acquired images.

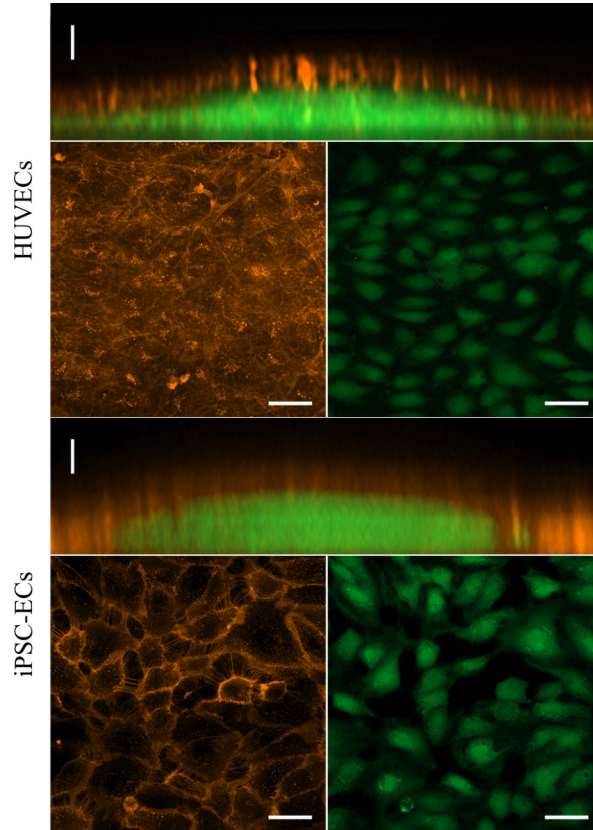
### 3 Evaluation of native glycocalyx thickness

To estimate glycocalyx thickness(es) under native, non-fixed conditions, ECs after static culture were stained with wheat germ agglutinin (WGA, labelled with Alexa™ 555, ThermoFisher) as well as CMFDA and subsequently imaged via confocal microscopy. Due to the behavior of thermoresponsive polymers and despite using an incubation chamber as well as rapid sample preparation, unfixed cells on PGE-coated substrate started to detach during image acquisition (data not shown). The experiment was therefore performed on tissue culture-treated polystyrene slides (TCPS). To exclude any influence of the cell culture substrate on glycocalyx expression, HUVECs and iPSC-ECs were seeded on TCPS and PGE-coated PS, stained with WGA and imaged via confocal microscopy (after fixation with PFA). As demonstrated in **Supplementary Figure S4**, no difference in glycocalyx expression as indicated by mean fluorescence intensity of WGA-staining was observed between both substrates for each cell type, respectively.



**Supplementary Figure S4.** Influence of culture substrate on WGA-staining of HUVECs and iPSC-ECs under static conditions (96 h) **(A)** Representative confocal image of lectin-staining (orange) on cells cultured on tissue culture and PGE-coated polystyrene. **(B)** Quantification of fluorescence intensities. Data shown as mean fluorescence units relative to the corresponding TCPS sample. No significant differences were found between the TCPS and PGE-coated PS culture substrates (Mann-Whitney Test,  $n=3$ ) (Scale bars: 100  $\mu\text{m}$ ).

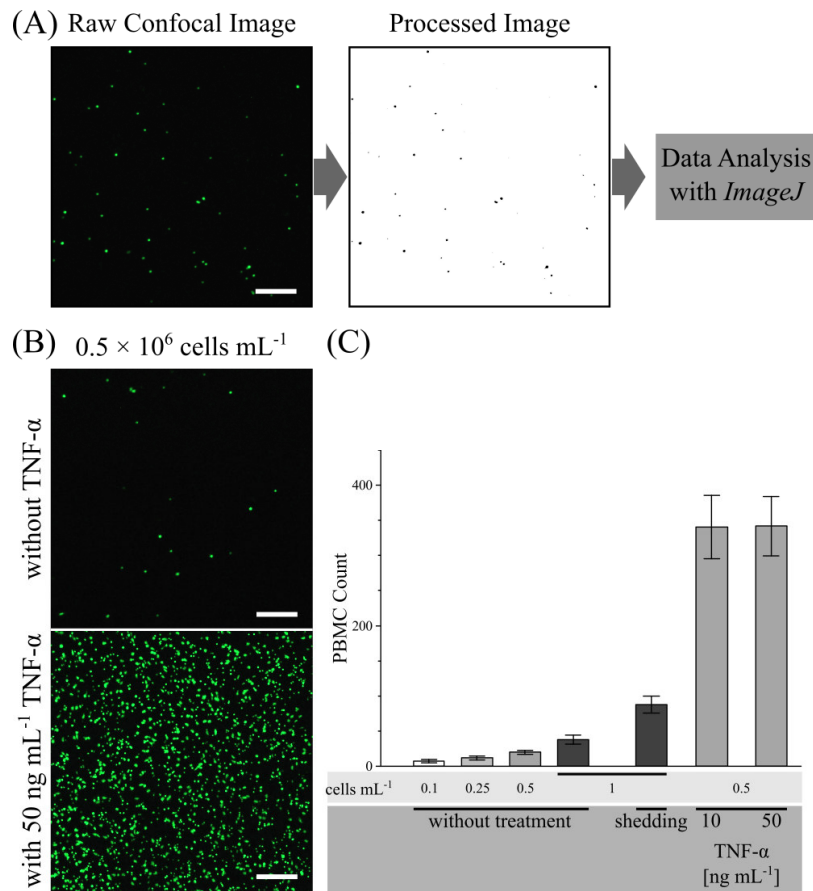
Subsequently, the glycocalyx thickness of non-fixed endothelial cells was estimated via confocal microscopy using Airyscan super-resolution mode. Orthogonal projections of Z-stacks demonstrate the native glycocalyx thickness being in the range of a few micrometers (2-4  $\mu\text{m}$ ), as shown in **Supplementary Figure S5**.



**Supplementary Figure S5.** Estimation of glycocalyx thickness under native conditions. Orthogonal projection and confocal images of HUVECs and iPSC-ECs after static culture for 96 h stained with WGA (glycocalyx, orange) and CMFDA (cytosol, green) under unfixed conditions. Scale bars: horizontal 50  $\mu\text{m}$ , vertical 2.5  $\mu\text{m}$ ).

#### 4 Evaluation of the PBMC adhesion assay

A peripheral blood mononuclear cell (PBMC) adhesion assay was established to investigate glycocalyx functionality. **Supplementary Figure S6A** illustrates the processing of the raw data and analysis. HUVECs were incubated with fluorescently labeled PBMCs, washed, fixed and subsequently imaged using fluorescence confocal microscopy. The images were processed with *ImageJ* (conversion from 16 to 8 bit, application of a gaussian filter,  $\sigma = 1 \mu\text{m}$  and manual thresholding ranging from 30 to 255) and analyzed using *ImageJ's Particle Analyzer*, counting the number of PBMCs per image (size: 30-125 pixel<sup>2</sup>).

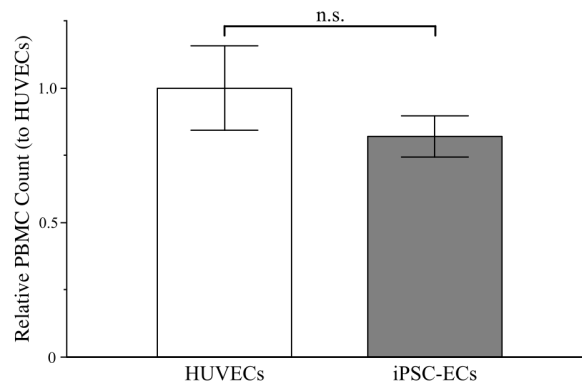


**Supplementary Figure S6.** Establishment of PBMC-assay to assess glycocalyx functionality. (A) Processing of the raw confocal image showing CMFDA-labelled PBMCs in green, by thresholding to create a binary image. The processed image was analyzed via *ImageJ particle analyzer* to obtain PBMC counts. (Scale bar: 200  $\mu\text{m}$ ) (B) Representative confocal images demonstrating the impact of a TNF- $\alpha$ -incubation (positive control) on PBMC adhesion to HUVECs after 96 h of static culture (Scale bars: 200  $\mu\text{m}$ ) (C) Influence of cell number as well as shedding of the glycocalyx (mechanical, TNF- $\alpha$  incubation) on adhesion of PBMCs to HUVEC monolayers after 96 h of static culture. Data are shown as mean  $\pm$  SEM (n=1).

Various PBMC concentrations were tested and ECs were differentially treated to validate the assay. As a positive control, HUVECs were incubated for 6 hours with 10 or 50 ng mL<sup>-1</sup> of the

proinflammatory cytokine TNF- $\alpha$ , which is known to increase leukocyte adhesion to ECs via upregulation of adhesion molecules (CAMs), and concomitant shedding of their glycocalyx [5, 6]. In addition, a concentration-dependent increase in adherent PBMCs was demonstrated. Finally, an apparent increase in PBMC adhesion after mechanical disruption of the glycocalyx via excessive pipetting demonstrated the assay's suitability to examine glycocalyx functionality.

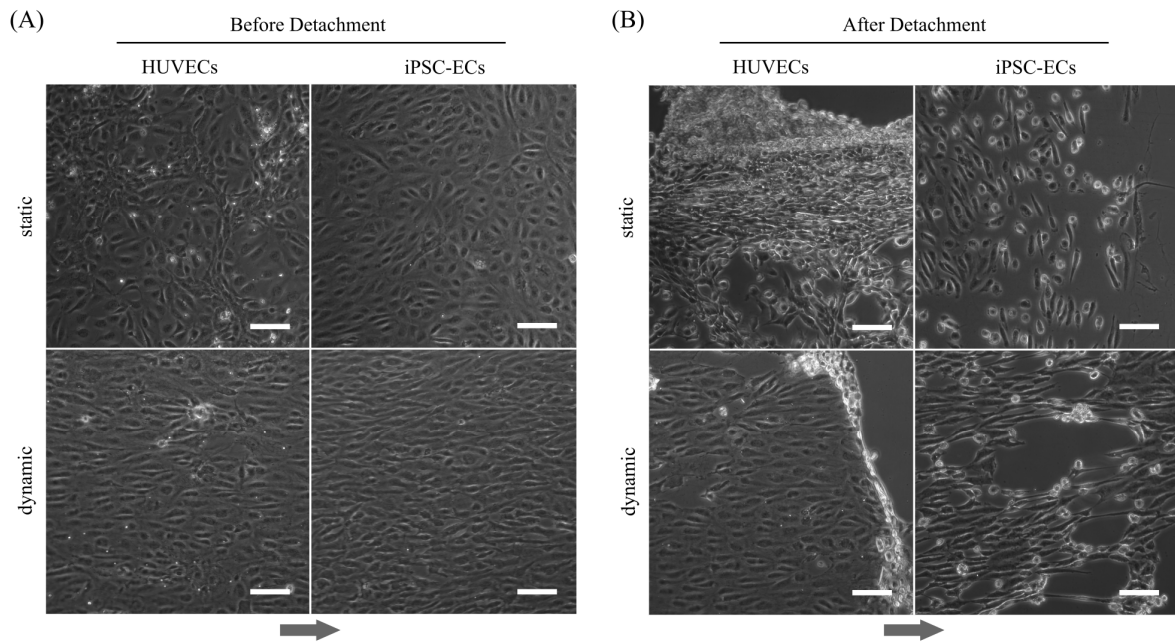
Subsequently, an analysis of PBMC adhesion to HUVECs and iPSC-ECs after static culture on PGE-coated PS as culture substrate was conducted. Results demonstrated no significant difference in leucocyte count on the monolayer surface for both cell types (**Supplementary Figure S7**).



**Supplementary Figure S7.** Comparison of relative PBMC adhesion to HUVECs and iPSC-ECs after 96 h of static culture. Relative data are presented as mean  $\pm$  SEM with respect to “HUVECs static” (n=4, Mann-Whitney Test).

## 5 Cell sheet detachment after 48 h

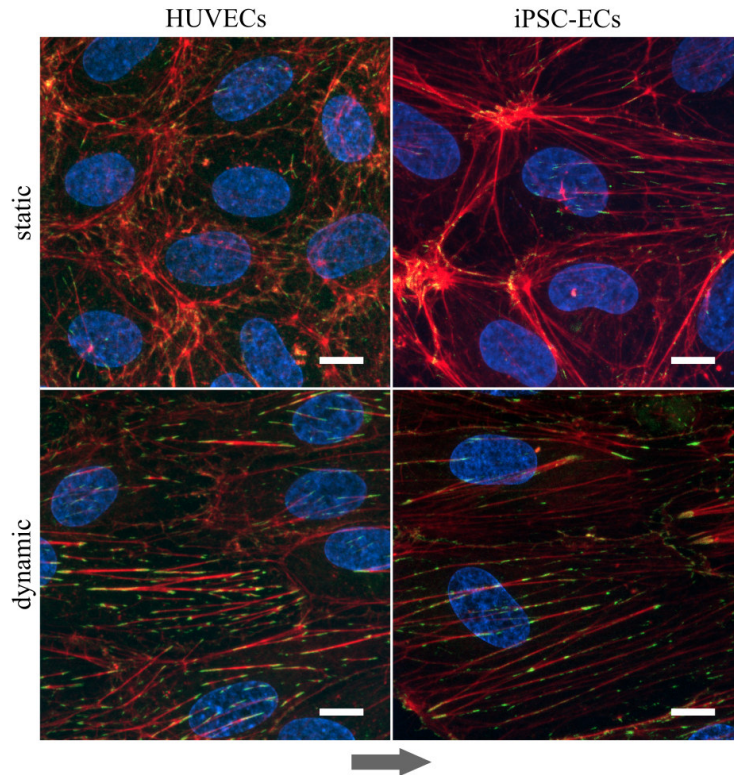
As previously shown in **Supplementary Figure S1**, the application of  $6.6 \text{ dyn cm}^{-2}$  for 48 h is sufficient for a pronounced alignment of both, HUVECs and iPSC-ECs on TCPS. Since one objective of this study was to generate confluent cell sheets of different endothelial cells, both under static (non-aligned) and dynamic (aligned) culture conditions, we attempted to detach cell sheets from PGE-coated PS first after 48 h. **Supplementary Figure S8A** demonstrates an elongation and alignment of HUVECs and iPSC-ECs on PGE-coated PS comparable to TCPS. By transferring the slides into room temperature PBS<sup>-</sup>, we triggered singularization and partial detachment of ECs under all culture conditions (**Supplementary Figure S8B**).



**Supplementary Figure S8.** Detachment of HUVECs and iPSC-ECs after 48h of static or dynamic culture. Phase contrast images were taken (A) before and (B) after (incomplete) detachment. (Arrow indicates flow direction. Scale bars:  $100 \mu\text{m}$ ,  $n=2$ ).

## 6 Formation of stress fibers due to fluid flow

The application of shear stress to ECs results in the formation of stress fibers, which are known to increase cellular adhesion to the underlying substrate [7]. **Supplementary Figure S9** displays confocal images of endothelial focal adhesions after static and dynamic culture conditions, stained with phalloidin (red) and vinculin (green), demonstrating the excessive formation of stress fibers after exposure to shear stress.



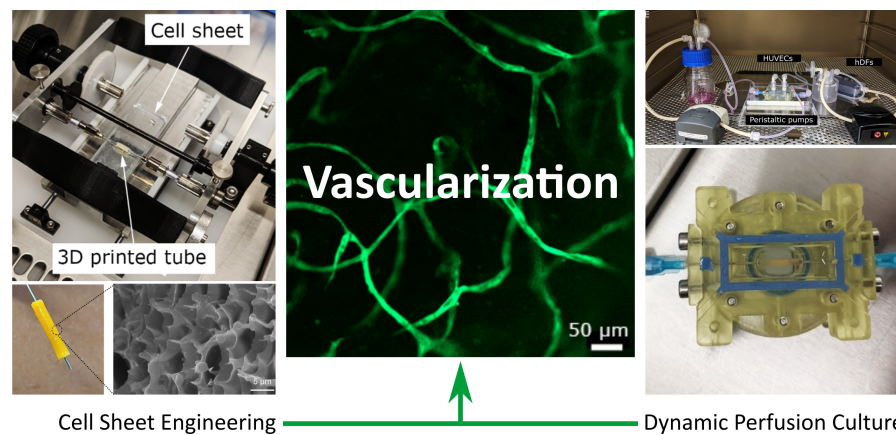
**Supplementary Figure S9.** Confocal images showing focal adhesions after static and dynamic culture of HUVECs and iPSC-ECs for 96 h. Cells were stained for phalloidin (red) and vinculin (green). Nuclei were counterstained with Hoechst 33342 (blue). (Arrow indicates flow direction. Scale bars: 10  $\mu$ m).

## 7 References

1. Rezakhaniha, R.; Ajianniotis, A.; Schrauwen, J.T.; Griffa, A.; Sage, D.; Bouten, C.V.; van de Vosse, F.N.; Unser, M.; Stergiopoulos, N. Experimental investigation of collagen waviness and orientation in the arterial adventitia using confocal laser scanning microscopy. *Biomech. Model. Mechanobiol.* **2012**, *11*, 461-473; DOI:10.1007/s10237-011-0325-z.
2. Xu, F.; Beyazoglu, T.; Hefner, E.; Gurkan, U.A.; Demirci, U. Automated and adaptable quantification of cellular alignment from microscopic images for tissue engineering applications. *Tissue Eng. Part C Methods* **2011**, *17*, 641-649; DOI:10.1089/ten.tec.2011.0038.
3. Huang, L.-K.; Wang, M.-J.J. Image thresholding by minimizing the measures of fuzziness. *Pattern Recognition* **1995**, *28*, 41-51; DOI:10.1016/0031-3203(94)e0043-k.
4. Brocher, J. "The BioVoxel image processing and analysis toolbox." Paper presented at the European BioImage Analysis Symposium 2015.
5. Mattila, P.; Majuri, M.L.; Mattila, P.S.; Renkonen, R. TNF alpha-induced expression of endothelial adhesion molecules, ICAM-1 and VCAM-1, is linked to protein kinase C activation. *Scand. J. Immunol.* **1992**, *36*, 159-165; DOI:10.1111/j.1365-3083.1992.tb03087.x.
6. Chappell, D.; Hofmann-Kiefer, K.; Jacob, M.; Rehm, M.; Briegel, J.; Welsch, U.; Conzen, P.; Becker, B.F. TNF-alpha induced shedding of the endothelial glycocalyx is prevented by hydrocortisone and antithrombin. *Basic Res. Cardiol.* **2009**, *104*, 78-89; DOI:10.1007/s00395-008-0749-5.
7. Franke, R.-P.; Gräfe, M.; Schnittler, H.; Seiffge, D.; Mittermayer, C.; Drenckhahn, D. Induction of human vascular endothelial stress fibres by fluid shear stress. *Nature* **1984**, *307*, 648-649.

### 3.4 *In vitro* vascularization of hydrogel-based tissue constructs via a combined approach of cell sheet engineering and dynamic perfusion cell culture

The study on *in vitro* vascularization was conceptualized by Dr. Laura Elomaa and Prof. Dr. Marie Weinhart. Dynamic culture chambers were designed, iteratively improved, characterized and manufactured by the author. The author conducted the experiments comprising dynamic culture with Dr. Laura Elomaa. The manuscript was written by Dr. Laura Elomaa and proof-read by Prof. Dr. Marie Weinhart.



Elomaa, L.; Lindner, M.; Leben, R.; Niesner, R.; Weinhart, M. *In vitro* vascularization of hydrogel-based tissue constructs via a combined approach of cell sheet engineering and dynamic perfusion cell culture. *Manuscript in preparation*.

# ***In vitro* vascularization of hydrogel-based tissue constructs via a combined approach of cell sheet engineering and dynamic perfusion cell culture**

Laura Elomaa<sup>1,§</sup>, Marcus Lindner<sup>1,§</sup>, Ruth Leben<sup>2</sup>, Raluca Niesner<sup>2</sup>, Marie Weinhart<sup>1,3</sup>

<sup>1</sup> Institute of Chemistry and Biochemistry, Freie Universität Berlin, Berlin, Germany

<sup>2</sup> Institute of the Leibniz Association, Deutsches Rheuma-Forschungszentrum (DRFZ), Berlin, Germany

<sup>3</sup> Institute of Physical Chemistry and Electrochemistry, Leibniz Universität Hannover, Hannover, Germany

§ Shared first authorship

E-mail: laura.elomaa@fu-berlin.de; marie.weinhart@pci.uni-hannover.de

## **Abstract**

Bioengineering of artificial tissue constructs requires special attention to their fast vascularization to provide the cells with sufficient nutrients and oxygen. We tackled the challenge of *in vitro* vascularization by employing a combined approach of cell sheet engineering, 3D printing, and cellular self-organization under dynamic maturation culture. A confluent cell sheet of human umbilical endothelial cells (HUVECs) was detached from a thermoresponsive cell culture substrate and transferred onto a 3D printed, perfusable tubular scaffold with the help of a custom-made cell sheet rolling device. Under indirect co-culture conditions with human dermal fibroblasts (HDFs), the cell sheet-covered vessel mimic embedded in a collagen gel containing additional singularized HUVECs started sprouting into the surrounding gel, while the suspended cells around the tube self-organized and formed a dense, lumen-containing 3D vascular network throughout the gel. The HDFs cultured below the HUVEC-containing cell culture insert provided angiogenic support to the HUVECs via molecular cross-talk without them competing for space with the HUVECs or inducing rapid collagen matrix remodeling. The resulting vascular network remained viable under these conditions throughout a 3-week cell culture period. This static indirect co-culture setup was further transferred to dynamic flow conditions, where the medium perfusion was enabled via two independently addressable perfusion circuits equipped with two different cell culture chambers, one hosting the HDFs and the other one the HUVEC-laden collagen gel. Using this system, we successfully connected the collagen-embedded HUVEC culture to a dynamic medium flow, and within one-week of the dynamic cell culture, we detected angiogenic sprouting as well as a dense microvascular network formation via HUVEC self-organization in the hydrogel. Our approach of combining a 3D printed and cell sheet-covered vascular precursor that retained its sprouting capacity together with the self-assembling HUVECs in a dynamic perfusion culture resulted in a vascular-like 3D network that we see as a critical step towards the long-term vascularization of bioengineered *in vitro* tissue constructs.

Keywords: Cell sheet rolling, perfusion culture, thermoresponsive surface, vascularization, vat photopolymerization

---

## 1. Introduction

Bioengineered *in vitro* tissue constructs are widely used both for regenerative medicine to aid tissue repair *in vivo* and for development of tissue models to replace or add on to existing *in vivo* animal models. However, growing a tissue mimic is still a great challenge as it requires sufficient vascularization to ensure efficient oxygen and nutrient supply to the cells. Several approaches to vascularize 3D tissue constructs have been introduced via various *in vitro* tissue engineering techniques,[1,2] including biofabrication of patterned channels of vascular endothelial cells inside a hydrogel structure[3–5] or via channel templating and reseeding with vascular endothelial cells throughout a tissue scaffold.[6] Even though these endothelialized channels can mature to biomimic vascular vessels within a native tissue, they can only reach a limited number of cells in the *in vitro* tissue construct, thereby requiring further microvascularization. This can be accomplished by implanting the *in vitro* engineered tissue construct into a living host system for a dedicated amount of time, after which ideally not only neovascularization within the transplanted tissue is observed but also its anastomosis to the host circulation.[7] However, even in *in vivo* conditions, the vascular in-growth from the host tissue triggered by the natural inflammatory and regenerative wound healing response is only several tenths of micrometers a day, which alone is not sufficient for the *in vivo* vascularization of thicker 3D tissue constructs.[8] Therefore, both the *in vivo* and *in vitro* vascularization of a whole bioengineered 3D tissue construct remains challenging.

An attractive approach towards the *in vitro* vascularization of 3D tissue constructs is to take advantage of cell sheet engineering, a technique originally introduced by Okano and coworkers.[9,10] In typical cell sheet engineering techniques, cells are cultured until the full confluency on a thermoresponsive surface that can undergo a transition from a hydrophobic, cell-adhesive state to a hydrophilic, cell-repellent state upon temperature decrease from 37 °C to room temperature.[11] When this confluent grown cell monolayer on a functional thermoresponsive substrate is transferred outside of a cell culture incubator, the whole cell sheet is mildly detached and can be harvested as a single layer together with its intact extracellular matrix.[12–15] Previously, a few groups have used cell sheets for building vascularized tissue constructs [16–19] as well as for the fabrication of large to medium diameter tissue engineered vascular grafts.[20,21] Asakawa *et al.*[16] induced vascularization of fibroblast sheets by sandwiching them together with a HUVEC sheet, and Sekine *et al.*[17] stacked together cell sheets derived from a co-culture of rat cardiac and endothelial cells. Besides endothelial cell sheets, also thin microstructured vascular smooth muscle sheets and patches have been produced for vascular tissue engineering applications.[18,19] Although piling up cell sheets with intended self-organization of endothelial cells into vascular structures is a feasible method for the fabrication of very thin tissue layers, it is yet insufficient for an effective vascularization of thicker tissue mimics.[17]

In contrast to patches made of thin cell sheet stacks, the use of self-standing cell sheet-covered vascular precursors with defined access ports could enable the *in vitro* vascularization of thicker tissue constructs under subsequent exposure to proangiogenic conditions. As an example of such vascular mimics of a medium diameter, Ahn *et al.*[20] fabricated non-endothelialized vascular tubes by manually wrapping a sheet of sheep vascular smooth muscle cells around an electrospun poly( $\epsilon$ -caprolactone) (PCL)/collagen tube (inner diameter: 4.75 mm). Similarly, Hibino *et al.* [21] applied a differentiated induced pluripotent stem cell sheet around a poly(glycolic acid) tube (inner diameter: 0.8 mm) to obtain tissue engineered vascular grafts. Furthermore, Kang *et al.* [22] wrapped a prevascularized co-culture sheet of human mesenchymal stem cells and HUVECs around a porous tricalcium phosphate scaffold (outer diameter: 4 mm), although this was not used as a vascular precursor but rather a vascularized bone tissue construct.

Within these studies, however, no long-term vascularization of 3D tissue constructs via the engineered, perfusable vascular mimics was explored

In our current study, we aimed to mimic a native vascular bed and vascularize thicker 3D collagen constructs by embedding a HUVEC sheet-covered perfusable vascular mimic into a collagen matrix together with singularized HUVECs. The small-diameter (outer/inner diameter: 1.5/0.5 mm) tubular scaffold was 3D printed with vat photopolymerization using a hybrid resin of gelatin methacryloyl (GelMA) and PCL-methacrylate (PCL-MA), and a confluent cell sheet of HUVECs was subsequently rolled around the tube using a customized rolling device. The formation of a vascular-like network of the HUVECs embedded in the collagen hydrogel was followed for three weeks in an indirect co-culture with human dermal fibroblasts (HDFs). Furthermore, the endothelialized vascular precursor was connected to a perfusion culture and the network formation under the dynamic culture was validated.

## 2. Material and Methods

### 2.1 Materials

Gelatin from porcine skin (gel strength 300, type A, 50–100 kDa, Aldrich),  $\epsilon$ -caprolactone (Aldrich), tin(II) 2-ethylhexanoate ( $\text{Sn}(\text{Oct})_2$ , Aldrich, 92.5%), di(trimethylolpropane) (diTMP, Aldrich, 97%), methacrylic anhydride (Aldrich, 94%), formamide (99.5%, Roth), ethyl(2,4,6-trimethylbenzoyl) phenylphosphinate (also known as Lucirin TPO-L) photoinitiator (Fluorochem), and Orasol Yellow 2RLN dye (Kremer Pigmente) were used as received. GFP-tagged HUVECs were purchased from Cellworks (Caltag Medsystems Company) and non-tagged HUVECs from Cellsystems<sup>®</sup>. HDFs were isolated from juvenile human foreskin (age between 5-18 months) with the ethical approval of the Ethics Committee at Charité Universitätsmedizin Berlin, Germany (EA1/081/13) using a collagenase/dispase-based protocol as published before.[23] High glucose Dulbecco's Eagle Medium (DMEM, Gibco<sup>®</sup>), fetal bovine serum (FBS, Biochrom), penicillin-streptomycin (Life Technologies), and supplemented Vasculife<sup>®</sup> vascular endothelial growth factor (VEGF) medium (LifeLine Cell Technology) were used in cell culture studies as received, if not otherwise noted. SpectraPor<sup>®</sup> dialysis tubing made from regenerated cellulose with a molecular weight cut-off (MWCO) of 3.5 kDa was purchased from Carl Roth GmbH + Co. KG (Karlsruhe). Colorimetric MTS solution (Abcam), Hoechst 33342 DNA-intercalating dye (Thermo Fisher), a LIVE/DEAD<sup>®</sup> cell viability kit (Invitrogen<sup>®</sup>), and green 5-chloromethylfluorescein diacetate dye (CMFDA, Thermo Fisher) were used in cell culture as described in the methods.

### 2.2 Synthesis of photocrosslinkable macromers, formulation of the resin, and 3D printing of a perfusable tube by vat photopolymerization

For the 3D printing of flexible and durable small-diameter tubes, a photocrosslinkable 3D printing resin of GelMA and four-arm PCL-MA for vat photopolymerization was formulated as reported in our previous study.[24] Briefly, the GelMA and PCL-MA in ratio of 70/30wt-% were dissolved in formamide (50wt-%) and was mixed with visible light sensitive 2 wt-% of ethyl(2,4,6-trimethylbenzoyl) phenylphosphinate photoinitiator and 0.05wt-% of Orasol Yellow dye to enable the highest spatial control over photocrosslinking. To 3D print a porous tube for cell sheet rolling, a CAD model of a hollow tube with an outside diameter of 1.5 mm, an inside diameter of 0.5 mm, and a length of 1 cm was designed using Rhinoceros 5 software. A digital light processing (DLP) 3D printer (Titan 2 from Kudo3D, Taiwan) was equipped with a UV-filtered projector (Acer Full HD 1080) that projects 1920x1080 pixels of visible light onto a bottom of a resin reservoir to crosslink a desired layer thickness. The crosslinking time was 25 s

for a 100  $\mu\text{m}$  layer and the temperature inside the printing hood was maintained at 32 °C with an additional set of a heater and a thermostat (IncuKit™ Mini, Incubator Warehouse). After 3D printing, the residual photoinitiator, non-crosslinked macromer, orange dye, and solvent was removed from the samples by extraction with ethanol for 3 days and water for 7 days.

### 2.3 Cell culture

Both GFP-labeled and unlabeled HUVECs (p 3-8) were cultured in Vasculife® VEGF endothelial medium with the Vasculife® supplements (2% of FBS), and HDFs (p 3-8) were cultured in high glucose Dulbecco's modified eagle medium (DMEM) mixed with 10% of FBS and 1% penicillin/streptomycin. Before seeding, all the cells were cultured under standard conditions (5% CO<sub>2</sub>, 37 °C, 95% humidity) until maximum of 70-80% confluency.

### 2.4 Cell sheet formation and the rolling process

For cell sheet formation, thermoresponsive poly(glycidyl methyl ether-*co*-ethyl glycidyl ether) (PGE,  $M_n$  = 30 kDa, monomer ratio of 1:3) functionalized with a short benzophenone anchor block was synthesized and self-assembled from a selective solvent as a monolayer on a polystyrene (PS) slide (7.5 cm x 2.5 cm x 0.1 cm) as described previously.[13,23] For the coating with PGE, the transparent PS slide was immersed in an aqueous/ethanolic polymer solution for 1 h (0.25 mg mL<sup>-1</sup> of PGE in 45% EtOH in H<sub>2</sub>O) and then irradiated it with UV-light (UV-KUB 2, KLOE) for 160 s. The coated slides were disinfected with 70% ethanol for 10 min and rinsed two times with cold PBS, after which a silicone frame (2 cm x 3 cm) was placed on the slide and HUVEC suspension (5.1 x 10<sup>5</sup> cells in 2 mL of medium) was pipetted inside the frame. The cells were cultured in the media supplemented with 2% FBS for the first day and with 10% FBS for further three days. After four days of cell culture, the cell-covered slide was transferred from warm medium into room temperature PBS for 10 min to partly detach the confluent cell layer from its edge. The sheet was then rolled around a 3D printed tube during the detachment process using a custom-made rolling device developed and prototyped with Ospin GmbH (Berlin, Germany). The GelMA/PCL tube was connected to the rolling device via a thin (diameter of 0.55 mm) stainless steel rod placed inside the tube that also enabled an easy transfer of the cell-covered tube from the rolling device to the collagen matrix. To prevent any contaminations, the rolling device was wiped before its use with 70% ethanol and all the parts in contact with the GelMA/PCL tube were disinfected for 15 min in 70% ethanol and rinsed twice with sterile PBS. The whole process of the cell sheet rolling and the subsequent adjustment of the tube to the dynamic perfusion chamber can be seen in **Supplementary Video S1**.

### 2.5 Network formation in a static culture of a 3D collagen construct

To form a cell-laden collagen solution (2.5 mg mL<sup>-1</sup>), acidic rat tail collagen solution (500  $\mu\text{L}$ , 5 mg mL<sup>-1</sup> in 20 mM acetic acid) was neutralized with 10x PBS (100  $\mu\text{L}$ ) and 0.1 M NaOH (110  $\mu\text{L}$ ) and was mixed with a HUVEC suspension in Vasculife® medium supplemented with 0.5% FBS (290  $\mu\text{L}$ , 2 x 10<sup>6</sup> cells mL<sup>-1</sup>). The vascular network formation was studied both in static and dynamic conditions (**Fig 1**). GFP-HUVECs were used in the static insert culture to enable easy detection of the cells in the collagen gel, while in the dynamic culture, the network formation was validated with the untagged HUVECs. For the static culture, the 3D hydrogels were prepared by first solidifying acellular collagen solution (160  $\mu\text{L}$ ) in a 12-well plate Transwell® insert (Corning® Costar®, 0.4  $\mu\text{m}$  pore size) for 30 min at 37 °C, after which the freshly rolled GFP-HUVEC-covered tube was carefully placed on the hydrogel surface together with

additional collagen/cell suspension (200  $\mu\text{L}$ ) (**Fig 1A**). The second collagen layer was solidified for 40 min at 37  $^{\circ}\text{C}$ . After the gelation, Vasculife<sup>®</sup> medium (500  $\mu\text{L}$ ) containing 0.5% of FBS was added on top of the gel and the insert was transferred to a 12-well suspension culture plate (Greiner Bio-One CELLSTAR<sup>®</sup>), where HDFs (25,000 cells  $\text{cm}^{-2}$ ) had been seeded in DMEM (1.5 mL) a day before. As controls, cell-laden collagen hydrogels without the rolled tube were prepared following the same protocol. The medium inside and outside of the insert was changed every 3 days.

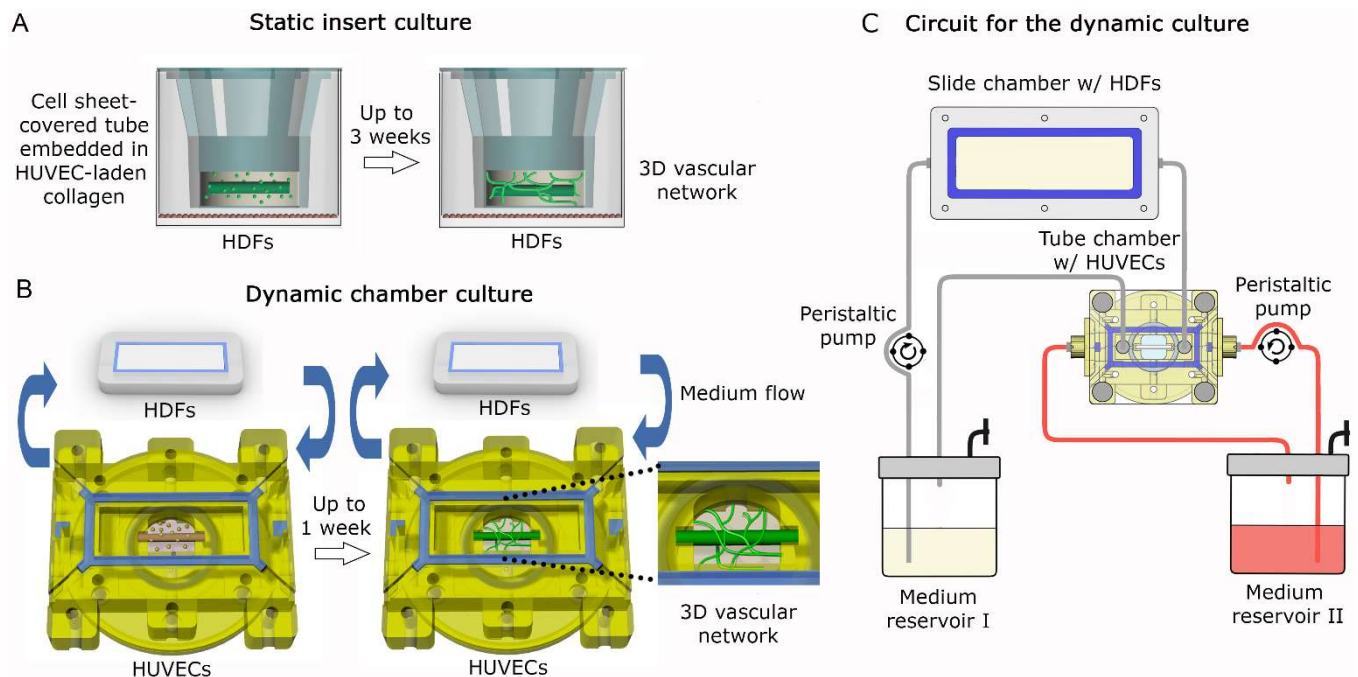


**Figure 1.** Schematic presentation of the respective setup to vascularize collagen hydrogels under A) static conditions in membrane insert culture and B) dynamic conditions in a 3D printed chamber that allows dynamic medium perfusion through the construct. C) Schematic drawing of the two circuits for the dynamic cell culture: While the grey circuit delivers HDF-conditioned medium to the suspended HUVECs in the gel to induce and assist their self-assembly into a microvascular network, the red circuit allows independent perfusion of the cell sheet-covered tubular scaffold.

## 2.6 Chamber design and dynamic culture for the network formation

For the dynamic vascularization culture, two different perfusion chambers were designed, one to host the HUVEC sheet-covered tube together with suspended HUVECs in collagen (called here a tube chamber) and the second to host the HDFs (*i.e.*, a slide chamber). The chambers were included in a row into a dynamic culture system comprising two bubble traps/medium reservoirs and two peristaltic pumps to generate two constant fluid flows that were controlled using an open-source hardware platform Arduino comprising a microcontroller (Arduino Uno Rev 3) (**Fig 1C**). A detailed description of the tube chamber design can be found in Supplementary Information (**Fig S1**). The tube chamber featured a confined collagen compartment (1 cm x 1 cm x 0.5 cm) with two sets of medium inlet and outlet connectors to enable medium flow both through the vascular tube and on top of the collagen hydrogel (**Fig 1B and 1C**), while the slide chamber featured a flat compartment for a HDF monolayer (7.7 cm x 2.6 cm x 0.1 cm) with one set of medium inlet and outlet connectors to allow medium flow on top of the cells (**Fig 1C**). The autoclavable and translucent tube chamber for hosting the collagen construct was CAD modelled with Rhinoceros<sup>®</sup> software and 3D printed with an Orange 30 SLA printer (Longer3D)[25] using a

biocompatible BioMed Amber Resin (Formlabs) with the burn-in time, range, and exposure time of 45.0 s, 0.25 mm, and 7.25 s, respectively. To enable real-time microscopy imaging of the HUVEC network formation in the collagen, the top lid of the tube chamber was made of transparent polycarbonate (Makroclear<sup>®</sup>, Arla Plast) and the center of the chamber bottom consists of a circular glass cover slip. Furthermore, the top lid of the chamber contains screw threads to connect an inlet and outlet silicone hose for the medium flow on top of the hydrogel. To construct the hydrogel, the bottom of the collagen compartment was first filled with the neutralized acellular collagen solution (500  $\mu\text{L}$ , 2.5  $\text{mg mL}^{-1}$ ) that was allowed to solidify at 37 °C for 30 min, after which the tube with a rolled HUVEC sheet was placed between two needles on top of the hydrogel together with HUVEC-laden collagen solution (200  $\mu\text{L}$ , 2.5  $\text{mg mL}^{-1}$ ,  $2 \times 10^6$  cells  $\text{mL}^{-1}$ ). As a control sample to the dynamically cultured gels, HUVEC-laden Transwell<sup>®</sup> inserts with HUVEC medium both inside and outside of the insert were prepared, like described above. After gelation of the collagen for 40 min at 37 °C, the tube in the dynamic samples was connected to perfusion of 8 mL of DMEM medium (0.7  $\text{mL min}^{-1}$ ) via syringe needles and silicone tubing (Tygon<sup>®</sup> 3350 and PharmaMed<sup>®</sup> BPT, Saint-Gobain Performance Plastic Corp.) using a peristaltic pump. Furthermore, the second set of inlet and outlet on top of the hydrogel were connected to perfusion with 8 mL of Vasculife<sup>®</sup> medium containing 0.5% of FBS (0.7  $\text{mL min}^{-1}$ ) that was first pumped through the slide chamber containing a TCPS slide (7.5 cm x 2.5 cm x 0.1 cm) on which HDFs (25,000 cells  $\text{cm}^{-2}$ ) had been seeded a day before. The slide chamber hosting the HDFs was fabricated by CNC-milling of the bulk polycarbonate (Makroclear<sup>®</sup>, Arla Plast). To ensure the contamination-free culture, the assembled circuits for the dynamic culture, excluding the peristaltic pumps, were autoclaved before their use.

### *2.7 Stiffness of the collagen hydrogel*

The elastic modulus of the acellular collagen hydrogels after 24 h incubation in PBS at 37 °C were studied with an oscillating rheometer (Kinexus pro+, Malvern Panalytical) using an 8 mm parallel plate geometry. First, the viscoelastic regime of wet samples ( $d = 8$  mm,  $h = 4$  mm) was determined with an amplitude sweep from a strain of 0.1% - 2% at 0.5 Hz, after which the storage modulus was measured with a frequency sweep from 0.1 - 3 Hz at 37 °C using a 0.5% strain. The final stiffness value was an average of three samples reported at the frequency of 0.5 Hz and the 0.5% strain.

### *2.8 Preparation of samples for microscopy*

The porous wall structure of the acellular 3D printed tubes was visualized by scanning electron microscopy (SEM, Hitachi SU8030, 15 kV) after first cutting 1-mm thick cross-sections of a lyophilized tube and making them electrically conductive by sputter coating them with a thin gold layer. To evaluate whether the HUVEC sheet covered the whole surface of the 3D printed tube after the cell sheet rolling, the tube was incubated in MTS solution (10% in PBS) for 10 min at 37°C to stain metabolizing, living cells with blue color, and after photographing, it was embedded in Tissue-Tek<sup>®</sup> cryomedia and shock-frozen by partly immersing the sample holder in liquid nitrogen. Thin layers (8  $\mu\text{m}$ ) of the frozen sample were sectioned with a cryotome at -16 °C (CM1510 S Leica Biosystems). The cryosections were then fixed with 4% PFA, stained with Hoechst 33342 (10  $\text{ng mL}^{-1}$ ) for 5 min at RT, and further visualized with a fluorescence microscope (Axio Observer Z1, Carl Zeiss). Self-organization and network formation of GFP-HUVECs in the collagen hydrogels were visualized during the course of the culture via fluorescence microscopy without additional staining and at the end point of the cell culture via confocal laser scanning microscopy (LSM800, Carl Zeiss) or 2-photon microscopy after fixation with 4% PFA and staining with Hoechst 33342. For the live/dead staining, the cells were incubated with fluorescein diacetate (FDA, 10

$\mu\text{M}$ ) and/or propidium iodide (PI,  $50 \mu\text{M}$ ) for 5 min before image acquisition via fluorescence microscopy. The untagged HUVECs used in the dynamic culture were fluorescence-stained with green CMFDA (1:1000 in PBS) for 15 min at  $37^\circ\text{C}$  before image acquisition with the confocal microscope to visualize the live cells.

### 2.9 Quantification of VEGF content in the HUVEC medium

The cell culture media from both static and dynamic culture were collected after a seven-day cell culture and stored at  $-20^\circ\text{C}$  for further analysis. The VEGF human ELISA kit (Invitrogen) was used following the manufacturer's protocol. Before the assay, the medium samples were diluted to half to maintain the VEGF concentration within the detection limit of the assay ( $15.6\text{-}1500 \text{ pg mL}^{-1}$ ). The light absorbance of the samples was determined at 450 nm and the values were translated to concentration using the provided VEGF standard samples.

### 2.10 Statistical analysis

The statistical significance of the gathered data was determined using a Kruskal-Wallis test followed by Dunn's multiple comparisons test ( $p < 0.05$ ), provided by Prism 9 software (GraphPad, USA).

## 3. Results

### 3.1 3D printing of porous tubes for cell sheet rolling

The small diameter tubes for cell sheet rolling were 3D printed using GelMA/PCL-MA hybrid resin that we have previously optimized for the visible light-based DLP printer (**Fig 2A**).[24] The concentration of 50% of GelMA/PCL-MA in formamide yielded a resin with suitable viscosity and crosslinking properties for the DLP when the printing temperature was maintained at  $32^\circ\text{C}$ . The hollow 3D printed tube with an outer diameter of 1.5 mm and an inner diameter of 0.5 mm (**Fig 2B**) was flexible and durable and therefore easy to handle. SEM imaging of a cross-section of the lyophilized tube revealed a highly microporous structure of the 3D printed material (**Fig 2C**), which is needed to secure medium and nutrient permeability of the tube wall.

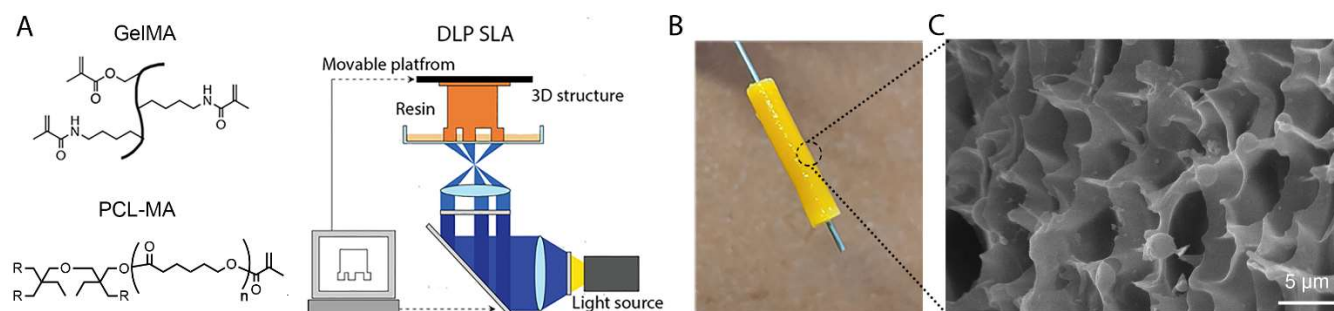


**Figure 2.** A) Schematic drawings of the chemical structures of GelMA and PCL-MA in the hybrid resin and the DLP 3D printer, B) photograph of a 3D printed GelMA/PCL-MA tube and C) a SEM image of a cross-section of the lyophilized tube showing the porosity of the tube wall.

### 3.2 Cell sheet detachment and rolling around the 3D printed tube

The 3D printed tubular scaffold was covered with a HUVEC cell sheet to form a vessel-mimic with a high cell seeding density. For the cell sheet, HUVECs were cultured on the thermoresponsive PGE-coated PS

slide for four days, until a dense, confluent monolayer was obtained. When the cell-covered slide was transferred from the medium in the incubator to PBS at RT, the sheet started to detach from its edges after 10 mins. An early attempt to detach the HUVECs at day 3 instead of a full 4-day culture resulted in holes in the cell sheet despite their full confluency (**Fig S2**), thereby emphasizing the importance of strong intercellular connections. The integrity of cell-cell contacts in the HUVEC monolayer at day 4 was verified by fluorescent staining of VE-Cadherin and ZO-1 tight junction proteins between the cells (**Fig S3**). Fluorescent staining of the GFP-HUVEC sheet with PI revealed only very few dead cells after its full detachment (**Fig 3B**). We used a custom-made rolling device shown in **Fig 3C** to efficiently transfer the polarized cell sheet during the detachment process onto the 3D printed tube with the luminal side of the sheet facing the scaffold. Turning the 3D printed GelMA/PCL-MA tube several times on top of the detaching cell sheet relocated the cells as a homogeneous, intact layer onto the tube surface. Visualization of the cells via a brief exposure of the tube to blue MTS solution proved its full coverage with viable cells as indicated by the dark blue color of the cells (**Fig 3D**). Furthermore, fluorescence microscopy of cryo-cuts of the cell-covered tube revealed a thin continuous cell layer on the tube surface (**Fig 3E**).

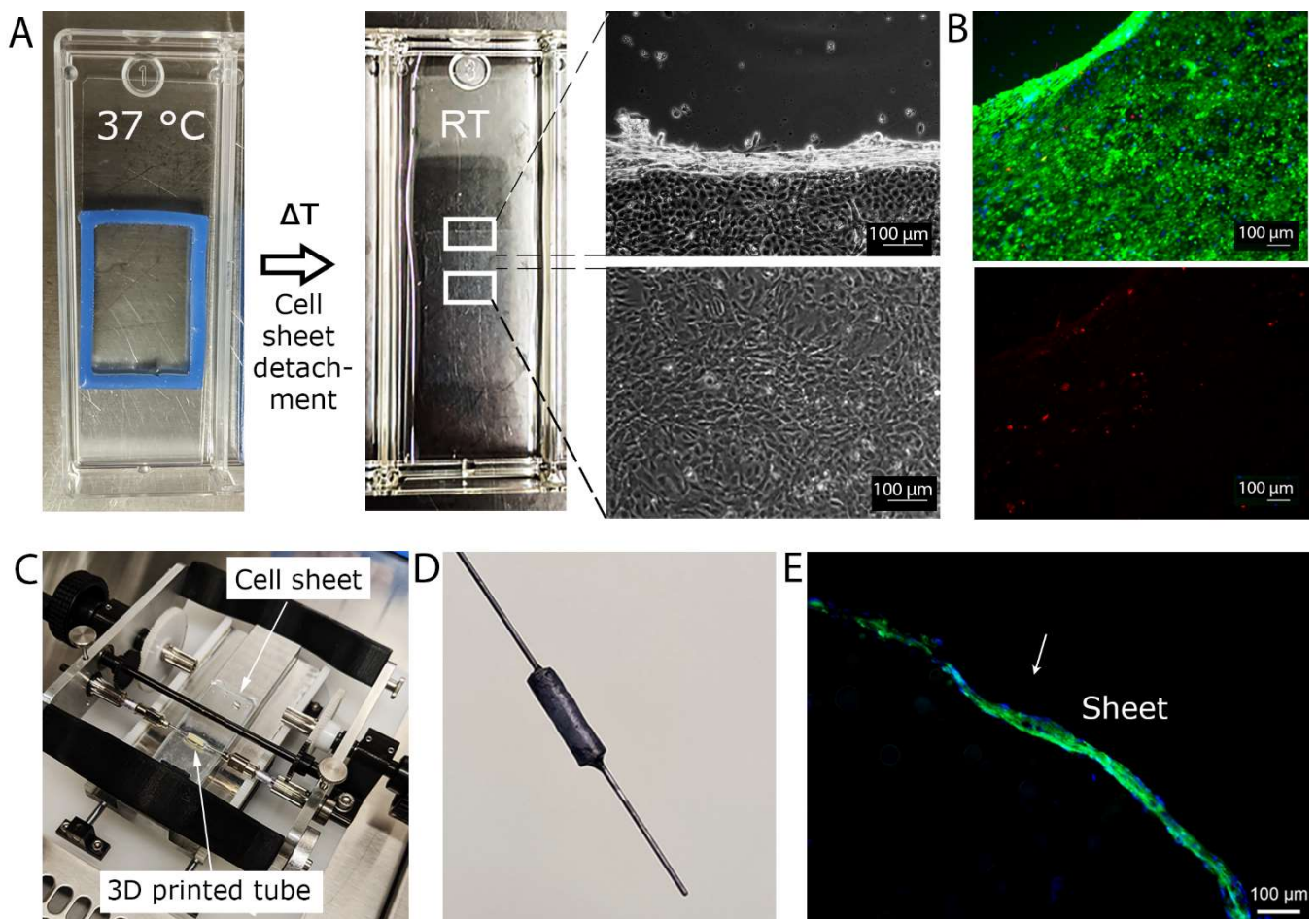


**Figure 3.** A) Representative photographs of the cell sheet before and after the cell sheet detachment and microscopy images of the partial detachment of the sheet at its upper edge. B) Fluorescent microscopy images of a PI-stained GFP-HUVEC sheet showing only very few dead cells (red color). C) Photograph of the custom-made rolling device used for transferring the cell sheet from a thermoresponsive slide onto the tube and D) a photograph of the MTS-stained (blue) cell sheet around the tube. E) Representative fluorescence microscopy image of a cryo-cut of the cell-covered tube showing a GFP-HUVEC monolayer (green) and cell nuclei (blue) on the tube surface.

### *3.3 Vascular network formation in a statically cultured 3D collagen construct*

Before combining the cell-sheet covered vascular vessel-mimic with self-organizing single HUVECs, we studied the network formation capacity of collagen-embedded HUVECs in a membrane insert under indirect co-culture conditions with HDFs. Previously, we have observed that the presence of HDFs outside of the insert is essential to maintain the long-lived vascular-like network structure of HUVECs seeded in 2D between two collagen layers.[26] Here, we studied the vascular network formation of suspended GFP-HUVECs encapsulated homogeneously within a 3D collagen gel. For that, the network formation of the cells was imaged with fluorescent confocal microscopy after fixing the samples at predetermined time points (**Fig 4A**). As seen in the images, the cells started organizing into a network soon after the seeding, with first morphological indications at day 3. Within the first week, an interconnected HUVEC network had formed, and during the full 3-week culture time, this vascular-like structure first became denser at day 14 and finally developed into a more defined network with longer tubular structures and less thick interconnections. Without the HDFs, no formation of HUVEC network was detected (data not shown). The collagen concentration of  $2.5 \text{ mg mL}^{-1}$  with the elastic modulus of  $246 \pm 4 \text{ kPa}$  required no further stiffness adjustment of the hydrogels to enable efficient HUVEC migration and vascular-like network formation. The resulting vasculature sprouted throughout the 3D collagen hydrogel and maintained its stability until the end of the 3-week study. Two-photon microscopy of the Hoechst-stained cells at day 21 allowed closer imaging of the network (**Fig 4B**), revealing a hollow lumen structure in this network that expanded up to 1 mm in the z-range (**Fig 4C**).

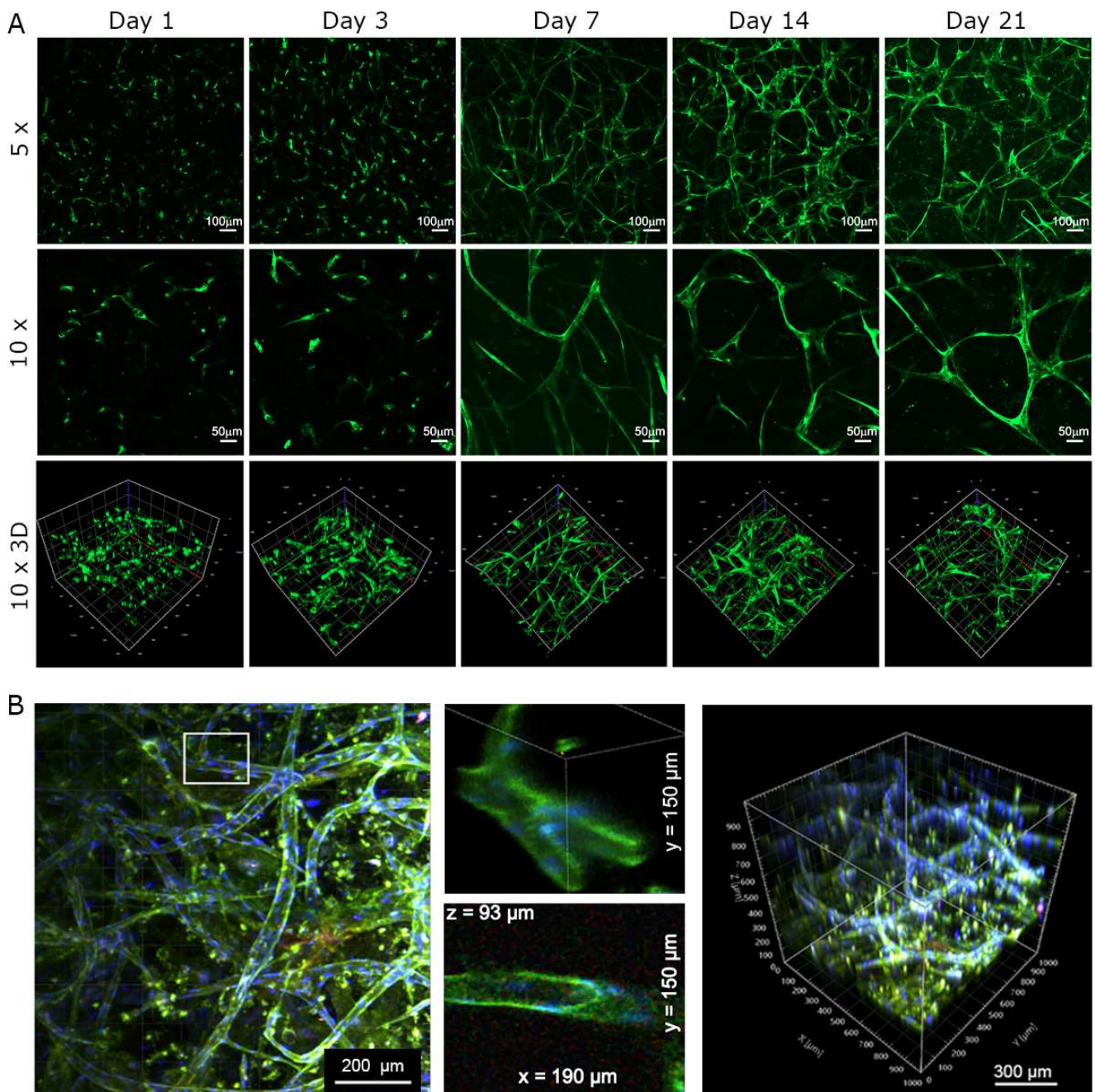


**Figure 4.** A) Representative confocal microscope images revealed the vascular-like network formation of GFP-HUVEC cells in the collagen matrix, illustrated by single z-layers (5  $\mu\text{m}$ ) of the fixed hydrogels (5x and 10x) and by z-stacks of the whole hydrogels (10x 3D). B) Two-photon microscope images of the network at day 21, revealing a hollow lumen of the formed vascular structures.

### 3.4 Vascular sprouting from the rolled sheet and combined vascularization from the tube and the surrounding cells

After proving the vascularization capacity of the collagen-embedded single HUVECs under indirect co-culture conditions, we proceeded with embedding the cell sheet-covered tube into a collagen gel. First, we studied the sprouting capacity of the rolled HUVEC sheets in the collagen hydrogels without added singularized HUVECs under indirect co-culture with HDFs (**Fig 5A**). With brightfield microscopy, we detected vascular sprouts protruding from the tube into the collagen matrix (**Fig 5B**), while the two-photon

microscopy enabled a closer look on the sprouting, revealing a thin cell layer on the tube surface and a bifurcating vascular sprout starting from this layer (**Fig 5C**). Encouraged by the detected sprouting capacity of the GFP-HUVEC sheet, we embedded the rolled cell sheet in a GFP-HUVEC-laden collagen gel. The network formation around the tube under indirect co-culture was imaged via fluorescence microscopy (**Fig 5D**). Even though the vicinity of the vessel-mimicking tube could not be zoomed in because of its bright fluorescence, the images showed the vascular-like network formation within the gel in a similar manner to the hydrogels without an embedded tube. An interconnected vascular-like network was detected throughout the collagen gel after seven days, and the network matured and became stronger within the full 3-week culture.

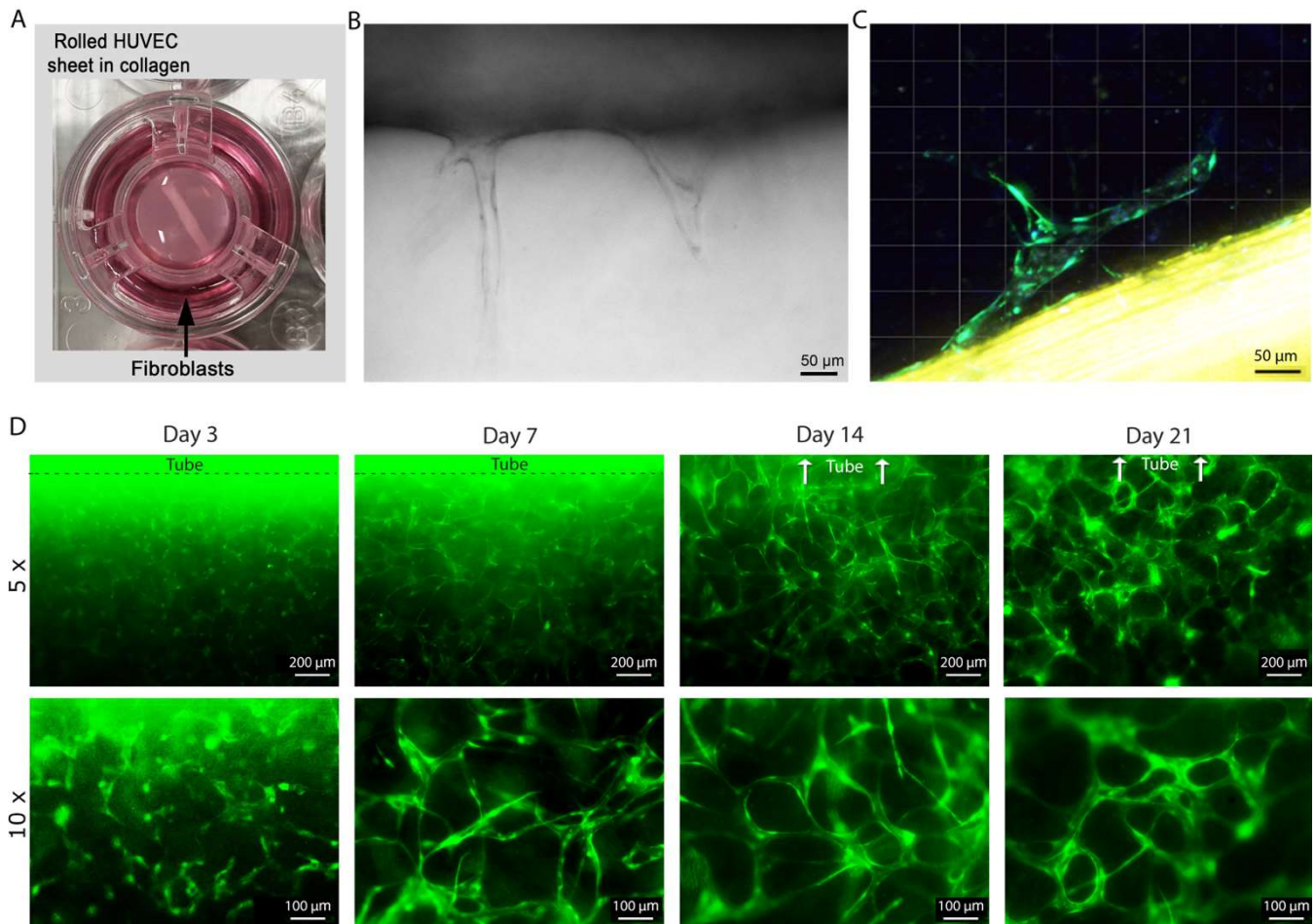


**Figure 5.** A) GFP-HUVEC-covered tubular scaffold embedded in a collagen matrix in a membrane insert; B) Brightfield and C) two-photon fluorescence microscopy image of sprouting cells from the rolled sheet. D) Representative fluorescence microscopy images of the collagen gels comprising tube and suspended single GFP-HUVECs, revealing vascular-like network formation around the central vessel-mimicking tube.

### 3.5 Dynamic perfusion of the collagen constructs

After establishing suitable conditions for the 3D vascularization in a static insert culture, we proceeded to demonstrate the physiologically more relevant vascularization in a dynamic perfusion culture. By connecting two separate chambers in a row in one circuit, the HUVECs could be cultured at a longer spatial distance from the HDFs. The tube chamber was designed to allow real-time visualization of the hydrogel-embedded cells through its transparent top and bottom lids (**Fig 6A**). Similar to the static

experiments in membrane inserts, the cell sheet-covered tube was placed on top of an acellular collagen gel in the chamber together with cell-laden collagen solution around the tube (**Fig 6B**). The hydrogel-containing tube chamber was connected to the first perfusion pump to provide constant medium flow through the cell-covered central tube as well as to the second perfusion pump (both pumps  $0.7 \text{ mL min}^{-1}$ ) to provide constant medium flow on top of the collagen gel (**Fig 6C**). As the presence of HDFs was seen to be necessary to maintain the vascular-like network, our new dynamic culture system enabled the continuous conditioning of the HUVEC medium with HDFs by perfusing the medium through the slide chamber before reaching the collagen gel (**Fig 6D and 6E**). Brightfield microscopy imaging revealed no difference in the morphology and density of the HDFs cultured in DMEM medium, as done in the static culture, versus in 0.5% FBS Vasculife<sup>®</sup> VEGF medium used in the dynamic circuit (**Fig S4**). Only slow diffusion of red medium from inside the cell-covered central tube to the surrounding gel was detected, indicating at the same time the desired porosity of the tube wall and the absence of leakages in the system.

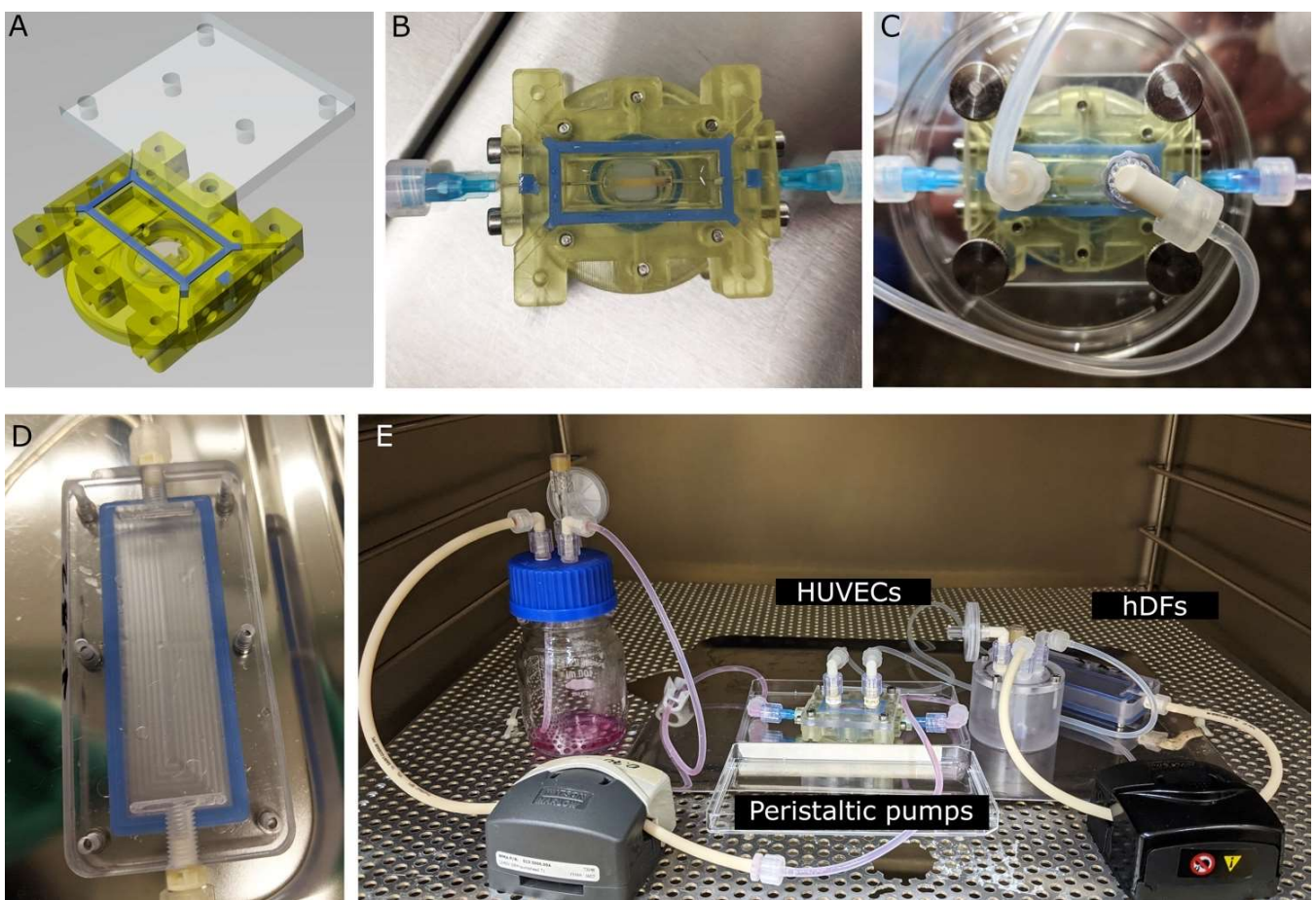


**Figure 6.** A) CAD model of the tube chamber and B) photograph of the 3D printed chamber filled with HUVEC-laden collagen gel and a HUVEC sheet-covered tube connected to a medium perfusion. C) The hydrogel-containing tube chamber was further covered with a transparent plastic lid and connected to the second medium flow circuit from above, additionally passing through the HDF-containing slide chamber to condition the medium with proangiogenic factors. D) Photograph of the slide chamber hosting the HDFs and E) the whole dynamic culture system comprising the HUVEC-hosting chamber connected to two independently addressable circuits, one connected to the tube inside the chamber (red DMEM medium) and one connected to the top of the chamber (transparent conditioned HUVEC medium via passing through the HDF slide chamber).

In the dynamic culture, the HUVEC-laden collagen gel ( $2 \times 10^6$  cells  $\text{mL}^{-1}$ , initial height of 2 mm) was maintained for one week under the constant flow ( $0.7 \text{ mL min}^{-1}$ ) of HDF-conditioned medium. Some visible shrinkage of the collagen gel was observed both in the dynamic and static culture, which was likely due to the traction forces applied by the networking HUVECs as well as the cell-mediated hydrogel remodeling. While in the absence of HDFs, the HUVECs did not form any network in this setup (data not shown), the 7-day dynamic cell culture under indirect co-culture with fibroblasts resulted in an interconnected vascular-like network similar to the static control in the HUVEC medium (**Fig 7A**). At the same time, an increased collagen thickness of above 2 mm resulted in poor network formation both in static and dynamic culture (**Fig S5**). In the dynamic culture, the HDFs formed a visibly thicker layer on the cell culture slide compared to the static culture, while the live/dead staining of the HDFs at the end point revealed only a few dead cells both in the dynamic and static culture (**Fig 7B**), indicating that the molecular crosstalk with HUVECs during the vascular-like network formation as well as the dynamic flow did not severely interfere with their viability. The ELISA growth factor assay of the cell culture medium at day 7 revealed a clearly higher VEGF content in the dynamic cell culture circuit compared to the static culture inside the insert, even though the increased VEGF content required the presence of both the HDFs and HUVECs in the circuit. The absence of one of them led to lower VEGF concentrations resembling the ones detected in VEGF-supplemented media in the beginning of the study at day 0 (**Fig 7C**).

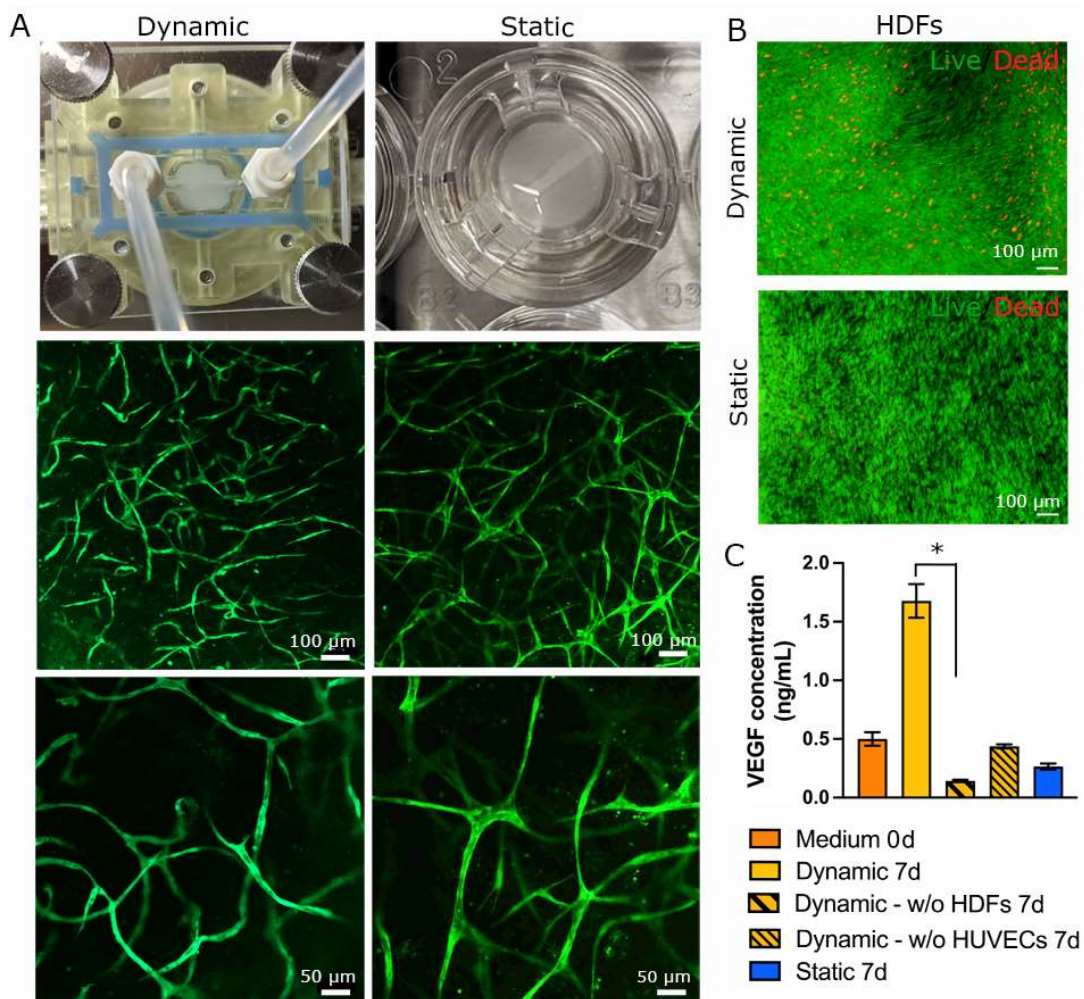


**Figure 7.** A) Representative fluorescence confocal microscopy images of the HUVEC-laden collagen gels, revealing the formation of an interconnected vascular-like network within a 7-day culture in the dynamic tube chamber

similar to a static insert control. B) Fluorescence microscopy imaging of the live (green)/dead (red) stained HDFs, showing their full confluency and high viability after the 7-day culture under both dynamic and static conditions. C) The amount of VEGF in the cell culture medium, showing highly increased amount in the dynamic culture at day 7, when both the HUVECs and HDFs were present in the circuit (error bar represent SD;  $n = 3$ ; \*indicates statistical significance ( $p < 0.05$ )).

#### 4. Discussion

Formation of an interconnected 3D vascular network has been a long-remaining challenge in tissue engineering, and due to its critical role in developing *in vitro* tissue constructs, new approaches are still urgently needed. In our vascularization strategy, we relied simultaneously on 3D printing, cell sheet engineering, and self-organization of endothelial cells into a vascular-like network under proangiogenic conditions. First of all, to provide a 3D collagen hydrogel with a central, perfusable blood vessel mimic to aid its vascularization, we rolled a confluent HUVEC sheet around a small-diameter (1.5 mm) tubular scaffold that was 3D printed of a GelMA/PCL-MA hybrid resin with a DLP printer. The GelMA-containing resin was previously developed and optimized by us for the vat photopolymerization to enable fast and reproducible fabrication of flexible, nutrient permeable, and biodegradable scaffolds that support cell adhesion and proliferation.[24] The reactive blending of GelMA resin with PCL-MA enhanced the stability of the material to be durable enough for the cell sheet rolling and for the long-term medium perfusion. By matching the inner diameter of the 3D printed tubular scaffold (0.5 mm) to tightly fit the needle diameter (0.55 mm), we ensured a leakage-free connection of the tube to the perfusion chamber via the syringe needles. The adjustable biodegradation of the hybrid GelMA/PCL-MA material shown in our previous work[24] allows the gradual diminishing of the mechanical support from the tube when the vascular vessel is maturing. In the establishing phase of our current work, long-term stability (> 3 weeks) of the material was applied.

For the fabrication of the cell sheets, we used PS slides covered with a thin layer (~5 nm) of a thermoresponsive PGE polymer previously developed and synthesized by our group.[23] Due to the carefully designed phase transition temperature in aqueous media and the fine-tuned surface coating parameters, the polymer coating remained hydrophobic and highly cell adhesive as long as it was maintained in the cell culture incubator at 37°C, while the partial cell sheet detachment could be detected after 10 min after transferring the slide to PBS at RT. Instead of using commercially available poly(*N*-isopropylacrylamide) (PNIPAM)-coated thermoresponsive cell culture dishes, such as Upcell® plates, the application of the PGE coating enabled the geometry-independent fabrication of custom size thermoresponsive slides for the cell sheet rolling. Notably, these PGE-coated slides did not require any additional coating with cell adhesion promoters to allow or improve attachment and growth of HUVECs. To enable an easy and efficient transfer of the cell sheet, we designed and prototyped a custom-made device for rolling and translocating the sheet to the outer surface of a tubular GelMA/PCL-MA-based scaffold. The wall-less slide geometry of the thermoresponsive cell culture substrate was needed to allow its placement underneath the manually-driven, rotating scaffold, ensuring pressure-free contact between the cell sheet and the scaffold as well as manual adjustment of the rotation speed of the tube (**Video S1**). Compared to the manual wrapping techniques reported elsewhere,[20,22] the rolling device enabled a fast and reliable transfer of the sheet as soon as the edges of the sheet had detached, resulting in a homogeneous HUVEC-containing layer around the tube, while the hybrid material used for the 3D printing of the tube ensured efficient and sustained adhesion between the scaffold and the transferred cells.

For the sake of potential long-term maturation of our bioengineered vessel-mimics, it was important to preserve the high viability and sprouting capacity of the HUVECs in the rolled cell sheet. The fluorescent staining revealed only very few dead cells in detached HUVEC sheets (**Fig 3**), indicating that the thermally-triggered, non-enzymatic detachment did not negatively impact the cell viability, as also previously reported by us and the others.[23,27] Importantly, bifurcating sprouts were detected in brightfield and fluorescent images (**Fig 5**) to protrude from the HUVEC-covered tube when embedded in collagen in the indirect co-culture with HDFs. Similar microvascular sprouting has been previously detected to start from an electrochemically deposited HUVEC layer in a collagen-based scaffold as well as from a HUVEC layer growing on dextran-coated beads in fibrin gels.[28] However, we showed for the first time that also HUVEC sheets that have been cultured on thermoresponsive substrates and non-enzymatically detached by a thermal trigger can retain their sprouting capacity. This makes the cell sheet engineering extremely useful for *in vitro* vascularization approaches, as with a cell sheet, a confluent monolayer of endothelial cells can be deposited at once in a highly defined manner into a 3D hydrogel. However, as we did not expect the sprouting from the cell-covered tube to vascularize the whole 3D collagen gel, we combined it with self-organizing suspended HUVECs to form a dense vascular bed around the tube in the hydrogel. To achieve the latter, we adapted the recently established indirect co-culture conditions of HUVECs with proangiogenic growth factor-producing HDFs[26] for the culture of a 3D vasculature. With the help of the HDFs, we obtained a dense, lumen containing vascular-like network that maintained its interconnected structure during the whole 3-week cell culture period. As expected from previous studies,[26,29] no HUVEC network was formed in the absence of HDFs. This was presumably related to the rapid loss in activity of the unbound medium-supplemented VEGF and fibroblast growth factor (FGF) in the presence of endothelial cells,[30] which is why the HDFs were needed to constantly supplement the medium with proangiogenic growth factors, especially VEGF and FGF, that are known to be essential for *in vitro* formation of a lumenized vascular network.[31] Differing from elsewhere published 3D HUVEC networks that were obtained in a direct co-culture approach with human adipose tissue derived stromal cells,[32,33] the HUVEC network formation in our study was purely supported by the molecular cross-talk with the HDFs, thereby lacking any direct cell-cell contacts between the two cell types that could interfere with each other's growth. The resulting vascular-like network expanded throughout the hydrogel (**Fig 4**).

To enable physiologically relevant dynamic medium flow within the vascularizing collagen hydrogels, we CAD modelled and 3D printed an autoclavable perfusion chamber that can be connected to two independent medium flows using peristaltic pumps, one providing medium through the tubular cell sheet-covered scaffold to mimic blood stream and another HDF-conditioned medium to the top surrounding of the collagen gel to ensure the constant presence of proangiogenic growth factors in the circuit. When setting up the dynamic culture system, 3D printing enabled us both to fabricate the hollow scaffold for the central vascular mimic as well as to rapid prototype the CAD modeled, adjustable cell culture chambers. Furthermore, with the Arduino microcontroller, we were able to control several peristaltic pumps at the same time. Contrary to the static insert culture, where the HUVECs and HDFs located in direct proximity, although membrane-separated, in the dynamic circuit the cells were cultured in different chambers. Despite the increased distance of these two cell types, an interconnected vascular-like network formed similar to the static culture within a 7-day dynamic culture period as long as the thickness of the HUVEC-laden collagen gel was below 2 mm (**Fig S5**). This indicated flexibility in the distance between the HUVECs and HDFs in their indirect co-culture, thereby enabling more versatile cell culture setups

compared to the static cell culture inserts. This is important especially when the physical proximity of HDFs and network-forming HUVECs is not desired or practical. To confirm the quality of the conditioned medium in this setup, we used an ELISA growth factor assay to exemplarily study the VEGF content of the medium after the 7-day cell culture, revealing a strong increase in its amount under the applied dynamic flow compared to the static culture conditions. This was primarily assigned to the higher surface area of the confluent HDF layer in the dynamic culture (19 cm<sup>2</sup> instead of the 3.8 cm<sup>2</sup>). However, within the one-week cell culture, the higher VEGF content did not increase the density of the HUVEC network compared to the static conditions, indicating that VEGF among the myriad of HDF-derived growth factors is not the limiting one for the observed network formation. In our current proof-of-concept study, we did not focus on the long-term maturation of the vasculature in the dynamic culture, and therefore also the anastomosis of the cell-covered central tube into the surrounding vascular network remains to be studied in detail. However, by combining these two elements in one system with the help of cell sheet engineering and 3D printed scaffolds and perfusion chambers, we took an important step toward the longer-term goal of a perfusable vascular network that can provide cells with nutrients for prolonged time within a bioengineered 3D tissue construct.

## 5. Conclusions

We successfully vascularized 3D hydrogel constructs by combining a rolled HUVEC sheet as a central vessel mimic with surrounding self-assembling HUVECs in a collagen matrix. In the resulting hydrogels indirectly co-cultured with HDFs, the HUVECs organized into an interconnected vascular-like network throughout the 3D matrix, while the cell sheet-covered tube sprouted to the vascularized gel. The central vascular vessel with its preserved sprouting capacity provided defined access ports to enable the connection of the hydrogel construct to a dynamic medium flow. Two independently addressable and fully dynamic medium flow circuits promoted the formation of an interconnected 3D vascular-like network in collagen gel even when the proximity of HDFs in the static culture conditions was replaced by their remote location under the dynamic conditions. As all the parts in our dynamic circuit system are easily available with relatively low costs, we hope to help readers gain an access to dynamic cell culture circuits without need for high-cost investments in bioreactors. Our achievements in this study pave the way to bioengineering of vascularized tissue constructs, in which the cells can be provided with nutrients all over a thicker 3D matrix for an extended time period.

## Acknowledgements

The authors thank German Federal Ministry of Education and Research (FKZ: 13N13523; MW, LE), Dahlem Research School and the Focus Area “Nanoscale” at Freie Universität Berlin (LE) as well as the Helmholtz Graduate School for Macromolecular Bioscience (ML, MW) for the financial support of the current work as well as the Core Facility BioSupraMol supported by Deutsche Forschungsgemeinschaft for the use of SEM facilities. Furthermore, Dr. Daniel Stöbener is thanked for providing the PGE polymer for the thermoresponsive coatings of the cell culture slides. MW is grateful to constant support from the institute of pharmacy (Prof. B. Kleuser, Prof. M. Schäfer-Korting and Prof. S. Hedtrich) at Freie Universität Berlin throughout this project.

## References

- [1] Lopes S V., Collins M N, Reis R L, Oliveira J M and Silva-Correia J 2021 Vascularization Approaches in Tissue Engineering: Recent Developments on Evaluation Tests and Modulation *ACS Appl. Bio Mater.* **4** 2941–56
- [2] Elomaa L and Yang Y P 2017 Additive Manufacturing of Vascular Grafts and Vascularized Tissue Constructs *Tissue Eng. - Part B Rev.* **23**
- [3] Kang Y, Mochizuki N, Khademhosseini A, Fukuda J and Yang Y 2015 Engineering a vascularized collagen-b-tricalcium phosphate graft using an electrochemical approach *Acta Biomater.* **11** 449–58
- [4] Tsai M-C, Wei S-Y, Fang L and Chen Y-C 2022 Viscous fingering as a rapid 3D patterning technique for engineering cell-laden constructs *Adv. Healthc. Mater.* **11** 2101392
- [5] Colosi C, Shin S R, Manoharan V, Massa S, Costantini M, Barbetta A, Dokmeci M R, Dentini M and Khademhosseini A 2016 Microfluidic Bioprinting of Heterogeneous 3D Tissue Constructs Using Low-Viscosity Bioink. *Adv. Mater.* **28** 677–84
- [6] Miller J S, Stevens K R, Yang M T, Baker B M, Nguyen D-H T, Cohen D M, Toro E, Chen A A, Galie P A, Yu X, Chaturvedi R, Bhatia S N and Chen C S 2012 Rapid casting of patterned vascular networks for perfusable engineered three-dimensional tissues. *Nat. Mater.* **11** 768–74
- [7] Hegen A, Blois A, Tiron C E, Hellesøy M, Micklem D R, Nör J E, Akslen L A and Lorens J B 2011 Efficient in vivo vascularization of tissue-engineering scaffolds *J. Tissue Eng. Regen. Med.* **5** e52–62
- [8] Clark E R and Clark E L 1939 Microscopic observations on the growth of blood capillaries in the living mammal *Am. J. Anat.* **64** 251–301
- [9] Yamada N, Okano T, Sakai H, Karikusa F, Sawasaki Y and Sakurai Y 1990 Thermo-responsive polymeric surfaces; control of attachment and detachment of cultured cells *Die Makromol. Chemie, Rapid Commun.* **11** 571–6
- [10] Yang J, Yamato M, Kohno C, Nishimoto A, Sekine H, Fukai F and Okano T 2005 Cell sheet engineering: Recreating tissues without biodegradable scaffolds *Biomaterials* **26** 6415–22
- [11] Kobayashi J, Kikuchi A, Aoyagi T and Okano T 2019 Cell sheet tissue engineering: Cell sheet preparation, harvesting/manipulation, and transplantation *J. Biomed. Mater. Res. Part A* **107** 955–67
- [12] Heinen S, Rackow S, Cuellar-Camacho J L, Donskyi I S, Unger W E S and Weinhart M 2018 Transfer of functional thermoresponsive poly(glycidyl ether) coatings for cell sheet fabrication from gold to glass surfaces *J. Mater. Chem. B* **6** 1489–500
- [13] Stöbener D D, Hoppensack A, Scholz J and Weinhart M 2018 Endothelial, smooth muscle and fibroblast cell sheet fabrication from self-assembled thermoresponsive poly(glycidyl ether) brushes *Soft Matter* **14** 8333–43
- [14] Okano T, Yamada N, Sakai H and Sakurai Y 1993 A novel recovery system for cultured cells using plasma-treated polystyrene dishes grafted with poly(N-isopropylacrylamide) *J. Biomed. Mater. Res.* **27** 1243–51
- [15] Tang Z and Okano T 2014 Recent development of temperature-responsive surfaces and their application for cell sheet engineering. *Regen. Biomater.* **1** 91–102
- [16] Asakawa N, Shimizu T, Tsuda Y, Sekiya S, Sasagawa T, Yamato M, Fukai F and Okano T 2010 Pre-vascularization of in vitro three-dimensional tissues created by cell sheet engineering *Biomaterials* **31** 3903–9
- [17] Sekine H, Shimizu T, Sakaguchi K, Dobashi I, Wada M, Yamato M, Kobayashi E, Umezu M and Okano T 2013 In vitro fabrication of functional three-dimensional tissues with perfusable blood vessels. *Nat. Commun.* **4** 1399
- [18] Backman D E, LeSavage B L, Shah S B and Wong J Y 2017 A Robust Method to Generate Mechanically

Anisotropic Vascular Smooth Muscle Cell Sheets for Vascular Tissue Engineering *Macromol. Biosci.* **17** 1600434

- [19] Rim N G, Yih A, Hsi P, Wang Y, Zhang Y and Wong J Y 2018 Micropatterned cell sheets as structural building blocks for biomimetic vascular patches *Biomaterials* **181** 126–39
- [20] Ahn H, Ju Y M, Takahashi H, Williams D F, Yoo J J, Lee S J, Okano T and Atala A 2015 Engineered small diameter vascular grafts by combining cell sheet engineering and electrospinning technology. *Acta Biomater.* **16** 14–22
- [21] Hibino N, Duncan D R, Nalbandian A, Yi T, Qyang Y, Shinoka T and Breuer C K 2012 Evaluation of the use of an induced pluripotent stem cell sheet for the construction of tissue-engineered vascular grafts. *J. Thorac. Cardiovasc. Surg.* **143** 696–703
- [22] Kang Y, Ren L and Yang Y 2014 Engineering Vascularized Bone Grafts by Integrating a Biomimetic Periosteum and  $\beta$ -TCP Scaffold *ACS Appl. Mater. Interfaces* **6** 9622–33
- [23] Stöbener D D, Uckert M, Cuellar-Camacho J L, Hoppensack A and Weinhart M 2017 Ultrathin Poly(glycidyl ether) Coatings on Polystyrene for Temperature-Triggered Human Dermal Fibroblast Sheet Fabrication *ACS Biomater. Sci. Eng.* **3** 2155–2165
- [24] Elomaa L, Keshi E, Sauer I M and Weinhart M 2020 Development of GelMA/PCL and dECM/PCL resins for 3D printing of acellular in vitro tissue scaffolds by stereolithography *Mater. Sci. Eng. C* **112** 110958
- [25] Lindner M, Laporte A, Block S, Elomaa L and Weinhart M 2021 Physiological shear stress enhances differentiation, mucus-formation and structural 3d organization of intestinal epithelial cells in vitro *Cells* **10**
- [26] Yavvari P, Laporte A, Elomaa L, Schraufstetter F, Pacharzina I, Daberkow A D, Hoppensack A and Weinhart M 2022 3D-cultured vascular-like networks enable validation of vascular disruption properties of drugs in vitro *Front. Bioeng. Biotechnol.*
- [27] Moran M T, Carroll W M, Gorelov A and Rochev Y 2007 Intact endothelial cell sheet harvesting from thermoresponsive surfaces coated with cell adhesion promoters *J. R. Soc. Interface* **4** 1151–7
- [28] Nakatsu M N, Sainson R C A, Aoto J N, Taylor K L, Aitkenhead M, Pérez-del-Pulgar S, Carpenter P M and Hughes C C W 2003 Angiogenic sprouting and capillary lumen formation modeled by human umbilical vein endothelial cells (HUVEC) in fibrin gels: the role of fibroblasts and Angiopoietin-1 *Microvasc. Res.* **66** 102–12
- [29] Costa-Almeida R, Gomez-Lazaro M, Ramalho C, Granja P L, Soares R and Guerreiro S G 2015 Fibroblast-endothelial partners for vascularization strategies in tissue engineering *Tissue Eng. - Part A* **21** 1055–65
- [30] Vempati P, Popel A S and Mac Gabhann F 2014 Extracellular regulation of VEGF: Isoforms, proteolysis, and vascular patterning *Cytokine Growth Factor Rev.* **25** 1–19
- [31] Newman A C, Nakatsu M N, Chou W, Gershon P D and Hughes C C W 2011 The requirement for fibroblasts in angiogenesis: Fibroblast-derived matrix proteins are essential for endothelial cell lumen formation *Mol. Biol. Cell* **22** 3791–800
- [32] Andrée B, Ichanti H, Kalies S, Heisterkamp A, Strauß S, Vogt P M, Haverich A and Hilfiker A 2019 *Sci. Rep.* **9** 1–11
- [33] Manikowski D, Andrée B, Samper E, Saint-Marc C, Olmer R, Vogt P, Strauß S, Haverich A and Hilfiker A 2018 Human adipose tissue-derived stromal cells in combination with exogenous stimuli facilitate three-dimensional network formation of human endothelial cells derived from various sources *Vascul. Pharmacol.* **106** 28–36

# ***In vitro* vascularization of hydrogel-based tissue constructs via a combined approach of cell sheet engineering and dynamic perfusion cell culture**

Laura Elomaa<sup>1</sup>, Marcus Lindner<sup>1</sup>, Ruth Leben<sup>2</sup>, Raluca Niesner<sup>2</sup>, Marie Weinhart<sup>1,3</sup>

<sup>1</sup> Institute of Chemistry and Biochemistry, Freie Universität Berlin, Berlin, Germany

<sup>2</sup> Institute of the Leibniz Association, Deutsches Rheuma-Forschungszentrum (DRFZ), Berlin, Germany

<sup>3</sup> Institute of Physical Chemistry and Electrochemistry, Leibniz Universität Hannover, Hannover, Germany

## **1. Detailed description of the chamber design used for the dynamic vascularization of collagen constructs**

To provide the readers with support for design and 3D printing of a dynamic perfusion chamber, several important details of our tube chamber are described in **Fig S1** and the text below.

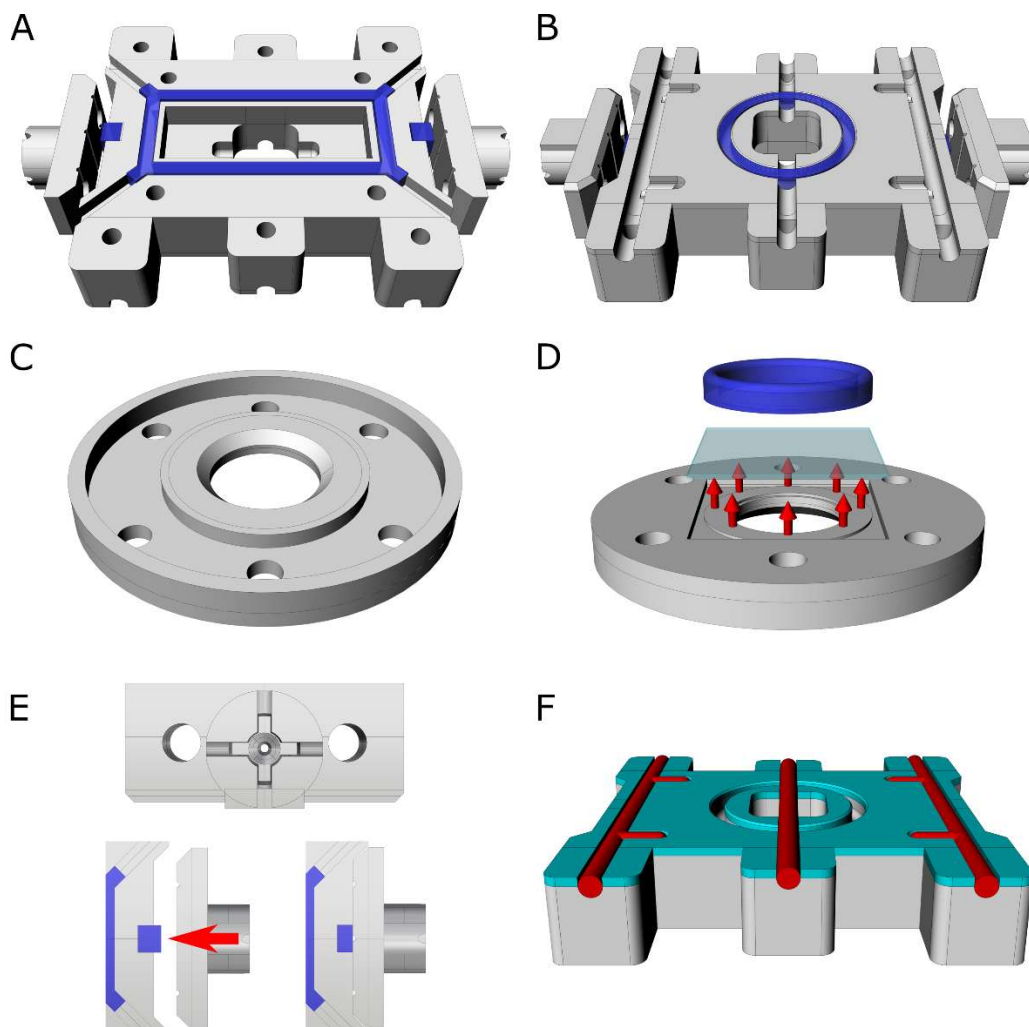


**Figure S1.** 3D-renders of the A) top and B) bottom perspective view of the tube chamber, showing the printed parts in grey and cast silicone gaskets in blue. C-D) A closer look of the design of the bottom lid hosting a glass cover slip to enable microscopy imaging of the vascularized gel and E) the needle holder with the spacer and F) red adaptations for 3D-printing to avoid closed structures inside the chamber.

#### *Chamber body:*

The tube chamber consists of the body (**Fig S1A and S1B**), a top lid and a bottom lid (**Fig S1C and S1D**), two needle holders (**Fig S1E**), as well as several sealings. Two needles can be mounted to hold and perfuse a tubular (3D-printed) scaffold. The diameter of the needles has to have a tight fit with the inner diameter of the tubular scaffold. The cut-outs in the chamber body to hold the scaffold were enlarged during chamber development to create more space for the handling and attachment of the cell sheet-covered tube to the needles.

#### *Bottom lid:*

The bottom lid has an oval shape and is fastened with six screws to the body, and its transparency allows microscopy imaging of the cell-laden gel during the cell culture without opening the chamber. A protruding edge around the lid increases its rigidity and avoids bending of the lid. On the opposite side, a cut-out for a coverslip (22 x 22 mm, 0.4 mm thickness) was implemented, bearing a slight elevation that matches the gasket in the chamber body. This ensures an even distribution of the contact pressure (as illustrated with red arrows in **Fig S1D**) and prevents previously observed rapid breakage of the coverslip due to slight deformations when closing the lid.

#### *Needle holders and spacers:*

The needle holders and the spacers (**Fig S1E**) are mounted to the chamber with screws, press-fitting a rectangular gasket that acts as a septum, and can be perforated with a needle. Its initial design was improved by a cross-shaped cut-out that prevents the needles from rotating when being integrated into the circuit. This part might be adjusted to fit the material and size of the printed scaffold. While keeping the needle length constant, the overlap of the scaffold and the needle being inserted is reduced with increasing thickness of the spacers. A balance between the tightness and the perfused length of the tube has to be maintained.

#### *3D printing and post processing:*

The tube chamber was printed directly on the building platform without support structures in order to obtain as even a surface as possible. Thus, deleting the red-marked areas shown in **Fig S1F** before 3D printing was necessary to avoid closed structures inside the chamber, creating a so-called drainage. This may vary from printer to printer, but was necessary in our case because of the rather viscous resin. In addition, the thickness of the bottom layer may need to be adjusted depending on the zero position of the 3D-printer and subsequently the thickness of the first layer(s). The overall chamber design and material choice has to be matched to guarantee a complete fastening of the bottom lid without breaking the cover glass but still achieving the tightness to prevent any leakages of the tube chamber.

## 2. Microscopy images of HUVEC sheets, HDFs, and vascular network formation

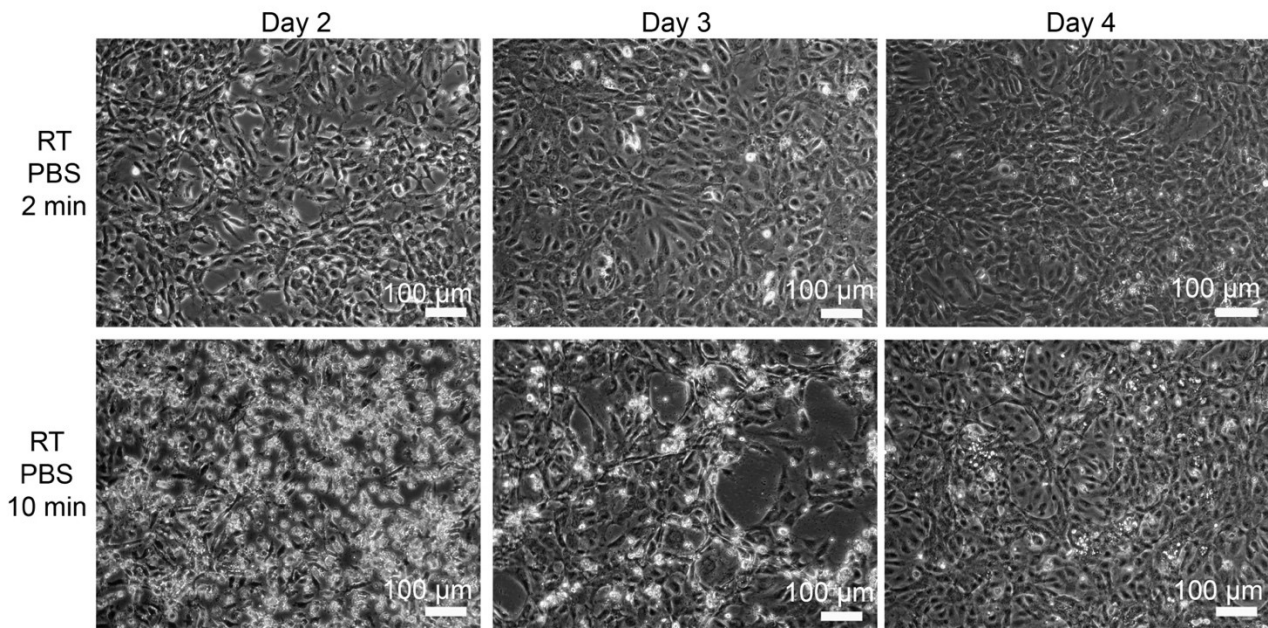


**Figure S2.** Representative brightfield microscopy images of HUVEC monolayers (seeding density:  $8.5 \times 10^4$  cells  $\text{cm}^{-2}$ ), when cells were detached after two, three, and four days of cell culture by temperature reduction to RT in PBS for 2 and 10 minutes, respectively.

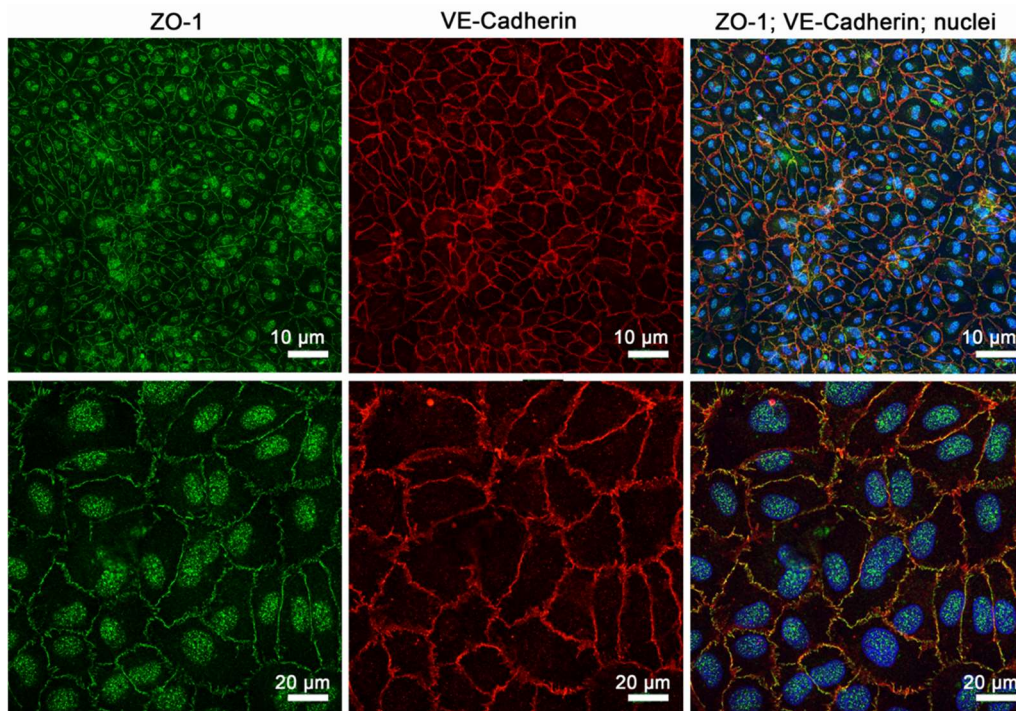


**Figure S3.** Representative fluorescent microscopy images of ZO-1 (green) and VE-Cadherin (red) staining of the tight junctions between cells in the confluent HUVEC monolayers after four days of culture on PGE-coated PS substrates before their temperature-triggered detachment. Nuclei were counterstained with Hoechst 33342 (blue).

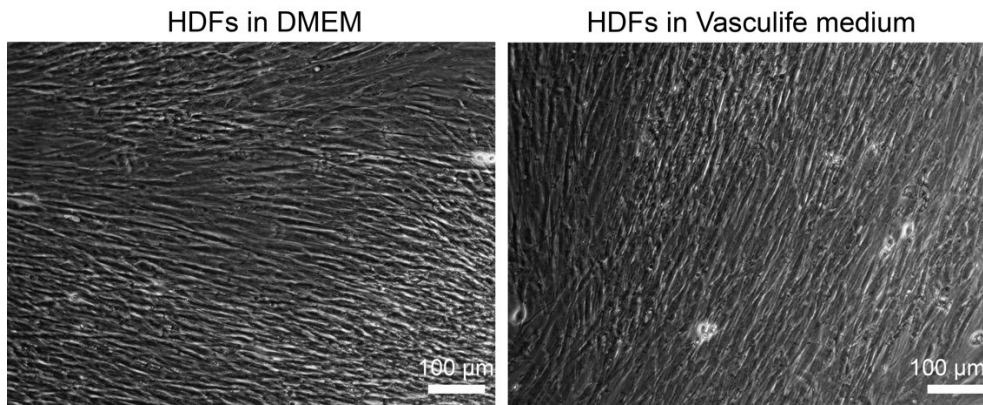


**Figure S4.** Representative brightfield microscopy images for morphological comparison of confluent HDFs cultured on TCPS for 21 days in DMEM medium and 0.5% FBS Vasculife® VEGF medium.

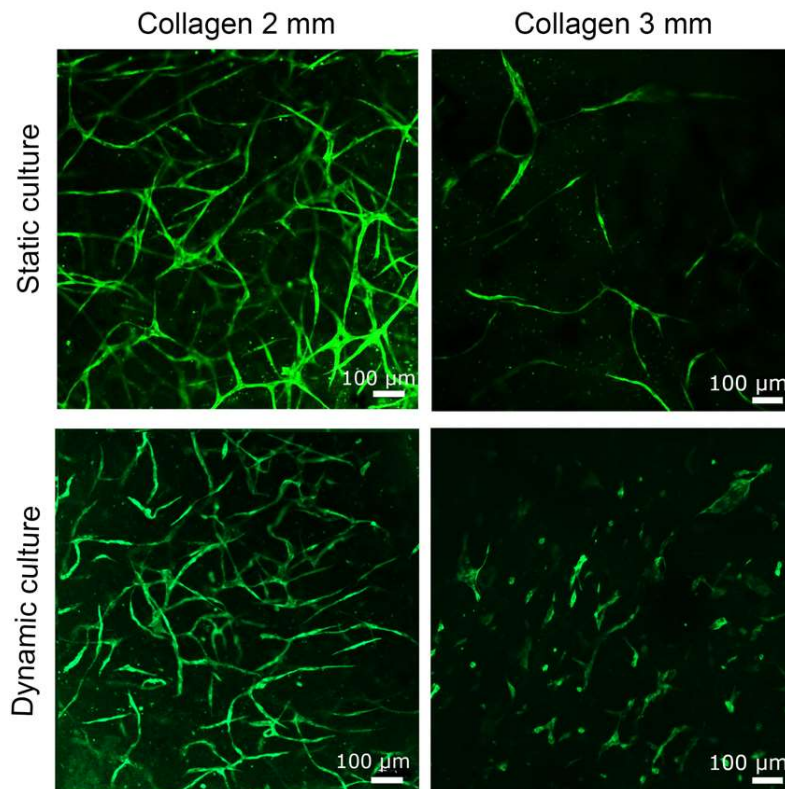


**Figure S5.** Representative fluorescence microscopy images of HUVECs in the insert-based static culture and chamber-based dynamic culture with varying collagen gel thicknesses.



# 4

## Summary and Conclusion

In this work, an easily accessible dynamic cell culture system that is capable to apply physiologically relevant fluid-derived shear stresses to anchorage-dependent mammalian cells was established. The impact of dynamic culture conditions on differentiation, functionality and advanced maturation of cells to generate improved *in vitro* tissue models was further investigated. The interdisciplinary approach combined an extensive range of methods and research areas, including the careful selection and validation of materials, the engineering of the control unit to generate defined flow conditions, and a computer-assisted design and characterization of flow chambers via CFD. The assembled setup was further validated for its suitability to host mammalian cells of different origins under flow conditions, and the impact of shear stress on its capacity to generate advanced *in vitro* barrier/tissue models was investigated. To initially address the scientific questions, a setup for the application of physiological shear stress on cells cultivated on standard cell culture substrates was established. For this purpose, an easy-to-use, cost-effective and versatile pump controller based on the open-source Arduino platform was built.<sup>205</sup> The microcontroller allows precise control of four independently running pumps that can be operated directly in the incubator. Subsequently, materials that can be used to build a closed-loop flow system were validated. Depending on their requirements (*e.g.*, biocompatibility, and mechanical properties) polycarbonate for culture chambers, polypropylene and nylon 66 (polyamide) for the adapters, and silicone and proprietary materials for the tubing were selected. The first cell culture chambers were manufactured via CNC milling and designed to fit standard

microscope slides with the possibility to apply a broad range of shear stresses spanning four orders of magnitude, from  $<0.004$  to  $>20$  dyn cm<sup>-2</sup>. Upon application of low physiological shear forces in the resulting cell culture system, the established epithelial intestinal HT29-MTX cell line capable of producing mucus showed a scaffold-free self-organization into villi-like 3D structures with highly proliferative tip cells and a heavily interconnected, mesh-like structured mucus. The native mucus thickness increased about two-fold from static to dynamic culture ( $29 \pm 14$   $\mu\text{m}$  vs.  $50 \pm 24$   $\mu\text{m}$ ), thus reaching physiological intestinal mucus thickness<sup>182</sup> and exceeding commonly produced *in vitro* mucus layers reported in literature.<sup>42,190</sup> At the same time, the designed modules in conjunction with the selected materials were tested which revealed versatility for the intended operation. Furthermore, by using CAD and 3D printing we were able to transfer the results of dynamic culture conditions from adherent cells grown on solid substrates to commercially available, membrane-comprising cell culture inserts. This allowed us to create an improved intestinal epithelial mucus model with *in vivo*-like cellular reorganization. To proceed towards increased physiological relevant vascular barriers, primary HUVECs and differentiated iPSC-derived endothelial cells (iPSC-ECs) were cultured under shear conditions with the aid of the aforementioned chamber for the slide culture. Both endothelial cell types were cultured under flow on thermoresponsive, well-defined PGE-coated surfaces.<sup>206</sup> Contradictory results regarding iPSC-EC response to flow can be found in the literature,<sup>207-209</sup> while the iPSC-ECs in our hand possessed an even increased capacity to respond to flow via alignment compared to HUVECs. Staining of individual glycocalyx components were in line with results from other groups and demonstrated the flow-induced increase in the amount of mechanotransducing component heparan sulfate<sup>201,210</sup> with the overall glycocalyx thickness reaching *in vivo*-relevant values ( $\sim 2$   $\mu\text{m}$  and  $\sim 2.5$   $\mu\text{m}$  for HUVECs and iPSC-ECs, respectively).<sup>183</sup> Moreover, for the first time, we were able to detach flow-induced isotropic HUVEC cell sheets as well as intact anisotropic iPSC-EC cell sheets. Furthermore, we were able to combine aligned iPSC-EC cell sheets with a 3D printed tubular scaffold by a wrapping process, providing an extra mechanical trigger

for the detachment. The transferred cells retained their alignment, which provided us with a useful tool to build small biomimetic blood-vessel like constructs. Finally, we investigated the vascularization of thick 3D hydrogel constructs. For this purpose, we expanded our repertoire for dynamic culture by an additional chamber that allows the formation of vascular networks by hydrogel-embedded endothelial cells in the presence of flow. The chamber was designed to hold and perfuse the aforementioned tubular scaffold with a wrapped (anisotropic) cell sheet and comprised an imaging window at the bottom for convenient monitoring of the network formation. Primary human dermal fibroblasts (HDFs) were incorporated into the second, independent flow circuit, which enabled their intercellular crosstalk with the endothelial cells. Thus, we permit the assembly of thick *in vitro* tissue constructs with active-perfused vascularization and circumvent previous limitation of these constructs related to the nutrient starvation and ineffective waste removal.<sup>80</sup> In conclusion, we developed a versatile platform that enables application of physiological relevant shear stress to create advanced *in vitro* tissue models. During this work, the system and models evolved in numerous ways, including the transition from simple cell lines to primary cells and stem cell-derived cells as well as the progressing from monoculture to co-culture comprising active cellular crosstalk. In addition, the dynamic cell culture system was extended by transition from simple solid glass substrates to membrane-comprising cell culture inserts and by the implementation of thermoresponsive surfaces in the dynamic culture as well as the combination of harvested cell sheets with vessel-mimetic tubular scaffolds embedded in a biological hydrogel. We were able to demonstrate the value of the system as a tool to create advanced *in vitro* 3D barrier models, and we are confident that its application is not limited to these. Even though we were able to take important steps towards the development of improved *in vitro* tissue models in the course of this work, the dynamic culture systems can be further improved in numerous ways. For example, it would be technically conceivable to implement on-line monitoring of barrier function via internal TEER measurements. The feasibility of this has already been demonstrated by application of the identical microcontroller which is used in our work to control the peristaltic

pumps.<sup>211</sup> Even though it was possible to control four pumps in parallel and several culture chambers per circuit with multiple samples per individual chamber, a further increase in throughput remains a challenge to be addressed in future studies. As we observed a surprising benefit of shear stress on an intestinal cell line that has been previously well characterized, an interesting task would be to transfer the established culture conditions to intestinal primary cells to improve the physiological relevance of *in vitro* intestinal barrier models. Moreover, in-depth analysis of endothelial differentiation markers of HUVECs and iPSC-ECs or other endothelial cells under different shear conditions are necessary to provide insight into their shear-induced differentiation toward arterial or venous phenotype. Finally, prolonged culture conditions with possibly adjusted mechanical and biodegradable properties of the scaffold-based vessel mimetics could lead to the generation of perfusable, fully vascularized hydrogels that are critically needed in tissue engineering.

# Short Summary / Kurzzusammenfassung

## Short Summary

In this thesis, a system for the application of flow-induced, physiologically relevant shear stress on mammalian cells was established. The circulation of cell culture medium in culture circuits was generated by peristaltic pumps, which can be operated with a self-built control unit. Culture chambers for different applications were computer-assisted designed, characterized by computational fluid dynamics and subsequently manufactured either by CNC milling or 3D printing. Using this system, shear-induced changes on the cellular functionality of *in vitro* barrier models were investigated. The application of low, physiologically relevant shear forces to an established intestinal epithelial cell line, HT29-MTX, resulted in increased mucus production, as well as structural reorganization of the confluent cell layer towards 3-dimensional villi-like structures. The results could be transferred from solid cell culture substrates to commercially available cell culture inserts bearing membranes, allowing us to develop an improved *in vitro* model of the intestinal barrier with a physiologically relevant mucus layer. We then proceeded with the endothelial barrier. Here, we investigated the effects of flow-induced stress comparatively for HUVECs and iPSC-ECs. Both cell types showed the characteristic alignment upon application of flow, as well as increased layer thicknesses and improved functionality of the endothelial glycocalyx. In addition, for the first time, we were able to detach isotropic (HUVECs) and anisotropic (iPSC-ECs) cell monolayers from thermoresponsive surfaces and wrapped them around a 3D-printed scaffold while maintaining alignment, which represents an important step toward the development of blood vessels *in vitro*. Finally, we implemented a similar tubular construct into dynamic culture. The indirect coculture of HUVECs with fibroblasts allowed intercellular communication and resulted in the formation of stable vascular networks, while a second independent circuit allowed perfusion of the tubular blood vessel mimick. In summary, we established a versatile and reliable platform for the

application of physiological shear forces to flat and lumenized tissues, enabling the development of improved *in vitro* barrier models.

## Kurzzusammenfassung

In dieser Arbeit wurde ein System zur Applikation fluss-induzierter, physiologisch relevanter Scherkräfte auf Säugerzellen etabliert. Die Zirkulation von Zellkulturmedium in Kulturkreisläufen wurde dabei über Peristaltikpumpen generiert, welche mit einer selbstgebauten Steuerung betrieben werden können. Kulturkammern für unterschiedliche Einsatzgebiete wurden computergestützt entworfen, mithilfe numerischer Strömungsmechanik charakterisiert und anschließend entweder durch CNC-Fräsen oder 3D-Druck hergestellt. Mithilfe dieses Systems wurde der Einfluss scherinduzierter Änderungen auf die zelluläre Funktionalität von *in vitro* Barriremodellen untersucht. Die Applikation geringer, physiologisch relevanter Scherkräfte auf eine etablierte intestinale epitheliale Zelllinie, HT29-MTX, führte zu einer erhöhten Mucusproduktion, sowie der strukturellen Reorganisation der konfluenten Zellschicht hin zu 3-dimensionalen, Darmzotten-artigen Gebilden. Die Ergebnisse konnten von festen Zellkultursubstraten auf kommerziell erhältliche Zellkultureinsätze mit mikroporösen Membranen übertragen werden, sodass wir ein verbessertes *in vitro* Modell der intestinalen Barriere mit physiologisch relevanten Mucusschichten entwickeln konnten. Im Anschluss widmeten wir uns dem Studium der Barrierefunktion von Endothelzellen. Dabei untersuchten wir die Auswirkungen von fluss-induziertem Stress vergleichend für HUVECs und iPSCs-ECs. Beide Zellarten zeigten die charakteristische Ausrichtung mit dem Fluss, sowie erhöhte Schichtdicken und verbesserte Funktionalität der endothelialen Glykokalix. Zudem konnten wir erstmalig intakte isotrope (HUVECs) und anisotrope (iPSC-ECs) Zellmonolagen temperatur-gesteuert von thermoresponsiven Oberflächen ablösen und um ein 3D-gedrucktes Gerüst rollen, wobei die Zellausrichtung erhalten blieb, was einen wichtigen Schritt zur Entwicklung von Blutgefäßen *in vitro* darstellt. Abschließend implementierten wir ein ähnliches Konstrukt in die dynamische Kultur. Die Erweiterung des Systems durch eine indirekte Kokultur der HUVECs mit

Fibroblasten ermöglichte die Ausbildung stabiler, vaskularer Netzwerke und ein zweiter unabhängiger Kreislauf erlaubte die Perfusion der künstlichen tubulären Blutgefäße. Zusammenfassend konnten wir eine vielseitige und verlässliche Plattform zur Applikation von physiologischen Scherkräften auf adhärenenten Säugerzellen in 2D oder in 3D etablieren, die den Aufbau von verbesserten *in vitro* Barriere-modellen ermöglicht.



# References

- (1) Benam, K. H. et al. *Annu Rev Pathol* **2015**, *10*, 195–262, DOI: 10.1146/annurev-pathol-012414-040418.
- (2) Gupta, A.; Lutolf, M. P.; Hughes, A. J.; Sonnen, K. F. *Stem Cell Rep* **2021**, *16*, 1104–1116, DOI: 10.1016/j.stemcr.2021.04.005.
- (3) Groneberg, D. A.; Grosse-Siestrup, C.; Fischer, A. *Toxicol Pathol* **2002**, *30*, 394–9, DOI: 10.1080/01926230252929972.
- (4) McKim J. M., J. *Comb Chem High Throughput Screen* **2010**, *13*, 188–206, DOI: 10.2174/138620710790596736.
- (5) Weinhart, M.; Hocke, A.; Hippenstiel, S.; Kurreck, J.; Hedtrich, S. *Pharmacol Res* **2019**, *139*, 446–451, DOI: 10.1016/j.phrs.2018.11.002.
- (6) Harrison, R. G.; Greenman, M. J.; Mall, F. P.; Jackson, C. M. *The Anatomical Record* **1907**, *1*, 116–128, DOI: 10.1002/ar.1090010503.
- (7) Hayflick, L. *Keio J Med* **1998**, *47*, 174–82, DOI: 10.2302/kjm.47.174.
- (8) Niu, N.; Wang, L. *Pharmacogenomics* **2015**, *16*, 273–85, DOI: 10.2217/pgs.14.170.
- (9) Donato, M. T.; Lahoz, A.; Castell, J. V.; Gomez-Lechon, M. J. *Curr Drug Metab* **2008**, *9*, 1–11, DOI: 10.2174/138920008783331086.
- (10) Lundberg, A. S.; Hahn, W. C.; Gupta, P.; Weinberg, R. A. *Curr Opin Cell Biol* **2000**, *12*, 705–9, DOI: 10.1016/s0955-0674(00)00155-1.
- (11) Lee, K. M.; Choi, K. H.; Ouellette, M. M. *Cytotechnology* **2004**, *45*, 33–8, DOI: 10.1007/s10616-004-5123-3.
- (12) Lagosz-Cwik, K. B.; Wielento, A.; Lipska, W.; Kantorowicz, M.; Darczuk, D.; Kaczmarzyk, T.; Gibbs, S.; Potempa, J.; Grabiec, A. M. *Sci Rep* **2021**, *11*, 10770, DOI: 10.1038/s41598-021-90037-5.
- (13) Masnikov, D.; Stafeev, I.; Michurina, S.; Zubkova, E.; Mamontova, E.; Ratner, E.; Menshikov, M.; Parfyonova, Y. *Anal Biochem* **2021**, *628*, 114268, DOI: 10.1016/j.ab.2021.114268.
- (14) Tyurin-Kuzmin, P. A.; Chechekhin, V. I.; Ivanova, A. M.; Dyikanov, D. T.; Sysoeva, V. Y.; Kalinina, N. I.; Tkachuk, V. A. *Int J Mol Sci* **2018**, *19*, DOI: 10.3390/ijms19123712.
- (15) Tan, B.; Gan, S.; Wang, X.; Liu, W.; Li, X. *J Mater Chem B* **2021**, *9*, 5385–5413, DOI: 10.1039/d1tb00172h.
- (16) Palakkan, A. A.; Hay, D. C.; Anil Kumar, P. R.; Kumary, T. V.; Ross, J. A. *Liver Int* **2013**, *33*, 666–76, DOI: 10.1111/liv.12134.
- (17) Takahashi, K.; Yamanaka, S. *Cell* **2006**, *126*, 663–76, DOI: 10.1016/j.cell.2006.07.024.
- (18) Raab, S.; Klingenstein, M.; Liebau, S.; Linta, L. *Stem Cells Int* **2014**, *2014*, 768391, DOI: 10.1155/2014/768391.
- (19) Haase, A. et al. *Cell Stem Cell* **2009**, *5*, 434–41, DOI: 10.1016/j.stem.2009.08.021.

- (20) Lee, C. A.; Sinha, S.; Fitzpatrick, E.; Dhawan, A. *J Mol Med (Berl)* **2018**, *96*, 469–481, DOI: 10.1007/s00109-018-1638-5.
- (21) Beltrão-Braga, P. C. B.; Pignatari, G. C.; Russo, F. B.; Fernandes, I. R.; Muotri, A. R. *Cytometry A* **2013**, *83*, 11–7, DOI: 10.1002/cyto.a.22231.
- (22) Ferreira, L. P.; Gaspar, V. M.; Mano, J. F. *Acta Biomater* **2018**, *75*, 11–34, DOI: 10.1016/j.actbio.2018.05.034.
- (23) Ponce de León-Rodríguez, M. D. C.; Guyot, J. P.; Laurent-Babot, C. *Crit Rev Food Sci Nutr* **2019**, *59*, 3648–3666, DOI: 10.1080/10408398.2018.1506734.
- (24) Polidoro, M. A.; Ferrari, E.; Marzorati, S.; Lleo, A.; Rasponi, M. *Liver Int* **2021**, *41*, 1744–1761, DOI: 10.1111/liv.14942.
- (25) Maji, S.; Lee, H. *Int J Mol Sci* **2022**, *23*, DOI: 10.3390/ijms23052662.
- (26) Grassel, S.; Ahmed, N. *Front Biosci* **2007**, *12*, 4946–56, DOI: 10.2741/2440.
- (27) Hussey, G. S.; Keane, T. J.; Badylak, S. F. *Nat Rev Gastroenterol Hepatol* **2017**, *14*, 540–552, DOI: 10.1038/nrgastro.2017.76.
- (28) Miki, Y.; Ono, K.; Hata, S.; Suzuki, T.; Kumamoto, H.; Sasano, H. *J Steroid Biochem Mol Biol* **2012**, *131*, 68–75, DOI: 10.1016/j.jsbmb.2011.12.004.
- (29) Fitzgerald, K. A.; Malhotra, M.; Curtin, C. M.; Brien, F. J. O.; Driscoll, C. M. O. *J Control Release* **2015**, *215*, 39–54, DOI: 10.1016/j.jconrel.2015.07.020.
- (30) Gasiorowski, J. Z.; Murphy, C. J.; Nealey, P. F. *Annu Rev Biomed Eng* **2013**, *15*, 155–76, DOI: 10.1146/annurev-bioeng-071811-150021.
- (31) Li, S.; Guan, J. L.; Chien, S. *Annu Rev Biomed Eng* **2005**, *7*, 105–50, DOI: 10.1146/annurev.bioeng.7.060804.100340.
- (32) Pavel, M.; Renna, M.; Park, S. J.; Menzies, F. M.; Ricketts, T.; Füllgrabe, J.; Ashkenazi, A.; Frake, R. A.; Lombarte, A. C.; Bento, C. F.; Franze, K.; Rubinsztein, D. C. *Nat Commun* **2018**, *9*, 2961, DOI: 10.1038/s41467-018-05388-x.
- (33) Nelson, P. J.; Daniel, T. O. *Kidney Int* **2002**, *61*, S99–105, DOI: 10.1046/j.1523-1755.2002.0610s1099.x.
- (34) Vermette, D.; Hu, P.; Canarie, M. F.; Funaro, M.; Glover, J.; Pierce, R. W. *Intensive Care Med Exp* **2018**, *6*, 37, DOI: 10.1186/s40635-018-0203-4.
- (35) Niessen, C. M. *J Invest Dermatol* **2007**, *127*, 2525–32, DOI: 10.1038/sj.jid.5700865.
- (36) Tarbell, J. M.; Pahakis, M. Y. *J Intern Med* **2006**, *259*, 339–50, DOI: 10.1111/j.1365-2796.2006.01620.x.
- (37) Meşe, G.; Richard, G.; White, T. W. *J Invest Dermatol* **2007**, *127*, 2516–24, DOI: 10.1038/sj.jid.5700770.
- (38) Söhl, G.; Willecke, K. *Cardiovasc Res* **2004**, *62*, 228–32, DOI: 10.1016/j.cardiores.2003.11.013.
- (39) Kook, Y. M.; Jeong, Y.; Lee, K.; Koh, W. G. *J Tissue Eng* **2017**, *8*, 2041731417724640, DOI: 10.1177/2041731417724640.
- (40) Mills, R. J.; Hudson, J. E. *Cell Stem Cell* **2020**, *26*, 799–801, DOI: 10.1016/j.stem.2020.05.009.

- (41) Borciani, G.; Montalbano, G.; Baldini, N.; Cerqueni, G.; Vitale-Brovarone, C.; Ciapetti, G. *Acta Biomater* **2020**, *108*, 22–45, DOI: 10.1016/j.actbio.2020.03.043.
- (42) Béduneau, A.; Tempesta, C.; Fimbel, S.; Pellequer, Y.; Jannin, V.; Demarne, F.; Lamprecht, A. *Eur J Pharm Biopharm* **2014**, *87*, 290–8, DOI: 10.1016/j.ejpb.2014.03.017.
- (43) Edling, Y.; Sivertsson, L. K.; Butura, A.; Ingelman-Sundberg, M.; Ek, M. *Toxicol In Vitro* **2009**, *23*, 1387–95, DOI: 10.1016/j.tiv.2009.07.026.
- (44) Chojkier, M. *Hepatology* **2005**, *41*, 237–46, DOI: 10.1002/hep.20567.
- (45) Duval, K.; Grover, H.; Han, L. H.; Mou, Y.; Pegoraro, A. F.; Fredberg, J.; Chen, Z. *Physiology (Bethesda)* **2017**, *32*, 266–277, DOI: 10.1152/physiol.00036.2016.
- (46) Frantz, C.; Stewart, K. M.; Weaver, V. M. *J Cell Sci* **2010**, *123*, 4195–200, DOI: 10.1242/jcs.023820.
- (47) Padhi, A.; Nain, A. S. *Ann Biomed Eng* **2020**, *48*, 1071–1089, DOI: 10.1007/s10439-019-02337-7.
- (48) Bershadsky, A. D.; Ballestrem, C.; Carramusa, L.; Zilberman, Y.; Gilquin, B.; Khochbin, S.; Alexandrova, A. Y.; Verkhovsky, A. B.; Shemesh, T.; Kozlov, M. M. *Eur J Cell Biol* **2006**, *85*, 165–73, DOI: 10.1016/j.ejcb.2005.11.001.
- (49) Chen, Y.; Ju, L.; Rushdi, M.; Ge, C.; Zhu, C. *Mol Biol Cell* **2017**, *28*, 3134–3155, DOI: 10.1091/mbc.E17-04-0228.
- (50) Discher, D. E.; Janmey, P.; Wang, Y. L. *Science* **2005**, *310*, 1139–43, DOI: 10.1126/science.1116995.
- (51) Engler, A. J.; Sen, S.; Sweeney, H. L.; Discher, D. E. *Cell* **2006**, *126*, 677–89, DOI: 10.1016/j.cell.2006.06.044.
- (52) Lerman, M. J.; Lembong, J.; Muramoto, S.; Gillen, G.; Fisher, J. P. *Tissue Eng Part B Rev* **2018**, *24*, 359–372, DOI: 10.1089/ten.TEB.2018.0056.
- (53) Lubarsky, G. V.; Davidson, M. R.; Bradley, R. H. *Surf Sci* **2004**, *558*, 135–144, DOI: 10.1016/j.susc.2004.03.054.
- (54) Rodrigues, J.; Heinrich, M. A.; Teixeira, L. M.; Prakash, J. *Trends Cancer* **2021**, *7*, 249–264, DOI: 10.1016/j.trecan.2020.10.009.
- (55) Fowler, S.; Roush, R.; Wise, J., *Concepts of Biology (OpenStax)*, 2013.
- (56) Wen, J. H.; Vincent, L. G.; Fuhrmann, A.; Choi, Y. S.; Hribar, K. C.; Taylor-Weiner, H.; Chen, S.; Engler, A. J. *Nat Mater* **2014**, *13*, 979–87, DOI: 10.1038/nmat4051.
- (57) Habanjar, O.; Diab-Assaf, M.; Caldefie-Chezet, F.; Delort, L. *Int J Mol Sci* **2021**, *22*, DOI: 10.3390/ijms222212200.
- (58) Petersen, O. W.; Rønnev-Jessen, L.; Howlett, A. R.; Bissell, M. J. *Proc Natl Acad Sci U S A* **1992**, *89*, 9064–8, DOI: 10.1073/pnas.89.19.9064.
- (59) Wade, R. J.; Burdick, J. A. *Mater Today* **2012**, *15*, 454–459, DOI: 10.1016/s1369-7021(12)70197-9.

- (60) Aisenbrey, E. A.; Murphy, W. L. *Nat Rev Mater* **2020**, *5*, 539–551, DOI: 10.1038/s41578-020-0199-8.
- (61) Noel, A.; Simon, N.; Raus, J.; Foidart, J. M. *Biochem Pharmacol* **1992**, *43*, 1263–7, DOI: 10.1016/0006-2952(92)90501-9.
- (62) Hughes, C. S.; Postovit, L. M.; Lajoie, G. A. *Proteomics* **2010**, *10*, 1886–90, DOI: 10.1002/pmic.200900758.
- (63) Auerbach, R.; Lewis, R.; Shinnars, B.; Kubai, L.; Akhtar, N. *Clin Chem* **2003**, *49*, 32–40, DOI: 10.1373/49.1.32.
- (64) Antoine, E. E.; Vlachos, P. P.; Rylander, M. N. *Tissue Eng Part B Rev* **2014**, *20*, 683–96, DOI: 10.1089/ten.TEB.2014.0086.
- (65) Rowe, S. L.; Lee, S.; Stegemann, J. P. *Acta Biomater* **2007**, *3*, 59–67, DOI: 10.1016/j.actbio.2006.08.006.
- (66) Dillow, A. K.; Tirrell, M. *Curr Opin Solid State Mater Sci* **1998**, *3*, 252–259, DOI: 10.1016/s1359-0286(98)80099-5.
- (67) Mahlstedt, M. M.; Anderson, D.; Sharp, J. S.; McGilvray, R.; Muñoz, M. D. B.; Buttery, L. D.; Alexander, M. R.; Rose, F. R.; Denning, C. *Biotechnol Bioeng* **2010**, *105*, 130–40, DOI: 10.1002/bit.22520.
- (68) Cruz-Acuña, R.; Quirós, M.; Farkas, A. E.; Dedhia, P. H.; Huang, S.; Siuda, D.; García-Hernández, V.; Miller, A. J.; Spence, J. R.; Nusrat, A.; García, A. J. *Nat Cell Biol* **2017**, *19*, 1326–1335, DOI: 10.1038/ncb3632.
- (69) Phelps, E. A.; Enemchukwu, N. O.; Fiore, V. F.; Sy, J. C.; Murthy, N.; Sulchek, T. A.; Barker, T. H.; García, A. J. *Adv Mater* **2012**, *24*, 64–70, 2, DOI: 10.1002/adma.201103574.
- (70) Phelps, E. A.; Headen, D. M.; Taylor, W. R.; Thulé, P. M.; García, A. J. *Biomaterials* **2013**, *34*, 4602–11, DOI: 10.1016/j.biomaterials.2013.03.012.
- (71) Evans, N. D.; Gentleman, E. *J Mater Chem B* **2014**, *2*, 2345–2356, DOI: 10.1039/c3tb21604g.
- (72) Hemmati-Sadeghi, S.; Dey, P.; Ringe, J.; Haag, R.; Sittinger, M.; Dehne, T. *J Biomed Mater Res B Appl Biomater* **2019**, *107*, 490–500, DOI: 10.1002/jbm.b.34139.
- (73) Zhu, J. *Biomaterials* **2010**, *31*, 4639–56, DOI: 10.1016/j.biomaterials.2010.02.044.
- (74) Guruswamy Damodaran, R.; Vermette, P. *Biotechnol Prog* **2018**, *34*, 1494–1505, DOI: 10.1002/btpr.2699.
- (75) Gilpin, A.; Yang, Y. *Biomed Res Int* **2017**, *2017*, 9831534, DOI: 10.1155/2017/9831534.
- (76) Fedecostante, M.; Westphal, K. G. C.; Buono, M. F.; Sanchez Romero, N.; Wilmer, M. J.; Kerkering, J.; Baptista, P. M.; Hoenderop, J. G.; Masereeuw, R. *Drug Metab Dispos* **2018**, *46*, 1338–1350, DOI: 10.1124/dmd.118.080721.
- (77) Gilpin, S. E.; Wagner, D. E. *Eur Respir Rev* **2018**, *27*, DOI: 10.1183/16000617.0021-2018.

- (78) Liu, G.; Wang, B.; Li, S.; Jin, Q.; Dai, Y. *J Cell Physiol* **2019**, *234*, 9447–9456, DOI: 10.1002/jcp.27630.
- (79) O'Brien, F. J. *Mater Today* **2011**, *14*, 88–95, DOI: 10.1016/s1369-7021(11)70058-x.
- (80) Auger, F. A.; Gibot, L.; Lacroix, D. *Annu Rev Biomed Eng* **2013**, *15*, 177–200, DOI: 10.1146/annurev-bioeng-071812-152428.
- (81) Zhu, N.; Che, X. In *Advances in Biomaterials Science and Biomedical Applications*, 2013; Chapter Chapter 12, DOI: 10.5772/54125.
- (82) Kanimozhi, K.; Basha, S. K.; Kumari, V. S.; Kaviyarasu, K. *J Nanosci Nanotechnol* **2018**, *18*, 4916–4922, DOI: 10.1166/jnm.2018.15306.
- (83) Mirtaghavi, A.; Luo, J.; Muthuraj, R. *J Compos Sci* **2020**, *4*, 152, DOI: 10.3390/jcs4040152.
- (84) Smith, J. A.; Mele, E. *Front Bioeng Biotechnol* **2021**, *9*, 674738, DOI: 10.3389/fbioe.2021.674738.
- (85) Ribba, L.; Parisi, M.; D'Accorso, N. B.; Goyanes, S. *J Biomed Nanotechnol* **2014**, *10*, 3508–35, DOI: 10.1166/jbn.2014.2046.
- (86) Yang, D. J.; Zhang, L. F.; Xu, L.; Xiong, C. D.; Ding, J.; Wang, Y. Z. *J Biomed Mater Res A* **2007**, *82*, 680–8, DOI: 10.1002/jbm.a.31099.
- (87) Do, A. V.; Khorsand, B.; Geary, S. M.; Salem, A. K. *Adv Healthc Mater* **2015**, *4*, 1742–62, DOI: 10.1002/adhm.201500168.
- (88) Esfahani, H.; Jose, R.; Ramakrishna, S. *Materials (Basel)* **2017**, *10*, DOI: 10.3390/ma10111238.
- (89) Pérez-Madrigal, M. M.; Shaw, J. E.; Arno, M. C.; Hoyland, J. A.; Richardson, S. M.; Dove, A. P. *Biomater Sci* **2020**, *8*, 405–412, DOI: 10.1039/c9bm01494b.
- (90) Elomaa, L.; Keshi, E.; Sauer, I. M.; Weinhart, M. *Mater Sci Eng C Mater Biol Appl* **2020**, *112*, 110958, DOI: 10.1016/j.msec.2020.110958.
- (91) Shin, Y. J.; Shafrank, R. T.; Tsui, J. H.; Walcott, J.; Nelson, A.; Kim, D. H. *Acta Biomater* **2021**, *119*, 75–88, DOI: 10.1016/j.actbio.2020.11.006.
- (92) Elomaa, L.; Teixeira, S.; Hakala, R.; Korhonen, H.; Grijpma, D. W.; Seppälä, J. V. *Acta Biomater* **2011**, *7*, 3850–6, DOI: 10.1016/j.actbio.2011.06.039.
- (93) Zhou, X.; Zhou, G.; Junka, R.; Chang, N.; Anwar, A.; Wang, H.; Yu, X. *Colloids Surf B Biointerfaces* **2021**, *197*, 111420, DOI: 10.1016/j.colsurfb.2020.111420.
- (94) Zhao, Y. Q.; Yang, J. H.; Ding, X.; Ding, X.; Duan, S.; Xu, F. J. *Bioact Mater* **2020**, *5*, 185–191, DOI: 10.1016/j.bioactmat.2020.02.006.
- (95) Erzenin, S.; Guler, E.; Eser, E.; Polat, E. B.; Gunduz, O.; Cam, M. E. *Int J Biol Macromol* **2022**, *204*, 429–440, DOI: 10.1016/j.ijbiomac.2022.02.030.
- (96) Weinhart, M.; Becherer, T.; Haag, R. *Chem Commun (Camb)* **2011**, *47*, 1553–5, DOI: 10.1039/c0cc04002a.

- (97) Garg, A.; Houlihan, D. D.; Aldridge, V.; Suresh, S.; Li, K. K.; King, A. L.; Sutaria, R.; Fear, J.; Bhogal, R. H.; Lalor, P. F.; Newsome, P. N. *Cytotherapy* **2014**, *16*, 545–59, DOI: 10.1016/j.jcyt.2013.10.003.
- (98) Sit, K. H.; Wong, K. P.; Bay, B. H. *J Tissue Cult Methods* **1991**, *13*, 257–259, DOI: 10.1007/bf02388258.
- (99) Kurashina, Y.; Imashiro, C.; Hirano, M.; Kuribara, T.; Totani, K.; Ohnuma, K.; Friend, J.; Takemura, K. *Commun Biol* **2019**, *2*, 393, DOI: 10.1038/s42003-019-0638-5.
- (100) Patel, N. G.; Zhang, G. *Organogenesis* **2013**, *9*, 93–100, DOI: 10.4161/org.25149.
- (101) Hong, Y.; Yu, M.; Weng, W.; Cheng, K.; Wang, H.; Lin, J. *Biomaterials* **2013**, *34*, 11–8, DOI: 10.1016/j.biomaterials.2012.09.043.
- (102) De Las Heras Alarcón, C.; Pennadam, S.; Alexander, C. *Chem Soc Rev* **2005**, *34*, 276–85, DOI: 10.1039/b406727d.
- (103) Kyriakides, T. R.; Cheung, C. Y.; Murthy, N.; Bornstein, P.; Stayton, P. S.; Hoffman, A. S. *J Control Release* **2002**, *78*, 295–303, DOI: 10.1016/s0168-3659(01)00504-1.
- (104) Doberenz, F.; Zeng, K.; Willems, C.; Zhang, K.; Groth, T. *J Mater Chem B* **2020**, *8*, 607–628, DOI: 10.1039/c9tb02052g.
- (105) Stöbener, D. D.; Weinhart, M. *Polymers (Basel)* **2020**, *12*, DOI: 10.3390/polym12091899.
- (106) Horiuchi, T.; Rikiyama, K.; Sakanaya, K.; Sanada, Y.; Watanabe, K.; Aida, M.; Katsumoto, Y. *J Oleo Sci* **2020**, *69*, 449–453, DOI: 10.5650/jos.ess20026.
- (107) Kim, M.; Schmitt, S.; Choi, J.; Krutty, J.; Gopalan, P. *Polymers* **2015**, *7*, 1346–1378, DOI: 10.3390/polym7071346.
- (108) Yamada, N.; Okano, T.; Sakai, H.; Karikusa, F.; Sawasaki, Y.; Sakurai, Y. *Macromol Rapid Commun* **1990**, *11*, 571–576, DOI: 10.1002/marc.1990.030111109.
- (109) Sumide, T.; Nishida, K.; Yamato, M.; Ide, T.; Hayashida, Y.; Watanabe, K.; Yang, J.; Kohno, C.; Kikuchi, A.; Maeda, N.; Watanabe, H.; Okano, T.; Tano, Y. *FASEB J* **2006**, *20*, 392–4, DOI: 10.1096/fj.04-3035fje.
- (110) Kushida, A.; Yamato, M.; Konno, C.; Kikuchi, A.; Sakurai, Y.; Okano, T. *J Biomed Mater Res* **2000**, *51*, 216–23, DOI: 10.1002/(sici)1097-4636(200008)51:2<216::aid-jbm10>3.0.co;2-k.
- (111) Halperin, A.; Kröger, M.; Winnik, F. M. *Angew Chem Int Ed Engl* **2015**, *54*, 15342–67, DOI: 10.1002/anie.201506663.
- (112) Akiyama, Y.; Kikuchi, A.; Yamato, M.; Okano, T. *Langmuir* **2004**, *20*, 5506–11, DOI: 10.1021/la036139f.
- (113) Ozdemir, M.; Yurteri, C. U.; Sadikoglu, H. *Crit Rev Food Sci Nutr* **1999**, *39*, 457–77, DOI: 10.1080/10408699991279240.
- (114) Da Silva, R. M.; Mano, J. F.; Reis, R. L. *Trends Biotechnol* **2007**, *25*, 577–83, DOI: 10.1016/j.tibtech.2007.08.014.

- (115) Cooperstein, M. A.; Canavan, H. E. *Biointerphases* **2013**, *8*, 19, DOI: 10.1186/1559-4106-8-19.
- (116) Kikuchi, A.; Okuhara, M.; Karikusa, F.; Sakurai, Y.; Okano, T. *J Biomater Sci Polym Ed* **1998**, *9*, 1331–48, DOI: 10.1163/156856298x00424.
- (117) Stöbener, D. D.; Uckert, M.; Cuellar-Camacho, J. L.; Hoppensack, A.; Weinhart, M. *ACS Biomater Sci Eng* **2017**, *3*, 2155–2165, DOI: 10.1021/acsbiomaterials.7b00270.
- (118) Heinen, S.; Rackow, S.; Schäfer, A.; Weinhart, M. *Macromolecules* **2016**, *50*, 44–53, DOI: 10.1021/acs.macromol.6b01904.
- (119) Stöbener, D. D.; Hoppensack, A.; Scholz, J.; Weinhart, M. *Soft Matter* **2018**, *14*, 8333–8343, DOI: 10.1039/c8sm01099d.
- (120) De Pieri, A.; Rochev, Y.; Zeugolis, D. I. *NPJ Regen Med* **2021**, *6*, 18, DOI: 10.1038/s41536-021-00133-3.
- (121) Zurina, I. M.; Presniakova, V. S.; Butnaru, D. V.; Svistunov, A. A.; Timashev, P. S.; Rochev, Y. A. *Acta Biomater* **2020**, *113*, 63–83, DOI: 10.1016/j.actbio.2020.06.016.
- (122) Lai, J. Y.; Chen, K. H.; Hsiue, G. H. *Transplantation* **2007**, *84*, 1222–32, DOI: 10.1097/01.tp.0000287336.09848.39.
- (123) Ohashi, K.; Yokoyama, T.; Yamato, M.; Kuge, H.; Kanehiro, H.; Tsutsumi, M.; Amanuma, T.; Iwata, H.; Yang, J.; Okano, T.; Nakajima, Y. *Nat Med* **2007**, *13*, 880–5, DOI: 10.1038/nm1576.
- (124) Sekine, W.; Haraguchi, Y.; Shimizu, T.; Yamato, M.; Umezawa, A.; Okano, T. *Sci World J* **2013**, *2013*, 359109, DOI: 10.1155/2013/359109.
- (125) Tsuda, Y.; Shimizu, T.; Yamato, M.; Kikuchi, A.; Sasagawa, T.; Sekiya, S.; Kobayashi, J.; Chen, G.; Okano, T. *Biomaterials* **2007**, *28*, 4939–46, DOI: 10.1016/j.biomaterials.2007.08.002.
- (126) Ngo, T. X.; Nagamori, E.; Kikuchi, T.; Shimizu, T.; Okano, T.; Taya, M.; Kino-oka, M. *Biotechnol Lett* **2013**, *35*, 1001–8, DOI: 10.1007/s10529-013-1174-x.
- (127) Kubo, H.; Shimizu, T.; Yamato, M.; Fujimoto, T.; Okano, T. *Biomaterials* **2007**, *28*, 3508–16, DOI: 10.1016/j.biomaterials.2007.04.016.
- (128) Rayatpisheh, S.; Heath, D. E.; Shakouri, A.; Rujitanaroj, P. O.; Chew, S. Y.; Chan-Park, M. B. *Biomaterials* **2014**, *35*, 2713–9, DOI: 10.1016/j.biomaterials.2013.12.035.
- (129) Höhfeld, J. et al. *EMBO Rep* **2021**, *22*, e52507, DOI: 10.15252/embr.202152507.
- (130) Watanabe, K.; Morishita, K.; Zhou, X.; Shiizaki, S.; Uchiyama, Y.; Koike, M.; Naguro, I.; Ichijo, H. *Nat Commun* **2021**, *12*, 1353, DOI: 10.1038/s41467-021-21614-5.
- (131) Scallan, J. P.; Zawieja, S. D.; Castorena-Gonzalez, J. A.; Davis, M. J. *J Physiol* **2016**, *594*, 5749–5768, DOI: 10.1113/JP272088.
- (132) Sasaki, D.; Matsuura, K.; Shimizu, T. *Methods Mol Biol* **2021**, *2320*, 161–170, DOI: 10.1007/978-1-0716-1484-6\_16.

- (133) Wakeling, J. M.; Ross, S. A.; Ryan, D. S.; Bolsterlee, B.; Konno, R.; Domínguez, S.; Nigam, N. *Front Physiol* **2020**, *11*, 813, DOI: 10.3389/fphys.2020.00813.
- (134) Viennet, C.; Bride, J.; Armbruster, V.; Aubin, F.; Gabiot, A. C.; Gharbi, T.; Humbert, P. *Arch Dermatol Res* **2005**, *297*, 10–7, DOI: 10.1007/s00403-005-0557-9.
- (135) Papaioannou, T. G.; Stefanadis, C. *Hellenic J Cardiol* **2005**, *46*, 9–15.
- (136) Malek, A. M.; Alper, S. L.; Izumo, S. *JAMA* **1999**, *282*, 2035–42, DOI: 10.1001/jama.282.21.2035.
- (137) Sidhaye, V. K.; Schweitzer, K. S.; Caterina, M. J.; Shimoda, L.; King, L. S. *Proc Natl Acad Sci U S A* **2008**, *105*, 3345–50, DOI: 10.1073/pnas.0712287105.
- (138) Kim, K.; Jeong, B.; Lee, Y. M.; Son, H. E.; Ryu, J. Y.; Park, S.; Jeong, J. C.; Chin, H. J.; Kim, S. *Micromachines (Basel)* **2022**, *13*, 688, DOI: 10.3390/mi13050688.
- (139) Kim, H. J.; Huh, D.; Hamilton, G.; Ingber, D. E. *Lab Chip* **2012**, *12*, 2165–74, DOI: 10.1039/c2lc40074j.
- (140) Rutkowski, J. M.; Swartz, M. A. *Trends Cell Biol* **2007**, *17*, 44–50, DOI: 10.1016/j.tcb.2006.11.007.
- (141) Chandel, N. S.; Sznajder, J. I. *Am J Physiol Lung Cell Mol Physiol* **2000**, *279*, L1003–4, DOI: 10.1152/ajplung.2000.279.6.L1003.
- (142) Yuan, L.; Yu, Y.; Sanders, M. A.; Majumdar, A. P.; Basson, M. D. *Am J Physiol Gastrointest Liver Physiol* **2010**, *298*, G994–G1003, DOI: 10.1152/ajpgi.00517.2009.
- (143) Takamizawa, K.; Hayashi, K. *Biorheology* **1988**, *25*, 555–65, DOI: 10.3233/bir-1988-25315.
- (144) Badeer, H. S. *Microvasc Res* **1986**, *31*, 119, DOI: 10.1016/0026-2862(86)90014-2.
- (145) Baturina, G. S.; Katkova, L. E.; Schmitt, C. P.; Solenov, E. I.; Zarogiannis, S. G. *Biomolecules* **2021**, *11*, DOI: 10.3390/biom11101452.
- (146) Brower, J. B.; Targovnik, J. H.; Caplan, M. R.; Massia, S. P. *Cytoskeleton (Hoboken)* **2010**, *67*, 135–41, DOI: 10.1002/cm.20430.
- (147) Curry, F. E.; Adamson, R. H. *Ann Biomed Eng* **2012**, *40*, 828–39, DOI: 10.1007/s10439-011-0429-8.
- (148) Nauli, S. M.; Alenghat, F. J.; Luo, Y.; Williams, E.; Vassilev, P.; Li, X.; Elia, A. E.; Lu, W.; Brown, E. M.; Quinn, S. J.; Ingber, D. E.; Zhou, J. *Nat Genet* **2003**, *33*, 129–37, DOI: 10.1038/ng1076.
- (149) Praetorius, H. A.; Spring, K. R. *Curr Opin Nephrol Hypertens* **2003**, *12*, 517–20, DOI: 10.1097/00041552-200309000-00006.
- (150) Mercado-Perez, A.; Beyder, A. *Nat Rev Gastroenterol Hepatol* **2022**, *19*, 283–296, DOI: 10.1038/s41575-021-00561-y.
- (151) Krueger, J. W.; Young, D. F.; Cholvin, N. R. *J Biomech* **1971**, *4*, 31–6, DOI: 10.1016/0021-9290(71)90013-3.

- (152) Banes, A. J.; Gilbert, J.; Taylor, D.; Monbureau, O. *J Cell Sci* **1985**, *75*, 35–42, DOI: 10.1242/jcs.75.1.35.
- (153) Moraes, C.; Chen, J. H.; Sun, Y.; Simmons, C. A. *Lab Chip* **2010**, *10*, 227–34, DOI: 10.1039/b914460a.
- (154) Wan, C. R.; Chung, S.; Kamm, R. D. *Ann Biomed Eng* **2011**, *39*, 1840–7, DOI: 10.1007/s10439-011-0275-8.
- (155) Giridharan, G. A.; Nguyen, M. D.; Estrada, R.; Parichehreh, V.; Hamid, T.; Ismahil, M. A.; Prabhu, S. D.; Sethu, P. *Anal Chem* **2010**, *82*, 7581–7, DOI: 10.1021/ac1012893.
- (156) Kamotani, Y.; Bersano-Begey, T.; Kato, N.; Tung, Y. C.; Huh, D.; Song, J. W.; Takayama, S. *Biomaterials* **2008**, *29*, 2646–55, DOI: 10.1016/j.biomaterials.2008.02.019.
- (157) Byun, C. K.; Abi-Samra, K.; Cho, Y. K.; Takayama, S. *Electrophoresis* **2014**, *35*, 245–57, DOI: 10.1002/elps.201300205.
- (158) Park, J. Y.; Morgan, M.; Sachs, A. N.; Samorezov, J.; Teller, R.; Shen, Y.; Pienta, K. J.; Takayama, S. *Microfluid Nanofluidics* **2010**, *8*, 263–268, DOI: 10.1007/s10404-009-0503-9.
- (159) Sung, J. H.; Shuler, M. L. *Lab Chip* **2009**, *9*, 1385–94, DOI: 10.1039/b901377f.
- (160) Khan, W. A.; Farooq, S.; Kadry, S.; Hanif, M.; Iftikhar, F. J.; Abbas, S. Z. *Comput Methods Programs Biomed* **2020**, *190*, 105355, DOI: 10.1016/j.cmpb.2020.105355.
- (161) Niculescu, A.-G.; Chircov, C.; Bîrcă, A. C.; Grumezescu, A. M. *Int J Mol Sci* **2021**, *22*, DOI: 10.3390/ijms22042011.
- (162) Zeller, P.; Legendre, A.; Jacques, S.; Fleury, M. J.; Gilard, F.; Tcherkez, G.; Leclerc, E. *J Appl Toxicol* **2017**, *37*, 287–295, DOI: 10.1002/jat.3360.
- (163) Maschmeyer, I.; Hasenberg, T.; Jaenicke, A.; Lindner, M.; Lorenz, A. K.; Zech, J.; Garbe, L. A.; Sonntag, F.; Hayden, P.; Ayehunie, S.; Lauster, R.; Marx, U.; Materne, E. M. *Eur J Pharm Biopharm* **2015**, *95*, 77–87, DOI: 10.1016/j.ejpb.2015.03.002.
- (164) Davis, C.; Lalitha Sridhar, R.; Chakraborty, S.; Zawieja, D.; Moreno, M. *FASEB J* **2021**, *35*, DOI: 10.1096/fasebj.2021.35.S1.03528.
- (165) Jang, K. J.; Mehr, A. P.; Hamilton, G. A.; McPartlin, L. A.; Chung, S.; Suh, K. Y.; Ingber, D. E. *Integr Biol (Camb)* **2013**, *5*, 1119–29, DOI: 10.1039/c3ib40049b.
- (166) Toepke, M. W.; Beebe, D. J. *Lab Chip* **2006**, *6*, 1484–6, DOI: 10.1039/b612140c.
- (167) Kang, S.-M. *BioChip J* **2021**, *16*, 13–26, DOI: 10.1007/s13206-021-00043-y.
- (168) Ahmed, S.; Chauhan, V. M.; Ghaemmaghami, A. M.; Aylott, J. W. *Biotechnol Lett* **2019**, *41*, 1–25, DOI: 10.1007/s10529-018-2611-7.
- (169) Nithiananthan, S.; Crawford, A.; Knock, J. C.; Lambert, D. W.; Whawell, S. A. *J Cell Biochem* **2017**, *118*, 878–890, DOI: 10.1002/jcb.25767.
- (170) Miranda-Azpiazu, P.; Panagiotou, S.; Jose, G.; Saha, S. *Sci Rep* **2018**, *8*, 8784, DOI: 10.1038/s41598-018-26480-8.

- (171) Mazzei, D.; Guzzardi, M. A.; Giusti, S.; Ahluwalia, A. *Biotechnol Bioeng* **2010**, *106*, 127–37, DOI: 10.1002/bit.22671.
- (172) Pedersen, J. M.; Shim, Y. S.; Hans, V.; Phillips, M. B.; Macdonald, J. M.; Walker, G.; Andersen, M. E.; Clewell H. J., 3.; Yoon, M. *Front Bioeng Biotechnol* **2016**, *4*, 72, DOI: 10.3389/fbioe.2016.00072.
- (173) Forde, H.; Harper, E.; Rochfort, K. D.; Wallace, R. G.; Davenport, C.; Smith, D.; Cummins, P. M. *Physiol Rep* **2020**, *8*, e14612, DOI: 10.14814/phy2.14612.
- (174) Ganguly, A.; Zhang, H.; Sharma, R.; Parsons, S.; Patel, K. D. *J Vis Exp* **2012**, e4032, DOI: 10.3791/4032.
- (175) Larasati, R. A.; Harbuwono, D. S.; Rahajeng, E.; Pradipta, S.; Nuraeni, H. S.; Susilowati, A.; Wibowo, H. *Biomedicines* **2019**, *7*, DOI: 10.3390/biomedicines7040074.
- (176) Oo, Z. Y.; Deng, R.; Hu, M.; Ni, M.; Kandasamy, K.; bin Ibrahim, M. S.; Ying, J. Y.; Zink, D. *Biomaterials* **2011**, *32*, 8806–15, DOI: 10.1016/j.biomaterials.2011.08.030.
- (177) Zhang, X.; Wang, X.; Keshav, V.; Wang, X.; Johanas, J. T.; Leisk, G. G.; Kaplan, D. L. *Biomaterials* **2009**, *30*, 3213–23, DOI: 10.1016/j.biomaterials.2009.02.002.
- (178) Saller, V.; Matilainen, J.; Grauschopf, U.; Bechtold-Peters, K.; Mahler, H. C.; Friess, W. *J Pharm Sci* **2015**, *104*, 1440–50, DOI: 10.1002/jps.24357.
- (179) Zhang, Z.; Szita, N.; Boccazzi, P.; Sinskey, A. J.; Jensen, K. F. *Biotechnol Bioeng* **2006**, *93*, 286–96, DOI: 10.1002/bit.20678.
- (180) Zare, M.; Ghomi, E. R.; Venkatraman, P. D.; Ramakrishna, S. *J Appl Polym Sci* **2021**, *138*, 50969, DOI: 10.1002/app.50969.
- (181) Kollias, N.; Sayre, R. M.; Zeise, L.; Chedekel, M. R. *J Photochem Photobiol B: Biol* **1991**, *9*, 135–160, DOI: 10.1016/1011-1344(91)80147-a.
- (182) Corfield, A. P.; Carroll, D.; Myerscough, N.; Probert, C. S. *Front Biosci* **2001**, *6*, D1321–57, DOI: 10.2741/corfield.
- (183) Reitsma, S.; Slaaf, D. W.; Vink, H.; van Zandvoort, M. A.; oude Egbrink, M. G. *Pflugers Arch* **2007**, *454*, 345–59, DOI: 10.1007/s00424-007-0212-8.
- (184) Paone, P.; Cani, P. D. *Gut* **2020**, *69*, 2232–2243, DOI: 10.1136/gutjnl-2020-322260.
- (185) Murgia, X.; Loretz, B.; Hartwig, O.; Hittinger, M.; Lehr, C. M. *Adv Drug Deliv Rev* **2018**, *124*, 82–97, DOI: 10.1016/j.addr.2017.10.009.
- (186) Tiffany, J. M. *Dev Ophthalmol* **2008**, *41*, 1–20, DOI: 10.1159/000131066.
- (187) Monin, L.; Whettlock, E. M.; Male, V. *Immunology* **2020**, *160*, 106–115, DOI: 10.1111/imm.13136.
- (188) Fischer, A. J.; Pino-Argumedo, M. I.; Hilkin, B. M.; Shanrock, C. R.; Gansemer, N. D.; Chaly, A. L.; Zarei, K.; Allen, P. D.; Ostedgaard, L. S.; Hoffman, E. A.; Stoltz, D. A.; Welsh, M. J.; Abou Alaiwa, M. H. *JCI Insight* **2019**, *4*, DOI: 10.1172/jci.insight.124863.

- (189) Schroeder, B. O. *Gastroenterol Rep (Oxf)* **2019**, *7*, 3–12, DOI: 10.1093/gastro/goy052.
- (190) Navabi, N.; McGuckin, M. A.; Lindén, S. K. *PLoS One* **2013**, *8*, e68761, DOI: 10.1371/journal.pone.0068761.
- (191) Reuter, C.; Alzheimer, M.; Walles, H.; Oelschlaeger, T. A. *Cell Microbiol* **2018**, *20*, e12812–e12812, DOI: 10.1111/cmi.12812.
- (192) Gagnon, M.; Zihler Berner, A.; Chervet, N.; Chassard, C.; Lacroix, C. *J Microbiol Methods* **2013**, *94*, 274–9, DOI: 10.1016/j.mimet.2013.06.027.
- (193) Johansson, M. E.; Hansson, G. C. *Nat Rev Immunol* **2016**, *16*, 639–49, DOI: 10.1038/nri.2016.88.
- (194) Aldecoa, C.; Llau, J. V.; Nuviols, X.; Artigas, A. *Ann Intensive Care* **2020**, *10*, 85, DOI: 10.1186/s13613-020-00697-1.
- (195) Zeng, Y.; Tarbell, J. M. *PLoS One* **2014**, *9*, e86249, DOI: 10.1371/journal.pone.0086249.
- (196) Dimitrievska, S.; Gui, L.; Weyers, A.; Lin, T.; Cai, C.; Wu, W.; Tuggle, C. T.; Sundaram, S.; Balestrini, J. L.; Slattery, D.; Tchouta, L.; Kyriakides, T. R.; Tarbell, J. M.; Linhardt, R. J.; Niklason, L. E. *Arterioscler Thromb Vasc Biol* **2016**, *36*, 1847–53, DOI: 10.1161/ATVBAHA.116.308023.
- (197) Dragovich, M. A.; Genemaras, K.; Dailey, H. L.; Jedlicka, S.; Frank Zhang, X. *Cell Mol Bioeng* **2017**, *10*, 102–113, DOI: 10.1007/s12195-016-0463-6.
- (198) Kalucka, J.; Bierhansl, L.; Wielockx, B.; Carmeliet, P.; Eelen, G. *Pflugers Arch* **2017**, *469*, 473–483, DOI: 10.1007/s00424-017-1946-6.
- (199) Butler, M. J.; Down, C. J.; Foster, R. R.; Satchell, S. C. *Am J Pathol* **2020**, *190*, 742–751, DOI: 10.1016/j.ajpath.2019.11.015.
- (200) Ebong, E. E.; Lopez-Quintero, S. V.; Rizzo, V.; Spray, D. C.; Tarbell, J. M. *Integr Biol (Camb)* **2014**, *6*, 338–47, DOI: 10.1039/c3ib40199e.
- (201) Florian, J. A.; Kosky, J. R.; Ainslie, K.; Pang, Z.; Dull, R. O.; Tarbell, J. M. *Circ Res* **2003**, *93*, e136–42, DOI: 10.1161/01.RES.0000101744.47866.D5.
- (202) Mochizuki, S.; Vink, H.; Hiramatsu, O.; Kajita, T.; Shigeto, F.; Spaan, J. A.; Kajiya, F. *Am J Physiol Heart Circ Physiol* **2003**, *285*, H722–6, DOI: 10.1152/ajpheart.00691.2002.
- (203) Uchimido, R.; Schmidt, E. P.; Shapiro, N. I. *Crit Care* **2019**, *23*, 16, DOI: 10.1186/s13054-018-2292-6.
- (204) El-Ali, J.; Sorger, P. K.; Jensen, K. F. *Nature* **2006**, *442*, 403–11, DOI: 10.1038/nature05063.
- (205) D'Ausilio, A. *Behav Res Methods* **2012**, *44*, 305–13, DOI: 10.3758/s13428-011-0163-z.
- (206) Stöbener, D. D.; Weinhart, M. *Acta Biomater* **2021**, *136*, 243–253, DOI: 10.1016/j.actbio.2021.09.012.
- (207) Sivarapatna, A.; Ghaedi, M.; Le, A. V.; Mendez, J. J.; Qyang, Y.; Niklason, L. E. *Biomaterials* **2015**, *53*, 621–33, DOI: 10.1016/j.biomaterials.2015.02.121.

- (208) Tiemeier, G. L.; Wang, G.; Dumas, S. J.; Sol, W.; Avramut, M. C.; Karakach, T.; Orlova, V. V.; van den Berg, C. W.; Mummery, C. L.; Carmeliet, P.; van den Berg, B. M.; Rabelink, T. J. *Stem Cell Rep* **2019**, *13*, 803–816, DOI: 10.1016/j.stemcr.2019.10.005.
- (209) Wang, L.; Xiang, M.; Liu, Y.; Sun, N.; Lu, M.; Shi, Y.; Wang, X.; Meng, D.; Chen, S.; Qin, J. *Biomicrofluidics* **2016**, *10*, 014106, DOI: 10.1063/1.4940041.
- (210) Giantsos-Adams, K. M.; Koo, A. J.; Song, S.; Sakai, J.; Sankaran, J.; Shin, J. H.; Garcia-Cardena, G.; Dewey C. F., J. *Cell Mol Bioeng* **2013**, *6*, 160–174, DOI: 10.1007/s12195-013-0273-z.
- (211) Jones, C. G.; Chen, C. *Sens Actuator A Phys* **2020**, *314*, DOI: 10.1016/j.sna.2020.112216.

# List of Publications and Conference Contributions

## Manuscripts and Publications

Step-by-Step Development of a Toolbox for Dynamic Cell Culture. *Unpublished manuscript*.

**Lindner, M.**; Laporte, A.; Block, S.; Elomaa, L.; Weinhart, M. Physiological Shear Stress Enhances Differentiation, Mucus-Formation and Structural 3D Organization of Intestinal Epithelial Cells *In Vitro*. *Cells* **2021**, *10*, 2062.

**DOI:** 10.3390/cells10082062

**Lindner, M.**; Laporte, A.; Elomaa, L.; Lee-Thedieck, C.; Olmer, R.; Weinhart, M. Flow-induced glycocalyx formation and cell alignment of HUVECs compared to iPSC-derived ECs for tissue engineering applications. *Manuscript in submission*.

Elomaa, L.; **Lindner, M.**; Leben, R.; Niesner, R.; Weinhart, M. *In vitro* vascularization of hydrogel-based tissue constructs via a combined approach of cell sheet engineering and dynamic perfusion cell culture. *Manuscript in preparation*.

## Poster Presentations

**Lindner, M.**; Stöbener, D. D.; Hoppensack, A.; Elomaa, L.; Weinhart, M. Establishment of a Platform for Dynamic Cell Cultivation on Thermoresponsive Surfaces. TERMIS European Chapter Meeting, Rhodes, Greece, **2019**.

**Lindner, M.**; Elomaa, L.; Stöbener, D.; Weinhart, M. Effect of Architecture of Photocurable PCL on Suitability for 3D-Scaffold Printing. Jahrestagung der Deutschen Gesellschaft für Biomaterialien, Braunschweig, Germany, **2018**.